

School of Civil and Mechanical Engineering

**Novel Data Analytics for Developing Sensitive and Reliable Damage
Indicators in Structural Health Monitoring**

**Zhen Peng
0000-0001-9352-9613**

**This thesis is presented for the Degree of
Doctor of Philosophy
of
Curtin University**

April 2022

Declaration

To the best of my knowledge and belief this thesis contains no material previously published by any other person except where due acknowledgement has been made.

This thesis contains no material which has been accepted for the award of any other degree or diploma in any university.

Signature:

Date:.....2022-03-02

ABSTRACT

Civil infrastructures are prone to deterioration due to routine services and exposure to extreme operational conditions, such as earthquake, typhoon and corrosive environment. The accumulation of structural damage will adversely affect the serviceability, integrity, reliability and shorten the life expectancy of civil engineering structures. Structural health monitoring (SHM) and condition assessment are crucial for ensuring safety and preserving the service life of existing infrastructure. With massively availability of vibration data collected from the long-term SHM applications, an immediate task is to accurately and effectively identify potential structural damage at an early stage. Based on the fact that structural damage will alter the structural vibration characteristics, vibration-based damage detection methods have been widely used in structural condition assessment during the past decades. The success of vibration-based damage detection methods largely relies on the extraction of reliable features that are sensitive to structural damage but robustness to variation of the operational condition. However, the variation of operational and environmental conditions, as well as the presence of nonlinearities and measurement noise, are common in SHM practice, which can adversely affect the accuracy of vibration-based damage detection methods if not properly addressed.

The research carried out in this thesis focuses on developing novel data analytics and damage detection methods that are applicable to SHM applications subjected to operational and environmental condition changes, nonlinearity and/or measurement noise. The contents of this thesis include:

(1) Time-frequency analysis is suitable for processing the time-varying and nonstationary signal, the estimated modal parameters can be further used for structural damage detection. To estimate the high-resolution instantaneous frequency for nonstationary vibration signal polluted with strong noise, an adaptive Duffing oscillator-based time-frequency analysis approach is proposed in this study. With a high sensitivity to detect slight frequency shift and immunity to noise effect, the intermittent chaotic of Duffing oscillator system is introduced to accurately identify the time-varying instantaneous frequencies. Furthermore, an adaptive Duffing oscillator array is adopted to improve the efficiency of instantaneous frequency identification. The proposed approach is compared with empirical wavelet transform (EWT) and Hilbert transform (EWT-HT)-based method to highlight the superiority of the proposed approach in obtaining high-resolution time-frequency analysis results for nonstationary signals with strong noise.

(2) Linear theory-based system parameter identification or modal analysis methods might result in biased parameter estimation results and fail to accurately detect nonlinear structural

damage. An output-only Volterra series model is proposed to quantify the nonlinearity of vibration responses and further used to perform nonlinear structural damage assessment. The main idea is to replace the excitation input to the Volterra model with the dynamic response measured from a specific location, and to describe the nonlinearity in the region between two nodes with output-only data. The contribution of nonlinearities is employed as damage feature to locate and quantify structural nonlinear damage.

(3) To improve the identifiability of structural damage, a systematic singular spectrum analysis (SSA) based phase space technique (PST) framework for structural damage detection by using the higher order frequency response components is proposed. The high dimensional dynamic acceleration response is decomposed into several low dimensional components via SSA. Then the change in phase space trajectory (CPST) reconstructed from the decomposed component with higher order responses of structures under intact and damaged states is utilized to identify the structural condition changes. To demonstrate the advantage of using the proposed method for structural damage detection in providing a higher sensitivity than the traditional modal information based indices, damage detection results by using the proposed SSA-CPST index are further compared with those from the relative change of other commonly used modal-based indices, i.e. natural frequency, flexibility, COMAC and ECOMAC.

(4) Due to the complexity in practical structural systems and uncertainties in loading scenarios, the in-situ measured responses are inevitable of high-dimensional frequency components, which may not be fully unfolded in the phase space. To address the issue faced by PST-based methods for identifying structural damage using high dimensional dynamic responses of structures under stochastic excitations, a data-driven structural damage assessment approach using phase space embedding strategy in conjunction with Koopman operator under stochastic excitations is proposed. The proposed approach consists of three main steps. Firstly, structural vibration responses from a single channel are projected to the dynamic attractor of high dimensional system in phase space using embedding strategy. The second step connects the consecutive embedded Hankel matrix with a mapping matrix, that is, Koopman operator, and obtains the eigenvalues approximation of Koopman operator with subspace DMD. Then, the Mahalanobis distance between the eigenvalue vectors approximated under intact and current testing states is served as DSF to detect the structural condition change.

(5) The change in modal parameters due to temperature variation could be contaminated by these induced by a medium degree of damage. A novel phase space based manifold learning approach is proposed to develop damage index for structural damage detection, taking into account of the variations in environmental and operational conditions. The feasibility and superiority of using manifold learning for revealing the inherent topological structure of the

underlying systems subjected to operational conditions with the long-term vibration monitoring responses are demonstrated. DSF that is sensitive to damage but insensitive to environmental effects is developed via the multivariate Gaussian process regression model. Long-term vibration responses measured from two in-situ bridges, namely Dowling Hall Footbridge and Z24 bridge are utilized to validate the applicability and performance of the proposed approach for structural damage detection under ambient operation conditions.

(6) Most structures are subjected to a certain extent of nonlinear and non-stationary vibration behavior, therefore, modal analysis techniques based on linearity assumption may fail to provide accurate estimation or prediction of nonlinear problems. To overcome this challenge, this thesis demonstrates that linear and nonlinear structural dynamic vibrations can be represented by a universal forced linear model in a finite dimension space projected by time-delay coordinates. Similar to the modal analysis of linear systems, the linearized model allows for handling nonlinear vibration responses as a superposition of the discovered nonlinear coordinate basis. Numerical and experimental studies on nonlinear structures are conducted to demonstrate that the finite dimensional DMD based on the discrete Hankel SVD coordinate is highly symmetrically structured, and is able to accurately predict the responses of nonlinear systems with limited training datasets.

(7) Application of the proposed linearization of nonlinear model for identifying the condition change of structures with initial nonlinearity. The eigen-frequencies extracted from the linearization model are served as damage features. The performance of using the eigen-frequencies from DMD for nonlinear structural damage detection is compared with the natural frequencies obtained from FFT and the time-frequency analysis method to emphasize the superiority of the proposed approach.

In summary, the research work conducted and the results obtained in this dissertation contribute to the development of robust and reliable vibration-based DSFs applicable to the SHM of civil engineering structures with the consideration of environmental condition change, system nonlinearities and measurement noise.

ACKNOWLEDGEMENTS

I would like to express my greatest thanks and respects to my supervisors, Prof. Hong Hao and Associate Prof. Jun Li for their outstanding guidance and add ideas throughout my study period for the PhD degree. Prof. Hong Hao has been a role model, who is always dedicated to supporting students in every possible way. Associate Prof. Jun Li has provided a supportive environment that has allowed me to explore my interests. I deeply appreciate how you have always been so friendly and encouraging of all of my efforts and struggles during my time at Curtin University.

I feel lucky to study at the Centre for Infrastructural Monitoring and Protection (CIMP). I would like to express my sincere thanks to the staff members in CIMP: Associate Prof. Kaiming Bi, Associate Prof. Wensu Chen for their assistance during my study. Many thanks are also extended to the current and former PhD students in CIMP: Dr. Yu Xin, Dr. Gao Fan, Dr. Ning Yang, Dr. Zhenghao Ding, Dr. Ruisheng Ma, Dr. Haoran Zuo, Dr. Zhejian Li, Dr. Chao Li, Dr. Huawei Li, Dr. Zhijie Huang, Mr. Yue Zhong, Ms. Han Li, Mr. Wenhao Zheng, Mr. Zhixing Li, Mr. Ruishan Chen for their great precious friendship and kind help.

All of my love and thanks go to my wife Yanlin Peng, who has stood by me through all this journey. This thesis would not have been possible without her understanding and encouragement. I would like to extend my sincere thanks to my parents for their unconditional love and endless support when I face difficulties.

I gratefully acknowledge the financial support from the China Scholarship Council Postgraduate Scholarship Grant 201806120049, and postgraduate top-up scholarship at Curtin University.

LIST OF PUBLISHED WORK

This thesis contains published work and/or work prepared for publication, which have been co-authored. The bibliographical details of the work and where they appear in the thesis are outlined below.

Chapter 2

Peng, Z., Li, J., Hao, H., & Xin, Y. (2020). High-resolution time-frequency representation for instantaneous frequency identification by adaptive Duffing oscillator. *Structural Control and Health Monitoring*, 27(12), e2635. <https://doi.org/10.1002/stc.2635>.

Chapter 3

Peng, Z., Li, J., Hao, H., & Li, C. (2021). Nonlinear structural damage detection using output-only Volterra series model. *Structural Control and Health Monitoring*, 28(9), e2802. <https://doi.org/10.1002/stc.2802>.

Chapter 4

Peng, Z., Li, J., Hao, H., & Nie, Z. (2021). Improving identifiability of structural damage using higher order responses and phase space technique. *Structural Control and Health Monitoring*, 28(10), e2808. <https://doi.org/10.1002/stc.2808>.

Chapter 5

Peng, Z., Li, J., Hao, H. (2022). Data Driven Structural Damage Assessment using Phase Space Embedding and Koopman Operator under Stochastic Excitations. *Engineering Structures*, 255, 113906. <https://doi.org/10.1016/j.engstruct.2022.113906>.

Chapter 6

Peng, Z., Li, J., Hao, H. (2022). Structural damage detection via phase space based manifold learning under changing environmental and operational conditions. *Engineering Structures*, 263, 114420. <https://doi.org/10.1016/j.engstruct.2022.114420>.

Chapter 7

Peng, Z., Li, J., Hao, H. Finite linear representation of nonlinear structural dynamics using phase space embedding coordinate. (Under review).

Chapter 8

Peng, Z., Li, J. (2022). Phase space reconstruction and Koopman operator based linearization of nonlinear model for damage detection of nonlinear structures. *Advances in Structural Engineering*, 25(7), 1652-1669. <https://doi.org/10.1177/13694332221082729>.

STATEMENT OF CONTRIBUTION OF OTHERS

The works presented in this thesis were primarily designed, numerically executed, interpreted and written by the candidate and also the first author of the publications (Zhen Peng). Significant input to the works was also provided by co-authors. Contributions of the co-authors are described below. The signed contribution form is attached in the appendix.

Chapters 2

Prof. Hong Hao and Associate Prof. Jun Li defined the overall scope and objectives of the works, revised and edited the manuscript, provided intellectual input towards data processing, analysis, and results discussion. Dr. Yu Xin provided some help on the MATLAB program of the EWT-HT approach and simulation of a two-storey shear building under the ground motion.

Chapters 3

Prof. Hong Hao and Associate Prof. Jun Li defined the overall scope and objectives of the works, revised and edited the manuscript, provided intellectual input towards data processing, analysis, and results discussion. Dr. Chao Li conducted the experimental test.

Chapter 4

Prof. Hong Hao, Associate Prof. Jun Li and Prof. Zhenhua Nie from Jinan University defined the overall scope and objectives of the works. Prof. Hong Hao and Associate Prof. Jun Li, revised and edited the manuscript, provided intellectual input towards data processing, analysis, and results discussion.

Chapter 5 to Chapter 7

Prof. Hong Hao and Associate Prof. Jun Li defined the overall scope and objectives of the works, revised and edited the manuscript, provided intellectual input towards data processing, analysis, and results discussion. The experimental test of the eight-storey shear-type steel frame structure used in Chapter 7 was conducted by Associate Prof. Jun Li. Associate Prof. Jun Li also assisted with the dynamic testing set-up, data recording of the test on aluminum column with magnet induced nonlinearity used in Chapter 7.

Chapter 8

Associate Prof. Jun Li defined the overall scope and objectives of the works, revised and edited the manuscript, provided intellectual input towards data processing, analysis, and results discussion. Associate Prof. Jun Li assisted with the dynamic testing set-up, data recording of the test on aluminum column with magnet induced nonlinearity.

LIST OF RELEVANT ADDITIONAL PUBLICATIONS

The additional publications relevant to the thesis with the bibliographical details are listed below.

[1] **Peng, Z.**, Li, J*, & Hao, H. (2022). Long-term Condition Monitoring of Cables for In-service Cable-stayed Bridges Using Matched Vehicle-induced Cable Tension Ratios. *Smart Structures and Systems*, 29(1), 167-179. <https://doi.org/10.12989/sss.2022.29.1.167>.

TABLES OF CONTENTS

ABSTRACT.....	I
ACKNOWLEDGEMENTS.....	IV
LIST OF PUBLISHED WORK.....	V
STATEMENT OF CONTRIBUTION OF OTHERS.....	VI
LIST OF RELEVANT ADDITIONAL PUBLICATIONS.....	VII
TABLES OF CONTENTS.....	VIII
LIST OF FIGURES.....	XI
LIST OF TABLES.....	XX
LIST OF ABBREVIATIONS.....	XXI
Chapter 1 INTRODUCTION.....	1
1.1 Background.....	1
1.2 Literature review of the vibration-based structural damage detection.....	3
1.3 Research Objectives.....	9
1.4 Research Outline.....	10
References.....	12
Chapter 2 HIGH RESOLUTION TIME FREQUENCY REPRESENTATION FOR INSTANTANEOUS FREQUENCY IDENTIFICATION BY ADAPTIVE DUFFING OSCILLATOR.....	16
ABSTRACT.....	16
2.1 Introduction.....	16
2.2 Theoretical Background and Development.....	19
2.3 Numerical verification.....	25
2.4 Experimental Validations.....	31
2.5 Conclusions.....	37
References.....	38
Chapter 3 NONLINEAR STRUCTURAL DAMAGE DETECTION USING OUTPUT-ONLY VOLTERRA SERIES MODEL.....	41
ABSTRACT.....	41
3.1 Introduction.....	41
3.2 Theoretical Background and Development.....	44
3.3 Numerical Studies.....	49
3.4 Experimental verifications.....	55
3.5. Conclusions.....	66
References.....	68
Chapter 4 IMPROVING IDENTIFIABILITY OF STRUCTURAL DAMAGE USING HIGHER ORDER RESPONSES AND PHASE SPACE TECHNIQUE.....	72

ABSTRACT.....	72
4.1 Introduction.....	72
4.2 Theoretical Background and Development.....	76
4.3 Numerical verification	81
4.4 Experimental Application	93
4.5 Conclusions.....	100
References.....	102
Chapter 5 DATA DRIVEN STRUCTURAL DAMAGE ASSESSMENT USING PHASE SPACE EMBEDDING AND KOOPMAN OPERATOR UNDER STOCHASTIC EXCITATIONS.....	105
ABSTRACT.....	105
5.1 Introduction.....	106
5.2 Theoretical Background and Development.....	109
5.3 Numerical verifications.....	117
5.4 Verifications with in-field testing data.....	124
5.5 Conclusions.....	128
References.....	130
Chapter 6 STRUCTURAL DAMAGE DETECTION VIA PHASE SPACE BASED MANIFOLD LEARNING UNDER CHANGING ENVIRONMENTAL AND OPERATIONAL CONDITIONS.....	133
ABSTRACT.....	133
6.1 Introduction.....	133
6.2 Theoretical Background and Development.....	138
6.3 Real-world Application 1: Dowling Hall Footbridge	142
6.4 Real-world Application 2: Z24 Bridge	149
6.5 Conclusions.....	159
References.....	161
Chapter 7 FINITE LINEAR REPRESENTATION OF NONLINEAR STRUCTURAL DYNAMICS USING PHASE SPACE EMBEDDING COORDINATE.....	164
ABSTRACT.....	164
7.1 Introduction.....	164
7.2 Data-driven decomposition of nonlinear dynamic into forced linear model	167
7.3 Experimental verification with a linear structure.....	173
7.4 Nonlinear structures	179
7.5 Conclusions.....	190
References.....	192
Chapter 8 PHASE SPACE RECONSTRUCTION AND KOOPMAN OPERATOR BASED LINEARIZATION OF NONLINEAR MODEL FOR DAMAGE DETECTION OF NONLINEAR STRUCTURES.....	195

ABSTRACT.....	195
8.1 Introduction.....	195
8.2 Data-driven decomposition of nonlinear dynamic system into linear model.....	199
8.3 Experimental verifications on an aluminum beam with magnet induced nonlinearity	203
8.4 Experimental verifications on a precast segmental concrete beam.....	214
8.5 Conclusions.....	219
References.....	221
Chapter 9 CHAPTER 9 CONCLUSIONS AND RECOMMENDATIONS	224
9.1 Main conclusions	224
9.2 Recommendations for future works.....	226
APPENDIX I	228
APPENDIX II.....	231
APPENDIX III.....	236
BIBLIOGRAPHY DISCLAIMER.....	243

LIST OF FIGURES

Figure 2-1. The vector chart of the overall driving force.....	20
Figure 2-2. Duffing oscillators array.....	21
Figure 2-3. The framework of the proposed approach based on adaptive Duffing oscillator for instantaneous frequency identification.....	25
Figure 2-4. The simulated nonstationary signal: (a) Time series with 30% (SNR=10.44dB) white noise; (b) Theoretical instantaneous frequency; and (c) Fourier spectrum.	26
Figure 2-5. Instantaneous frequency identification results by using EWT-HT based method: (a) without noise; (b) with 30% noise.....	28
Figure 2-6. Time-frequency analysis results by using the proposed adaptive Duffing approach: (a) without noise; (b) with 30% noise.....	29
Figure 2-7. Two-storey shear building.....	30
Figure 2-8. The applied seismic ground motion and the corresponding response of the structural model: (a) El Centro ground acceleration record; (b) The horizontal acceleration response of the first floor.	31
Figure 2-9. Time-frequency analysis results by using: (a) EWT-HT method; (b) The proposed approach.....	31
Figure 2-10. Schematic experimental setup: (a) plan view; (b) cross-sections. (unit: mm)...	32
Figure 2-11. Overview of experimental setup of the bridge-vehicle system	32
Figure 2-12. Vertical acceleration response at the mid-span under moving vehicle: (a) Normalized acceleration; (b) Frequency spectrum.	34
Figure 2-13. Vertical acceleration response at the mid span under hammer impact loads: (a) Normalized acceleration; (b) Frequency spectrum	34
Figure 2-14. Instantaneous frequency identification results by using EWT-HT method.	35
Figure 2-15. Instantaneous frequency identification results by the proposed approach	36
Figure 3-1. Flowchart of the proposed output-only nonlinear structural damage assessment	48
Figure 3-2. DOFs at the crack element when the crack is: (a) open; (b) closed.	49
Figure 3-3. Finite element beam model and the cross-section.....	51

Figure 3-4. Frequency spectra of the measured responses from: (a) intact beam; (b) open crack with 10% damage; (c) breathing crack with 10% damage.....	52
Figure 3-5. The prediction error and kernel parameters number with different memory lengths.	53
Figure 3-6. Comparison of true responses and predicted responses from Volterra series model under white noise excitations: (a) time domain responses; (b) zoom in time domain response; (c) frequency domain spectrum.....	53
Figure 3-7. Nonlinear contribution index and its standard derivation under different excitation amplitudes: (a) 5% damage; (b) 10% damage; (c) 15% damage; and (d) 20% damage.	55
Figure 3-8. The experimental setup for shake table tests of precast segmental column reinforced with FRP bars (Specimen 1): (a) overall view and (b) schematic diagram. (unit: mm).....	57
Figure 3-9. Input ground motion along the E-W direction: (a) Time domain, (b) Frequency domain.	57
Figure 3-10. Measured acceleration responses in: (a) time domain; (b) frequency domain. .	58
Figure 3-11. Time-frequency analysis results of input excitation and measured responses of Specimen 1: (a) ground motion excitation (PGA=0.1 g); (b) #A1; (c) #A2; (d) #A3; (e) #A4; and (f) #A5.....	59
Figure 3-12. Damage observations of the precast segmental column (Specimen 1) reinforced with FRP bars under different PGA values: (a) 0.6 g; (b) 0.7 g; (c) 0.8 g; (d) 1.1 g.	60
Figure 3-13. Damage observations of the precast segmental column (Specimen 2) reinforced with ordinary steel bars under different PGA values: (a) 0.5 g; (b) 0.6 g; (c) 0.7 g; (d) 0.8 g.	60
Figure 3-14. The prediction error and kernel parameters number with different memory lengths.	61
Figure 3-15. Contribution of component signal corresponding to each of the three kernels: (a) #A1 - #A2; (b) #A2-#A3; and (c) #A4-#A5.	62
Figure 3-16. Comparison of true responses and predicted responses from Volterra series model under white noise excitations: (a) time domain responses; (b) zoom in time domain response; (c) frequency domain spectrum.....	63
Figure 3-17. The evolution of nonlinear contribution index of segmental columns subjected to white noise excitations: (a) Specimen 1; and (b) Specimen 2.	65

Figure 3-18. Histogram plot of the nonlinear contribution index of segmental columns subjected to white noise excitations: (a) Specimen 1; and (b) Specimen 2.	65
Figure 4-1. Schematic demonstration of CPST calculation	80
Figure 4-2. Flowchart of the proposed SSA based PST technique for structural damage detection.....	81
Figure 4-3. Planar truss model used in the numerical study.	82
Figure 4-4. Response of node 7 under the impact load: (a) Accelerations; (b) Frequency spectra.	83
Figure 4-5. Singular values from SVD of acceleration responses at node 7.....	84
Figure 4-6. Frequency spectra of decomposed components of the response at node 7 by using SSA: (a) 1 st ; (b) 2 nd ; (c) 3 rd ; (d) 4 th	85
Figure 4-7. Singular values of each decomposed component: (a) 1 st ; (b) 2 nd ; (c) 3 rd ; (d) 4 th	85
Figure 4-8. Time delay parameters obtained from the normalized auto-correlation functions of each component: (a) 1 st ; (b) 2 nd ; (3) 3 rd ; (4) 4 th	86
Figure 4-9. Reconstructed PST of: (a) 1 st SSA component; (b) 2 nd SSA component; (3) 3 rd SSA component; (4) 4 th SSA component.	87
Figure 4-10. Comparison of average CPST value of four decomposed response components by SSA.	88
Figure 4-11. Scatterplot for the CPST values under different structural conditions: (a) Original signal; (b) The 4 th component.	88
Figure 4-12. Damage detection results for single damage case when using different decomposed components without noise: (a) 1 st ; (b) 2 nd ; (c) 3 rd ; (d) 4 th and with 10% white noise: (e) 1 st ; (f) 2 nd ; (g) 3 rd ; (h) 4 th	91
Figure 4-13. Damage detection results for single damage case with 10% pink noise when using different decomposed components: (a) 1 st ; (b) 2 nd ; (c) 3 rd ; (d) 4 th and with 1% modelling error when using different decomposed components: (e) 1 st ; (f) 2 nd ; (g) 3 rd ; (h) 4 th	91
Figure 4-14. Damage detection results for multiple damage case when using different decomposed components: without noise: (a) 1 st ; (b) 2 nd ; (c) 3 rd ; (d) 4 th and with 10% white noise: (e) 1 st ; (f) 2 nd ; (g) 3 rd ; (h) 4 th	93
Figure 4-15. Damage detection results for multiple damage case with 10% pink noise when using different decomposed components: (a) 1 st ; (b) 2 nd ; (c) 3 rd ; (d) 4 th and with 1% modelling error when using different decomposed components: (e) 1 st ; (f) 2 nd ; (g) 3 rd ; (h) 4 th	93

Figure 4-16. The sketch of pre-stressed concrete beam: (a) plan view; (b) cross-sections. (unit: mm).....	94
Figure 4-17. Experimental setup.....	95
Figure 4-18. The crack distribution pattern in the damaged beam model under different loads: (a) Increment 1; (b) Increment 2; (c) Increment 3.	96
Figure 4-19. Observed crack locations and heights.	96
Figure 4-20. Acceleration responses of sensor #1 under hammer loads and different loading increments: (a) Time domain; (b) Frequency spectra.	97
Figure 4-21. Fourier spectra of decomposed components from sensor #1: (a) 1 st ; (b) 2 nd ; (c) 3 rd ; (d) 4 th	98
Figure 4-22. Damage detection results by SSA based CPST: (a) 3 rd component; (b) 4 th component.....	99
Figure 4-23. Comparison of the proposed damage index and traditional ones.....	100
Figure 5-1. An example response of Duffing oscillator: (a) Time series displacement x_1 ; (b) The phase space attractor plotted with state vector x ; (c) Attractor reconstructed from x_1 with embedding strategy.	111
Figure 5-2. Schematic diagram of Koopman operator.....	112
Figure 5-3. The flowchart of the proposed structural damage assessment approach.....	117
Figure 5-4. Sixty-one elements planar truss structure.....	118
Figure 5-5. Singular values calculated from the acceleration responses at node 6 of the truss structure under reference and damaged states; (b) The slope of singular values.	121
Figure 5-6. Distributions of DSF values obtained by using different window lengths:.....	122
Figure 5-7. Damage identification results by using the vertical acceleration responses of node 6 under six loading scenarios (log-scale).....	123
Figure 5-8. Damage identification results by using the vertical acceleration responses of node 15 under six loading scenarios (log-scale).....	124
Figure 5-9. The Z24 bridge and its sensor locations: (a) Front and top views; (b) Installed accelerometer locations.....	125
Figure 5-10. Measured acceleration responses at V2 from reference state and each damage scenario.	126

Figure 5-11. Singular values calculated from the acceleration responses of Z24 bridge under reference and damage states, (b) the slope of singular value.	126
Figure 5-12. Distribution of DSF values identified with different window size parameters: (a) $n=3000$; (b) $n=4000$; (c) $n=5000$	127
Figure 5-13. (a) Damage identification results (log-scale) under the reference state and different damage scenarios, (b) Sensitivity analysis and comparison.....	128
Figure 6-1. An illustrative example of manifold learning: (a) Original data in a high dimensional phase space with a Swiss roll-like topologic inherent structure; (b) Two-dimensional embedding via manifold learning.	137
Figure 6-2. Flowchart of the proposed approach for structural damage detection from data obtained with varying environmental conditions.....	142
Figure 6-3. (a) Overview of the Dowling Hall footbridge; (b) Locations of installed sensors [32].....	143
Figure 6-4. The identified first four natural frequencies during the monitored period.	143
Figure 6-5. Air temperature variations during the monitored period.....	144
Figure 6-6. Visualisation of the relationships between the pairs of the first four natural frequencies. (The color bar denotes the environmental temperature).	144
Figure 6-7. Visualisation of the nonlinear manifold of the Dowling Hall footbridge in the phase space spanned by the first three natural frequencies. (The color bar denotes the environmental temperature).	145
Figure 6-8. Effect of live load on natural frequency: (a) weekly RMS variation; (b) weekly frequency variation; (c) daily RMS variation; (b) daily frequency variation.	146
Figure 6-9. Manifold structures of the Dowling Hall Footbridge discovered by: (a) Laplacian Eigenmap method; (b) Kernel PCA method. (The color bar denotes the environmental temperature).	147
Figure 6-10. DI results of Dowling Hall footbridge: (a) Laplacian Eigenmaps with 400 training data; (b) Kernel PCA with 400 samples; and (c) Kernel PCA with 1500 samples.	149
Figure 6-11. The first five natural frequencies during the monitoring period (the progressive damage scenarios are denoted by green background color).....	151
Figure 6-12. Air temperature measurements during the monitoring period.	151
Figure 6-13. Visualisation of the relationships between any two of the first five natural frequencies. (Colored dots: the healthy state; Black dots: the damage state).	152

Figure 6-14. Visualisation of the nonlinear manifold of Z24 bridge in the phase space spanned by the first three natural frequencies.....	153
Figure 6-15. Manifold structures of the Z24 bridge discovered by: (a) Laplacian Eigenmap method; and (b) Kernel PCA method. (The symbols shown in this figure are the same as those defined in Fig. 14).....	154
Figure 6-16. (a) The relationship between environmental temperature and the Gaussian process regression model predicted third Laplacian component; and (b) zoom in view of the samples corresponding to health state. Symbol *: training dataset (samples 1-1200); symbol .:Gaussian process regression model predicted samples corresponding to health state and symbol +: Gaussian process regression model predicted samples corresponding to damage state.	155
Figure 6-17. Comparison of damage detection results: (a) The proposed approach with training datasets of 1200 samples; (b) Kernel PCA with 1200 samples; and (c) Kernel PCA with 3000 samples.....	157
Figure 6-18. Damage detection results of using: (a) The proposed approach with 1200 training samples; and (b) Kernel PCA with 1200 training samples.	159
Figure 7-1. Procedure for representing nonlinear dynamic system as a forced linearized model using the DMD based on discrete Hankel SVD coordinate.....	172
Figure 7-2. Laboratory steel frame model.	177
Figure 7-3. (a) Comparison of power spectrum and eigen-frequencies obtained from time-delay DMD; (b) Visualization of the structure of the time-delay DMD.....	177
Figure 7-4. Comparison of the mode shapes obtained by time-delay DMD, FDD and CMIF.	178
Figure 7-5. Prediction performance of time-delay DMD algorithm.	179
Figure 7-6. (a) A six DOFs nonlinear system with ATSD and (b) mechanical modeling of the ATSD.....	180
Figure 7-7. (a) Acceleration time history of the 1 st DOF; and (b) the restoring force-displacement curve.....	181
Figure 7-8. Visualization of Koopman operator approximated from: (a) Time-delay DMD; (b) DMD with continuous Hankel SVD coordinate; and (c) DMD with discrete Hankel SVD coordinate.....	182
Figure 7-9. Comparison of prediction errors by using different DMD algorithm.	184

Figure 7-10. Violin plot of NRMSE of each DOF corresponding to different lengths of training dataset.	185
Figure 7-11. Violin plot of NRMSE of each DOF corresponding to different lengths of training dataset with 5% measurement noise.	186
Figure 7-12. Using the DMD with discrete Hankel SVD coordinate to forecast the future 50 s of the vibration data.	187
Figure 7-13. The experimental setup: (a) Layout of the aluminum specimen with a tip magnet; (b) schematic diagram; and (c) spring equivalents for the magnet induced repulsive force, resulting in stiffness hardening.	188
Figure 7-14. The free decay vibration responses in: (a) Time domain; and (b) Frequency domain.	188
Figure 7-15. Visualizing the structure of: (a) Time-delay DMD; (b) DMD with continuous Hankel SVD coordinate; and (c) DMD with discrete Hankel SVD coordinate.	190
Figure 7-16. Response forecasting results of a nonlinear structure by using DMD with discrete Hankel SVD coordinate.	190
Figure 8-1. Schematic diagram of Koopman operator.	200
Figure 8-2. The procedure of obtaining the damage feature from the nonlinear linearization framework.	202
Figure 8-3. The experimental setup: (a) Layout of the aluminum specimen with magnet installed at the top tip; (b) Schematic diagram of experimental setup.	205
Figure 8-4. Spring equivalents for the magnet induced repulsive force resulting in stiffness hardening effect: (a) Magnet induced repulsive force; (b) Equivalent spring model.	205
Figure 8-5. Use of nuts to simulate the structural condition change.	205
Figure 8-6. The measured acceleration responses and obtained frequency spectra from the specimen subjected to free vibration (a-b), seismic excitation with a GPA of 0.05g (c-d) and seismic excitation with a GPA of 0.1g (e-f).	206
Figure 8-7. (a) Time frequency representation of the free vibration responses of specimen; (b) the relationship between the dynamic displacement measured by LVDT #L2 and the first order natural frequency.	207
Figure 8-8. The singular value spectrum, SVD modes and the corresponding Fourier spectrum of right-singular vector of the considered nonlinear system subjected to ground motion excitation with a PGA of 0.05g.	208

Figure 8-9. Comparison of Fourier spectrum and the DMD eigen-frequencies (The Fourier spectrum is plotted in blue and the vertical red line represents the opt-DMD eigen-frequencies).

..... 209

Figure 8-10. The distributions of the first two order instantaneous frequencies under different structural conditions. Red and black lines represent the mean value and medium of instantaneous frequencies, respectively. IF means instantaneous frequency..... 210

Figure 8-11. The first two order natural frequencies identified from free vibration responses: (a) FFT frequencies;(b) mean values of time-varying instantaneous frequencies; (c) opt-DMD eigen-frequencies. The symbols \times , \star , \circ and $*$ represent structural states with one nut, two nuts, three nuts and four nuts, respectively..... 211

Figure 8-12. Comparison among the first three order eigen-frequencies identified from the structural responses subjected to seismic excitation of PGA 0.05g: (a) 1st and 2nd, (b) 1st and 3rd and (c) 2nd and 3rd FFT frequencies; (d) 1st and 2nd, (e) 1st and 3rd and (f) 2nd and 3rd mean values of time-varying instantaneous frequencies; (g) 1st and 2nd, (h) 1st and 3rd and (i) 2nd and 3rd opt-DMD eigen-frequencies. The symbols \times , \star , \circ and $*$ represents the one nut, two nuts, three nuts and four nut state, respectively..... 212

Figure 8-13. Comparison among the first three order eigenfrequency identified from structural responses subjected to seismic excitation of PGA 0.1g: (a) 1st and 2nd, (b) 1st and 3rd and (c) 2nd and 3rd FFT frequencies; (d) 1st and 2nd, (e) 1st and 3rd and (f) 2nd and 3rd mean values of time-varying instantaneous frequencies; (g) 1st and 2nd, (h) 1st and 3rd and (i) 2nd and 3rd opt-DMD eigen-frequencies. The symbols \times , \star , \circ and $*$ represents the 1 nut, two nuts, three nuts and four nut state, respectively. 213

Figure 8-14. The first three order opt-DMD eigen-frequencies identified via the proposed method using the structural responses subjected to ground motion excitation of PGA 0.05g with 10% noise. The symbols \times , \star , \circ and $*$ represents the states with one nut, two nuts, three nuts and four nuts, respectively..... 214

Figure 8-15. The first three order opt-DMD eigen-frequencies identified via the proposed method using the structural responses subjected to ground motion excitation of PGA 0.1g with 10% noise. The symbols \times , \star , \circ and $*$ represents the states with one nut, two nuts, three nuts and four nuts, respectively. 214

Figure 8-16. Experimental setup: (a) Schematic diagram of experimental setup and sensor configuration; and (b) Experiment testing specimen. 216

Figure 8-17. (a) Progressive loading intervals to simulate structural damage accumulation. Blue lines represents the damage scenarios. (b) load-deflection curves of the beam. The load-

deflection curve in the region of 10-20 kN is highlighted. (c) The slope of load-deflection curve in the load range 10-20 kN for each structural state. 216

Figure 8-18. Time frequency analysis results: (a) Measured acceleration responses; (b) Fourier spectrum; and (c) The instantaneous frequency of hammer load induced vibration..... 217

Figure 8-19. Statistical distributions of the identified instantaneous frequencies by VMD-HT method: (a) The first order; and (b) The second order. Red and black lines represent the mean value and median, respectively. 219

Figure 8-20. (a) Frequencies from Fourier spectrum analysis; (b) IF mean values ; (c) DMD eigen-frequencies under different damage scenarios. The symbols ☆ , * , Δ, +, ○ and □ represent the damage scanerios DS0, DS1, DS2, DS3, DS4 and DS5, respectively. 219

LIST OF TABLES

Table 2-1. Motion states of Duffing oscillator and its corresponding Lyapunov exponents.	22
Table 2-2. Relative errors of identified instantaneous frequency results.....	29
Table 2-3. Relative errors of identified instantaneous frequency results.....	31
Table 2-4. Standard deviations and relative errors of instantaneous frequency results.	36
Table 4-1. Damage scenarios and the first three natural frequencies of the numerical truss model before and after damage.....	82
Table 4-2. MAC values (in %) between the baseline and damage states.....	82
Table 4-3. PST reconstruction parameters of each decomposed component.....	86
Table 5-1. The first five order natural frequencies of planar truss structure.....	118
Table 5-2. The excitation type and level of each loading scenario	120
Table 5-3. Natural frequencies of Z24 bridge with different pier settlements under different damage scenarios	125
Table 6-1. Z24 progressive damage test scenarios.....	150
Table 7-1. Comparison of natural frequencies obtained by time-delay DMD, FDD and CMIF	175
Table 7-2. MAC (in %) between the modes obtained by time-delay DMD and FDD.....	176
Table 7-3. MAC (in %) between the modes obtained by time-delay DMD and CMIF	176
Table 8-1. The effect of delay number on the estimation of DMD eigen-frequencies	208
Table 8-2. Comparison of the first order frequency identified from time frequency analysis, Fourier frequency and the proposed DMD Eigen frequency.	218

LIST OF ABBREVIATIONS

AMI	average mutual information
ATSD	adjustable template stiffness device
ARMA	autoregressive–moving-average
CMIF	complex mode indicator function
COMAC	coordinate modal assurance criteria
CPST	change in phase space trajectory
DI	damage indices/indicators
DMD	dynamic mode decomposition
DSF	damage sensitive feature
EMD	empirical modal decomposition
EDMD	extended dynamic mode decomposition
EEMD	ensemble empirical modal decomposition
ECOMAC	enhanced coordinate modal assurance criteria
ERA	Eigen-system realization algorithm
EWT	empirical wavelet transform
EWT-HT	empirical wavelet transform and Hilbert transform
FDD	frequency domain decomposition
FE	finite element
FFT	fast Fourier transform
FNN	false nearest neighbors
FRP	fiber-reinforced plastic
HAVOK	Hankel alternative view of Koopman
HT	Hilbert transform
IMFs	intrinsic mode functions
LLE	locally linear embedding
LSE	least squares estimation

MDOF	multi-degree-of-freedom
MDPST	Mahalanobis distance in phase space trajectory
MLE	maximum Lyapunov exponent
NARMA	nonlinear autoregressive moving average
NDT	non-destructive test
NRMSE	normalized root-mean-square-error
opt-DMD	optimized DMD
PCA	principal component analysis
PGA	peak ground acceleration
PST	phase space trajectory
RDS	random dynamical system
RMS	root mean square
SINDy	sparse identification of nonlinear dynamical systems
SHM	structural health monitoring
STFT	short time Fourier transform
SVD	singular value decomposition
SSA	singular spectrum analysis
VIV	vortex-induced vibration
VMD	variational mode decomposition
VMD-HT	variational mode decomposition-Hilbert transform

CHAPTER 1 INTRODUCTION

1.1 Background

Existing infrastructure, such as bridges and buildings exposed to the operational environment for long service life, are prone to performance degradation, owing to material deterioration, natural hazards and human-made loading conditions. As of 2020, there were more than 617,000 and 912,000 bridges across the United States and China, respectively [1]. According to the 2021 Bridge Conditions Report of the American Road & Transportation Builders Association, more than 45,000 bridges were in poor condition and classified as “structurally deficient” in 2020 [2]. The same health condition problem of civil structures is common worldwide. With an increasing number of bridges approaching to the end of their designed lifespan, conducting timely condition assessment and maintenance of existing bridges will significantly extend its life expectancy and decrease the life-cycle overall cost [3]. Structural health monitoring (SHM) techniques have gained a significant amount of attention from the academy and industry in the last several decades. The wide applications of SHM systems have accumulated massive real measured structural long-term vibration responses as well as environmental condition measurements. The massive available SHM data provide opportunities to reveal the structural performance degradation mechanism and evaluate the structural health condition under operational conditions [4].

Damage identification and condition assessment can be considered as one of the most crucial aspects in the field of SHM. Structural damage, such as cracking and spalling of the concrete, corrosion of reinforcing steel, and settlement of supports are commonly found in bridges and buildings [5]. The accumulation of structural damage will alter the stiffness, mass, damping properties, boundary condition and system connectivity. As a result, the mechanical properties and dynamic characteristics of the civil structures corresponding to different states will be different. Identifying the presence of the minor damage at an early stage can provide important evidence to understand the root causes of the structural performance anomaly and make immediate maintenance action recommendations. Four levels are usually defined in structural damage detection, namely, level 1: diagnosing the presence of damage; level 2: detecting the location; level 3: identifying the extent of damage; and level 4: predicting the remaining life of structures [6].

Available structural damage identification methods can be broadly classified into the following two main types: (i) non-destructive test (NDT); and (ii) vibration-based methods. The NDT mainly includes acoustic emission testing (AE), electromagnetic testing (ET), laser testing methods (LM), leak testing (LT), magnetic flux leakage (MFL), liquid penetrant testing

(PT), magnetic particle testing (MT), neutron radiographic testing (NR), radiographic testing (RT), thermal/infrared testing (IR), ultrasonic testing (UT) and visual testing (VT) [7]. However, the NDT methods encounter some difficulties in the application to damage detection of civil structures. Primarily, the most widely used material, concrete, is inhomogeneous and highly variable from place to place. Secondly, only the personnel and equipment assessable components of large-scale civil structures can be evaluated by using NDT methods [8]. Owing to these constraints, the NDT methods are often limited to damage detection on or beneath the surface of the structure. In comparison, vibration-based damage detection methods globally identify the occurrence, location and extent of structural damage by tracking the vibration characteristics variations between undamaged and damaged states [9]. The vibration-based methods have attracted considerable attention due to their unique ability to detect minor structural condition changes inside the structures that are invisible via regular inspection. Vibration-based damage diagnosis methods are based on the fact that structural damage, such as stiffness reduction resulting from the presence of cracks or loosening of connection, will cause changes in the vibration characteristics. Thus, structural damage is generally identified by tracking the variation of the extracted damage-sensitive features from vibration acceleration, velocity, displacement and strain responses. The scope of this thesis is limited to developing vibration-based damage detection methods.

According to whether the physical finite element (FE) model of the monitored structure is required or not, the vibration-based damage detection methods can be classified into two large groups, namely FE model updating methods and data-driven methods. Each type has its intrinsic advantages and limitations. Model updating methods usually modify structural stiffness, mass and damping matrices to minimize the residual error of modal parameters, such as vibration frequency and mode shape estimated from the analytical model and the experimental measurement [10]. It is possible to achieve Level 1-3 damage identification by using the model-based methods when the iteratively updated FE model is fine and accurate enough. However, it is time and computation resource consuming to construct a fine FE model for large-scale infrastructure and repeatedly update the model parameters. The data-driven methods usually extract damage features from time-domain, frequency-domain and time-frequency domain. Structural damage can be detected by statistically evaluating the dissimilarity in the defined damage sensitive feature (DSF) between baseline (healthy) and the currently inspected states. With the superiority in data-driven monitoring strategy which does not require FE modelling and updating, the data feature-based methods have been widely developed in the last decades [11]. However, since the physical model is not used, the data-driven methods primarily provide Level 1-2 damage detection.

In this chapter, literature review on the model-based and data-driven damage detection

methods will be conducted. Then, the research gaps and research objectives of this thesis are provided. Finally, the outline of this thesis is presented.

1.2 Literature review of the vibration-based structural damage detection methods

1.2.1 FE model updating methods

FE model updating methods can be utilized to identify the presence, location and severity of structural damage. These methods iteratively modify the structural parameters, such as stiffness, damping and mass matrices at elemental or sub-structural level as well as boundary conditions, to minimize the difference between the indexes obtained from measurement and FE model [12]. The indexes used in the model updating can be natural frequencies, mode shapes, damping coefficients, frequency response functions (FRF) and/or structural dynamic responses [13]. For large-scale structures with a large number of elements, the sub-structuring techniques can significantly enhance the computation efficiency by dividing a global structure into several independent substructures [14, 15].

The FE updating based damage detection is an inverse problem and typically ill-posed. In particular, sensors will only be installed on parts of crucial nodes or components, which means that the number of measurements is significantly less than the overall DOFs. Therefore, regularization techniques should be employed in the model updating process by introducing additional prior physical information. The value range of stiffness reduction coefficient and the sparsity of damaged locations can be used as constraints or physical-informed terms to regularize the damage identification [16].

1.2.2 Data-driven methods

The ultimate goal of data-driven damage diagnosis is to extract damage features that are sensitive to structural condition change, but is robustness to external loading, environmental conditions change, and measurement noise. The success of vibration-based damage detection largely relies on the choice of DSF [17]. In literature, the DSF extracted from structural vibration responses can be categorized into three domains: time-domain, frequency-domain and time-frequency domain. Therefore, the data-driven damage identification methods involving DSF extracted from different domains are reviewed.

1.2.2.1 Frequency domain based methods

With the development of experimental and operational modal analysis techniques, the majority of damage features are derived from frequency domain. Frequency domain

parameters, such as natural frequencies, mode shapes, mode shape curvatures, flexibility, modal strain energy, frequency response function (FRF) and transmissibility, etc., have been commonly used as indicators in structural damage detection [18]. Natural frequency is a global index that is related to the stiffness matrix, mass matrix and boundary conditions. Therefore, changes in natural frequencies have been used to conduct the Level 1 damage identification.

The mode shape is related to the element stiffness, thus the mode shape curvature and its derivatives, such as coordinate modal assurance criteria (COMAC) and enhanced coordinate modal assurance criteria (ECOMAC), have been used to detect the location of structural damage. However, as stated by Farrar and Worden [19], the damage location accuracy depends on the number of modes considered and the spatial density of sensors deployed. The flexibility matrix is defined as the inverse of the static stiffness matrix and thus can be used to alarm the damage-induced stiffness reduction. The flexibility matrix can be experimentally derived from the natural frequency and mode shape. The change in flexibility matrix before and after damage has been served as DSF to identify the location of damage [20, 21]. The FRF of a linear mechanical system is the quantitative measure of the output responses spectrum divided by the input excitation in frequency domain, which is a comprehensive representation of the original structure and is not dependent on the externally applied loads. The FRF delivers adequate information on the dynamic behavior of a structure, which has been widely applied to Level 1-2 damage detection of linear structures. More recently, some attempts have been made to quantify the damage extent (Level 3) by using the FRF-based methods. Nevertheless, the external excitation and synchronized structural responses should be measured to estimate the FRF. The dynamic excitation of large-scale structures under operating conditions is difficult or expensive to measure, which could greatly limit the applications of using FRF-based method in practical applications. To address this limitation, the power spectral density transmissibility has been studied in Ref. [22-24] and demonstrated to be sensitive to structural damage without known input excitation.

A major challenge is that modal parameters can also be significantly affected by the environmental conditions, such as temperature, wind characteristics and humidity that the structures are faced with [25]. For example, temperature affects structural properties in a complicated manner. The variations in the thermal coefficient of Young's modulus and the thermal expansion coefficient will directly or indirectly vary the stiffness, geometric dimension and boundary conditions of structures. Consequently, false structural damage detection results may occur when the temperature effects are not correctly considered.

1.2.2.2 Time domain based methods

The time-domain methods directly extract DSF from the vibration time series and quantify the statistical and/or geometrical dissimilarity of dynamic responses before and after the damage. Compared with the FE model updating based methods, the time-domain methods may not suffer from the limitation of constructing a precise FE model. Furthermore, the time-domain based DSFs are usually more sensitive to structural damage and applicable to nonlinear structures. In literature, most of the time domain methods are based on two kinds of principle. One is to establish a mathematic alternative model to represent the underlying system. Structural damage will alter the statistical distribution of mathematic model parameters or the prediction residual by using the model trained with baseline data. The mathematic alternative model can either characterize the transfer function between the external excitation and structural measurable responses, or between the responses measured from different locations. In terms of this, the representative methods includes, ARMA [26], Kalman filter [27], PST [28] and Volterra series [29] have been developed. Another principle is to characterize the irregularities or nonstationary induced by structural damage. To this end, the feasibility of using WT [30], Cointegration [31] and fractal dimension [32] based techniques have been investigated. Since the quantitative relation between the vibration responses and the damage severity cannot be explicitly established, the time domain based methods are usually limited to the Level 1-2 damage detection.

The time-domain based methods are usually not only sensitive to structural damage but also to the operational conditions, especially the external loading conditions. Therefore, reliable time-domain damage feature that is robust to the variation of operational condition, is desirable.

1.2.2.3 Time-frequency domain based methods

Real-world structures may inherently be nonlinear to a certain extent, because of the geometric nonlinearities, materials with nonlinear constitutive relationships, complex boundary conditions and joint interfaces [33]. Besides, structures may exhibit nonlinear behaviors due to the accumulation of structural damage (e.g., breathing crack, plastic deformation and joint looseness) [34]. Under this situation, linear theory-based system parameter identification or modal analysis methods might result in biased parameter estimation results and fail to accurately detect structural damage. The time-frequency analysis techniques, such as short time Fourier transform (STFT), discrete wavelet transform, Hilbert transform (HT), Wigner distribution and Choi-Williams distribution have been widely used to characterize the temporal evolution of the instantaneous frequencies, mode shapes and amplitude of nonlinear structure [35]. The above-mentioned features extracted from the time-

frequency analysis contain structural damage information. As stated by Bao et al. [36], the spikes of the identified instantaneous frequency, instantaneous phase, the Hilbert marginal spectrum, the slope of instantaneous phase can be used to identify the presence, location and relative extent of damage. In addition, the instantaneous mode shapes curvature is demonstrated to be able to identify the location of structural damage [37]. A comprehensive review of time-frequency analysis and application in system identification and damage detection is provided in Ref. [35]. A crucial procedure of time-frequency analysis is the decomposition of the original signal into several intrinsic mode functions (IMF). The empirical mode decomposition (EMD) and its variants, analytical mode decomposition, variational mode decomposition (VMD) and EWT are commonly used for nonstationary signal decomposition.

One important focus of recent research in signal processing is to represent accurately the time-frequency distribution of non-stationary signals polluted by strong noise. Despite the long success of existing time-frequency analysis approaches in processing nonstationary signals with high signal-to-noise ratios (SNR), the significant noise contamination in signals poses a challenge to the accuracy and resolution of time-frequency analysis representation, especially for the nonstationary signals with low SNR.

1.2.3 Machine learning and deep learning based methods

With emerging computing power and sensing technology in the last decade, machine learning and deep learning-based methods have been extensively applied to structural damage detection. The damage detection problem can be viewed as a pattern recognition process, which consists of three parts: (i) data acquisition; (ii) feature extraction; and (iii) classification. Depending on the requirement of pre-defining the label of structural condition in healthy state and different damage states, the machine learning-based methods can be broadly divided into supervised, unsupervised and semi-supervised learning modes. As stated in Ref. [38], deep learning is a specialized subset of machine learning based on artificial neural network. Deep learning algorithms are incredibly complex, and there are different types of neural networks to address specific problems or datasets. Therefore, the deep learning and machine learning-based damage detection methods are reviewed together.

1.2.3.1 Supervised learning methods

In the past decade, most machine learning algorithms are based on a supervised learning

manner. Usually, the frequency-domain features such as natural frequency [39], mode shape [40], transmissibility [41], FRFs [42] and time-domain features such as variance, skewness, kurtosis, wavelet energy and AR coefficients of vibration responses [39] have been found in literature. The efficiency and accuracy of commonly used machine learning classifiers, i.e. support vector machine (SVM) [43], decision tree, random forest [44], artificial neural network [45] and its variants have been extensively investigated. With sufficient input data and labelled output, the machine learning classifier can achieve a desirable damage identification accuracy.

The performance of machine learning-based methods is highly dependent on the selection of input features. However, the suitable features that can accurately characterize the measured vibration responses are structure and problem-dependent. To this end, the reliable features that can be used to maximize the classification accuracy are designed by expert knowledge or repeatedly obtained by trial-and-error during the model training procedure. In comparison, the input of deep learning-based methods, i.e., convolutional neural network (CNN), can be raw measurement, which automatically learns to extract the optimal features from data that maximize the classification accuracy [46]. This advantage made the deep learning-based methods more attractive and applicable to complicated SHM applications when massive data are available. Various alternative deep learning models have been reported, such as deep CNN [47], recurrent neural network [48] and recursive neural network [9] and deep residual network [49].

1.2.3.2 Unsupervised learning methods

In SHM practices, the data measured from the damage state is absent or significantly less than samples under the healthy state. Therefore, the unsupervised methods are more applicable to practical SHM. The unsupervised machine learning-based damage detection methods, such as k -means clustering [50] and hierarchical clustering [41], have been studied. The basic principle is to separate different structural conditions in the output space via clustering analysis. The alternative unsupervised deep learning methods, such as auto-encoders, deep belief networks, and generative adversarial networks have been developed in data science community. However, only the auto-encoders and their variants have been reported in vibration-based structural damage detection [51-53]. The main advantage of auto-encoder is to discover low-dimensional features that are most representative of the original data. However, owing to no damage label being used in the training process, the unsupervised methods are mainly applied to identify the presence of structural damage (Level 1).

1.2.3.3 Semi-supervised learning methods

The semi-supervised learning methods fall between supervised and unsupervised learning, which are suitable for the situation when a small range of changing operational and damage condition labelled data are available. It has been found that the damage identification accuracy can be substantially improved by combining the unlabeled data with a small number of labelled data [19]. For example, a novel adaptive graph filter-based semi-supervised classifier is proposed in [54] to indirectly classify the bridge damage by using drive-by measurement. Rogers et al. [55] proposed a Bayesian non-parameter clustering approach for the damage detection of bridge under operational conditions based on online feature extraction. Compared with the unsupervised learning methods, the semi-supervised learning methods can identify the presence and location of damage (level 1-2).

However, a common concern of the deep learning-based methods is the lack of physical interpretability of the models built through the deep networks.

1.2.4 Bayesian methods

The presence of measurement noise and modelling errors induce considerable uncertainties, which adversely affect the accuracy of the deterministic damage detection methods. The probabilistic methods, i.e. Bayesian framework, can explicitly quantify the posterior probability of uncertainties based on observation and prior knowledge. In this regard, the Bayesian framework has been extensively cooperated with the FE model updating, system identification, machine learning methods in the context of structural damage detection. For example, Xin et al. [56] proposed a Bayesian-based nonlinear model updating method using instantaneous characteristics of structural dynamic responses. A Bayesian FE model updating method with incomplete complex modal data has been developed in Ref. [57] and applied to probabilistic damage detection. A sparse Bayesian learning approach has been proposed by Hou et al. [58] for structural damage detection with the consideration of uncertainties and varying temperature conditions. An extensive review of the Bayesian approach in structural system identification and damage assessment is provided in Ref. [59].

1.3 Research Gaps

In literature, although vibration-based SHM methods have been extensively developed and investigated through numerical and experimental studies, the application of SHM techniques for effective condition assessment of practical structures still encounters some technical problems: 1) in time frequency analysis, the accuracy of instantaneous frequency identified from existing methods may be significantly affected when the vibration responses

are polluted with strong measurement noise; 2) it is a challenge to reliably evaluate the health condition of nonlinear structures in a data-driven manner when only the output responses are provided; 3) the sensitivities of DSF to minor structural damage occurred at an early stage is vulnerable to environmental and loading conditions ; 4) the robustness of DSF extracted from vibration responses under change environmental and operational conditions needs to be enhanced.

1.4 Research Objectives

The primary goal of this thesis is to identify reliable damage features from vibration responses that are sensitive to structural damage and insensitive to nonlinear effects, operational condition change and measurement noise. The research work includes:

1. To accurately identify the instantaneous frequency of nonstationary signals with a strong noise pollution, an adaptive Duffing oscillator-based time frequency representation approach will be developed;

2. To perform damage assessment of nonlinear structure without the prior knowledge of external excitations, an output-only Volterra series model approach, by quantifying the nonlinear behavior of structures will be developed;

3. To extend the applicability of phase space based methods to process high dimensional responses, a systematic SSA based PST framework for structural damage detection, by using the higher order frequency response components will be developed;

4. To address the issue faced by PST based methods for identifying structural damage using high dimensional dynamic responses of structures under stochastic excitations, a novel data driven approach for structural damage assessment based on phase space embedding in conjunction with stochastic Koopman operator will be proposed;

5. To detect possible condition change of structures from long term SHM data subjected to operational conditions, a phase space based manifold learning method for structural damage detection under changing environmental and operational conditions will be developed;

6. To characterize nonlinear systems from a linearized perspective for nonlinear dynamics analysis, a finite linear representation of nonlinear structural dynamics using phase space embedding coordinate will be developed;

7. To verify the feasibility and applicability of the phase space reconstruction and Koopman operator based linearization of nonlinear model for damage detection of nonlinear structures.

1.5 Research Outline

This thesis comprises nine chapters. The contents of these chapters following the introduction are presented as follows:

Chapter 2 proposes a high resolution time-frequency representation approach for nonstationary signals polluted with strong noise. With a high sensitivity to detect slight frequency shift and an immunity to noise effect, the intermittent chaotic of Duffing oscillator system is introduced to accurately identify the time varying instantaneous frequencies. Furthermore, an adaptive Duffing oscillator array is adopted to improve the instantaneous frequency identification efficiency. The feasibility and effectiveness of the proposed method are verified with numerical studies on a multi-component synthetic nonstationary signal as well as on a two-storey shear building with time varying stiffness under seismic loads, and experimental studies on a laboratory bridge model under moving vehicle load.

Chapter 3 proposes an output-only-based approach using Volterra series model for nonlinear structural damage detection, by quantifying the nonlinear behavior of structures without the prior knowledge of external excitations. The capability and accuracy of using the proposed approach for nonlinear structural damage detection are validated with numerical studies on a beam structure with a breathing crack under different levels of white noise excitations and experimental studies on a precast segmental concrete column subjected to ground motions with different peak ground acceleration (PGA) values.

Chapter 4 proposes a novel approach for improving the identifiability of structural damage by using higher order responses and SSA based PST technique. The accuracy and reliability of the proposed approach are verified with numerical studies on a planar truss structure and experimental studies on a Tee-section pre-stressed concrete beam model. The effects of white noise, pink noise, modelling uncertainties on the accuracy of damage detection are investigated.

Chapter 5 proposes a novel data driven approach for structural damage assessment based on phase space embedding in conjunction with stochastic Koopman operator. The feasibility and applicability of the proposed approach are verified with numerical studies on a planar truss model and experimental studies on the Z24 benchmark bridge. The robustness of the proposed approach under operational and environmental variations is tested by considering 10% white noise in vibration measurement and six different ambient loading scenarios.

Chapter 6 proposes a novel structural damage detection approach based on manifold learning for the effective condition assessment of real-world structures under environmental and operational conditions. The effectiveness and superiority of the proposed approach are

demonstrated by two real-world engineering structures, that is, the Dowling Hall Footbridge and Z24 bridge.

Chapter 7 proposes a finite linear representation of nonlinear structural dynamics using phase space embedding coordinate. Experimental studies on an eight-story shear-type linear steel frame is conducted to identify natural frequencies and the corresponding mode shapes. Numerical and experimental studies on nonlinear structures are conducted to demonstrate that the finite dimensional DMD based on the discrete Hankel SVD coordinate is highly symmetrically structured, and is able to accurately obtain a linear representation of structural nonlinear vibration.

Chapter 8 builds on the finding of Chapter 7 in order to identify the condition change of structures with initial nonlinearity. The eigen-frequencies extracted from the Koopman operator are served as damage features. Two experimental structures exhibiting inherent nonlinearity, namely a magneto-elastic system and a precast segment beam, are employed to demonstrate the feasibility and effectiveness of using the proposed method for identifying condition change of nonlinear structures.

Chapter 9 summarizes the main finding from this study, as well as some future works.

It should be noted that this thesis is compiled by combining the technical papers prepared by the candidate during his PhD study. Therefore, Chapters 2 to 8 can be read independently. On the other hand, to make each technical paper complete, the numerical simulations and experimental applications are introduced in almost every chapter (i.e. in each independent chapter). These parts thus might be slightly repetitive with each other.

References

- [1] M. Azimi, A.D. Eslamlou, G. Pekcan, Data-driven structural health monitoring and damage detection through deep learning: State-of-the-art review, *Sensors*, 20 (2020) 2778.
- [2] E.A. Oskoui, T. Taylor, F. Ansari, Reference-free dynamic distributed monitoring of damage IN multispan bridges, *Journal of Structural Engineering*, 147 (2021) 04020292.
- [3] Z. Peng, J. Li, H. Hao, Data driven structural damage assessment using phase space embedding and Koopman operator under stochastic excitations, *Engineering Structures*, 255 (2022) 113906.
- [4] Z. Peng, J. Li, H. Hao, Long-term condition monitoring of cables for in-service cable-stayed bridges using matched vehicle-induced cable tension ratios, *Smart Structures and Systems*, 29 (2022) 167-179.
- [5] C. Liu, J. Teng, Z. Peng, Optimal sensor placement for bridge damage detection using deflection influence line, *Smart Struct. Syst*, 25 (2020) 169-181.
- [6] A. Rytter, *Vibrational based inspection of civil engineering structures*, (1993).
- [7] S.K. Dwivedi, M. Vishwakarma, A. Soni, Advances and researches on non-destructive testing: A review, *Materials Today: Proceedings*, 5 (2018) 3690-3698.
- [8] J. Helal, M. Sofi, P. Mendis, Non-destructive testing of concrete: A review of methods, *Electronic Journal of Structural Engineering*, 14 (2015) 97-105.
- [9] O. Avci, O. Abdeljaber, S. Kiranyaz, An overview of deep learning methods used in vibration-based damage detection in civil engineering, *Dynamics of Civil Structures*, Volume 2, (2022) 93-98.
- [10] J. Li, H. Hao, Substructure damage identification based on wavelet-domain response reconstruction, *Structural Health Monitoring*, 13 (2014) 389-405.
- [11] Y. Bao, Z. Chen, S. Wei, Y. Xu, Z. Tang, H. Li, The state of the art of data science and engineering in structural health monitoring, *Engineering*, 5 (2019) 234-242.
- [12] S. Sehgal, H. Kumar, Structural dynamic model updating techniques: a state of the art review, *Archives of Computational Methods in Engineering*, 23 (2016) 515-533.
- [13] A. Esfandiari, F. Bakhtiari-Nejad, A. Rahai, M. Sanayei, Structural model updating using frequency response function and quasi-linear sensitivity equation, *Journal of sound and vibration*, 326 (2009) 557-573.
- [14] S. Weng, H. Zhu, Y. Xia, J. Li, W. Tian, A review on dynamic substructuring methods for model updating and damage detection of large-scale structures, *Advances in Structural Engineering*, 23 (2020) 584-600.
- [15] J. Li, S. Law, Y. Ding, Substructure damage identification based on response reconstruction in frequency domain and model updating, *Engineering structures*, 41 (2012) 270-284.
- [16] X. Li, S. Law, Adaptive Tikhonov regularization for damage detection based on nonlinear model updating, *Mechanical Systems and Signal Processing*, 24 (2010) 1646-1664.
- [17] S. Hoell, P. Omenzetter, Improved damage detectability in a wind turbine blade by optimal selection of vibration signal correlation coefficients, *Structural Health Monitoring*, 15 (2016) 685-705.
- [18] W.J. Yan, W.X. Ren, Operational modal parameter identification from power spectrum density transmissibility, *Computer - Aided Civil and Infrastructure Engineering*, 27 (2012) 202-217.
- [19] C.R. Farrar, K. Worden, *Structural health monitoring: a machine learning perspective*,

John Wiley & Sons, 2012.

- [20] S. Weng, H.-P. Zhu, Y. Xia, L. Mao, Damage detection using the eigenparameter decomposition of substructural flexibility matrix, *Mechanical Systems and Signal Processing*, 34 (2013) 19-38.
- [21] J. Li, B. Wu, Q. Zeng, C.W. Lim, A generalized flexibility matrix based approach for structural damage detection, *Journal of Sound and Vibration*, 329 (2010) 4583-4587.
- [22] N.M. Maia, R.A. Almeida, A.P. Urgueira, R.P. Sampaio, Damage detection and quantification using transmissibility, *Mechanical Systems and Signal Processing*, 25 (2011) 2475-2483.
- [23] J. Li, H. Hao, J.V. Lo, Structural damage identification with power spectral density transmissibility: numerical and experimental studies, *Smart structures and systems*, 15 (2015) 15-40.
- [24] J. Li, H. Hao, Y. Xia, H.-P. Zhu, Damage assessment of shear connectors with vibration measurements and power spectral density transmissibility, *Struct. Eng. Mech*, 54 (2015) 257-289.
- [25] Y. Xia, B. Chen, S. Weng, Y.-Q. Ni, Y.-L. Xu, Temperature effect on vibration properties of civil structures: a literature review and case studies, *Journal of civil structural health monitoring*, 2 (2012) 29-46.
- [26] J.-B. Bodeux, J.-C. Golinval, Application of ARMAV models to the identification and damage detection of mechanical and civil engineering structures, *Smart materials and structures*, 10 (2001) 479-489.
- [27] Y. Lei, F. Chen, H. Zhou, An algorithm based on two - step Kalman filter for intelligent structural damage detection, *Structural Control and Health Monitoring*, 22 (2015) 694-706.
- [28] Z. Nie, T. Ngo, H. Ma, Reconstructed phase space-based damage detection using a single sensor for beam-Like structure subjected to a moving mass, *Shock and Vibration*, 2017 (2017).
- [29] L.G. Villani, S. Da Silva, A. Cunha Jr, M.D. Todd, Damage detection in an uncertain nonlinear beam based on stochastic Volterra series: an experimental application, *Mechanical Systems and Signal Processing*, 128 (2019) 463-478.
- [30] D. Hester, A. González, A wavelet-based damage detection algorithm based on bridge acceleration response to a vehicle, *Mechanical Systems and Signal Processing*, 28 (2012) 145-166.
- [31] E.S. Tomé, M. Pimentel, J. Figueiras, Damage detection under environmental and operational effects using cointegration analysis—Application to experimental data from a cable-stayed bridge, *Mechanical Systems and Signal Processing*, 135 (2020) 106386.
- [32] H. Li, Y. Huang, J. Ou, Y. Bao, Fractal dimension - based damage detection method for beams with a uniform cross - section, *Computer - Aided Civil and Infrastructure Engineering*, 26 (2011) 190-206.
- [33] J.-P. Noël, G. Kerschen, Nonlinear system identification in structural dynamics: 10 more years of progress, *Mechanical Systems and Signal Processing*, 83 (2017) 2-35.
- [34] F. Wang, G. Song, Bolt early looseness monitoring using modified vibro-acoustic modulation by time-reversal, *Mechanical Systems and Signal Processing*, 130 (2019) 349-360.
- [35] Z.-C. Wang, W.-X. Ren, G. Chen, Time–frequency analysis and applications in time-varying/nonlinear structural systems: A state-of-the-art review, *Advances in Structural*

Engineering, 21 (2018) 1562-1584.

- [36] C. Bao, H. Hao, Z.-X. Li, Multi-stage identification scheme for detecting damage in structures under ambient excitations, *Smart materials and structures*, 22 (2013) 045006.
- [37] Y. Xin, J. Li, H. Hao, Damage detection in initially nonlinear structures based on variational mode decomposition, *International Journal of Structural Stability and Dynamics*, 20 (2020) 2042009.
- [38] O. Avci, O. Abdeljaber, S. Kiranyaz, M. Hussein, M. Gabbouj, D.J. Inman, A review of vibration-based damage detection in civil structures: From traditional methods to Machine Learning and Deep Learning applications, *Mechanical systems and signal processing*, 147 (2021) 107077.
- [39] A.A. Mosavi, D. Dickey, R. Seracino, S. Rizkalla, Identifying damage locations under ambient vibrations utilizing vector autoregressive models and Mahalanobis distances, *Mechanical systems and signal processing*, 26 (2012) 254-267.
- [40] J.J. Lee, J.W. Lee, J.H. Yi, C.B. Yun, H.Y. Jung, Neural networks-based damage detection for bridges considering errors in baseline finite element models, *Journal of Sound and Vibration*, 280 (2005) 555-578.
- [41] Y.-L. Zhou, N.M. Maia, R.P. Sampaio, M.A. Wahab, Structural damage detection using transmissibility together with hierarchical clustering analysis and similarity measure, *Structural health monitoring*, 16 (2017) 711-731.
- [42] U. Dackermann, J. Li, B. Samali, Identification of member connectivity and mass changes on a two-storey framed structure using frequency response functions and artificial neural networks, *Journal of Sound and Vibration*, 332 (2013) 3636-3653.
- [43] R. Ghiasi, P. Torkzadeh, M. Noori, A machine-learning approach for structural damage detection using least square support vector machine based on a new combinational kernel function, *Structural Health Monitoring*, 15 (2016) 302-316.
- [44] Chenchao, J. Li, H. Hao, R. Wang, L. Li, Development and application of random forest technique for element level structural damage quantification, *Structural Control and Health Monitoring*, 28 (2021) e2678.
- [45] N. Bakhary, H. Hao, A.J. Deeks, Structure damage detection using neural network with multi-stage substructuring, *Advances in Structural Engineering*, 13 (2010) 95-110.
- [46] Y.z. Lin, Z.h. Nie, H.w. Ma, Structural damage detection with automatic feature - extraction through deep learning, *Computer - Aided Civil and Infrastructure Engineering*, 32 (2017) 1025-1046.
- [47] F. Nex, D. Duarte, F.G. Tonolo, N. Kerle, Structural building damage detection with deep learning: Assessment of a state-of-the-art CNN in operational conditions, *Remote sensing*, 11 (2019) 2765.
- [48] S. Sony, S. Gamage, A. Sadhu, J. Samarabandu, Vibration-based multiclass damage detection and localization using long short-term memory networks, in: *Structures*, Elsevier, 2022, pp. 436-451.
- [49] R. Wang, Chenchao, S. An, J. Li, L. Li, H. Hao, W. Liu, Deep residual network framework for structural health monitoring, *Structural Health Monitoring*, 20 (2021) 1443-1461.
- [50] S.-S. Jin, H.-J. Jung, Vibration-based damage detection using online learning algorithm for output-only structural health monitoring, *Structural Health Monitoring*, 17 (2018) 727-746.
- [51] Z. Rastin, G. Ghodrati Amiri, E. Darvishan, Unsupervised structural damage detection technique based on a deep convolutional autoencoder, *Shock and Vibration*, 2021 (2021).

- [52] Z. Shang, L. Sun, Y. Xia, W. Zhang, Vibration-based damage detection for bridges by deep convolutional denoising autoencoder, *Structural Health Monitoring*, 20 (2021) 1880-1903.
- [53] Z. Wang, Y.-J. Cha, Unsupervised deep learning approach using a deep auto-encoder with a one-class support vector machine to detect damage, *Structural Health Monitoring*, 20 (2021) 406-425.
- [54] S. Chen, F. Cerda, P. Rizzo, J. Bielak, J.H. Garrett, J. Kovačević, Semi-supervised multiresolution classification using adaptive graph filtering with application to indirect bridge structural health monitoring, *IEEE Transactions on Signal Processing*, 62 (2014) 2879-2893.
- [55] T. -J. Rogers, K. Worden, R. Fuentes, N. Dervilis, U.-T. Tygesen, & E.-J. Cross. (2019). A Bayesian non-parametric clustering approach for semi-supervised Structural Health Monitoring. *Mechanical Systems and Signal Processing*, 119, 100-119.
- [56] Y. Xin, H. Hao, J. Li, Z.-C. Wang, H.-P. Wan, W.-X. Ren, Bayesian based nonlinear model updating using instantaneous characteristics of structural dynamic responses, *Engineering Structures*, 183 (2019) 459-474.
- [57] A. Das, N. Debnath, A Bayesian model updating with incomplete complex modal data, *Mechanical Systems and Signal Processing*, 136 (2020) 106524.
- [58] R. Hou, X. Wang, Q. Xia, Y. Xia, Sparse Bayesian learning for structural damage detection under varying temperature conditions, *Mechanical Systems and Signal Processing*, 145 (2020) 106965.
- [59] Y. Huang, C. Shao, B. Wu, J.L. Beck, H. Li, State-of-the-art review on Bayesian inference in structural system identification and damage assessment, *Advances in Structural Engineering*, 22 (2019) 1329-1351.

CHAPTER 2 HIGH RESOLUTION TIME FREQUENCY REPRESENTATION FOR INSTANTANEOUS FREQUENCY IDENTIFICATION BY ADAPTIVE DUFFING OSCILLATOR

ABSTRACT¹

Time frequency analysis of structural vibration responses provides essential information for structural system identification, modal updating and condition assessment. However, spurious peaks introduced by the strong noise will significantly increase the false positive rate as well as compromise the sparse time frequency signal representation. This chapter proposes a high resolution time frequency representation approach for nonstationary signals polluted with strong noise. With a high sensitivity to detect slight frequency shift and an immunity to noise effect, the intermittent chaotic of Duffing oscillator system is introduced to accurately identify the time varying instantaneous frequencies. Furthermore, an adaptive Duffing oscillator array is adopted to improve the instantaneous frequency identification efficiency. The feasibility and effectiveness of the proposed method are verified with numerical and experimental studies. Numerical studies are conducted on a multi-component synthetic nonstationary signal as well as on a two-storey shear building with time varying stiffness under seismic loads. In experimental validations, the acceleration response of a laboratory bridge model under moving vehicle load is also analysed by using the proposed approach to obtain the instantaneous frequency variations induced by the bridge-vehicle interaction. These results are compared with those obtained from a method based on empirical wavelet transform (EWT) and Hilbert transform (EWT-HT), to highlight the superiority of the proposed approach in obtaining high resolution time frequency analysis results for nonstationary signals with strong noise.

2.1 Introduction

One important focus of recent researches in signal processing is to represent accurately the time frequency distribution of non-stationary signals polluted by strong noise. Existing methods, such as, STFT, discrete wavelet transform, HT, Wigner distribution and Choi-

¹This chapter was published in *Structural Control & Health Monitoring* with the full bibliographic citation as follows: Peng, Z., Li, J., Hao, H., & Xin, Y. (2020). High-resolution time-frequency representation for instantaneous frequency identification by adaptive Duffing oscillator. *Structural Control and Health Monitoring*, 27(12), e2635. <https://doi.org/10.1002/stc.2635>.

Williams distribution, have been studied in various disciplines for different applications. The detailed theoretical background of those algorithms and the improvements developed to improve the existing methods have been reviewed in Ref. [1-6]. Despite its success in processing nonstationary signals with high signal-to-noise ratios (SNR), the significant noise contamination in signals poses a challenge to the analysis accuracy and resolution of time frequency analysis representation, especially for the nonstationary signals with low SNR.

For vibration signals submerged in strong background noise, signal denoising methods by using Wiener filter [7], wavelet filter [8] and singular value decomposition (SVD) [9] have been commonly used to reduce the influence of noise and improve the quality of time frequency analysis. In fact, most of the above-mentioned methods remove noise in the frequency domain, and are only suitable for signals with energy compact spectra. Conversely, the nonstationary signals in real situations usually contain multiple and even varying frequency components that are broadly distributed in a range of frequency band and maybe even overlapped in the frequency domain. Consequently, non-negligible level of noise remains in the signals, which may not be fully filtered by using conventional signal denoising methods. Considering the sparse feature of nonstationary signals in time frequency domain representation, more advanced methods, i.e. compressive sensing technique [10] and envelope-tracking filter [11], have been developed to improve the effectiveness and performance of nonstationary signal denoising and processing.

During the last two decades, nonlinear chaotic oscillator has attracted more and more research attention owing to its excellent performance in sensitively detecting weak periodic signals under strong noise effect. The motion of human eardrum, which can sensitively distinguish a faint sound from the noisy environment, motivated the very first discovered chaotic oscillators in weak signal detection. Duffing equation, as the second-order differential model simplified from eardrum vibrations, has been widely used in weak signal detection [12, 13]. The nonlinear behavior of Duffing oscillator usually exhibits by introducing a high order nonlinear term. A Duffing system will experience fixed-point state, cyclic attractor state, periodic state and chaotic state with the increase of driving force amplitude. Existing studies [14, 15] demonstrated the potential use of Duffing oscillator in noise contaminated weak signal detection by adjusting the system into a critical state between periodic state and chaotic state [16]. Phase transition can be observed in the PST when the external weak signal with the same frequency as that of the internal driving force is served as input to the Duffing system. The effect of noise on the phase lag and frequency responses of Duffing oscillator is comprehensively investigated in Ref. [17, 18]. However, strong noise will only roughen the local PST but introduce an insignificant effect on the critical state. Wang et al. [19] applied the intermittent chaotic motion of Duffing oscillator to detect the frequency of weak signals

polluted by a strong noise. Studies in Ref. [20, 21] utilized the Duffing oscillator to detect the nonlinear Lamb wave reflected from the crack surface and identify the crack location by using the difference between arrive time instants of lamb wave. More recently, it has been pointed out [22] that intermittent chaotic phenomenon will present when a slight frequency shift (less than 3%) exists in the internal reference signal and the signal to be detected. Accordingly, several attempts have been made to precisely estimate the frequency shift of weak signal to be detected by using an array of uncoupled Duffing oscillators covering the possible frequency range of signals to be detected. Then the actual frequency can be indirectly estimated with a high resolution according to the inversely proportional relationship between frequency shift and intermittent chaotic transition period [19].

Little work has been devoted to estimating time varying frequency of nonstationary signals with Duffing system, mainly because of two reasons. One is that sufficient uncoupled oscillators ought to be arranged to cover the possible frequency variation of the target signal. Therefore the efficiency of instantaneous frequency identification will be significantly affected to execute numerous sets of oscillators at the same time. Furthermore, the phase transition period in a special oscillator will change with the variation of frequency, and the intermittent chaotic phenomenon may even disappear if the frequency shift exceeds 3%. Inspired by the STFT method, this study attempts to extend the applicability of Duffing system in analysing nonstationary signals by dividing the target signal into several separate segments with a sliding rectangular time window. Therefore, the signal segment in each time window can be viewed as stationary if the time window size is sufficiently short. Instead of estimating the instantaneous frequency in each time window with Fast Fourier Transform (FFT), the proposed approach develops an array of adaptive Duffing oscillators to recursively identify the time varying instantaneous frequency of nonstationary signals with high resolution and efficiency. With a good noise immunity and a high sensitivity to minor frequency change, the main contribution of this study is to develop a novel approach using Duffing oscillators to accurately identify the instantaneous frequency of nonstationary signals with a strong noise pollution.

The remaining sections of this chapter are organised as follows. Section 2 provides the theoretical derivation and implementation procedure of the proposed approach to obtain high resolution time frequency analysis results with an adaptive Duffing oscillators array. Section 3 demonstrates the accuracy of using the proposed adaptive Duffing oscillators array system to conduct the instantaneous frequency identification of a multiple-component synthetic nonstationary signal. Numerical studies on a building structure with time-varying stiffness under seismic loads are also conducted to validate the accuracy of the proposed approach. Section 4 further verifies the effectiveness of using the proposed approach for identifying the

instantaneous vibration frequency variation of a vehicle-bridge interaction system. In Section 5, conclusions and some discussions for future studies are provided.

2.2 Theoretical Background and Development

2.2.1 Duffing oscillator operation for high resolution frequency shift detection

In this study, a damped Duffing oscillator with a cubic-quintic nonlinearity term ($-x^3+x^5$) is chosen as the Duffing oscillator model. This nonlinear equation has been demonstrated to have an enhanced sensitivity to periodic weak signal detection and a good input-to-state stability (ISS) owing to the higher order nonlinear term [20, 21]. This damped cubic-quintic Duffing oscillator equation is expressed as

$$\ddot{x}(t) + \delta\dot{x}(t) - x(t)^3 + x(t)^5 = F\cos(\omega_0 t) \quad (2.1)$$

where δ and $-x(t)^3+x(t)^5$ are the damping ratio and nonlinear recovery force term of Duffing oscillator model, respectively; F and ω_0 are the amplitude and reference angular frequency of the internal harmonic driving force, respectively. The corresponding space state equation of Eq. (2.1) is

$$\begin{cases} \dot{x}(t) = y(t) \\ \dot{y}(t) = -\delta y(t) + x(t)^3 - x(t)^5 + F\cos(\omega_0 t) \end{cases} \quad (2.2)$$

The Duffing oscillator described in Eq. (2.2) is parameter sensitive and its phase trajectory can be dramatically changed if a small disturbance is applied to the damping ratio δ or the internal harmonic driving force F . Without loss of generality, the damping ratio δ is set as 0.5 according to Ref. [12]. Once δ is fixed, the evolution of motion state will be: fixed point \rightarrow periodic doubling \rightarrow chaotic state \rightarrow large-scale periodic state, with the gradual increase of the driving force amplitude. A clear state transition can be observed between the chaotic state and large-scale periodic state, thus the internal driving force of Duffing system is usually adjusted to a corresponding threshold value F_c . The transition in PST will be observed when a tiny increment is applied to F_c . For the purpose of weak signal detection, the state of the Duffing oscillator will be transformed when the external signal to be detected with the same frequency ω_0 is introduced. Another potential application of Duffing system is to accurately detect a slight frequency shift. For this purpose, Eq. (2.1) can be revised as follows when external signal to be detected with the frequency shift and noise is added.

$$\ddot{x}(t) + \delta\dot{x}(t) - x(t)^3 + x(t)^5 = F_c\cos(\omega_0 t) + F_A\cos[(\omega_0 + \Delta\omega)t + \varphi] + N_L n(t) \quad (2.3)$$

in which $F_A\cos[(\omega_0+\Delta\omega)t+\varphi]$ represents the external signal to be detected (amplitude F_A , angular frequency shift $\Delta\omega$ and phase difference φ). N_L denotes the additive noise level, and

$n(t)$ is a zero mean and unit standard deviation vector with the same length as the reference signal. Eq. (2.3) can be simplified by combining the internal reference signal and external signal to be detected with trigonometric function transformations, and can be expressed as

$$\ddot{x}(t) + \delta\dot{x}(t) - x(t)^3 + x(t)^5 = F(t)\cos[\omega_0 t + \theta(t)] + N_L n(t) \quad (2.4)$$

where

$$\begin{cases} F(t) = \sqrt{F_c^2 + 2F_c F_A \cos(\Delta\omega + \varphi) + F_A^2} \\ \theta(t) = \arctan\left[\frac{F_A \sin(\Delta\omega + \varphi)}{F_c + F_A \cos(\Delta\omega + \varphi)}\right] \end{cases} \quad (2.5)$$

In Eq. (2.5), the amplitude of the combined signal $F(t)$ will change between $[F_c - F_A, F_c + F_A]$ periodically with a constant angular speed of $\Delta\omega$. Figure 2-1 describes the changing process of the overall driving force $F(t)$ over time. Since the overall driving force will pass through the threshold value F_c periodically, the corresponding phase state of Duffing system will also vary from chaotic state to large periodic state with a period of $T=2\pi/\Delta\omega$. This phenomenon is also referred to as intermittent chaotic motion. The angular frequency difference between reference signal and signal to be detected can be indirectly estimated by calculating the intermittent chaotic T with phase state sensitivity indicators, i.e. Lyapunov exponent, Lyapunov dimension and Poincaré section [23, 24].

It should be noted that intermittent chaotic based frequency shift estimation method has its limitation, namely, the boundary between chaotic and periodic states is obvious and easy to be identified when the relative frequency shift $\Delta\omega/\omega \leq 3\%$. However, the intermittent chaotic phenomenon might be destroyed when $\Delta\omega/\omega$ is larger than 3%. One reason is that some response time is required to cause Duffing system phase state to change when the overall driving force exceeds the critical value. If the overall driving force $F(t)$ changes quickly, the Duffing system could not respond well when the relative frequency shift is larger than 3%.

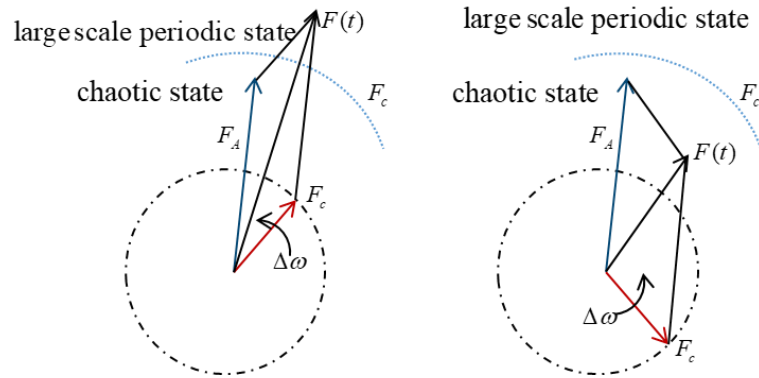


Figure 2-1. The vector chart of the overall driving force.

2.2.2 Time varying instantaneous frequency identification with adaptive Duffing oscillator

Duffing intermittent chaotic described in Section 2.1 has been proven to be potentially promising in detecting frequency shift of stationary signals under strong noise environment [22, 25]. It is inspired to develop a new time frequency analysis approach, to analyse the nonstationary signal that is divided into segments by using small sliding time windows. These windows are short enough to assume that, within each window, the frequency can be considered as time-invariant. Moreover, since the nonstationary signal is broken into segments in a set of time windows, Duffing oscillator array should be deployed densely and widely to cover all the possible frequency ranges of the signal to be detected. Figure 2-2 depicts how to arrange the reference frequency of each oscillators in an array to cover the whole frequency range of to-be-detected signal. In Figure 2-2, the middle oscillator with the reference frequency $\omega_{OS(mid)}$ is deployed to detect the signal with instantaneous frequency belonging to the range $[\omega_{OS(mid)}/1.03, \omega_{OS(mid)} \times 1.03]$ [16]. The frequency range can be extended by subsequently adding adjacent oscillators to the left and right sides of the middle one. In particular, the left frequency boundary of the middle oscillator OS(*mid*) is equal to the right frequency boundary of the left oscillator OS(*L1*). For instance, 79 uncoupled oscillators with different values of ω should be involved in an array to identify the instantaneous frequency varying between 1 ~100 Hz. However, the intermittent chaotic will not occur in most Duffing oscillators when the reference frequency is located far away from the actual frequency of a certain time window, which thus provides less benefit to the instantaneous frequency identification.

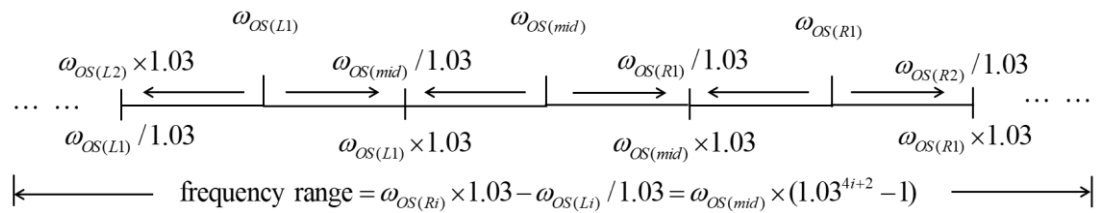


Figure 2-2. Duffing oscillators array.

To improve the efficiency of the proposed approach and avoid the use of a large array of Duffing oscillators, this study attempts to propose a practical solution that consists of generating an adaptive array of oscillators. The proposed approach is able to recursively identify the evolution of instantaneous frequency. This means that the array will adjust itself to the changes in instantaneous frequency of the selected time window, according to the frequency estimated in the previous time window. Firstly, the nonstationary signal will be

divided into a number of time windows and the signal in the first time window will be used as input to a large Duffing oscillator array which covers all the possible frequency ranges of to-be-detected signal to obtain an initial frequency estimation ω_1 . Then, the large size of Duffing oscillators array will be replaced by a small one with three default oscillators to estimate the instantaneous frequency in the second time window. In a default oscillator array, the reference frequency of the middle default oscillator (referred to as $\omega_{OS(mid)}$) will be adjusted to the instantaneous frequency estimated in the previous time window. Other two default oscillators will be respectively deployed in the left side ($\omega_{OS(L)}$) and right side ($\omega_{OS(R)}$) of the middle oscillator with the frequency interval illustrated in Figure 2-2. Then, the signal in the second time window will be used as input to the above-mentioned Duffing array as the external driving force. The phase state transition will present in one of these three oscillators response if the actual signal frequency of current time window falls into the frequency detection range of a certain oscillator. Therefore phase state transition period is used to estimate the frequency shift between the actual and reference signals. Although such transition between periodic state and chaotic state can indeed be observed in the PST intuitively, it is difficult to highlight any of these two states from the PST at which the transition occurs, especially in scenarios with strong noise. The Lyapunov exponent is a quantitative index to evaluate the rate of separation of nonlinear dynamic system. For the two-dimensional (2D) Duffing oscillator used in this study, Table 2-1 gives the relationship between motion states and the corresponding three Lyapunov exponents [26, 27]. It can be found that the Duffing system will be in the chaotic state only when the sign of the maximum Lyapunov exponent (MLE) λ_1 is positive. This is because the phase trajectory will become dispersed when MLE is larger than 0. Therefore, the sign of MLE is introduced to distinguish the chaotic and periodic states of Duffing system as well as to calculate the exact intermittent chaotic periodic T .

Table 2-1. Motion states of Duffing oscillator and its corresponding Lyapunov exponents.

Lyapunov exponents	Exponent sign	Motion state	Phase space trajectory
$\lambda_1, \lambda_2, \lambda_3$	- , - , -	stationary motion	fixed point
	0 , - , -	periodic motion	cyclic attractor
	0 , 0 , -	quasi-periodic motion	two-dimension torus
	+ , 0 , 0	chaotic state	unstable 2D torus
	+ , 0 , -	chaotic state	strange attractor

It should be noticed that the initial size of Duffing oscillator array is set as 3 to improve the computational efficiency. Inevitably, frequency mutation may exist in two adjacent time

windows due to the strong dynamic feature of to-be-detected signal. Therefore intermittent chaotic state might not occur in the current Duffing oscillator array. In this case, current Duffing array will extend its frequency detection range by symmetrically absorbing more oscillators in both sides until intermittent chaotic phenomenon presents. The same procedure will be recursively implemented to obtain the instantaneous frequency of the rest time windows. Then the time frequency representation of the original signal is generated by integrating those instantaneous frequencies identified by the adaptive Duffing oscillator in each time window. The framework of the proposed approach is as follows:

Steps of the proposed approach include

Obtain the nonstationary signal contaminated with strong noise for detection;

Determine the window size and segment the original signal into n time windows;

Estimate the instantaneous frequency of the first time window ω_1 with a large array of Duffing oscillator;

Process the i -th time window signal, where $2 \leq i \leq n-1$;

- a) set the reference frequency of the oscillator as $\omega_{OS(mid)} = \omega_{i-1}$; $\omega_{OS(LI)} = \omega_{i-1}/1.03^2$; $\omega_{OS(RI)} = \omega_{i-1} \times 1.03^2$;
- b) input the signal of the i -th time window into the updated Duffing oscillator array, and obtain the state responses of each oscillator;
- c) calculate the Lyapunov exponent of each oscillator;
- d) if intermittent chaotic does not occur in the current Duffing oscillator, oscillators are added to the left and right sides of the current Duffing oscillator array;
- e) conduct sub-step b)~c) until the intermittent chaotic occurs in the current Duffing oscillator;
- f) quantify the intermittent period T according to Lyapunov exponent;
- g) estimate and record the instantaneous frequency ω_i corresponding to the i -th time window.

Update the reference frequency for the next cycle;

Repeat sub-step a)~g) until the window index i is equal to n ;

Generate the time frequency representation.

Similar to the conventional STFT method, the main challenge faced by the proposed approach for instantaneous frequency identification is to determine the suitable window size.

Usually, a trade-off should be made between the signal resolution in time and frequency domains according to the frequency variation characteristic of the signal as well as the emphasis of individual applications. In this study, the time window size is fixed as 1s for the signal length, and 0.5s time window overlapping is considered to provide a more smooth time frequency analysis result.

A prerequisite of the proposed adaptive Duffing oscillator based time frequency representation approach is that the to-be-detected signal only contains one main frequency component. For signals with multiple frequency components, previous studies demonstrated that the phase state transition will only occur when the actual frequency is the same or very close to the reference frequency of Duffing oscillator, however, is insensitive to other frequency components. However, the main contribution of this study is to demonstrate the feasibility of using Duffing oscillator for identifying time varying instantaneous frequency as well as taking advantages of its superiority in noise immunity. It should be noted that a pre-processing procedure is applied to the original nonstationary signal. In particular, the multiple frequency component signals is decomposed into a number of components with individual frequencies.

In literature, a variety of alternative time varying vibration signal decomposition methods, i.e. empirical modal decomposition (EMD), ensemble EMD, analytical mode decomposition, VMD, singular spectrum analysis (SSA) and EWT have been developed. Especially, the newly developed EWT method is selected in a library of candidate signal decomposition methods owing to its excellent performance in decomposing nonstationary signals [28]. The theoretical background and implementation procedure of EWT are detailed in Ref. [29, 30], and are not elaborated in this chapter. For the sake of better understanding the proposed approach, a flowchart of the whole framework as described in Figure 2-3 is presented for instantaneous frequency identification.

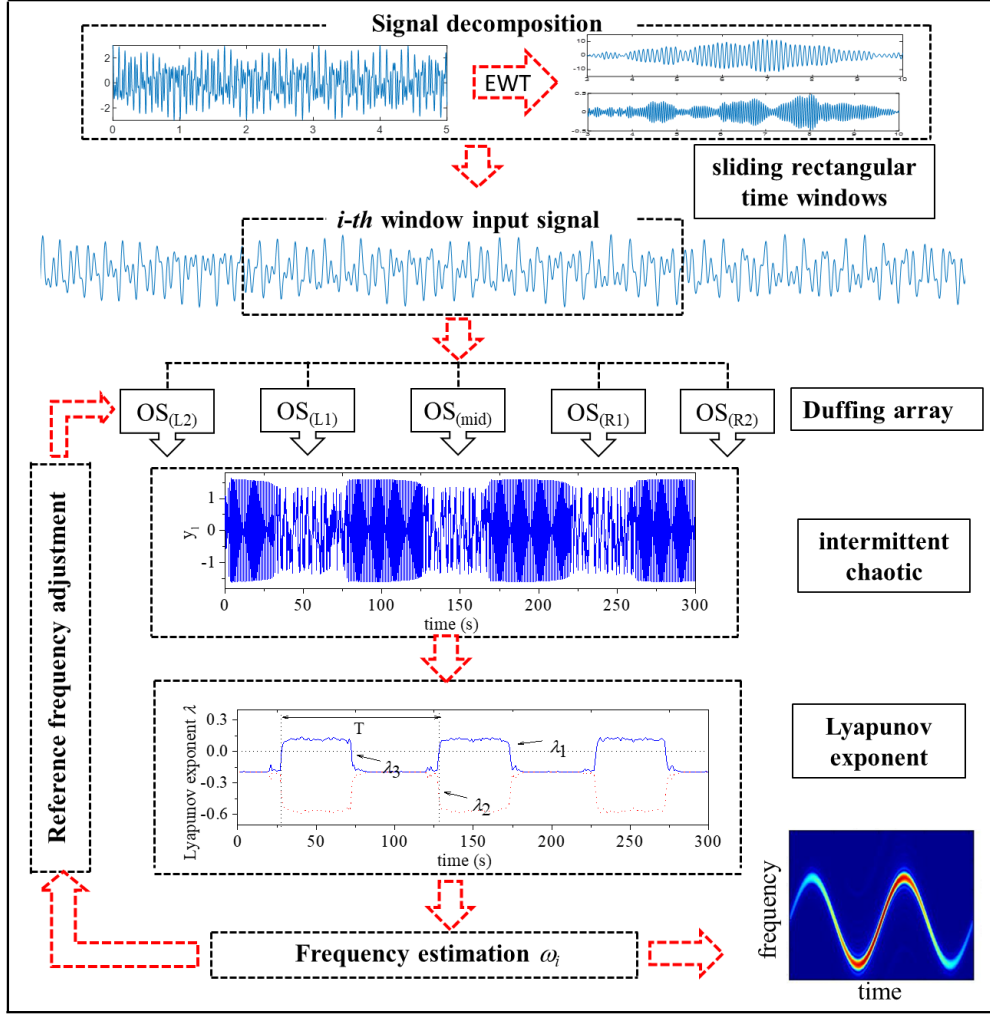


Figure 2-3. The framework of the proposed approach based on adaptive Duffing oscillator for instantaneous frequency identification.

2.3 Numerical verification

2.3.1 Numerical case 1

To verify the effectiveness and performance of using the proposed approach for identifying the instantaneous frequency of nonstationary signals, a multi-component simulated nonstationary signal with frequency components ranged approximately from 5 Hz to 35 Hz and additional measurement noise is defined as

$$y(t) = y_1(t) + y_2(t) + y_3(t) + \sigma \cdot n(t) \quad (2.6)$$

where σ denotes the noise level and $n(t)$ is a zero mean and unit standard deviation vector with the same length as $y(t)$. Three individual signal components $y_1(t)$, $y_2(t)$ and $y_3(t)$ are defined in Eqs. (2.7-2.9), respectively. Each signal component consists of three sections, namely two sections of frequency-modulated signals and a section of amplitude-modulated-frequency-

modulated signal. The signal length of each section is 15s. This signal with discontinuities is simulated to be time varying and have sudden changes in vibration characteristics.

$$y_1(t) = \begin{cases} \cos[20\pi t + 20\sin(0.15\pi t)] & t \in [0, 15s] \\ \cos\{16\pi t + 20\sin[0.1\pi(t-15)]\} & t \in (15, 30s] \\ e^{-0.005[8\pi(t-30)]} \cos\{16\pi t + 20\sin[0.1\pi(t-30)]\} & t \in (30, 45s] \end{cases} \quad (2.7)$$

$$y_2(t) = \begin{cases} \cos[40\pi t + 10\sin(0.3\pi t)] & t \in [0, 15s] \\ \cos\{36\pi t + 10\sin[0.2\pi(t-15)]\} & t \in (15, 30s] \\ e^{-0.005[8\pi(t-30)]} \cos\{32\pi t + 10\sin[0.25\pi(t-30)]\} & t \in (30, 45s] \end{cases} \quad (2.8)$$

$$y_3(t) = \begin{cases} \cos[64\pi t + 10\sin(0.3\pi t)] & t \in [0, 15s] \\ \cos\{58\pi t + 10\sin[0.3\pi(t-15)]\} & t \in (15, 30s] \\ e^{-0.005[8\pi(t-30)]} \cos\{55\pi t + 10\sin[0.3\pi(t-30)]\} & t \in (30, 45s] \end{cases} \quad (2.9)$$

The noise contaminated time domain signal with a sampling ratio of 400 Hz and its corresponding instantaneous frequency distribution and Fourier spectrum distribution are shown in Figure 2-4. Three main frequency components are obviously shown in the Fourier spectrum and the energy of each main frequency component is distributed in a wide frequency band, owing to the frequency variation with time as simulated in Eq. (2.6).

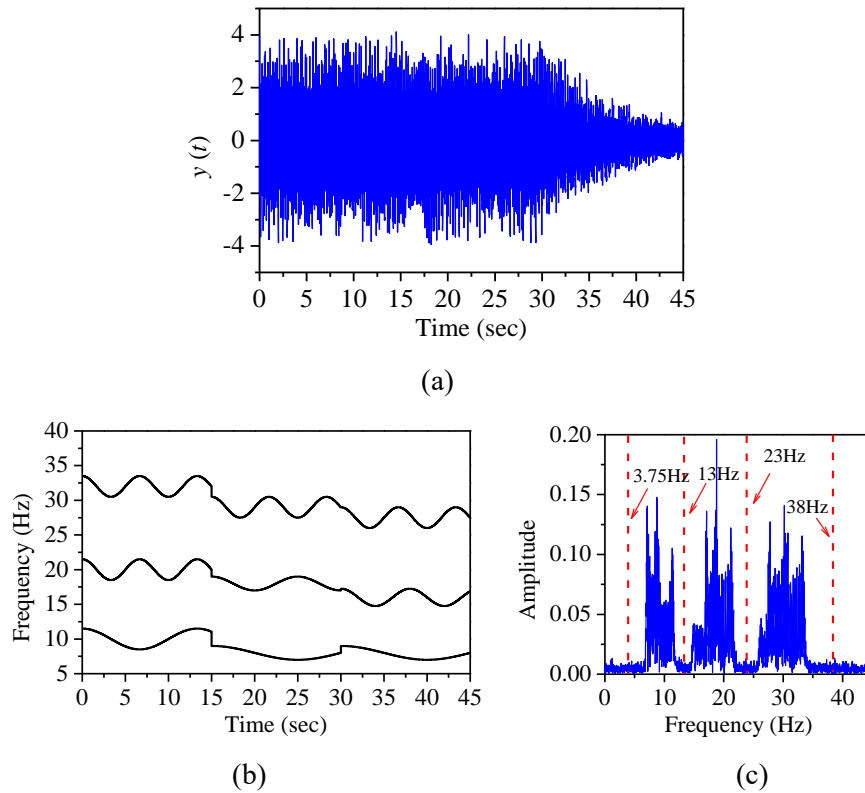


Figure 2-4. The simulated nonstationary signal: (a) Time series with 30% (SNR=10.44dB) white noise; (b) Theoretical instantaneous frequency; and (c) Fourier spectrum.

For signal decomposition by using EWT, the number of frequency components, that are also referred to as IMFs, along with the filtering boundaries of each IMF should be determined in advance. According to the observations from Fourier spectrum in Figure 2-4(c), the number of IMFs for EWT based signal decomposition is defined as 3. The filtering boundaries of three IMFs are respectively determined as 3.75 Hz, 13 Hz, 23 Hz and 38 Hz according to the average values of the maximum frequency of the left side frequency component and the minimum frequency of the right side component [29]. When the filtering boundaries are well determined, three signal components with sparse frequency distribution can be decomposed by conducting EWT analysis.

For comparison purpose, the same nonstationary signal is also analyzed by a commonly utilized time-frequency analysis method, e.g. HT [30, 31], which has been intensively demonstrated to provide desirable performance in instantaneous frequency identification when the SNR is relatively high [32]. Conventional HT integrated empirical mode decomposition (EMD) and classical HT are conducted to obtain the time frequency representation. EMD method is affected by mode mixing phenomenon, which is non-negligible especially when the frequency distribution of signal components is not sparse or intermittent [33, 34]. Most recently, EWT has been demonstrated to be effective in ensuring the stable accuracy of decomposing multiple frequency components [35, 36]. To obtain an unbiased comparison of HT and the proposed approach in identifying instantaneous frequency under strong noise environment, EWT is used in both methods for signal decomposition.

2.3.1.1 Instantaneous frequency identification by using counterpart EWT-HT method

Figure 2-5 shows the time frequency distribution from the EWT-HT based method without or with 30% noise. Despite the errors at both boundaries and discontinuities, three individual signals are well distinguished and reliable time frequency analysis resolution is observed in Figure 2-5(a). Nonetheless, frequency fluctuations occur at the boundaries of two sections of synthetic signal, i.e. time instants at 15 s and 30 s. Slight frequency fluctuations caused by signal discontinuity are involved for the case without noise. As observed in Figure 2-5(b), 30% white noise submerged in the synthetic signal significantly affects the performance of time frequency analysis resolution, especially in the amplitude-modulated signal section ranged from 30s to 45s. One possible reason is that the signal amplitude during this time period shows a decaying trend, thus, the SNR in this region is lower than that between 0s and 30s. It should be noticed that the uncertainties of identified instantaneous frequency are more obvious in the higher frequency component, and the fluctuations are more significant. Hence, it can be preliminarily concluded that signals with high frequencies are more likely to

be affected by using EWT-HT based method when high-level noise is considered.

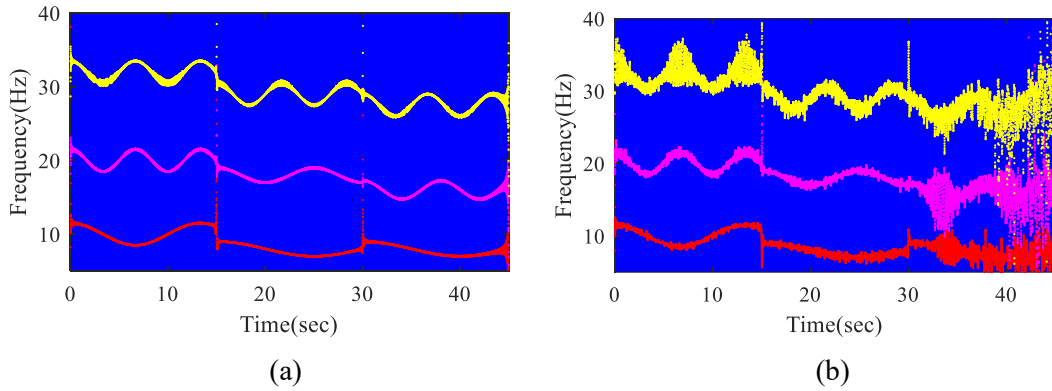


Figure 2-5. Instantaneous frequency identification results by using EWT-HT based method: (a) without noise; (b) with 30% noise.

2.3.1.2 Instantaneous frequency identification by using the proposed approach

According to the implementation procedure of the proposed instantaneous frequency identification approach presented in Figure 2-3, a large array of Duffing oscillators should be deployed to estimate the actual frequency in the first time window. As can be found in the Fourier spectrum that is shown in Figure 2-4(c), the frequency variation range of the simulated signal is between 3.75Hz - 38 Hz. Therefore an array with 40 Duffing oscillators is designed to cover the frequency variation range of the signal. Figure 2-6 shows the instantaneous frequency identification results from the proposed adaptive Duffing approach. It is shown that although slight deviations are observed at some time instants, the overall instantaneous frequency are tracked accurately with a high resolution even when 30% noise is added. The relative errors as defined in Eq. (2.10) of identification results for the cases without and with noise effect by using the proposed approach are calculated based on the following equation

$$relative\ error = \frac{\sum_{i=1}^N |Fre_{identified}(i) - Fre_{theoretical}(i)|}{N \times Fre_{theoretical}(i)} \quad (2.10)$$

where $Fre_{identified}$ and $Fre_{detected}$ denote the identified frequencies and theoretical frequencies, respectively. N denotes the number of identified instantaneous frequencies during a specific vibration duration. The relative errors of using the proposed adaptive Duffing approach and EWT-HT based method for instantaneous frequency identification are listed in Table 2-2. It is observed that the relative errors of EWT-HT based method significantly increased when 30% noise is added to the original signal. In comparison, the relative errors of the proposed approach increase slightly for the case with 30% noise, indicating that the reliable

accuracy of using the proposed approach for identifying the instantaneous frequency of nonstationary signals under a strong noise scenario. The calculations are performed on a desktop with an Intel(R) Core(TM) i7-7700 CPU (3.6 GHz) and 16GB RAM. For numerical case 1, the computational time of using the proposed approach and EWT-HT method are 1.52 s and 0.10 s, respectively.

Table 2-2. Relative errors of identified instantaneous frequency results.

	Adaptive Duffing approach		EWT-HT approach	
	No noise	30% noise	No noise	30% noise
Component 1 (y1)	2.29%	2.45%	2.88%	7.55%
Component 2 (y2)	0.46%	0.52%	4.85%	8.26%
Component 3 (y3)	0.40%	0.65%	7.83%	10.39%

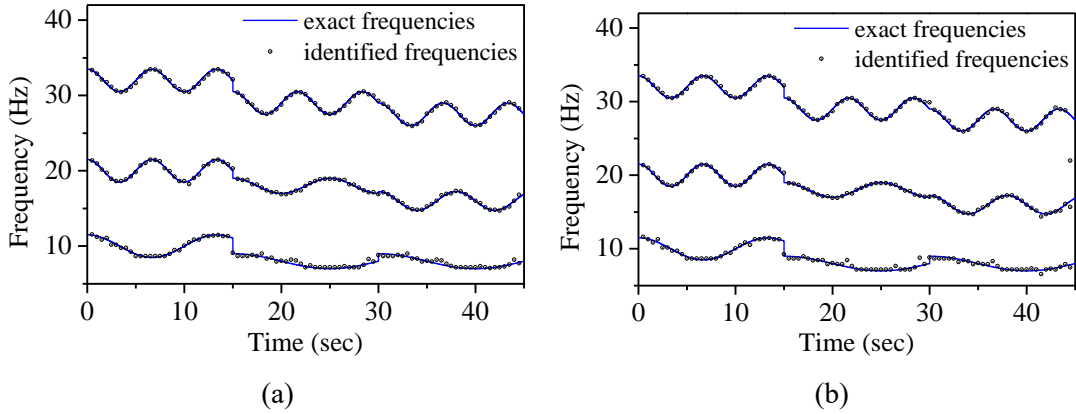


Figure 2-6. Time-frequency analysis results by using the proposed adaptive Duffing approach: (a) without noise; (b) with 30% noise.

2.3.2 Numerical case 2

Structural responses under seismic excitations are usually nonstationary and contain a certain level of uncertainties due to nonlinear dynamic characteristics and measurement noise [37]. Time frequency analysis of structural responses under seismic loads can reveal the structural nonlinear dynamic behavior and earthquake resistant performance [38]. In order to investigate the effectiveness and reliability of using the proposed approach in identifying the instantaneous frequency of time varying structures under seismic loads, a two-storey shear building under the 1940 El Centro ground motion is simulated and taken as an example, as shown in Figure 2-7. The equivalent masses of floors 1 and 2 are defined as $m_1=1.60 \times 10^4$ kg and $m_2=8 \times 10^3$ kg, respectively. The damping values of two floors c_1 and c_2 are assumed to be

0.27×10^5 and 0.36×10^5 , respectively. Time varying stiffness parameters of two floors are defined in Eqs. (2.11) and (2.12) to generate the nonstationary responses under seismic loads.

$$k_1 = \begin{cases} 2.1 \times 10^5 \text{ kN} \cdot \text{m} & [0\text{s}, 4\text{s}) \\ 2.1 - 0.058(t - 4) - 0.131 \sin[0.5\pi(t - 4)] \times 10^5 \text{ kN} \cdot \text{m} & [4\text{s}, 16\text{s}) \\ 1.404 \times 10^5 \text{ kN} \cdot \text{m} & [16\text{s}, 30\text{s}) \end{cases} \quad (2.11)$$

$$k_2 = \begin{cases} 1.05 \times 10^5 \text{ kN} \cdot \text{m} & [0\text{s}, 4\text{s}) \\ \{0.75 \times 10^4 t + 1.3 \times 10^5 \text{ kN} \cdot \text{m}\} & [4\text{s}, 8\text{s}) \\ 0.7 \times 10^5 \text{ kN} \cdot \text{m} & [8\text{s}, 30\text{s}] \end{cases} \quad (2.12)$$

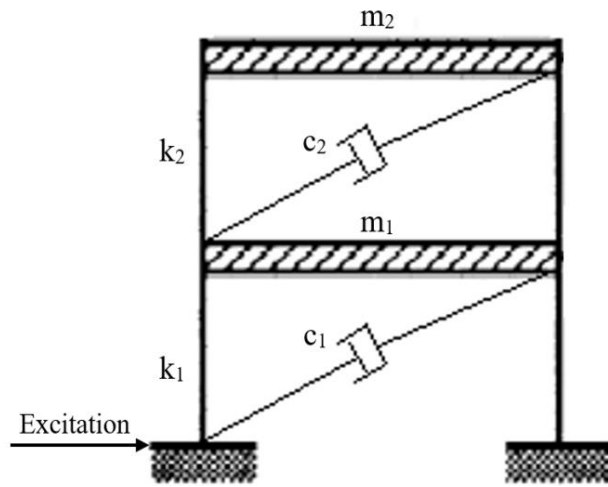


Figure 2-7. Two-storey shear building

Figure 2-8 presents the applied seismic ground motion and the horizontal acceleration response of the first floor. It can be found that the amplitude of ground motion excitation in 0~3s and 28s~30s are relatively small. As a result, the acceleration responses are also small during these two periods. Figure 2-9 compares time-frequency analysis results by using EWT-HT based method and the proposed adaptive Duffing approach. It is obviously observed that the instantaneous frequency results identified by the proposed approach are more smooth and closer to the theoretical values. The relative identification errors listed in Table 2-3 further demonstrate the accuracy of the proposed method. However, the frequency resolution at both ends by using the EWT-HT based method is lower than that of the time domain responses at other time. Slight oscillations can also be observed in the results obtained from the proposed adaptive Duffing approach at the two ends of signals. The possible reason is that the signal amplitude in those periods are relatively small, and the end effect presents in the time frequency analysis. However, the proposed approach improves the accuracy and resolution of time frequency analysis results significantly compared with the method based on EWT and

HT. For numerical case 2, the computational time of using the proposed approach and EWT-HT method are 8.80 s and 0.65 s, respectively.

Table 2-3. Relative errors of identified instantaneous frequency results.

	Adaptive Duffing approach	EWT-HT approach
1st IF	3.07%	8.99%
2nd IF	2.00%	13.45%

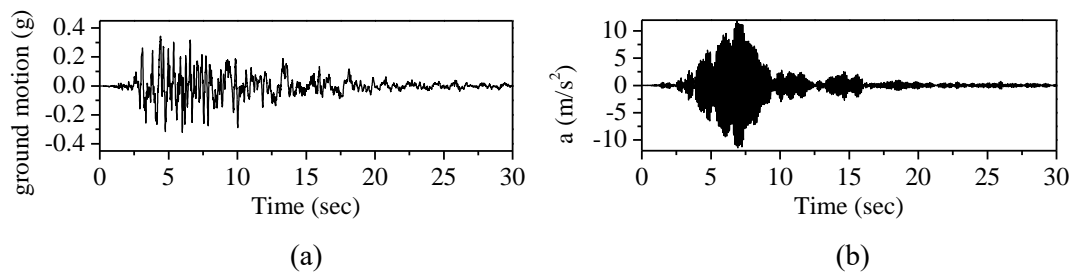


Figure 2-8. The applied seismic ground motion and the corresponding response of the structural model: (a) El Centro ground acceleration record; (b) The horizontal acceleration response of the first floor.

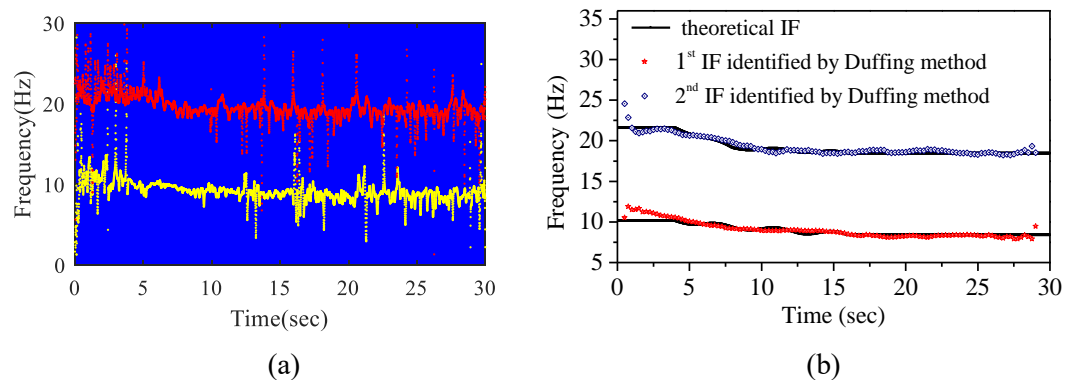


Figure 2-9. Time-frequency analysis results by using: (a) EWT-HT method; (b) The proposed approach

2.4 Experimental Validations

Structural frequency variations caused by the vehicle-bridge interaction have been reported in several theoretical and experimental studies [31, 39, 40]. Dynamic responses of the bridge will inevitably be affected by several factors, i.e. road surface roughness, moving vehicle properties and measurement noise. In this study, measured vibration responses of a time varying system, namely a T-section prestressed concrete beam subjected to a moving vehicle load, are used to verify the proposed instantaneous frequency identification approach

in laboratory environment. Figure 2-10 shows the schematic experimental setup.

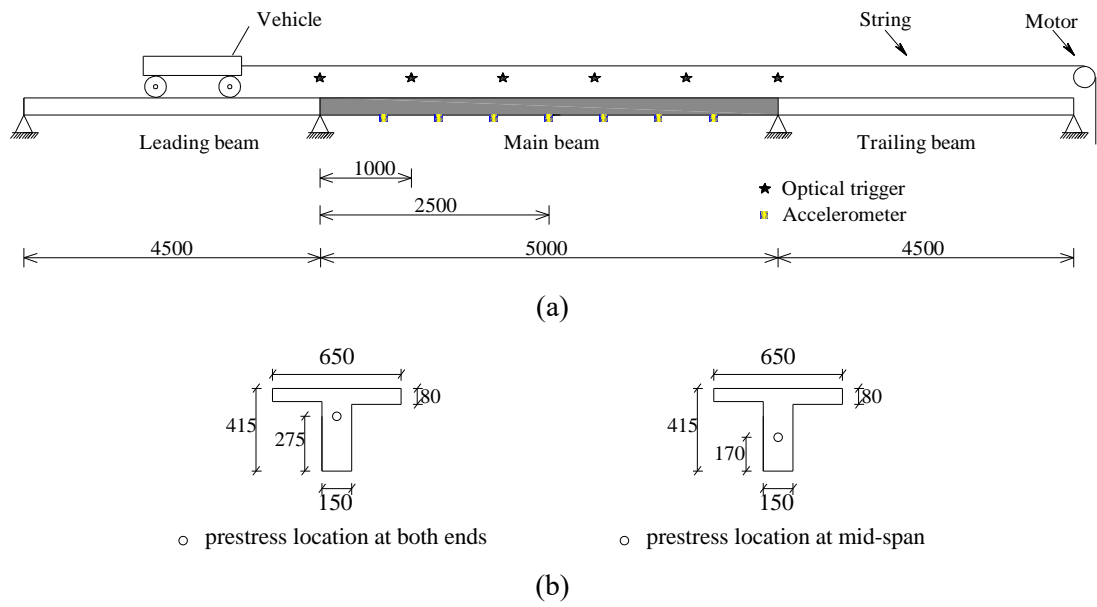


Figure 2-10. Schematic experimental setup: (a) plan view; (b) cross-sections. (unit: mm)



Figure 2-11. Overview of experimental setup of the bridge-vehicle system

The bridge model mainly contains three separate components, a leading beam, a main span and a trailing zone, as shown in Figure 2-11. The boundary of the main span is simply

supported with steel rollers. Three prestressing tendons, as shown in Figure 2-10(b), are applied in the web of the main span with a total prestress force of 140 kN. Leading and trailing beams are used for accelerating and decelerating of the moving vehicle, respectively. The vehicle, as shown in Figure 2-11, is driven by an electrical motor to move through the main span with an approximately constant speed of 0.4 m/s. The wheel spacing and width of the vehicle are 0.8 m and 0.4 m, respectively. A previous study [39] observed an incremental impact of vehicle to bridge mass ratio on the variations of vehicle and bridge frequencies. In this experiment, additional weights are added on the top of vehicle to increase the vehicle to bridge mass ratio. The total weight of the vehicle and T-shaped main beam are 9.48 kN and 12.441 kN, respectively. Six optical triggers are distributed along the main beam with an equal spacing of 1 m to measure the vehicle speed as well as record the exact time instants when vehicle axles move in and exit the main beam. More detailed information about the experimental setup and description can also be found in [41]. The vertical acceleration responses at the mid span of the bridge from the front axle entering the main beam to the rear axle leaving the main beam are recorded to analyse the time-varying frequency owing to the significant vehicle to bridge mass ratio, change location of moving vehicle and vehicle-bridge coupling effects. The duration of the measured acceleration time responses is about 15s with a sampling rate of 1000 Hz. According to the modal analysis of the bridge without the vehicle placing on the top of the bridge, the first two natural frequencies of the main span are 33.4 Hz and 97.3 Hz, respectively. Considering the responses from the bridge subjected to a moving vehicle are dominated by the first fundamental frequency component, a band-pass filter with a lower cutoff frequency of 4 Hz and a higher cutoff frequency of 60 Hz is applied to analyse the originally measured signal from the bridge subjected to the vehicle loads and to extract the instantaneous frequency from measured responses. Experimental response data are normalized in the interval [-1, 1]. Figure 2-12 shows the normalized acceleration responses at the mid-span of the bridge beam after filtering, and its frequency spectrum. As can be found in the frequency spectrum, signal energy is mainly distributed in the range of 30-45 Hz and peaked at 33Hz. It is also worth noting that a small energy in the frequency range of 7.5-25 Hz can be observed, which is likely to be related to the vehicle's vibration characteristics. For comparison, a hammer load is applied at the 3/8 span of the main beam when the vehicle is parked at the leading beam. The vertical acceleration responses of the mid-span under the hammer impact loads are shown in Figure 2-13(a). The small energy distributed from 7-25Hz no longer presents in the frequency spectrum as shown in Figure 2-13(b), when the vehicle is parked at the leading beam. This indirectly indicates that the natural frequency of the vehicle could be distributed in this frequency range. The wheel spacing and speed of vehicle in this study are respectively 0.8 m and 0.4 m/s, hence, the possible axis loading frequency is 0.5 Hz

[42, 43]. Another possibility is that the frequency component is due to the driving speed of vehicle. According to discussions presented in Ref. [40], the bridge frequency may shift about $\pm\pi v/L$ (1.57 Hz) due to the vehicle movement. From the above discussions, it could be concluded that the small energy from 7.5-25 Hz in the frequency spectrum is neither caused by the vehicle loading frequency nor the effect of vehicle movement. Therefore, it is reasonable to consider that the frequency range 7.5-25 Hz might be from the vehicle frequency variation during the vehicle moving cross the bridge.

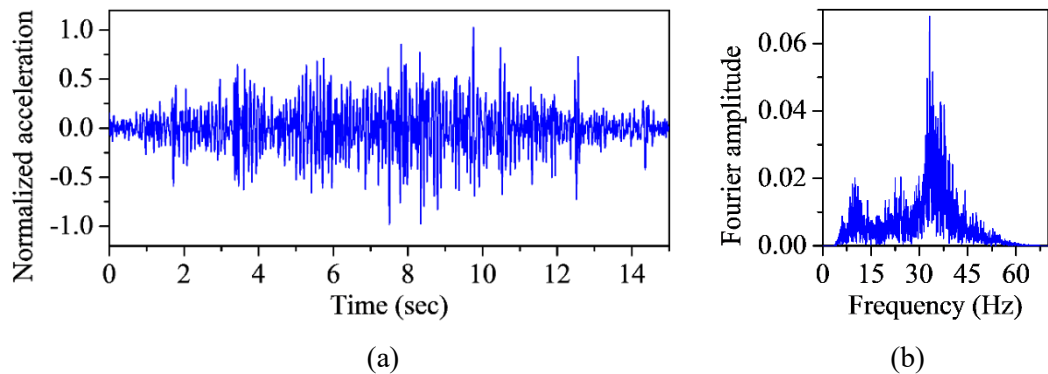


Figure 2-12. Vertical acceleration response at the mid-span under moving vehicle: (a) Normalized acceleration; (b) Frequency spectrum.

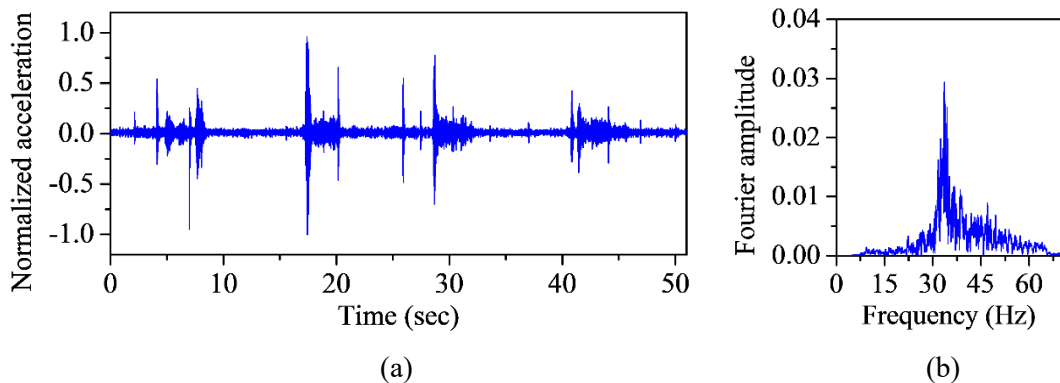


Figure 2-13. Vertical acceleration response at the mid span under hammer impact loads: (a) Normalized acceleration; (b) Frequency spectrum

To obtain a better understanding of the frequency evolution when the vehicle moves along the bridge, EWT is employed to decompose the measured acceleration responses into two components. Then, the time frequency spectrum of decomposed signals will be respectively displayed by performing HT and the proposed approach. The instantaneous frequency identification results by using both methods are shown in Figure 2-14 and Figure 2-15, respectively. Figure 2-14 shows the identified instantaneous frequency results from two EWT

components. The second-order curve fitting of both bridge frequency (blue scatter) and vehicle frequency (red scatter) are also presented. The bridge frequency at both ends of the signal is about 33.2 Hz, which is very close to the natural frequency when the vehicle is not on the testing beam. During the vehicle passing through the main beam, an increasing trend is observed and the instantaneous frequency reaches 36.3 Hz when the vehicle is located at the middle of main span. Intuitively, bridge frequency will decrease when additional mass is added to different locations of a bridge span. However, Chang and Yang [39] revealed that both the natural frequency of bridge and vehicle vary in a half-sine form with respect to the vehicle position. Namely, for a vehicle with relatively smaller natural frequency compared to the bridge, a convex trend in the variation of bridge instantaneous frequency and a concave varying trend will be found for the vehicle. This frequency deviation will be intensified when the fundamental frequency ratio of vehicle to bridge is close to one or the vehicle to bridge mass ratio is increased. The instantaneous frequency observation represented by the red scatter is consistent with the results reported in [39], which indicates that the frequency range 7.5-25 Hz corresponds to the variation of the vehicle resonance frequency.

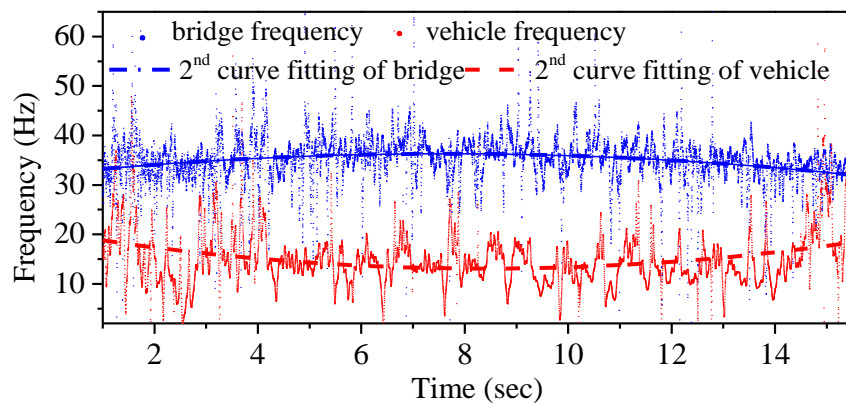


Figure 2-14. Instantaneous frequency identification results by using EWT-HT method.

Figure 2-15 shows the time frequency analysis spectrum obtained by using the proposed approach to analyse the signal components decomposed by EWT. As observed from Figure 2-15, the evolution trends of bridge and vehicle frequencies are quite similar as the results in Figure 2-14. However, better convergent performance is achieved in the identified instantaneous frequencies and more stable results are obtained. Affected by vehicle-bridge interaction effect, road surface roughness and measurement noise, significant fluctuations may inevitably exist in the instantaneous frequency identification results when the vehicle crosses over the bridge. The curve fitting results are assumed as the baseline to calculate the relative errors since theoretical values are not available. Standard deviations and relative errors are

adopted herein to quantify the fluctuations of identified instantaneous frequencies by using both methods, as listed in Table 2-4. It can be observed that more stable results are obtained with the proposed approach. For experiment study, the computational time of the proposed approach and EWT-HT method are 3.66 s and 0.56 s, respectively. Although the proposed approach requires more computational time, the method is still efficient. The improvement on the identification results are substantial, demonstrated by the numerical and experimental results, especially the two numerical examples as given in Table 2-2 and Table 2-3.

Table 2-4. Standard deviations and relative errors of instantaneous frequency results.

Approach	EWT-HT		The proposed approach	
	Standard deviation	Relative error	Standard deviation	Relative error
Bridge instantaneous frequency	7.22	9.74%	4.05	8.8%
Vehicle instantaneous frequency	6.56	26.43%	4.11	23.64%

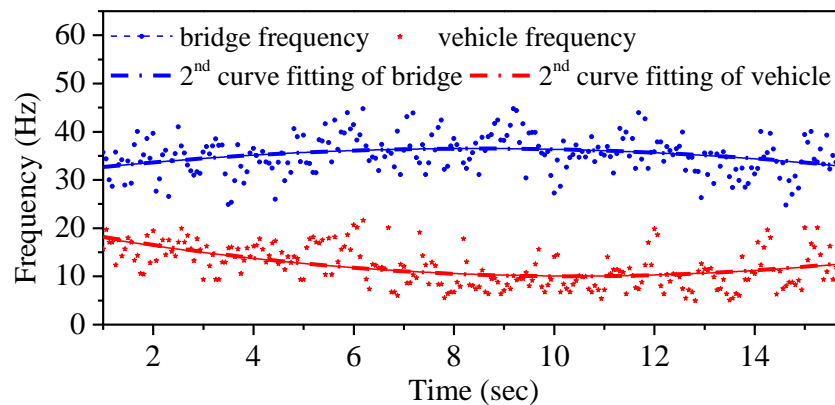


Figure 2-15. Instantaneous frequency identification results by the proposed approach

In Table 2-4, the standard deviations and relative errors of instantaneous frequency identification results by using the proposed approach are smaller than those from the EWT-HT method, which means that time-varying instantaneous frequencies identified by the proposed approach are more stable with less oscillations. In other words, a high frequency resolution is achieved in the instantaneous frequency identification. One possible explanation is that the noise-induced frequency perturbation can be well eliminated by Duffing system with the proposed approach. It is also noted that the improvement in experimental results is not as significant as results in numerical studies. The instantaneous frequency identification of bridge-vehicle system is a challenge task, especially separating the bridge and vehicle

frequencies accurately. The dynamic responses of the bridge subjected to a moving vehicle include the effects of measurement noise, the road surface roughness and bridge-vehicle interaction. These effects may increase the fluctuations in instantaneous frequencies of the bridge-vehicle system.

2.5 Conclusions

This chapter proposes a novel time frequency analysis approach based on an adaptive Duffing oscillator array to identify the instantaneous frequency of nonstationary signals under strong noise with a high resolution. To avoid the use of a large array of oscillators, improvement is made by recursively adjusting the central reference frequency in each time window according to the frequency estimated in the previous time window. A simulated multiple frequency component nonstationary signal, and the response of a frame structure with time varying stiffness parameters under seismic loads are utilized to investigate the capability of the proposed approach. The proposed method is further validated by analyzing the responses of a laboratory reinforced concrete beam subjected to moving vehicle load. Both numerical and experimental validation results show that the proposed adaptive Duffing oscillator approach can reveal a more stable and clear time-frequency transient feature and instantaneous frequency identification results with a high resolution than the counterpart EWT-HT based time-frequency analysis method. In future work, the superiority of the proposed approach in noise immunity will be further investigated by introducing pink noise and other types of strong noise and system uncertainties.

References

- [1] Z. Feng, M. Liang, F. Chu, Recent advances in time–frequency analysis methods for machinery fault diagnosis: A review with application examples, *Mechanical Systems and Signal Processing*, 38 (2013) 165-205.
- [2] Z.-C. Wang, W.-X. Ren, G. Chen, Time–frequency analysis and applications in time-varying/nonlinear structural systems: A state-of-the-art review, *Advances in Structural Engineering*, 21 (2018) 1562-1584.
- [3] S. Nagarajaiah, Adaptive passive, semiactive, smart tuned mass dampers: identification and control using empirical mode decomposition, Hilbert transform, and short - term Fourier transform, *Structural Control and Health Monitoring*, 16 (2009) 800-841.
- [4] S. Zhong, S.O. Oyadiji, Crack detection in simply supported beams using stationary wavelet transform of modal data, *Structural Control and Health Monitoring*, 18 (2011) 169-190.
- [5] P. Tratskas, P. Spanos, Linear multi-degree-of-freedom system stochastic response by using the harmonic wavelet transform, *J. Appl. Mech.*, 70 (2003) 724-731.
- [6] P. Spanos, A. Giaralis, N. Politis, Time–frequency representation of earthquake accelerograms and inelastic structural response records using the adaptive chirplet decomposition and empirical mode decomposition, *Soil Dynamics and Earthquake Engineering*, 27 (2007) 675-689.
- [7] D. He, X. Wang, M.I. Friswell, J. Lin, Identification of modal parameters from noisy transient response signals, *Structural Control and Health Monitoring*, 24 (2017) e2019.
- [8] S.K. Yadav, R. Sinha, P.K. Bora, Electrocardiogram signal denoising using non-local wavelet transform domain filtering, *IET Signal Processing*, 9 (2015) 88-96.
- [9] S. Gan, Y. Chen, S. Zu, S. Qu, W. Zhong, Structure-oriented singular value decomposition for random noise attenuation of seismic data, *Journal of Geophysics and Engineering*, 12 (2015) 262-272.
- [10] I. Orović, S. Stanković, M. Amin, Compressive sensing for sparse time-frequency representation of nonstationary signals in the presence of impulsive noise, *Compressive Sensing II*, International Society for Optics and Photonics, 2013, pp. 87170A.
- [11] S. Chen, X. Dong, Y. Xiong, Z. Peng, W. Zhang, Nonstationary Signal Denoising Using an Envelope-Tracking Filter, *IEEE/ASME Transactions on Mechatronics*, 23 (2017) 2004-2015.
- [12] N. Hu, X. Wen, The application of Duffing oscillator in characteristic signal detection of early fault, *Journal of Sound and Vibration*, 268 (2003) 917-931.
- [13] G.-W. Kim, D.R. Johnson, F. Semperlotti, K. Wang, Localization of breathing cracks using combination tone nonlinear response, *Smart Materials and Structures*, 20 (2011) 055014.
- [14] Z.-h. Lai, Y.-g. Leng, Weak-signal detection based on the stochastic resonance of bistable Duffing oscillator and its application in incipient fault diagnosis, *Mechanical Systems and Signal Processing*, 81 (2016) 60-74.
- [15] V. Rashtchi, M. Nourazar, FPGA implementation of a real-time weak signal detector using a duffing oscillator, *Circuits, Systems, and Signal Processing*, 34 (2015) 3101-3119.
- [16] J. Hou, X.p. Yan, P. Li, X.h. Hao, Adaptive time - frequency representation for weak chirp signals based on Duffing oscillator stopping oscillation system, *International Journal of Adaptive Control and Signal Processing*, 32 (2018) 777-791.

- [17] E. Perkins, B. Balachandran, Effects of phase lag on the information rate of a bistable Duffing oscillator, *Physics Letters A*, 379 (2015) 308-313.
- [18] V. Agarwal, X. Zheng, B. Balachandran, Influence of noise on frequency responses of softening Duffing oscillators, *Physics Letters A*, 382 (2018) 3355-3364.
- [19] G. Wang, D. Chen, J. Lin, X. Chen, The application of chaotic oscillators to weak signal detection, *IEEE Transactions on industrial electronics*, 46 (1999) 440-444.
- [20] X. Liu, L. Bo, Y. Liu, Y. Zhao, J. Zhang, M. Deng, N. Hu, Location identification of closed crack based on Duffing oscillator transient transition, *Mechanical Systems and Signal Processing*, 100 (2018) 384-397.
- [21] W. Zhang, H. Hao, J. Wu, J. Li, H. Ma, C. Li, Detection of minor damage in structures with guided wave signals and nonlinear oscillator, *Measurement*, 122 (2018) 532-544.
- [22] Z. Zhao, F.-L. Wang, M.-X. Jia, S. Wang, Intermittent-chaos-and-cepstrum-analysis-based early fault detection on shuttle valve of hydraulic tube tester, *IEEE Transactions on Industrial Electronics*, 56 (2009) 2764-2770.
- [23] M. Zabihi, S. Kiranyaz, A.B. Rad, A.K. Katsaggelos, M. Gabbouj, T. Ince, Analysis of high-dimensional phase space via Poincaré section for patient-specific seizure detection, *IEEE Transactions on Neural Systems and Rehabilitation Engineering*, 24 (2015) 386-398.
- [24] J. Wu, Y. Wang, W. Zhang, Z. Nie, R. Lin, H. Ma, Defect detection of pipes using Lyapunov dimension of Duffing oscillator based on ultrasonic guided waves, *Mechanical Systems and Signal Processing*, 82 (2017) 130-147.
- [25] L. Tian-liang, Frequency estimation for weak signals based on chaos theory, 2008 International Seminar on Future BioMedical Information Engineering, IEEE, 2008, pp. 361-364.
- [26] A. Neyfeh, B. Balachandran, *Applied nonlinear dynamics: analytical, computational and experimental methods*, John Wiley & Sons, Inc., New York, 1995.
- [27] J.M.T. Thompson, H.B. Stewart, *Nonlinear dynamics and chaos*, John Wiley & Sons, 2002.
- [28] S. Dong, M. Yuan, Q. Wang, Z. Liang, A modified empirical wavelet transform for acoustic emission signal decomposition in structural health monitoring, *Sensors*, 18 (2018) 1645.
- [29] Y. Xin, H. Hao, J. Li, Time-varying system identification by enhanced Empirical Wavelet Transform based on Synchroextracting Transform, *Engineering Structures*, 196 (2019) 109313.
- [30] Y. Xin, H. Hao, J. Li, Operational modal identification of structures based on improved empirical wavelet transform, *Structural Control and Health Monitoring*, 26 (2019) e2323.
- [31] P. Ni, J. Li, H. Hao, Y. Xia, X. Wang, J.M. Lee, K.H. Jung, Time - varying system identification using variational mode decomposition, *Structural Control and Health Monitoring*, 25 (2018) e2175.
- [32] S. Stanković, I. Orović, M. Amin, Compressed sensing based robust time-frequency representation for signals in heavy-tailed noise, 2012 11th International Conference on Information Science, Signal Processing and their Applications (ISSPA), IEEE, 2012, pp. 605-610.
- [33] T. Wang, M. Zhang, Q. Yu, H. Zhang, Comparing the applications of EMD and EEMD on time-frequency analysis of seismic signal, *Journal of Applied Geophysics*, 83 (2012) 29-34.

- [34] Y.-J. Xue, J.-X. Cao, D.-X. Wang, H.-K. Du, Y. Yao, Application of the variational-mode decomposition for seismic time–frequency analysis, *IEEE Journal of Selected Topics in Applied Earth Observations and Remote Sensing*, 9 (2016) 3821-3831.
- [35] M. Sahani, P.K. Dash, FPGA-based online power quality disturbances monitoring using reduced-sample HHT and class-specific weighted RVFLN, *IEEE Transactions on Industrial Informatics*, 15 (2019) 4614-4623.
- [36] K. Thirumala, S. Pal, T. Jain, A.C. Umarikar, A classification method for multiple power quality disturbances using EWT based adaptive filtering and multiclass SVM, *Neurocomputing*, 334 (2019) 265-274.
- [37] J. Suhardjo, B. Spencer Jr, M. Sain, Feedback-feedforward control of structures under seismic excitation, *Structural Safety*, 8 (1990) 69-89.
- [38] F. Pioldi, E. Rizzi, Earthquake - induced structural response output - only identification by two different Operational Modal Analysis techniques, *Earthquake Engineering & Structural Dynamics*, 47 (2018) 257-264.
- [39] Y. Yang, M. Cheng, K. Chang, Frequency variation in vehicle–bridge interaction systems, *International Journal of Structural Stability and Dynamics*, 13 (2013) 1350019.
- [40] Y.-B. Yang, C. Lin, J. Yau, Extracting bridge frequencies from the dynamic response of a passing vehicle, *Journal of Sound and Vibration*, 272 (2004) 471-493.
- [41] J. Li, S. Law, H. Hao, Improved damage identification in bridge structures subject to moving loads: numerical and experimental studies, *International Journal of Mechanical Sciences*, 74 (2013) 99-111.
- [42] D. Cantero, D. Hester, J. Brownjohn, Evolution of bridge frequencies and modes of vibration during truck passage, *Engineering Structures*, 152 (2017) 452-464.
- [43] D. Milne, L. Le Pen, D. Thompson, W. Powrie, Properties of train load frequencies and their applications, *Journal of Sound and Vibration*, 397 (2017) 123-140.

CHAPTER 3 NONLINEAR STRUCTURAL DAMAGE DETECTION USING OUTPUT-ONLY VOLTERRA SERIES MODEL

ABSTRACT²

Volterra series is a promising technique with great potential for nonlinear system identification. The conventional Volterra series model computes the output responses by performing multiple convolutions between the input excitation and Volterra kernels function. However, the difficulty in acquiring the excitation forces of civil engineering structures under operating conditions greatly limits the application of using Volterra series-based method for system identification. This chapter proposes an output-only-based approach using Volterra series model for nonlinear structural damage detection, by quantifying the nonlinear behavior of structures without the prior knowledge of external excitations. The proposed approach uses the structural responses measured at two different locations to identify the kernel function parameters and evaluate the contribution of nonlinear components in the measured responses. The ratio between the standard deviation of the nonlinear components and that of the overall structural response is adopted as damage-sensitive index to quantify the contributions from these two adjacent sensors for performing nonlinear structural damage detection. Numerical studies on a beam structure with a breathing crack under different levels of white noise excitations and experimental studies on a precast segmental concrete column subjected to ground motions with different PGA values are conducted to validate the capability and accuracy of using the proposed approach for nonlinear structural damage detection. The results demonstrate that the proposed approach is capable of performing nonlinearity quantification effectively and locating structural nonlinear damage. The increasing damage index value can also be used to register the increasing damage severity.

3.1 Introduction

Detection of structural local damage with vibration data measured from installed SHM systems is an important but still challenging task, especially when the structural vibration is nonlinear. It has received a considerable amount of research attentions in the structural

²This chapter was published in *Structural Control & Health Monitoring* with the full bibliographic citation as follows: Peng, Z., Li, J., Hao, H., & Li, C. (2021). Nonlinear structural damage detection using output-only Volterra series model. *Structural Control and Health Monitoring*, 28(9), e2802. <https://doi.org/10.1002/stc.2802>.

dynamics community during the last two decades [1]. In this scope, DSF extracted from structural vibration responses under the current state are compared with those under baseline (healthy) state to evaluate the occurrence, location and even severity of structural damage [2]. Most of the established vibration based damage detection methods can be divided into two categories: physical model-based and data feature-based [3, 4]. With the superiority in data driven monitoring strategy which does not require finite element modelling and updating, the data feature-based methods have been widely developed in the last decades [5, 6]. Developing the features or damage indices (DI) which are sensitive to structural condition but insensitive to operational effects or measurement noise is considered as one of the most essential components in data feature-based methods for evaluating the feasibility and effectiveness of using vibration data for damage detection. With this motivation, a number of novel time series analysis methods including the Autoregressive–moving-average (ARMA) model [7], PST technique [8] and autocorrelation function [9], etc., have been developed and successfully applied to detecting structural damage of numerical, experimental and in-field structures.

Damage such as the breathing crack [10, 11], concrete crushing [12], column rocking, post-buckling and bolt rattling (impacting, stick-slip) [13], occurred in a structure or mechanical element is frequently manifested by nonlinear response manners, i.e. harmonic generation [14] and/or nonlinear attenuation [15] in vibrational responses. Breathing crack is one of the most commonly observed types of nonlinear damage that occurs in civil engineering or mechanical structures subjected to fatigue loading. The distinctive harmonic resonance features are usually used to evident the presence of breathing cracks. Chatterjee [14] analysed the acceleration responses of a cantilever beam with a breathing crack and found that the amplitude of the second harmonic component was positively proportional to the crack depth. Semperlotti et al. [11] pointed out that the phase information associated with the super-harmonic components can be used to locate the crack damage. However, it should be noted that harmonic resonance based methods may suffer from several major drawbacks: 1) Compared with well excited low order natural frequency components of the structure, the signal energy of high order nonlinear component responses is relatively weak and not easily identified; and 2) The frequency of generated harmonic component is related to the excitation frequency, which is difficult to measure or even unavailable for in-field applications.

It has been intensively demonstrated [16-18] that the damage-induced nonlinearity degree will increase with the damage severity, which provides a new damage assessment perspective by quantifying the proportion of nonlinearity component presented in vibration responses. In the past decade, many methods, e.g. Wiener–Hammerstein models [19], nonlinear autoregressive moving average (NARMA) model [20], frequency-domain subspace identification [21], principal component analysis (PCA) [22], deep learning [23] and Volterra

series model [24, 25] have been developed to effectively characterize nonlinearities with the system input and output data. Among those methods, Volterra series model has been demonstrated to have the feasibility and applicability in estimating the nonlinear properties presented in mechanical systems. Prawin and Rao [26] developed an adaptive filter based Volterra series model estimation method and applied it to the nonlinear parameter identification of multiple degrees-of-freedom (DOF) system subjected to a harmonic load. Villani et al. [25] proposed a stochastic Volterra series model and experimentally verified the feasibility of using this method in evaluating the state of structure with initial nonlinearity subjected to chirp excitations. The weak hysteresis behavior, i.e. vortex-induced vibration (VIV) can be accurately approximated by Volterra series model with the finite order polynomial. The single-input, single output second-order Volterra system is used in Ref. [27] to model the hysteresis phenomenon of the VIV of Tacoma Narrows Bridge at lock-in condition. Results shown that the nonlinear approximation using the identified Volterra kernels converges to the reference results. However, the Volterra series model dose not lead to a finite order convergent solution for system with strong hysteresis behavior. A state-of-the-art review on the Volterra series based nonlinear system modelling and its engineering applications has been comprehensively provided in Ref. [24]. In those studies, the external excitation and synchronized structural responses should be respectively used as input and output of the Volterra series model to estimate the kernel function coefficients. However, the dynamic excitation of structures under operating conditions is difficult to measure and therefore is usually unavailable, which could greatly limit the applications of using Volterra series based methods from laboratory-based experiment to the field tests. To overcome this limitation, attempts have been made in literature to estimate the system parameters without information of excitations. Tan et al. [28] proposed a sparse blind Volterra kernel parameter identification method and applied it to a single DOF system under distributed stationary random excitations. However, this method is considered oversimplified by removing all the memory terms. This method was extended by Fernandes et al. [29] to a parallel factor decomposition for blind identification of the first two orders of kernel parameters.

The main objective of this study is to develop an output only based Volterra series model to quantify the nonlinearity associated with nonlinear structures, which can be used to perform nonlinear structural damage assessment. The main idea is to replace the excitation input to the Volterra model by the dynamic response measured from a specific location, and to describe the nonlinearity in the region between two nodes with output-only data. In the proposed method, the optimal kernel parameters of Volterra series model will be obtained through the LSE to minimize the normalized root-mean-square-error (NRMSE) between the measured output response and the prediction obtained from Volterra series model. Then a damage index

is defined based on the contribution of nonlinearities in Volterra series model to identify damage in nonlinear structures.

The remaining sections of this chapter are organised as follows. The theoretical derivation from input-output based Volterra series to output-only based Volterra series representation, as well as the implementation procedure of the proposed approach in quantifying the nonlinearity associated with structural responses will be detailed in Section 2. In Section 3, a 2D numerical beam with a breathing crack is used as an example to verify the effectiveness and applicability of using the proposed approach for detecting the location and severity of crack damage. In Section 4, the proposed approach will be further applied to detect the nonlinear damage of a precast segmental column introduced by seismic excitations in the laboratory shaking table tests. Conclusions and discussions will be provided in Section 5.

3.2 Theoretical Background and Development

3.2.1 From input–output Volterra series to output-only Volterra series response representation

The Volterra series theory [24] has been widely applied in several fields, including electronic, biomedical, mechanical, and civil engineering communities, to model and analyze the nonlinear process among measurable variables. Before stating the proposition, it is supposed that the nonlinear system involved in this study has a convergent expansion through Volterra series and the output response can be estimated by multiple convolutions involving the input series with the following discrete expression

$$y(t) = \sum_{\eta=1}^{\infty} \sum_{n_1=0}^{N_1} \sum_{n_2=0}^{N_2} \cdots \sum_{n_{\eta}=0}^{N_{\eta}} H_{\eta}(n_1, n_2, \dots, n_{\eta}) \prod_{i=1}^{\eta} u(t - n_i) = \sum_{n=1}^{\infty} y_n(t) \quad (3.1)$$

where $u(t)$, $y(t) \in \mathbf{R}$ are the one-dimensional input and output responses of nonlinear system at time instant t , respectively. $H_{\eta}(n_1, n_2, \dots, n_{\eta})$ is the η -th order discrete Volterra kernel function. N_i is the memory length of the i -th order Volterra kernel. As expressed in Eq. (3.1), the output time series can be viewed as the infinite combination of linear component y_1 and higher-order nonlinear components $y_2(t) + y_3(t) + \cdots + y_{\infty}(t)$. The first three components are expanded as follows

$$y_1(t) = \sum_{n_1=0}^{N_1} H_1(n_1)u(t - n_1) \quad (3.2)$$

$$y_2(t) = \sum_{n_1=0}^{N_1} \sum_{n_2=0}^{N_2} H_2(n_1, n_2)u(t - n_1)u(t - n_2) \quad (3.3)$$

$$y_3(t) = \sum_{n_1=0}^{N_1} \sum_{n_2=0}^{N_2} \sum_{n_3=0}^{N_3} H_3(n_1, n_2, n_3)u(t - n_1)u(t - n_2)u(t - n_3) \quad (3.4)$$

Eq. (3.1) is the extension of the one-dimensional convolution theory to multi-dimensional

convolutional integrals with infinite series and memory terms. It should be noted that Volterra system is degraded into a linear system if all the higher order Volterra kernels except the first order are set as zero. For an unknown nonlinear system, the output prediction will be more accurate when a sufficient number of higher order kernels (can also be referred to as truncation order) is involved [30]. However, the parameters to be identified in each kernel function exponentially grow with the increasing truncation order, which eventually requires large size input-output observations as well as excessive computation to obtain a converged estimation of parameters associated with higher-order kernels [31, 32]. Existing studies suggest that a truncation order of 3 is commonly used to approximate the nonlinear dynamics of mechanical and civil structures with fading memory [33, 34]. Hence, the truncation order is predetermined as 3 in this study, and the corresponding Volterra series response representation is given in Eq. (3.5).

$$\begin{aligned}
y(t) &\approx \underbrace{y_1(t)}_{\text{linear}} + \underbrace{y_2(t) + y_3(t)}_{\text{nonlinear}} + e(t) \\
&= \sum_{n_1=0}^{N_1} H_1(n_1)u(t - n_1) + \sum_{n_1=0}^{N_1} \sum_{n_2=0}^{N_2} H_2(n_1, n_2)u(t - n_1)u(t - n_2) \quad (3.5) \\
&\quad + \sum_{n_1=0}^{N_1} \sum_{n_2=0}^{N_2} \sum_{n_3=0}^{N_3} H_3(n_1, n_2, n_3)u(t - n_1)u(t - n_2)u(t - n_3) + e(t)
\end{aligned}$$

where $e(t)$ is the sum of prediction error at time instant t owing to ignoring the higher-order terms.

The Volterra series response representation using input and output data detailed in Eq. (3.5) has been intensively demonstrated to be an efficient tool for modelling the nonlinear features and predicting the output of nonlinear mechanical system [24, 25, 35]. Unfortunately, as mentioned above for SHM applications under operating conditions, the input excitations could come from multiple sources at multiple locations, which poses an extreme difficulty to measure if not impossible [36]. To overcome this limitation, this study proposes a novel approach to identify the structural nonlinearity by developing an output data only Volterra series model. It is widely recognised that the accumulation of structural damage, especially crack damage, will gradually increase the contribution of nonlinear component in vibration responses [16]. Instead of investing efforts in measuring the barely accessible environmental excitation under operating conditions, the main idea of this study is to replace the excitation input by using an available structural response from a specific measurable location, and to estimate the development of structural damage in a certain region through investigating the nonlinearity between two used vibration responses (one as input and the other one as output in Volterra series model). To relate structural responses measured from two different locations as performed by the conventional Volterra model, the prediction of $y(t)$ from Eq. (3.5) is modified as

$$\begin{aligned}
y(t) &\approx \underbrace{y_1(t)}_{\text{linear}} + \underbrace{y_2(t) + y_3(t)}_{\text{nonlinear}} + e(t) \\
&= \sum_{n_1=0}^{N_1} G_1(n_1) \bar{y}(t - n_1) + \sum_{n_1=0}^{N_1} \sum_{n_2=0}^{N_2} G_2(n_1, n_2) \bar{y}(t - n_1) \bar{y}(t - n_2) \\
&\quad + \sum_{n_1=0}^{N_1} \sum_{n_2=0}^{N_2} \sum_{n_3=0}^{N_3} G_3(n_1, n_2, n_3) \bar{y}(t - n_1) \bar{y}(t - n_2) \bar{y}(t - n_3) + e(t)
\end{aligned} \tag{3.6}$$

in which the term $\bar{y}(t)$ refers to the output response measured at another location at time t , $G_1(n_1)$, $G_2(n_1, n_2)$ and $G_3(n_1, n_2, n_3)$ denote the first, second and third orders of kernel functions that can be used to describe the output $y(t)$ in a similar way by using $H_n(n_1, n_2, \dots, n_\eta)$. The above equation can be rewritten as follows

$$y(t) = \bar{\mathbf{y}}^T(t) \mathbf{G} + e(t) \tag{3.7}$$

in which $\bar{\mathbf{y}}^T(t)$ denotes the input vector measured from another location to predict $y(t)$ with a length of N_p . \mathbf{G} denotes the unknown kernel parameters vector of length N_p . $N_p = (N_1+1) + (N_2+1)^2 + (N_3+1)^3$ is the overall number of kernel parameters to be estimated. For the sake of simplicity, the same memory length of each order kernel is considered, namely, $N_1=N_2=N_3=N$ [26]. The expansion forms of $\bar{\mathbf{y}}^T(t)$ and \mathbf{G} of the order $(N_p \times 1)$ are given as follows

$$\bar{\mathbf{y}}^T(t) = [\bar{y}(t), \dots, \bar{y}(t - N_1), \bar{y}^2(t), \dots, \bar{y}^2(t - N_2), \dots, \bar{y}^3(t), \dots, \bar{y}^3(t - N_3)] \tag{3.8}$$

$$\mathbf{G} = \left[\underbrace{G(0), \dots, G(N_1)}_{G_1}, \underbrace{G(0,0), \dots, G(N_2, N_2)}_{G_2}, \underbrace{G(0,0,0), \dots, G(N_3, N_3, N_3)}_{G_3} \right] \tag{3.9}$$

It is concluded from Eqs. (7-9) that the output $y(t)$ measured at time t is predicted by the convolution operation of current and past N samples measured from another location $\bar{\mathbf{y}}^T(t)$. The involvement of memory terms allows the Volterra series model to describe the effect of the past input on the current response. Considering continuously measured input time history with $m+1$ observation $[\bar{y}(0), \bar{y}(1), \dots, \bar{y}(m)]$, and an equal length measured output time series $[y(0), y(1), \dots, y(m)]$, the output can be successively estimated by substituting the input signal into Eq. (3.7). The estimation process can be rewritten in the following matrix equation form

$$\mathbf{Y} = \bar{\mathbf{Y}} \mathbf{G} + \mathbf{e} \tag{3.10}$$

where the output estimation vector \mathbf{Y} of the order $(m+1-N \times 1)$, the prediction error vector \mathbf{e} of the order $(m+1-N \times 1)$ and the input matrix $\bar{\mathbf{Y}}$ of the order $(m+1-N \times N_p)$ are defined as follows

$$\mathbf{Y} = [y(N), y(N+1), \dots, y(m)]^T \tag{3.11}$$

$$\mathbf{e} = [e(N), e(N+1), \dots, e(m)] \tag{3.12}$$

$$\bar{\mathbf{Y}} = \begin{bmatrix} \bar{y}(N), \dots, \bar{y}(0) & \bar{y}(N)^2, \dots, \bar{y}(0)^2 & \bar{y}(N)^3, \dots, \bar{y}(0)^3 \\ \bar{y}(N+1), \dots, \bar{y}(1) & \bar{y}(N+1)^2, \dots, \bar{y}(1)^2 & \bar{y}(N+1)^3, \dots, \bar{y}(1)^3 \\ \vdots & \vdots & \vdots \\ \bar{y}(m), \dots, \bar{y}(m-N) & \bar{y}(m)^2, \dots, \bar{y}(m-N)^2 & \bar{y}(m)^3, \dots, \bar{y}(m-N)^3 \end{bmatrix} \quad (3.13)$$

The optimal estimation of the Volterra series kernel parameters can be obtained analytically by using Eq. (3.9) in a least-squares manner, which yields

$$\hat{\mathbf{G}} = (\bar{\mathbf{Y}}^T \bar{\mathbf{Y}})^{-1} \bar{\mathbf{Y}}^T \mathbf{Y} \quad (3.14)$$

With the least squares estimation (LSE), Volterra series kernel coefficient $\hat{\mathbf{G}}$, the linear component \mathbf{y}_1 and nonlinear component $\mathbf{y}_2, \mathbf{y}_3$ can be effectively calculated as

$$\mathbf{y}_1 = \bar{\mathbf{Y}}_1 \hat{\mathbf{G}}_1, \quad \mathbf{y}_2 = \bar{\mathbf{Y}}_2 \hat{\mathbf{G}}_2, \quad \mathbf{y}_3 = \bar{\mathbf{Y}}_3 \hat{\mathbf{G}}_3 \quad (3.15)$$

3.2.2 Output only based nonlinear DSF

Using the methodology described in Section 2.1, it is possible to identify the nonlinear relationship between two adjacent sensor locations by estimating the Volterra kernels parameters. The nonlinear proportion will increase with the severity of damage, thus, structural damage can be effectively detected by analysing the nonlinearity in dynamic responses introduced by the degradation of structural integrity. A damage-sensitive index, which has already been successfully applied to detect the nonlinear damage [25, 37], including breathing crack and bolt loosen, is described as

$$\lambda_i = \frac{std(\mathbf{y}_i)}{std(\mathbf{y}_1) + std(\mathbf{y}_2) + std(\mathbf{y}_3)}, \quad (1 \leq i \leq 3) \quad (3.16)$$

where $std(\mathbf{y}_i)$ is the standard deviation of the component signal corresponding to the i -th order kernel. λ_i denotes the normalized contribution of \mathbf{y}_i to the overall system response. For instance, $\lambda_1 \approx 1$ means that the relationship between two different sensor locations is nearly linear, indicating that no nonlinear damage occurs in this region. The system nonlinear level can be estimated as follows by subtracting the linear contribution from the overall contribution

$$\lambda_{inonlinear} = 1 - \frac{std(\mathbf{y}_1)}{std(\mathbf{y}_1) + std(\mathbf{y}_2) + std(\mathbf{y}_3)} \quad (3.17)$$

The higher the above index, the more significant nonlinear response is expected. Figure 3-1 presents the computational flowchart of using the proposed approach for nonlinear structural damage detection. In Step 1, structural dynamic responses at different locations are acquired and pre-processed. In Step 2, the truncation order and memory length of Volterra series model are pre-initialized as 3 and 1, respectively. Then the LSE method is adopted to estimate the optimal kernel parameters of the initialized Volterra series model. In Step 3, the

memory length will be adjusted in each iteration until the prediction error between measured and Volterra series model estimated responses meets the convergence criterion. It should be noted that the prediction error is related to the nonlinear degree of the system, which may be affected by the operational condition and may vary from case to case. Hence, it seems not reasonable to fix the allowable error level as a constant. NRMSE is defined as

$$NRMSE = \frac{\sqrt{E((\hat{\mathbf{y}}-\mathbf{y})^2)}}{\max(\mathbf{y})-\min(\mathbf{y})} \quad (3.18)$$

where $E(\cdot)$ denotes the mathematical expectation; \mathbf{y} and $\hat{\mathbf{y}}$ represent the actual response vector and predicted responses vector from Volterra series model, respectively; $\max(\mathbf{y})$ and $\min(\mathbf{y})$ are respectively the maximum and minimum values of actual responses vector. To this end, the relationship between memory length and NRMSE is carefully evaluated in each case to achieve a tradeoff between modelling accuracy and the number of kernel parameter numbers. In Step 4, the output response and the corresponding nonlinearity contribution will be estimated by using the Volterra series model determined in Steps 2-3.

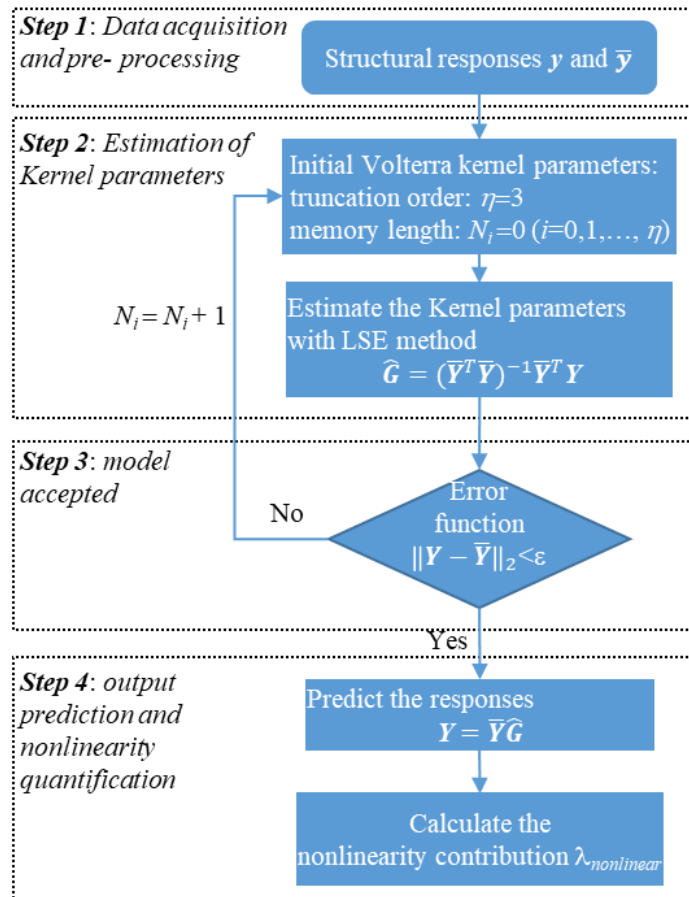


Figure 3-1. Flowchart of the proposed output-only nonlinear structural damage assessment

It should be noted that the proposed approach conducts the nonlinear damage assessment

based on a developed Volterra series model using output vibration data only. The proposed approach can effectively evaluate the nonlinearity contribution between two sensor locations, and this feature can be explored for nonlinear damage detection. The proposed approach will be further validated in the following numerical and experimental studies.

3.3 Numerical Studies

3.3.1 Modeling of a beam structure with a breathing crack

Cracks are the most commonly occurred type of structural damage in the aerospace, civil and mechanical structures subjected to fatigue loading. Typically, a crack can be classified into open crack and breathing crack according to the state of crack during the vibration. As the name suggests, open crack means that the crack is open under external excitations, usually leading to a reduction of physical stiffness. Apart from loss of stiffness, previous numerical and experimental studies demonstrated that the vibration of structures with breathing crack becomes nonlinear due to the fluctuation of stiffness during the periodical open and close of breathing crack. Douka and Hadjileontiadis [38] pointed out that considering the nonlinear behavior of breathing crack is more practical for the real situation and make the vibration based damage detection method more applicable. The bilinear stiffness model as shown in Figure 3-2 has been widely used to describe the breathing behavior in an element with a breathing crack [39, 40]. For a crack propagating from the upper surface of beam, the crack will open when the upper surface suffers tensile stress, otherwise, the crack will close. As a result, the element stiffness matrix will vary with the open and close of crack surface. The crack opening mechanism along with the time-dependent element stiffness matrix in both states is given in Eq. (3.19).

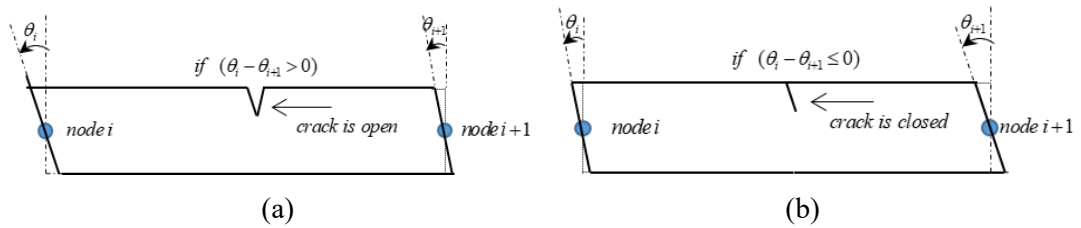


Figure 3-2. DOFs at the crack element when the crack is: (a) open; (b) closed.

$$\mathbf{K}_d(t) = \mathbf{K} - H_{step}(\theta_i - \theta_{i+1})\mathbf{K}_c \begin{cases} H_{step}(\theta_i - \theta_{i+1}) = 1, \theta_i - \theta_{i+1} > 0 \\ H_{step}(\theta_i - \theta_{i+1}) = 0, \theta_i - \theta_{i+1} \leq 0 \end{cases} \quad (3.19)$$

where H_{step} is the unit step function that is dependent on the relative rotations between the nodes i and $i+1$. \mathbf{K} is the element stiffness matrix corresponding to the healthy state, θ_i denotes the rotational displacement DOF corresponding to the i -th node. \mathbf{K}_c refers to the element

stiffness reduction when the breathing crack opens. For a standard plane beam element with three DOFs per node, the element stiffness matrix \mathbf{K} and \mathbf{K}_c are described as

$$\mathbf{K} = \frac{EI_u}{l} \begin{bmatrix} \frac{A}{I_u} & 0 & 0 & -\frac{A}{I_u} & 0 & 0 \\ 0 & \frac{12}{l^2} & \frac{6}{l} & 0 & -\frac{12}{l^2} & \frac{6}{l} \\ 0 & \frac{6}{l} & 4 & 0 & -\frac{6}{l} & 4 \\ 0 & 0 & 0 & \frac{A}{I_u} & 0 & 0 \\ 0 & 0 & 0 & 0 & \frac{12}{l^2} & -\frac{6}{l} \\ 0 & 0 & 0 & 0 & -\frac{6}{l} & 4 \end{bmatrix}, \mathbf{K}_c = \mu \frac{E}{l} \begin{bmatrix} 0 & 0 & 0 & 0 & 0 & 0 \\ 0 & \frac{12I_u}{l^2} & \frac{6I_u}{l} & 0 & -\frac{12I_u}{l^2} & \frac{6I_u}{l} \\ 0 & \frac{6I_u}{l} & 4I_u & 0 & -\frac{6I_u}{l} & 4I_u \\ 0 & 0 & 0 & 0 & 0 & 0 \\ 0 & 0 & 0 & 0 & \frac{12I_u}{l^2} & -\frac{6I_u}{l} \\ 0 & 0 & 0 & 0 & -\frac{6I_u}{l} & 4I_u \end{bmatrix} \quad (3.20)$$

where A and l represent the section area and element length, respectively; I_u and I_d are respectively the moments of inertial of the healthy element and damaged element; $\mu = (I_u - I_d)/I_u$ is the non-dimensional reduction ratio of moment of inertia, which is in the range from 0 to 1. For example, $\mu = 1$ denotes that no damage is occurred, $\mu = 0$ denotes that the element is entirely damaged.

As shown in Figure 3-3, a steel simply-supported bridge model with a breathing crack described in Eqs. (3.19-3.20) is introduced to demonstrate the effectiveness and feasibility of using the proposed approach for nonlinear damage detection. It is noted that structural responses along the axial direction are not used as input to estimate the damage feature, therefore, the DOF in the axial direction of each node is not shown in Figure 3-3. The beam bridge model is represented by a FE model discretized into 20 equal length beam elements with a total length of $L=4\text{m}$. The material properties are assumed as: Young's modulus $E=206\text{ GPa}$, cross-section $A=6 \times 10^{-4}\text{ m}^2$, density $\rho=7800\text{ kg/m}^3$, Poisson's ratio $\nu=0.3$. Rayleigh damping model with damping matrix $\mathbf{C}=\gamma\mathbf{M} + \delta\mathbf{K}$ is assumed in this study, with damping coefficients $\gamma = 0.025$ and $\delta=0.002$. The first three natural frequencies are 43.33 Hz, 85.67 Hz and 122.67 Hz, respectively. As suggested in Ref. [41], the effect of crack damage on the variations of global mass and Rayleigh damping matrix is not considered in this study. Stationary zero-mean Gaussian white noise is applied in the vertical direction at both supports to simulate the ambient excitations [42], unless specifically defined otherwise below for particular analysis.

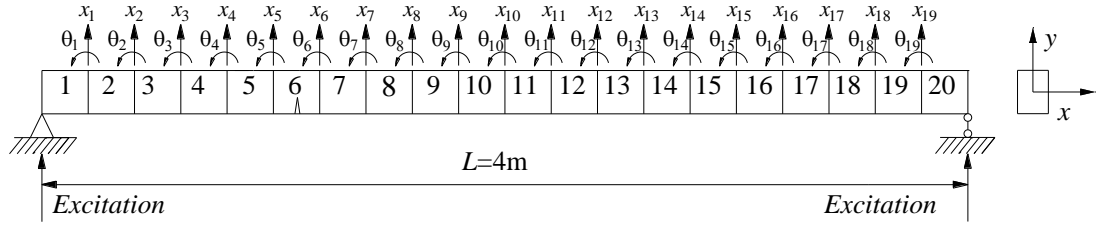


Figure 3-3. Finite element beam model and the cross-section

3.3.2 Validation of the breathing crack modelling

Three damage scenarios with 5%, 10%, 15% and 20% damage extent are respectively assumed in the bottom surface of element No. 6. It should be noted that the above damage extent is considered as the ratio of the crack depth to the overall height of healthy beam [43]. The system nonlinear behavior comes from the breathing effect of damaged element. Before conducting the nonlinear damage detection, the vertical acceleration response of DOF x_{16} with a breathing crack of 10% damage in element No. 6 is compared with those from the healthy beam and a beam with the same damage level of open crack to verify that breathing crack is correctly modelled. The FE model of the beam is excited by applying a sinusoidal load with an amplitude of 20 N and a single excitation frequency of 30 Hz on the vertical DOF x_7 . The open crack scenario is considered by changing the unit step function H in Eq. (3.19) as a constant value of 1. The frequency spectra of vertical acceleration responses in the vertical DOF x_{16} of the beam model under the healthy state, open crack state and breathing crack state are respectively shown in Figure 3-4. The sampling rate and duration of acceleration responses are set as 1000 Hz and 4 seconds, respectively. The comparison of frequency spectra in Figure 3-4 shows that the excitation frequency dominates the dynamic response of the beam model under three different states. It should be noted that “1X” in Figure 3-4 is defined as the excitation frequency, and “2X” is twice of the excitation frequency. From Figure 3-4(a) and Figure 3-4(b), the first natural frequency is clearly observed besides the excitation frequency. The first natural frequency in Figure 3-4(b) is a little smaller than that in Figure 3-4(a). As observed in Figure 3-4(c), higher order harmonics of the excitation frequency are clearly observed in the frequency spectrum when the beam has a breathing crack. The generation of higher order harmonic phenomenon is usually recognized as nonlinear behavior introduced by the breathing crack damage [44], and the amplitude of the second harmonic component (2X) is widely reported in literature to be a good DSF in identifying the severity of crack damage [14, 45]. Hence, it can be clearly implied that the breathing crack is correctly modelled in this bridge beam model.

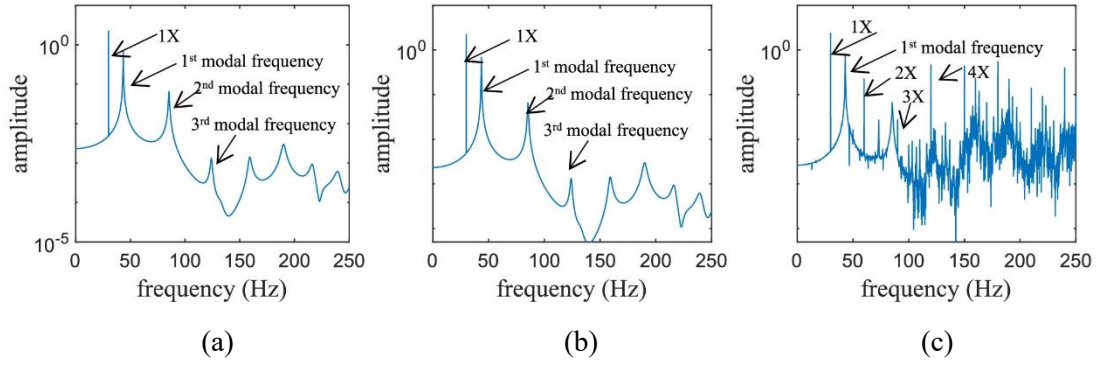


Figure 3-4. Frequency spectra of the measured responses from: (a) intact beam; (b) open crack with 10% damage; (c) breathing crack with 10% damage

3.3.3 Output based nonlinear damage detection

Dynamic responses from the beam model under the above defined ambient excitations are used for the subsequent analysis. It should be noted that ambient excitations are used here to simulate a realistic loading condition in the real world, and then the effect of the applied loads, e.g. hammer impact, at certain locations is not involved. The accuracy of Volterra series model in describing the nonlinear behavior of structural responses is based on the proper estimation of Volterra kernel parameters. According to Eq. (3.8), the number of kernel parameters will be exponentially growing with the truncation order and the memory length. The truncation order is predetermined as 3. In Figure 3-5, NRMSE defined in Eq. (3.18) is adopted to evaluate the prediction error between numerical responses and predicted output responses obtained from Volterra series model [46]. To well locate the location and source of nonlinearities, pairs of two adjacent sensors are selected for the calculation. To optimally select the parameters for the Volterra model, the nonlinearity features between responses at vertical DOFs $x_3 \sim x_4$, $x_4 \sim x_5$, $x_5 \sim x_6$, $x_6 \sim x_7$ and $x_7 \sim x_8$ are respectively analysed. Overall, the NRMSE curve values show a decreasing trend with the increasing memory length, and turn to stable when the memory length reaches 2. The y -axis on the right side gives the increase of kernel parameters number with the memory length. When the memory length is considered as 2 or 3 to construct the Volterra model, the number of kernel parameters to be estimated are respectively 39 and 84. Hence, the memory length is determined as 2 in this case study to keep a good balance between the prediction accuracy and computational efficiency. It is worth noting that a relatively high prediction error is observed in the region between x_5 and x_6 than that of other regions. One main reason is that the nonlinearity generated by the breathing crack damage in element 6 will increase the prediction error of Volterra series model. Similar phenomenon was also reported in existing studies [34] [47], thus the prediction error was utilized as a nonlinear damage sensitive index in those studies.

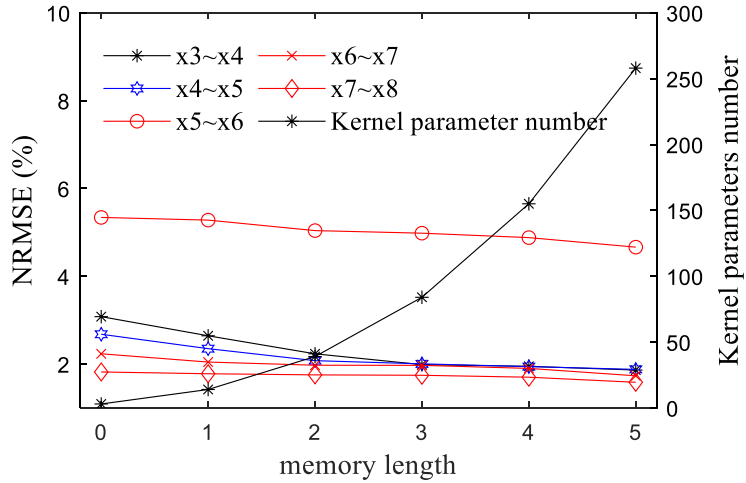


Figure 3-5. The prediction error and kernel parameters number with different memory lengths.

Figure 3-6 shows the acceleration outputs predicted by using Volterra series model with a truncation order of 3 and a memory length of 2, compared with the simulated responses in time and frequency domains. The input and output of Volterra series model are the acceleration responses of x_5 and x_6 under white noise excitations with an amplitude of 10m/s^2 . Overall, a good agreement is observed between the true and predicted responses, demonstrating that the Volterra series model with the above-defined parameters can effectively model the breathing crack damage-introduced nonlinearity under white noise excitations. According to the comparison results as shown in Figure 3-5, the output prediction error level in region $x_5\sim x_6$ is relatively higher than that in other regions, hence better match than the results presented in Figure 3-6 is expected in other regions. Due to the page limit, these results from different sensor locations are not presented here.

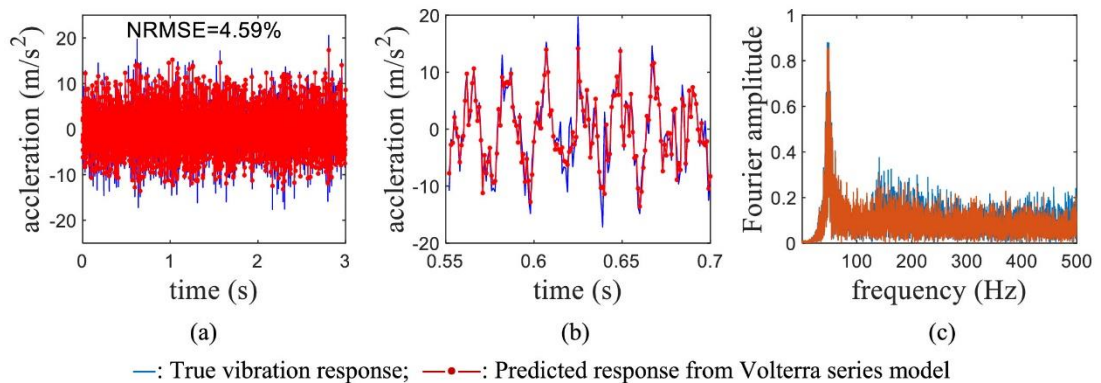


Figure 3-6. Comparison of true responses and predicted responses from Volterra series model under white noise excitations: (a) time domain responses; (b) zoom in time domain response; (c) frequency domain spectrum.

To detect the damage location, the adjacent neighbor nodes are respectively used as input by using the proposed approach described in Figure 3-1 to estimate the optimal Volterra series kernel parameters and evaluate the corresponding nonlinear component contribution. The noise robustness of proposed method is validated by adding 5% measurement noise to the vibration responses. Then, the nonlinear contribution of each structural element in total response is calculated with Eq. (3.17). Generally speaking, the nonlinearity level in structural response is not only related to the presence and severity of damage but also affected by external excitation condition, i.e. loading type and level. To gain more robust and reliable damage detection results, the procedure detailed in Figure 3-1 is repeated by changing the amplitude of randomly generated white noise excitation from 2.5 m/s^2 to 15 m/s^2 N with a load increment of 2.5 m/s^2 at each test. Moreover, the random white noise excitation series are regenerated in every simulation to ensure that different ambient excitations are used. Statistical results, such as mean and standard deviations are obtained from tests under different ambient excitations. Figure 3-7 shows the nonlinear damage detection results when 5%, 10%, 15% and 20% damage levels of breathing crack are respectively introduced in element 6. It can be clearly observed that the nonlinearity level in elements close to the damage location are relatively higher, and peaks are accurately observed at the damaged element 6. It is noted when a relatively small damage (5%) is considered in element 6, the nonlinear contribution index $\lambda_{nonlinear}$ at the damaged element is about 2% but larger than that of healthy elements. The uncertainties caused by white noise excitation levels increase the standard deviations in the results of minor damage detection case. Nevertheless, a lower level of uncertainties is observed when further increasing the damage severity. Owing to the fact that structural responses at different locations are obtained and excited by the same external load from a certain dynamic testing, the influences of the amplitude, type and duration of load on the measured structural responses at different locations in a single test are similar. This is a promising advantage of the proposed approach since the damage index is identified by using two dynamic acceleration responses at different locations, therefore the proposed damage index is independent of the loading. The results in Figure 3-7 demonstrate that the proposed method obtains good damage detection results in nonlinear structures with a breathing crack, and a robust performance under different loading amplitudes is achieved.

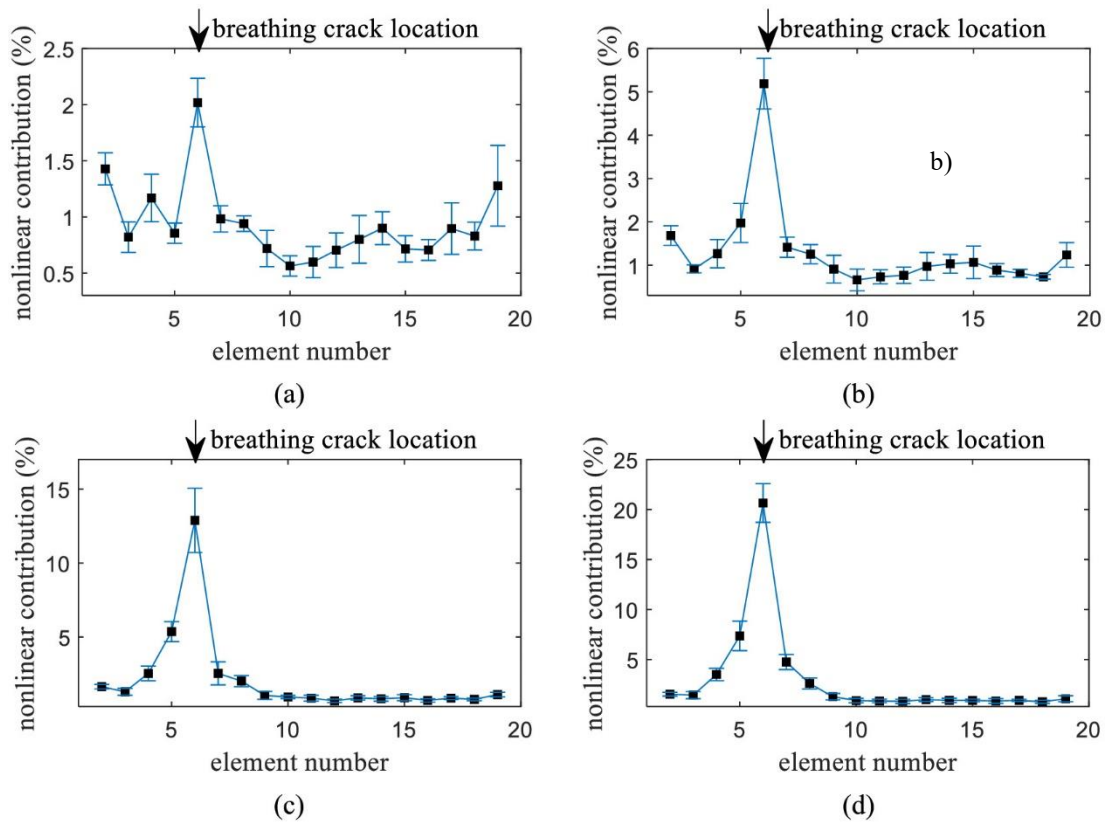


Figure 3-7. Nonlinear contribution index and its standard derivation under different excitation amplitudes: (a) 5% damage; (b) 10% damage; (c) 15% damage; and (d) 20% damage.

3.4 Experimental verifications

3.4.1 Experimental setup

Experimental verifications on two precast segmental column models are conducted in this section to validate the performance of the proposed approach for nonlinear structural damage detection. A series of shaking table tests are conducted on two scaled precast segmental concrete columns constructed in laboratory subjected to seismic loads with different magnitudes of PGA to simulate the accumulated structural condition variations for damage detection of nonlinear structures. Figure 3-8 shows a testing specimen and experimental setup for the shake table tests. As shown in Figure 3-8, the precast segmental column used in this study is a 1/12 scaled model of a full-scale bridge column in Ref. [50]. The horizontal base slab was connected with four shake tables to support the specimen as well as to transfer the generated ground motions to the column model. Three segments, a footing block and a cap block were concatenated by a post-tensioned tendon to form the precast segmental column. More information about the dimensions of specimens are detailed in Ref. [48]. The only difference between these two precast segmental column models are the used reinforcement bars. In particular, one specimen (referred to as Specimen 1) is reinforced with fiber-reinforced

plastic (FRP) bars, and the other specimen (referred to as Specimen 2) is reinforced with ordinary steel reinforcing bars. The weight of the superstructure undertaken by the pier column is equalized by fixing two top masses with a dimension of 1000 mm × 1000 mm × 150 mm on the upper surface of the cap block through four bolts. The total weight of the specimen placed on the shake table is about 1456 kg.

The ground motions recorded at the Niland Fire Station during the 1979 Imperial Valley Earthquake are selected as the excitation loads of the testing specimens. The PGA values of the recorded ground motions in E-W and N-S directions are 0.108 g and 0.068 g, respectively. The PGA of the E-W direction ground motion was scaled to 0.1 g and that in the N-S direction was also proportionally scaled in the first test. It should be noted that the uniaxial (only in the E-W direction) and bi-direction ground motions are applied to Specimen 1 and Specimen 2, respectively. To obtain the process of structural damage accumulation under different seismic loading levels, PGA value was increased with an interval of 0.1 g in the subsequent tests until the column was collapsed. To measure the evolution of dynamic characteristic and identify the integrity of specimens with the increasing ground motion intensities, small white noise excitations were also applied after each test. The vibration duration and amplitude of white noise excitations are 40 s and 0.02 g, respectively. Meanwhile, the seismic excitation duration is correspondingly scaled by dividing by the square root of the reduced-scale 12 [51]. Only the acceleration responses in E-W direction are used for verifying the performance of the proposed approach in this study. As shown in Figure 3-8(b), five accelerometers, namely #A1~#A5 were respectively installed on the base slab, footing block, the first, third segment column and the top mass to measure vibration accelerations along the E-W direction of the specimen. The acceleration responses were measured with a sampling rate of 200 Hz. More details of the experimental setup and test descriptions can be found in [48].

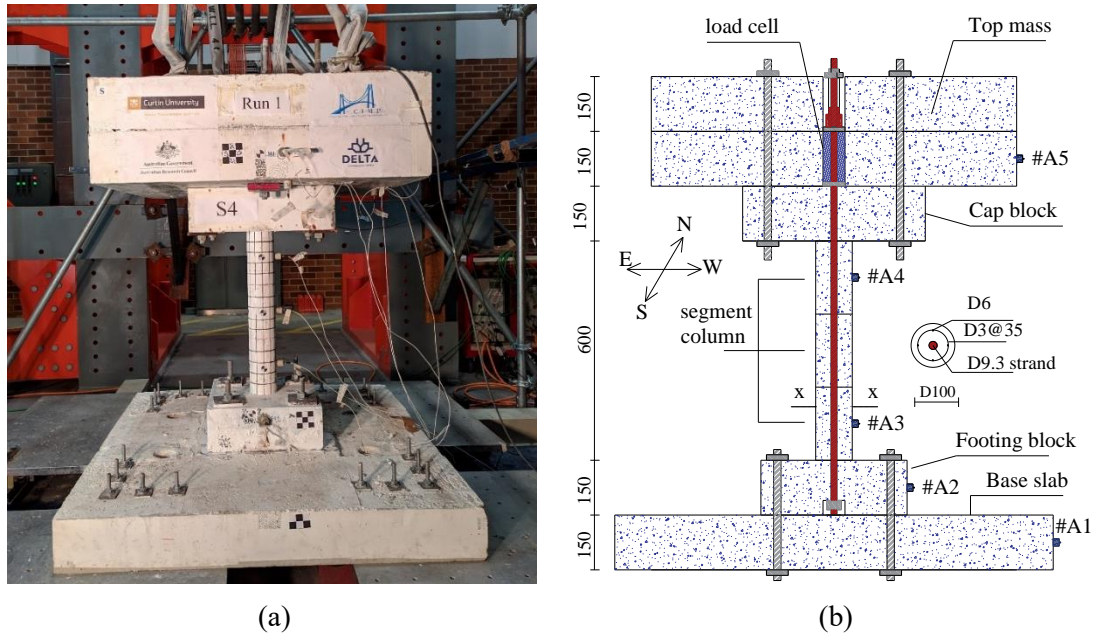


Figure 3-8. The experimental setup for shake table tests of precast segmental column reinforced with FRP bars (Specimen 1): (a) overall view and (b) schematic diagram. (unit: mm).

3.4.2 Dynamic tests and observed damage

Figure 3-9 shows the input ground motion along E-W direction with the PGA scaled to 0.1 g. The overall duration of excitation is about 12s and the energy of ground motion is mainly distributed in the frequency range of 0-50 Hz. The time-domain and frequency-domain acceleration responses subjected to this seismic load are shown in Figure 3-10. As evidenced in Figure 3-10(a) and Figure 3-10(b), dynamic responses of the precast segment column model under ground motion excitations and the free decay responses after the excitation are included in the measurement, and the first two natural frequencies are excited by the input seismic load and observed in the frequency spectrum at 3.86 Hz and 26.05 Hz, respectively.

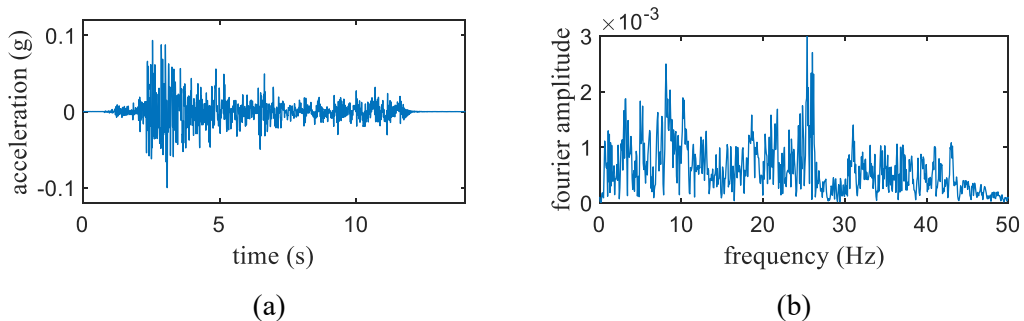


Figure 3-9. Input ground motion along the E-W direction: (a) Time domain, (b) Frequency domain.

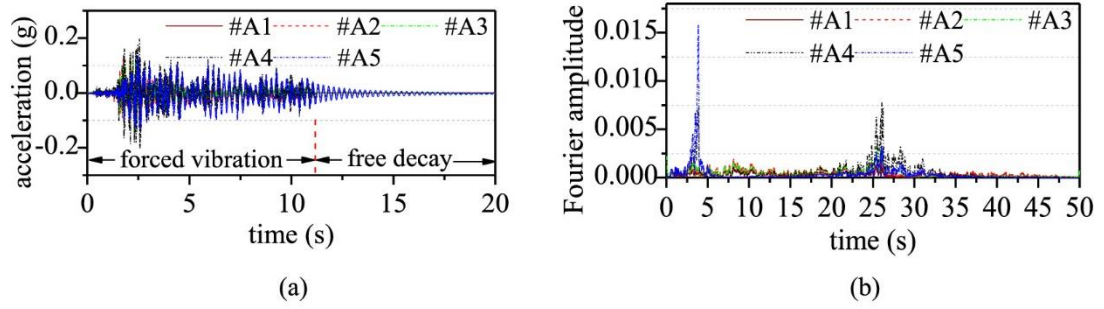


Figure 3-10. Measured acceleration responses in: (a) time domain; (b) frequency domain.

Time-frequency analysis is one of the widely used methods for better understanding structural vibration behavior during earthquake excitations [52]. HT is applied to analyse the measured dynamic responses. Figure 3-11 shows the time-frequency analysis results of seismic load and the corresponding responses at five sensor locations from #A1 to #A5. In Figure 3-11, the first two natural frequencies are observed in the response of #A3, #A4 and #A5. The time-frequency representations of sensors #A1 and #A2 are similar as that of the input ground motion, since the base slab and footing block are directly connected with the shake table. Dynamic responses from these two sensors are highly correlated with the input ground motion of the shake table. In addition, as can be observed from Figure 3-11(e) and Figure 3-11(f), the responses at the precast segmental column and the top mass clearly indicate the first two natural frequencies, and the free decay responses are dominated by the fundamental frequency of the column model.

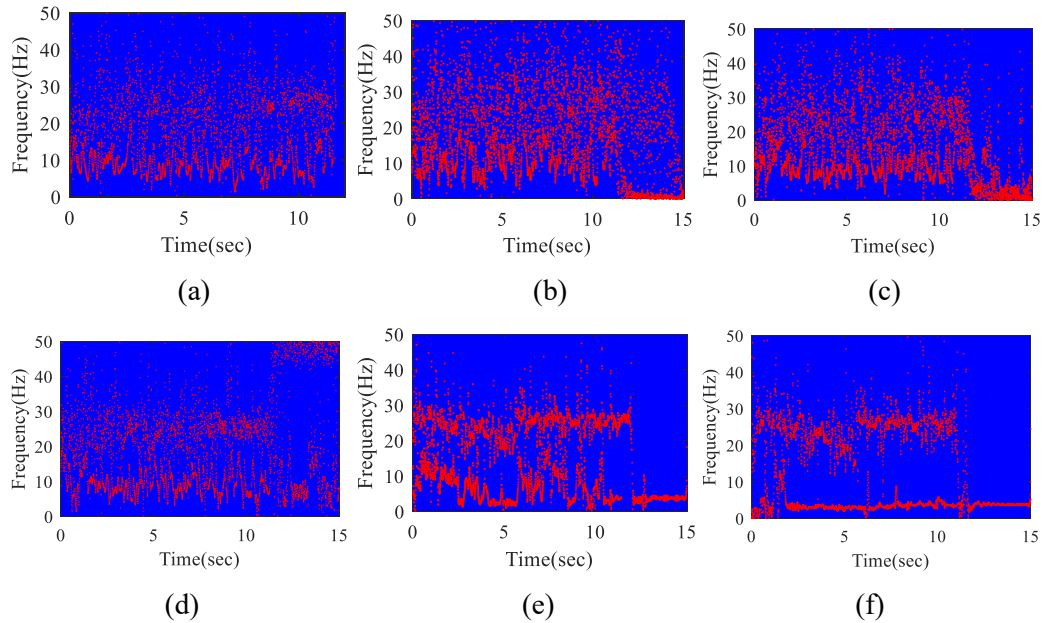


Figure 3-11. Time-frequency analysis results of input excitation and measured responses of Specimen 1: (a) ground motion excitation (PGA=0.1 g); (b) #A1; (c) #A2; (d) #A3; (e) #A4; and (f) #A5.

The precast segmental column model has increasing significant vibrations observed under the seismic loads, and the acceleration responses increase with the increasing PGA value. The observed damages of the precast segmental column reinforced with FRP bars (Specimen 1) and ordinary steel bars (Specimen 2) under different PGA magnitudes are shown in Figure 3-12 and Figure 3-13, respectively. For Specimen 1, it can be observed that no visible concrete crack is observed in the tested specimen before the PGA reaches to 0.6 g. Nevertheless, owing to the periodically open and close behavior of precast segmental column joints, the contact surfaces of joints may experience significant compressive stress during the vibrations. As a result, when the PGA of the applied ground motion is higher than 0.7 g, concrete crushing is observed at the toes of the bottom segment of the column model. The severity of concrete crushing damage continues to increase with the increasing intensity of ground motions, and Specimen 1 finally loses stability and collapses at ground excitation with PGA of 1.1 g. Figure 3-13 shows the observed damage and final failure of Specimen 2 under different ground motion intensities. In particular, visible concrete spalling and crushing is observed at the toes of the bottom segment at a PGA of 0.6 g. The severity of structural damage is further accumulated with an increase of ground motion intensities, and Specimen 2 collapses when the PGA reaches to 0.8 g.

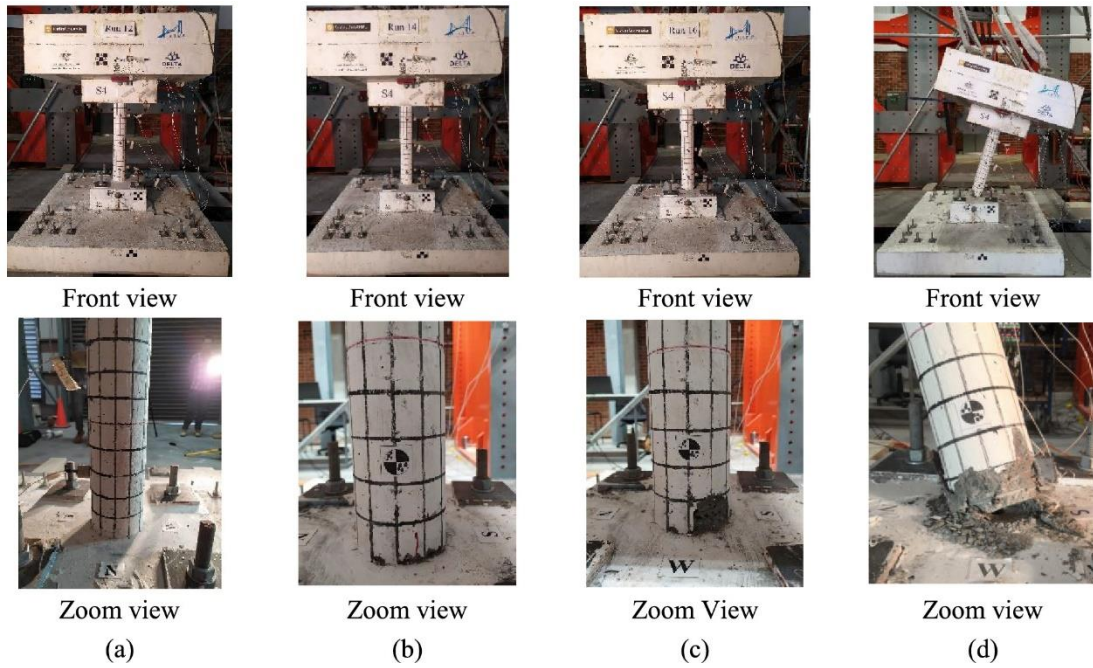


Figure 3-12. Damage observations of the precast segmental column (Specimen 1) reinforced with FRP bars under different PGA values: (a) 0.6 g; (b) 0.7 g; (c) 0.8 g; (d) 1.1 g.

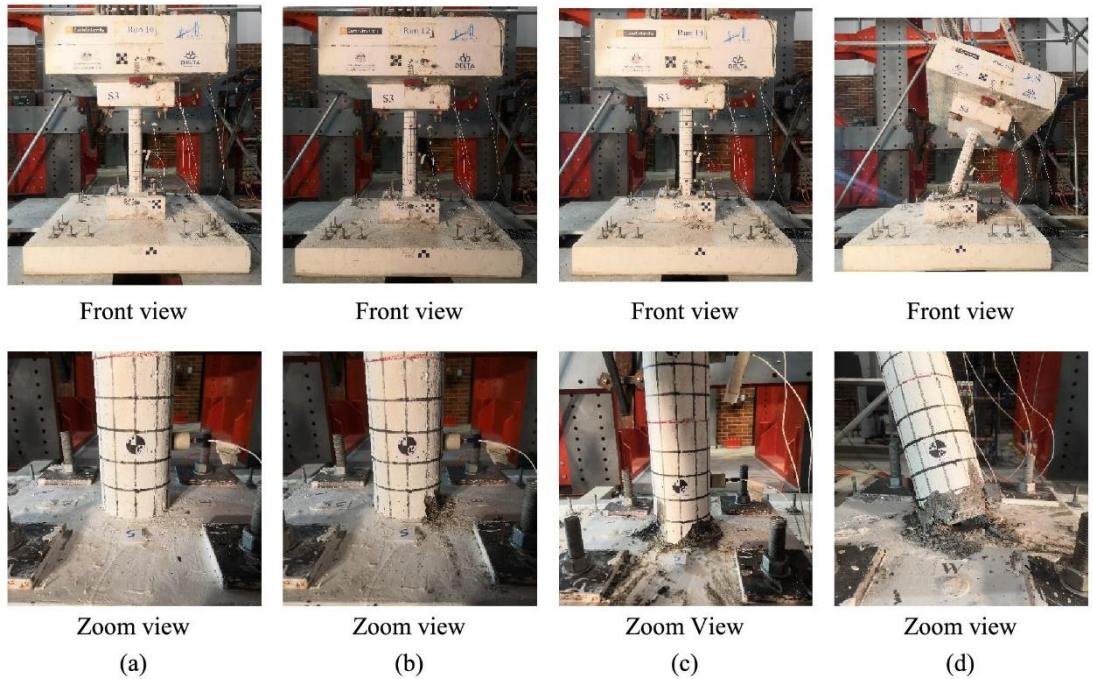


Figure 3-13. Damage observations of the precast segmental column (Specimen 2) reinforced with ordinary steel bars under different PGA values: (a) 0.5 g; (b) 0.6 g; (c) 0.7 g; (d) 0.8 g.

3.4.3 Nonlinear structural damage detection

Pairs of acceleration responses measured from the precast segmental column model

Specimen 1 subjected to white noise excitations after each ground motion with different PGA values, are used as input to the Volterra series model with the proposed approach detailed in Section 2.1 to quantify the nonlinearity between every two adjacent sensors, i.e. #A1 and #A2, #A2 and #A3, and #A4 and #A5. The pair of #A3 and #A4 is not used since two joints are involved in this region, and there is no damage in these two joints as observed in Figure 3-12 and Figure 3-13. Similar to the numerical study in Section 3.2, a parametric analysis is conducted to determine the optimal memory length for Volterra series model. Figure 3-14 shows the NRMSE values and numbers of kernel parameters with different memory lengths using the responses under white noise excitations after the applied ground motion with a PGA value of 0.2 g. It can be observed that the prediction error between the accelerometers #A4 and #A5 is significantly higher than that of other two sensor pairs. Hence, it can be preliminarily concluded that the region between those two sensors is of a higher level of initial nonlinearity. Moreover, a significant decreasing trend followed with a stable evolution is observed in the NRMSE of the region between accelerometers #A4 and #A5 when the memory length reaches to 2. The other two sensor pairs, such as #A1 and #A2, and #A2 and #A3, have relatively stable NRMSE values with different memory lengths. However, the number of kernel parameters significantly increases with an increasing memory length, which implies that a high computational demand is required. Considering the balance between the accuracy of the calculated Volterra series model and computational efficiency, the memory length is set as 2 in the following experimental studies.

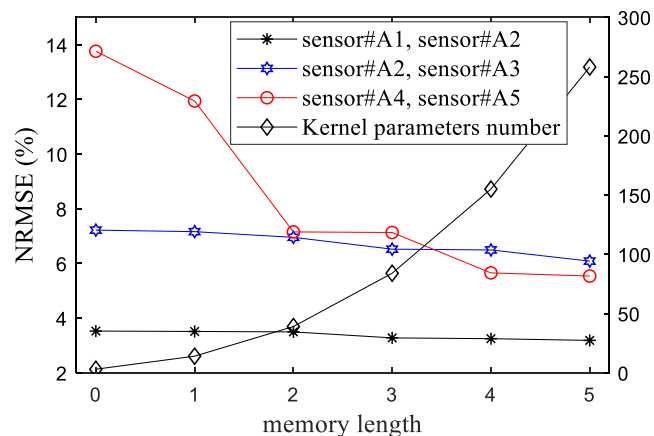


Figure 3-14. The prediction error and kernel parameters number with different memory lengths.

Similar as the numerical study, the truncation order is predetermined as 3. Volterra series model with a memory length of 2 and a truncation order of 3 is applied to simulate the vibration responses of a segmental column subjected to white noise excitations in the experimental studies. The contribution of the component signal corresponding to each of the three kernels

are presented in Figure 3-15. It can be found that the nonlinear vibrations are dominated by the linear component (Kernel order 1), while the contribution of nonlinear term 1 (Kernel order 2) and nonlinear term 2 (Kernel order 3) are non-negligible. It is noteworthy that the contribution of kernel order 3 is higher than that of kernel order 2, which means that the nonlinearity within the joint is manifested as a cubic term. Therefore, Volterra series model with two nonlinear terms are more suitable than only one nonlinear term in this study.

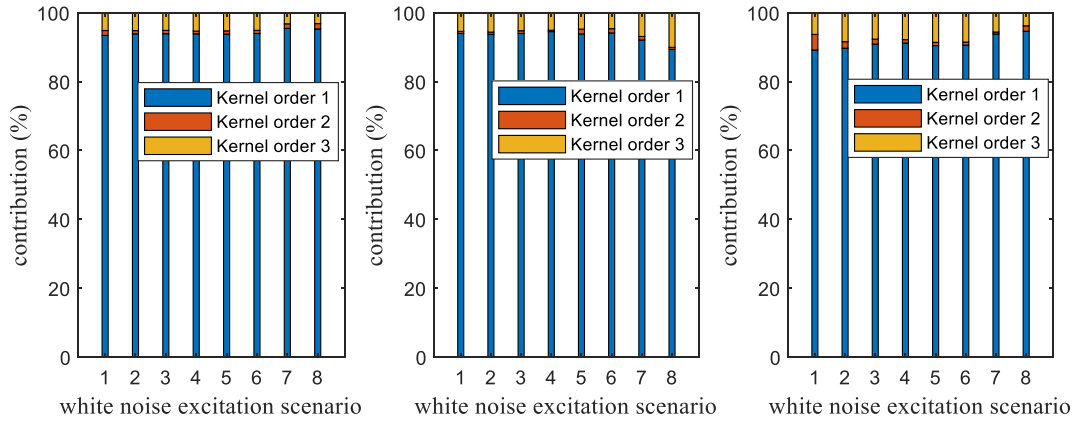


Figure 3-15. Contribution of component signal corresponding to each of the three kernels: (a) #A1 - #A2; (b) #A2-#A3; and (c) #A4-#A5.

When the memory length and the truncation order of kernel function are determined, dynamic responses of two adjacent accelerometers, such as #A1 and #A2, #A2 and #A3, and #A4 and #A5, measured from the structure subjected to white noise excitations after shake table tests with different PGA values are respectively utilized as input and output of Volterra series model. Figure 3-16 compares the measured response at sensor location #A3 under white noise excited responses after the ground excitation with a PGA value of 0.4 g and the predicted response from Volterra series model in time and frequency domains, by using sensor response measured from #A2 as input to Volterra series model. The prediction NRMSE is 3.83%. Comparison results intuitively illustrate the effectiveness and accuracy of using the proposed approach in modelling the structural nonlinear behavior of segmental column models under white noise excitations in experimental studies.

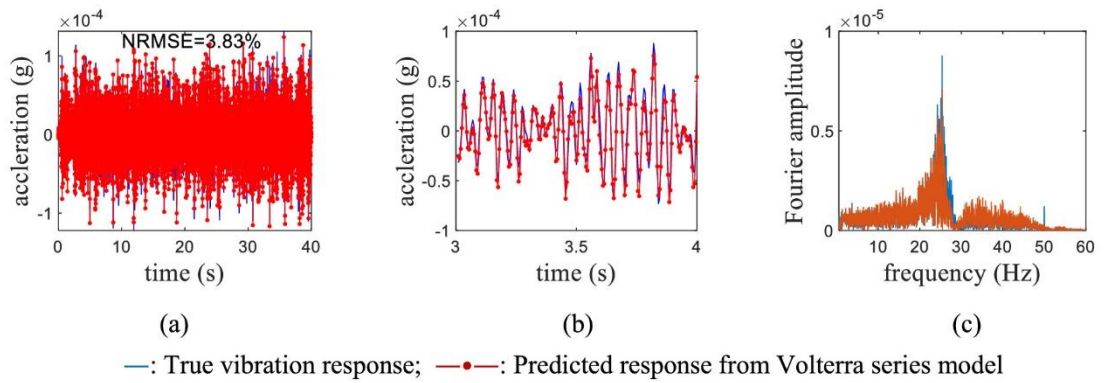


Figure 3-16. Comparison of true responses and predicted responses from Volterra series model under white noise excitations: (a) time domain responses; (b) zoom in time domain response; (c) frequency domain spectrum.

Figure 3-17(a) and Figure 3-17(b) show the evolution of the nonlinear contribution index $\lambda_{nonlinear}$ of Specimens 1 and 2 subjected to white noise excitations. It should be noted that the nonlinearities in this structure mainly consist of two components. The initial nonlinearity existed in the segmental column structure comes from the joints between segments, and the nonlinearity induced by the structural damage subjected to ground excitation, which increases with the intensity of the applied seismic excitation. Owing to the open and close of joint during significant vibrations under applied ground motions, concrete crushing damage usually occurs at the joint region owing to significant compressive stress induced by rocking response of the joint. The mechanical properties, such as damping, stiffness and friction of the joint interface, may change. Therefore, structural damage can be identified by quantifying the nonlinear responses between two adjacent sensors. With the increasing intensity of applied ground motions, structural damage accumulated in the structural model will introduce the presence of nonlinear behavior in structural dynamic responses. To mitigate the loading effect and highlight the evolution of nonlinearity level before and after the ground motion excitation with different PGA intensities, structural vibration responses subjected to white noise excitations with constant loading level will be analysed in this study.

As can be found in Figure 3-17(a), the lowest nonlinearity is observed in the region between #A1 and #A2, which shows a slight increase with the increasing PGA. This is because the footing block is fixed on the base slab by using four strong bolts, and these two responses are highly correlated and less nonlinearity is observed. The highest nonlinearity result is estimated from the region between #A4 and #A5 in the first two white noise excitation scenarios, followed by a decreasing trend with the increasing ground motion intensities. This could be owing to the initial friction forces existed between the added top masses on the precast segmental column model. After several ground motion excitations, the initial nonlinearity as

evidenced by the results between #A4 and #A5 in Figure 3-14 due to this friction force becomes smaller, indicating a smaller nonlinear contribution index between sensors #A4 and #A5 with the increasing ground motion intensities. It should be noted the trend of the defined nonlinear contribution index is used for locating the damage occurred in this structure. With the increasing ground motion PGA value, the nonlinear contribution index at the damage location shows an increasing trend. Among all of these three sensor pairs, only the nonlinearity contribution index values obtained from the region between #A2 and #A3 show an increasing trend. The results from the pair #A4 and #A5 at some scenarios are even larger than other sensor pairs, however, as discussed above, the nonlinearity at the top joint between the segmented column and the added slab was not caused by structural damage. The increase in the nonlinearity at the column base between sensor #A2 and #A3 is associated with the damage accumulation, as shown in Figure 3-12 and Figure 3-13.

In particular, no obvious change in the nonlinearity level is found between #A2 and #A3 before the white noise excitation scenario 5 (after ground motion with a PGA of 0.4 g), followed by a slight increasing trend in the next two white noise excitation scenarios. The nonlinearity contribution index obviously increases, since white noise excitation 8 (after ground motion with a PGA of 0.7 g) until the specimen collapses. These results are consistent with the observed concrete crushing damage occurred at the bottom of the precast segmental column, as shown in Figure 3-12. The sensor pair #A2 and #A3 shows an increase trend and finally has the highest nonlinear contribution value, indicating the region between these two sensors has the highest probability of damage occurrence at the joint interface. The results also demonstrate that the proposed nonlinear damage index is sensitive to detect structural nonlinear damage at an early stage, when the actual concrete crushing is not visible. As can be found in Figure 3-17(b), similar evolution trend of the nonlinear contribution index estimated from Specimen 2 is observed. In detail, significant nonlinear contribution index increase is observed between sensor pair #A2 and #A3 after the white noise excitation scenario 6 (after ground motion with a PGA of 0.5 g), which indicates that the nonlinear damage is located in this region.

To highlight the evolution of nonlinearity contribution since the visible concrete crush damage occurred in these two specimens, the identified nonlinear contribution index values of Specimen 1 (from white noise excitation scenarios 8 to 11) and Specimen 2 (from white noise excitation scenarios 6 to 8) are presented in Figure 3-17(a) and Figure 3-17(b), respectively. The highest and increasing nonlinear contribution index values observed in the sensor pair #A2 and #A3 indicate that the nonlinear damage is located in this region, which is well consistent with the damage patterns observed in Figure 3-12 and Figure 3-13. The above experimental results demonstrate the reliability of using the proposed approach for nonlinear

structural damage detection.

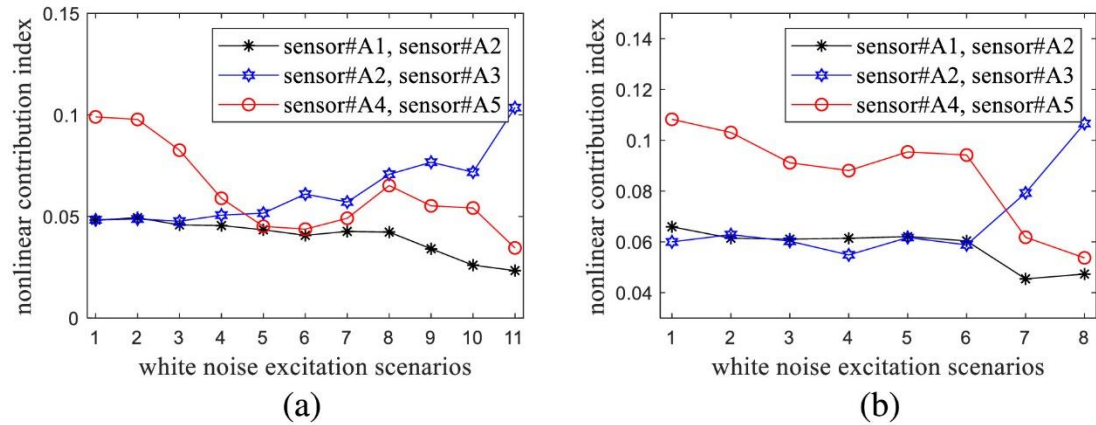


Figure 3-17. The evolution of nonlinear contribution index of segmental columns subjected to white noise excitations: (a) Specimen 1; and (b) Specimen 2.

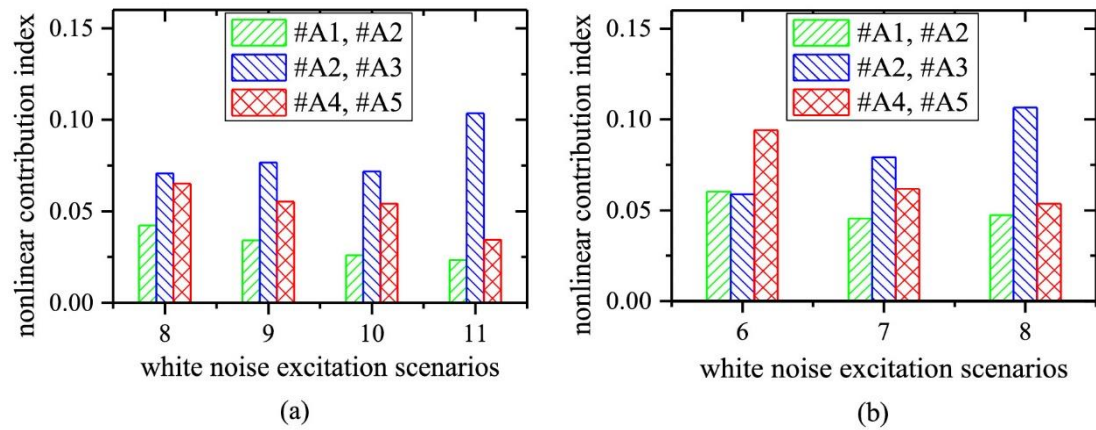


Figure 3-18. Histogram plot of the nonlinear contribution index of segmental columns subjected to white noise excitations: (a) Specimen 1; and (b) Specimen 2.

The number of to be estimated parameters of Volterra series model exponentially increases with the memory length and truncation order, which poses challenges to guarantee the global maximum solution. One common prescription to this issue is to limit the complexity based on the reasonable selection of parameters, i.e. the order and the memory length of Volterra series model. Another way that is found in literature to reduce the number of parameters to be estimated is to replace the conventional Volterra series kernel by Kautz filter [30, 53]. In this study, the overall number of kernel parameters to be estimated for a Volterra series model with a memory length of 2 and a truncation order of 3, is 39. The maximum NRMSE values in numerical and experimental studies for structures subjected to white noise excitation are 4.59% and 3.83%, which means that the nonlinear approximation converge

accurately to the reference results by using the Volterra series model with the above-selected parameters.

The main objective of this study is to develop an output only based Volterra series model to localize and quantify the source of nonlinearity. Therefore, the vibration responses of adjacent node are selected as input and output of Volterra series model. Nonlinearity contribution index defined in this study does not satisfy superposition principle. For example, the nonlinearity contribution index between DOF $x_4 \sim x_6$ is not equal to the sum of that from $x_4 \sim x_5$ and $x_5 \sim x_6$. Therefore when only responses from two nodes are used to calculate the nonlinearity contribution between them, it represents the nonlinearity contribution in this region between these two nodes only, but is not able to distinguish the nonlinearity contribution from any other two nodes inside this region.

3.5. Conclusions

This chapter proposes a novel structural nonlinear detection approach based on the output responses only, by quantifying the nonlinear contribution in structures using Volterra series model. Compared with the existing studies which mainly focus on input-output based Volterra series model, the main contribution of the presented study resides in the fact that the external excitation is not required in the proposed approach, which overcomes the practical difficulties in reliably obtaining the ambient excitations to structures. With the merit of using Volterra series expansion for separating the linear and high order nonlinear components, a nonlinearity contribution index is introduced to quantify the nonlinearity degree corresponding to structural responses at two selected sensors, which are used as the input and output of the used Volterra series model. The performance and reliability of the proposed approach are demonstrated by numerical studies on a simply-supported beam model with a breathing crack under different levels of white noise excitations and experimental studies on a precast segmental concrete column subjected to ground motions with different PGA values. The results in numerical and experimental studies demonstrate that the nonlinear behavior can be modelled qualitatively by using the Volterra series model with the optimally selected parameters. By using measurement data under different structural conditions, the location of nonlinear structural damage can be identified accurately, and the severity can be indicated by comparing the evolution of nonlinearity contribution index value obtained in each structural region.

Although the proposed method based on measured structural responses can locate the structural damage, there are still some limitations and further investigations could arise from this work. In reality, the energy of environmental excitation is relatively low. As a result, the civil engineering structure may usually respond linearly or with only weak nonlinear behavior

under operating conditions. Under this situation, the proposed method may not be able to identify the damage. The proposed approach is effective to detect damage of structures with significant nonlinear behavior. Many factors, such as geometric nonlinearity, nonlinear boundary conditions, joints of prefabricated structures and material nonlinearity, etc., may make the structural system exhibit nonlinear behavior. This may confuse the damage detection performance when the uncertainties caused by the above-mentioned factors are not fully considered. Therefore, appropriate methodologies or indicators with adequate capacity to distinguish the sources of nonlinear characteristics could be further investigated. Experimental study will be designed to acquire structural responses with a significant inelastic hysteresis behavior of structures during excitations in the future study. Furthermore, the improvement of the proposed method will be made in the future study to extend the feasibility of Volterra series to model the inelastic hysteresis behavior of nonlinear structures.

References

- [1] J. Li, H. Hao, J.V. Lo, Structural damage identification with power spectral density transmissibility: numerical and experimental studies, *Smart Struct. Syst*, 15 (2015) 15-40.
- [2] J. Li, H. Hao, A review of recent research advances on structural health monitoring in Western Australia, *Structural Monitoring and Maintenance*, 3 (2016) 33.
- [3] D. Chelidze, J.P. Cusumano, A. Chatterjee, A dynamical systems approach to damage evolution tracking, part 1: description and experimental application, *J. Vib. Acoust.*, 124 (2002) 250-257.
- [4] H. Ebrahimian, R. Astroza, J.P. Conte, C. Papadimitriou, Bayesian optimal estimation for output - only nonlinear system and damage identification of civil structures, *Structural Control and Health Monitoring*, 25 (2018) e2128.
- [5] S. Das, P. Saha, S. Patro, Vibration-based damage detection techniques used for health monitoring of structures: a review, *Journal of Civil Structural Health Monitoring*, 6 (2016) 477-507.
- [6] Z. Lai, S. Nagarajaiah, Semi - supervised structural linear/nonlinear damage detection and characterization using sparse identification, *Structural Control and Health Monitoring*, 26 (2019) e2306.
- [7] L. Chen, L. Yu, Structural Nonlinear Damage Identification Algorithm Based on Time Series ARMA/GARCH Model, *Advances in Structural Engineering*, 16 (2013) 1597-1609.
- [8] Z. Nie, H. Hao, H. Ma, Structural damage detection based on the reconstructed phase space for reinforced concrete slab: Experimental study, *Journal of Sound and Vibration*, 332 (2013) 1061-1078.
- [9] L. Yu, J.-C. Lin, Cloud computing-based time series analysis for structural damage detection, *Journal of Engineering Mechanics*, 143 (2017) C4015002.
- [10] N.P. Yelve, M. Mitra, P.M. Mujumdar, Spectral damage index for estimation of breathing crack depth in an aluminum plate using nonlinear Lamb wave, *Structural Control and Health Monitoring*, 21 (2014) 833-846.
- [11] L. Zhao, F. Semperlotti, Detection of breathing - type damage using multiharmonic electrical impedance tomography, *Structural Control and Health Monitoring*, 26 (2019) e2330.
- [12] K. Kolozvari, L. Biscombe, F. Dashti, R.P. Dhakal, A. Gogus, M.F. Gullu, R.S. Henry, L.M. Massone, K. Orakcal, F. Rojas, State-of-the-art in nonlinear finite element modeling of isolated planar reinforced concrete walls, *Engineering Structures*, 194 (2019) 46-65.
- [13] J. Nichols, M. Seaver, S. Trickey, A method for detecting damage-induced nonlinearities in structures using information theory, *Journal of Sound and Vibration*, 297 (2006) 1-16.
- [14] A. Chatterjee, Structural damage assessment in a cantilever beam with a breathing crack using higher order frequency response functions, *Journal of Sound and Vibration*, 329 (2010) 3325-3334.
- [15] R. DeSalvo, Passive, nonlinear, mechanical structures for seismic attenuation, *Journal of Computational and Nonlinear Dynamics*, 2 (2007) 290-298.
- [16] J. Prawin, A.R.M. Rao, A method for detecting damage-induced nonlinearity in structures using weighting function augmented curvature approach, *Structural Health Monitoring*, 18 (2019) 1154-1167.

- [17] R. Wang, Q. Wu, F. Yu, Y. Okabe, K. Xiong, Nonlinear ultrasonic detection for evaluating fatigue crack in metal plate, *Structural Health Monitoring*, 18 (2019) 869-881.
- [18] H. Li, D. Tao, Y. Huang, Y. Bao, A data - driven approach for seismic damage detection of shear - type building structures using the fractal dimension of time - frequency features, *Structural Control and Health Monitoring*, 20 (2013) 1191-1210.
- [19] M. Ławryńczuk, Nonlinear predictive control of dynamic systems represented by Wiener–Hammerstein models, *Nonlinear Dynamics*, 86 (2016) 1193-1214.
- [20] A. Zabidi, N. Md Tahir, I. Mohd Yassin, Z.I. Rizman, The performance of binary artificial bee colony (BABC) in structure selection of polynomial NARX and NARMAX models, *International Journal on Advanced Science, Engineering and Information Technology*, 7 (2017) 373-379.
- [21] J.-P. Noël, G. Kerschen, Nonlinear system identification in structural dynamics: 10 more years of progress, *Mechanical Systems and Signal Processing*, 83 (2017) 2-35.
- [22] X. Deng, X. Tian, S. Chen, C.J. Harris, Nonlinear process fault diagnosis based on serial principal component analysis, *IEEE transactions on neural networks and learning systems*, 29 (2016) 560-572.
- [23] B. Lusch, J.N. Kutz, S.L. Brunton, Deep learning for universal linear embeddings of nonlinear dynamics, *Nature communications*, 9 (2018) 1-10.
- [24] C. Cheng, Z. Peng, W. Zhang, G. Meng, Volterra-series-based nonlinear system modeling and its engineering applications: A state-of-the-art review, *Mechanical Systems and Signal Processing*, 87 (2017) 340-364.
- [25] L.G. Villani, S. da Silva, A. Cunha, M.D. Todd, On the detection of a nonlinear damage in an uncertain nonlinear beam using stochastic Volterra series, *Structural Health Monitoring*, (2019) 1475921719876086.
- [26] J. Prawin, A.R.M. Rao, Nonlinear identification of MDOF systems using Volterra series approximation, *Mechanical Systems and Signal Processing*, 84 (2017) 58-77.
- [27] T. Wu, A. Kareem, Vortex-induced vibration of bridge decks: Volterra series-based model, *Journal of Engineering Mechanics*, 139 (2013) 1831-1843.
- [28] H.Z. Tan, Y. Huang, J. Fu, Blind identification of sparse Volterra systems, *International Journal of Adaptive Control and Signal Processing*, 22 (2008) 652-662.
- [29] C.A. Fernandes, G. Favier, J.C.M. Mota, Blind identification of multiuser nonlinear channels using tensor decomposition and precoding, *Signal Processing*, 89 (2009) 2644-2656.
- [30] S. da Silva, S. Cogan, E. Foltête, Nonlinear identification in structural dynamics based on Wiener series and Kautz filters, *Mechanical Systems and Signal Processing*, 24 (2010) 52-58.
- [31] M.J. Korenberg, I.W. Hunter, The identification of nonlinear biological systems: Volterra kernel approaches, *Annals of biomedical engineering*, 24 (1996) 250-268.
- [32] N. Bjorsell, P. Suchánek, P. Handel, D. Ronnow, Measuring Volterra kernels of analog-to-digital converters using a stepped three-tone scan, *IEEE Transactions on Instrumentation and measurement*, 57 (2008) 666-671.
- [33] M. Schetzen, Nonlinear system modeling based on the Wiener theory, *Proceedings of the IEEE*, 69 (1981) 1557-1573.
- [34] S.B. Shiki, S. da Silva, M.D. Todd, On the application of discrete-time Volterra series for the damage detection problem in initially nonlinear systems, *Structural Health Monitoring*, 16 (2017) 62-78.

- [35] Y. Lee, A. Vakakis, D. McFarland, L. Bergman, A global–local approach to nonlinear system identification: a review, *Structural Control and Health Monitoring*, 17 (2010) 742-760.
- [36] Y.-C. Ni, F.-L. Zhang, Fast Bayesian approach for modal identification using forced vibration data considering the ambient effect, *Mechanical Systems and Signal Processing*, 105 (2018) 113-128.
- [37] Z. Peng, Z. Lang, C. Wolters, S. Billings, K. Worden, Feasibility study of structural damage detection using NARMAX modelling and nonlinear output frequency response function based analysis, *Mechanical Systems and Signal Processing*, 25 (2011) 1045-1061.
- [38] E. Douka, L. Hadjileontiadis, Time–frequency analysis of the free vibration response of a beam with a breathing crack, *NDT & E International*, 38 (2005) 3-10.
- [39] O. Giannini, P. Casini, F. Vestroni, Nonlinear harmonic identification of breathing cracks in beams, *Computers & Structures*, 129 (2013) 166-177.
- [40] S. He, C.T. Ng, Modelling and analysis of nonlinear guided waves interaction at a breathing crack using time-domain spectral finite element method, *Smart Materials and Structures*, 26 (2017) 085002.
- [41] M. Ge, E.M. Lui, Structural damage identification using system dynamic properties, *Computers & structures*, 83 (2005) 2185-2196.
- [42] J.-B. Bodeux, J.-C. Golinval, Application of ARMAV models to the identification and damage detection of mechanical and civil engineering structures, *Smart materials and structures*, 10 (2001) 479-489.
- [43] C. Liu, J. Teng, Z. Peng, Optimal sensor placement for bridge damage detection using deflection influence line, *Smart Structures and Systems*, 25 (2020) 169-181.
- [44] M. Carminati, S. Ricci, Structural Damage Detection Using Nonlinear Vibrations, *International Journal of Aerospace Engineering*, 2018 (2018) 1901362.
- [45] A. Shah, Y. Ribakov, Non-linear ultrasonic evaluation of damaged concrete based on higher order harmonic generation, *Materials & Design*, 30 (2009) 4095-4102.
- [46] M.V. Shcherbakov, A. Brebels, N.L. Shcherbakova, A.P. Tyukov, T.A. Janovsky, V.A.e. Kamaev, A survey of forecast error measures, *World Applied Sciences Journal*, 24 (2013) 171-176.
- [47] H. Sohn, C.R. Farrar, Damage diagnosis using time series analysis of vibration signals, *Smart materials and structures*, 10 (2001) 446.
- [48] C. Li, K. Bi, H. Hao, Seismic performances of precast segmental column under bidirectional earthquake motions: Shake table test and numerical evaluation, *Engineering Structures*, 187 (2019) 314-328.
- [49] M.A. Kuddus, J. Li, H. Hao, C. Li, K. Bi, Target-free vision-based technique for vibration measurements of structures subjected to out-of-plane movements, *Engineering Structures*, 190 (2019) 210-222.
- [50] M. Schoettler, J. Restrepo, G. Guerrini, D. Duck, F. Carrea, A full-scale, single-column bridge bent tested by shake-table excitation. PEER report 2015/02. Pacific Earthquake Engineering Research Center (PEER), University of California, Berkeley, CA, (2015).
- [51] E. Guler, O. Selek, Reduced-scale shaking table tests on geosynthetic-reinforced soil walls with modular facing, *Journal of Geotechnical and Geoenvironmental Engineering*, 140 (2014) 04014015.
- [52] C. Michel, P. Guéguen, Time-frequency analysis of small frequency variations in civil

engineering structures under weak and strong motions using a reassignment method,
Structural health monitoring, 9 (2010) 159-171.

- [53] O. Scussel, S. Da Silva, Output-only identification of nonlinear systems via volterra series,
Journal of Vibration and Acoustics, 138 (2016).

CHAPTER 4 IMPROVING IDENTIFIABILITY OF STRUCTURAL DAMAGE USING HIGHER ORDER RESPONSES AND PHASE SPACE TECHNIQUE

ABSTRACT³

This chapter proposes a novel approach for improving the identifiability of structural damage by using higher order responses and SSA based PST technique. SSA is employed to decompose the structural dynamic acceleration response into several low dimensional components. Then the CPST reconstructed from the decomposed component with higher order responses of structures under intact and damaged states is utilized to identify the structural condition changes. Numerical studies on a planar truss structure are conducted to investigate the accuracy and reliability of the proposed approach. The dynamic acceleration responses of the truss structure corresponding to intact and several damage scenarios are utilized for signal decomposition by using SSA and damage detection with CPST. The effects of white noise, pink noise, modelling uncertainties on the accuracy of damage detection are investigated. The proposed method is also validated through experimental studies on a Tee-section pre-stressed concrete beam model. Vibration acceleration responses under hammer impact loads are measured under intact and damaged states, which are used for the damage detection with the proposed approach. Damage patterns identified by using the proposed approach under different loading levels agree well with the observed crack distributions. Both numerical and experimental results demonstrate that using the higher order response components decomposed by SSA and the proposed method is sensitive to damage and reliable for structural damage detection.

4.1 Introduction

SHM techniques have gained a significant amount of attention in the last several decades, mainly for large scale structures to ensure the designed performance, functionality and safety during their long service life. Damage identification and condition assessment can be considered as one of the most crucial aspects in the field of SHM. Identifying the presence of

³This chapter was published in *Structural Control & Health Monitoring* with the full bibliographic citation as follows: Peng, Z., Li, J., Hao, H., & Nie, Z. (2021). Improving identifiability of structural damage using higher order responses and phase space technique. *Structural Control and Health Monitoring*, 28(10), e2808. <https://doi.org/10.1002/stc.2808>.

the minor damage owing to, for example, degradation in material properties and/or changes in geometric properties that influence the dynamic behavior of structures adversely at an early stage, can provide important evidence to understand the root causes of the structural performance anomaly and make immediate maintenance action recommendations.

Three levels are usually defined in structural damage detection, namely, 1) diagnosing the presence; 2) detecting the location; and 3) identifying the extent of damage, by using indices or indicators derived from structural static and dynamic vibration responses [1]. Static responses based methods usually utilize the DI extracted from strain and deflection responses in the critical locations of structures under static load tests to reveal the global mechanical behavior of structures. Some of these methods can be found in the literature [2, 3]. Vibration-based damage diagnosis methods are based on the fact that structural damage will cause changes in its vibration characteristics. Thus, structural damage is generally identified by tracking the variation of the extracted damage-sensitive features from vibration acceleration, velocity, displacement and strain responses in the frequency or time domain. Frequency domain parameters, such as natural frequencies, mode shapes, mode shape curvatures, flexibility, modal strain energy and frequency response function (FRF), etc., have been commonly used as indicators in structural damage detection [4, 5]. Although most of the modal information based methods have been intensively studied for structural damage detection, there are still some challenges related to the practical applications. For example, many studies have proved that lower order frequency shifts are insensitive to minor structural damage compared with higher order frequency components [6, 7]. Meanwhile, the modal energy is usually concentrated in the first several lower order frequency components, which introduces a significant challenge to accurately identify higher order frequency components from the real measured responses to make use of their high sensitivity to structural damage. Additionally, the changes in dynamic behavior and vibration characteristics due to structural degradation may even be overwhelmed by environmental noise and other instrumental errors and uncertainties [8, 9]. As a result, the modal information based methods may have a poor sensitivity and noise immunity when applied to the detection of early minor damage, with the lower order frequency components. To address the drawback of the low sensitivity of using lower order frequency components for structural damage detection, some attempts were conducted to obtain the accurate measurement of higher order FRF [10], which was proven to be potentially promising for damage assessment [11, 12].

On the other hand, the time domain methods, which can be used to quantify the statistical and/or geometrical dissimilarity of dynamic responses before and after the damage, may not necessarily suffer from the above limitation. Chen and Yu [13] proposed a structural nonlinear identification algorithm based on a model of ARMA with generalized autoregressive

conditional heteroscedasticity, by using the acceleration series from the baseline and the unknown state as input to estimate the nonlinear damage in a three-story building structure. Li et al. [14] proposed a damage detection and optimal sensor placement method for structures under unknown traffic-induced vibrations. Xin et al. [15] proposed an enhanced EWT approach based on synchroextracting transform for the time varying system identification. Numerical simulations and experimental results showed that the proposed method is effective and accurate for time-varying system identification to obtain the instantaneous frequencies of structures, even under the significant noise effect. Other time frequency analysis methods, such as HT and wavelet-based methods, have also been used for structural linear or nonlinear damage detection [16, 17].

Phase space reconstruction is one of promising time series data-driven methods for structural condition monitoring. Structural dynamic state variable is a graphical representation in the multidimensional orthogonal coordinate system, and any underlying system model relies upon the phase trajectory. PST reconstructed from dynamic responses in the healthy state is viewed as a baseline. Structural damage can be detected by quantifying the dissimilarity between the trajectories under the intact and damaged states. Based on this principle, several studies have been conducted recently to identify damage of structures under impact loads or chaotic loads. The results indicate that phase space-based methods have a great potential in damage detection of both linear and nonlinear structures. Nie et al. [18, 19] developed an index named change in phase space trajectory (CPST) to identify damage in a circular arch structure and a RC slab. The results showed that CPST can be used as a DI with a higher sensitivity than conventional modal information-based features, such as the mode shape curvature, flexibility matrix change, COMAC and ECOMAC [20]. Todd et al. [21] extracted local attractor variance ratio from nonlinear time series corresponding to the baseline and damaged structures under chaotic excitations, for vibration based damage assessment.

However, the input signal of the above-mentioned studies should be low dimensional that can be embedded in the phase space by Taken's embedding theorem [22]. For example, the first several lower order frequencies are excited by the hammer impact or moving loads [14, 15]. This can limit the potential applications of such methods to real-world structure. It has been demonstrated in the existing studies [23, 24] that using higher order vibration modes is more sensitive to detect structural damage than the lower order modes. Due to the complexity in practical structural systems and uncertainties in loading scenarios, the in-situ measured responses are inevitably of high-dimensional frequency components, which may not be fully unfolded in the phase space [25, 26]. Though this limitation could be overcome by carefully choosing a low dimensional chaotic signal, i.e. Lorenz chaotic or Hyper-chaotic oscillators [27] as the excitation signal, it is difficult and costly, if it is not realistically impossible, to

generate a chaotic waveform load to excite a real structure. The feasibility and applicability of phase space based damage detection methods will be largely enhanced if a generalized dynamic load with multiple frequency components can be used. Therefore, suitable dimensionality reduction techniques ought to be explored and applied to decompose the original vibration signal into several low dimensional components. Several commonly used vibration signal decomposition methods, such as EMD, VMD and SSA, can serve this purpose. It is noteworthy that the signal components after decomposition should not only be low dimensional that is suitable for PST reconstruction, but also has a certain degree of oscillatory performance to ensure that the sufficient vibration based damage information is retained in the decomposed components.

SSA is a powerful automatic time-series decomposition method for extracting the original signal into slowly varying trends, oscillatory components and noise [28]. Jinane and Dominique [29] and Xu et al. [30] have demonstrated its efficiency for processing stationary and non-stationary signals without restriction on the length of the analyzed signals. Recently, SSA has been demonstrated to be effective in decomposing the dynamic responses of bridges under the moving vehicle into several signal components to improve the visibility of high order bridge frequencies from low order frequencies dominated responses [31-33]. In these studies, the frequency spectrum of each signal component is dominated by a certain frequency component, in another word, the dimensionality of signal components after the decomposition is reduced. With the superiority in modal decomposition and signal dimensionality reduction, SSA is used in this study to conduct signal decomposition to separate the high frequency components reliably from the original vibration responses. In this study, ‘high dimension’ means that the signal consists of multiple frequency components in the frequency spectrum, which indicates that a high embedding dimension parameter is required for phase space reconstruction by using dynamic responses. In contrast, low dimension signal means that only one or two peaks appeared in the frequency spectrum. The low/high order frequency refers to low/high order natural frequency components in the frequency spectrum.

With the main objective of extending the applicability of phase space based methods to processing high dimensional responses, this chapter proposes a systematic SSA based phase space technique framework for structural damage detection, by using the higher order frequency response components. The SSA decomposed low dimensional components with higher order frequency responses that are extracted from original dynamic vibration measurements, are used to reconstruct phase space with Taken’s theorem. Structural damage is identified by using a damage index developed based on CPST. Theoretical background and development of the proposed approach will be briefly introduced in Section 2. In Section 3, the procedure of the proposed structural damage detection framework will be illustrated and

verified using numerical studies on a 2D truss structure. The effects of white noise, pink noise and modelling uncertainties on the accuracy and performance of damage detection are investigated. In Section 4, the proposed approach will be further applied to perform the damage detection in an experimental Tee-section pre-stressed concrete beam model. Finally, Section 5 provides the concluding remarks and recommendations for further work.

4.2 Theoretical Background and Development

The proposed structural damage detection approach using SSA based phase space technique and higher order frequency response consists of several important steps. First, the acquired acceleration responses are decomposed into a set of low dimensional signal components through SSA. Then, the decomposed signal components are analyzed by using SVD to evaluate the dimensionality for embedding. The time delay parameter for PST reconstruction is determined by using the auto-correlation function of the respective SSA components. Lastly, the damage index, named as SSA-CPST_{average}, is defined to identify the structural damage based on the phase space of higher order frequency response component.

4.2.1 SSA for signal dimensionality reduction

This section provides a brief theoretical background of SSA for signal decomposition. SSA is nonparametric signal decomposition technique, which consists of three main steps, namely, embedding, SVD, grouping, skew diagonal averaging. More details can be referred to the literature [34]. The theoretical background and major procedure to conduct SSA are summarized as follows.

4.2.1.1 Embedding

Given a set of single channel acceleration response time series at a certain node described as $\mathbf{a}(t) = [a_0, a_1, a_2, \dots, a_{N-1}]$ and a window length as $2 \leq L \leq N/2$, the one-dimensional signal $\mathbf{a}(t)$ can be embedded into a $L \times K$ trajectory matrix \mathbf{X} as

$$\mathbf{X} = [\mathbf{X}_1, \mathbf{X}_2, \dots, \mathbf{X}_K] = \begin{bmatrix} a_0 & a_1 & \cdots & a_{K-1} \\ a_1 & a_2 & \cdots & a_K \\ \vdots & \vdots & \ddots & \vdots \\ a_{L-1} & a_L & \cdots & a_{N-1} \end{bmatrix} \quad (4.1)$$

where $\mathbf{X}_i = [a_{i-1}, a_i, \dots, a_{i+L-2}]^T$, $i=1, 2, \dots, K$ and $K=N-L+1$. Since the (i, j) element of \mathbf{X} is $x_{ij} = a_{i+j-2}$, the embedded trajectory matrix \mathbf{X} corresponds to the features of Hankel matrix, which can be viewed as a multivariate representation of $\mathbf{a}(t)$.

4.2.1.2 SVD

Applying SVD to analyse the trajectory matrix formulated in Eq. (4.1), we have $\mathbf{X}=\mathbf{U}\mathbf{Q}\mathbf{V}^T$, where \mathbf{U} and \mathbf{V} represent the left-singular eigenvectors and right-singular eigenvectors with dimensions of $(L \times L)$ and $(K \times K)$, respectively. \mathbf{Q} denotes the rectangular diagonal matrix with non-negative singular values, which are sorted in the descending order. Here, the signal dimensionality of the original time series can be obtained from the number of singular values which are significantly greater than zero. Supposing that $X^{(l)} = \mathbf{u}_l \mathbf{q}_l \mathbf{v}_l'$ with \mathbf{u}_l , \mathbf{v}_l and \mathbf{q}_l defined respectively as the l -th left-singular eigenvector of \mathbf{U} , the right-singular eigenvector of \mathbf{V} and the l -th eigenvalue of \mathbf{Q} , the trajectory matrix \mathbf{X} can be expanded as

$$\mathbf{X} = \mathbf{X}^{(1)} + \mathbf{X}^{(2)} + \dots + \mathbf{X}^{(L)} \quad (4.2)$$

After performing SVD, the trajectory matrix \mathbf{X} is decomposed into L elementary matrices of rank 1 with the norm equal to the singular value [32].

4.2.1.3 Grouping and skew diagonal averaging

Grouping procedure is the most important step in SSA, in which all the elementary matrices should be divided into M groups according to the analysis results of SSA, e.g., noise elimination, smoothing, trend component analysis and specific frequency extraction, etc. Defining a group index, $g_m=1, \dots, N_g$, the elementary matrices in g_m group can be represented by $\mathbf{X}_{g_m} \subseteq \{\mathbf{X}^{(1)}, \mathbf{X}^{(2)}, \dots, \mathbf{X}^{(L)}\}$. Then the elementary matrix in the same group are accumulated, and M grouped matrices, i.e. $\mathbf{X}_{g_1}, \mathbf{X}_{g_2}, \dots, \mathbf{X}_{g_{N_g}}$ can be obtained. The trajectory matrix \mathbf{X} can be rewritten as

$$\mathbf{X} = \mathbf{X}_{g_1} + \mathbf{X}_{g_2} + \dots + \mathbf{X}_{g_{N_g}} \quad (4.3)$$

The signal components with the same length as the original single-channel acceleration time series is recovered by adopting a skew averaging procedure to each resultant matrix. Let \mathbf{Y} be any of the resultant matrices \mathbf{X}_{g_l} , with elements $y_{i,j}$, $i=1,2,\dots,L$, $j=1,2,\dots,K$, the l -th component signal $\mathbf{a}^{gl}=[a_0^{gl}, a_1^{gl}, \dots, a_{N-1}^{gl}]$ can be reconstructed as

$$a_k^{g_m} = \begin{cases} \frac{1}{k} \sum_{m=1}^{k+1} y_{m,k-m+1} & \text{for } 1 \leq k < L \\ \frac{1}{L} \sum_{m=1}^L y_{m,k-m+1} & \text{for } L \leq k \leq K \\ \frac{1}{N-k} \sum_{m=1}^{N-K+1} y_{m,k-m+1} & \text{for } K < k \leq N-1 \end{cases} \quad (4.4)$$

SSA decomposes the original time series $\mathbf{a}(t)$ into M component series, that is $\alpha_k^{g_m}$ for $m=1, \dots, M$. It should be noted that both the embedding dimension m and delay time parameters τ in PST reconstruction are related to the frequency of a certain signal component obtained

from SSA. To achieve the signal dimensionality reduction effectively, decomposed components from SSA with similar frequency features will be deployed in one group.

4.2.2 Phase space reconstruction

It is known that phase space can recover all possible states of a dynamic system. The possible values of position (displacement) and motion status (velocity and acceleration) correspond to a unique point. For a structure, the excitation mechanisms are balanced by the dissipative mechanisms to result into an invariant trajectory in the phase space, also referred to as phase portrait [25, 26]. Generally, the phase space can be regarded as a model that comprehensively reflects all the physical parameters. Minor structural damage (change in mass, damping and stiffness) may not be straightforwardly extracted from directly analysing the time history and frequency spectrum, but can be reflected in the phase space sensitively. Therefore this feature makes phase space as a good and sensitive DI for structural damage detection, as presented and validated in previous studies.

To construct a multi-dimensional phase space, acceleration, velocity and displacement time series can be arranged in three directions of a coordinate system. However, measuring the dynamic velocity and displacement with a high accuracy experiences difficulties in practice [35]. Fortunately, this limitation is overcome by applying Takens' embedding theorems, where the complete information of system dynamics can be unfolded in the phase space by a single status variable with the time delay method [26]. Hence, the delayed series of single-channel acceleration response at the time instant n is used herein to reconstruct the PST as

$$\mathbf{a}(n) = [a(n), a(n + \tau), \dots, a(n + (m - 1)\tau)] \quad (4.5)$$

where m and τ denote the embedding dimension and time delay, respectively.

The selection of embedding dimension and time delay parameters will significantly affect the PST reconstruction. For the embedding dimension, SVD and false nearest neighbor methods are the most commonly used methods to calculate the optimal embedding dimension. In this chapter, the dimension of the original measured signal is reduced by using SSA described in Section 2.1, in which the embedding dimension of the signal can be reflected by the number of relatively larger singular values. In other words, all the singular values are sorted in the descending order with SVD analysis, and the number of singular values that are significantly larger than zero is selected as the optimal value of embedding dimension [26].

Regarding the time delay, the phase space will be collapsed into a 45° line if the selected time delay parameter is too small or too large, which causes difficulties in the extraction of

damage-sensitive indicator. The auto-correlation function is one of the most effective tools in selecting the best suitable time delay [36], which can be expressed as

$$c_{aa} = \frac{\sum_{n=0}^{N-1} [a(n) - \bar{a}][a(n+t) - \bar{a}]}{\sum_{n=0}^{N-1} [a(n) - \bar{a}]^2} \quad (4.6)$$

where \bar{a} is the average value of the given time series. The time instant corresponding to the first zero of the auto-correlation function is selected as the best time delay parameter.

4.2.3 SSA and phase space based damage detection

As mentioned above, the dynamic response of the structural system can be represented by using PST. The occurrence and development of structural damage cause changes in PST. Based on the fact that the higher order frequency responses are more sensitive to structural damage, the higher order decomposed component from SSA is used for constructing the PST. This can be developed as a sensitive index to evaluate structural degradation by quantifying the difference between PST before and after damage. A DI CPST proposed by Nichols [37] is proved to be sensitive and accurate in damage detection. PST defined in Eq. (4.5) corresponding to the structural healthy state is considered as the baseline trajectory. The trajectory extracted from the response data under the damaged state can be expressed as

$$\mathbf{a}_d(n) = [a_d(n), a_d(n + \tau), \dots, a_d(n + (m - 1)\tau)] \quad (4.7)$$

where m and τ correspond to the optimal embedding dimension and time delay, respectively.

As shown in Figure 4-1, for the purpose of demonstration, it is assumed that the structural response is represented by a two dimensional PST. A fiducial point on the damaged PST with time index k is selected as $a_d(k)$, then the nearest p neighbors of this point on the baseline PST can be found by minimizing the Euclidean distance as

$$\mathbf{a}_{nnk}(p_j): \min \|a(p_j) - a_d(k)\| \quad j = 1, 2, \dots, p \quad (4.8)$$

where the subscript ‘ nnk ’ means the nearest neighbors to the fiducial point k . It is noted that the size of the nearest neighboring points p should be chosen according to the total number of sample points N . Ørstavik and Jaroslav [38] and Nichols [37] suggested that the range of neighbors size should be $10^{-4} N \leq p \leq 10^{-3} N$.

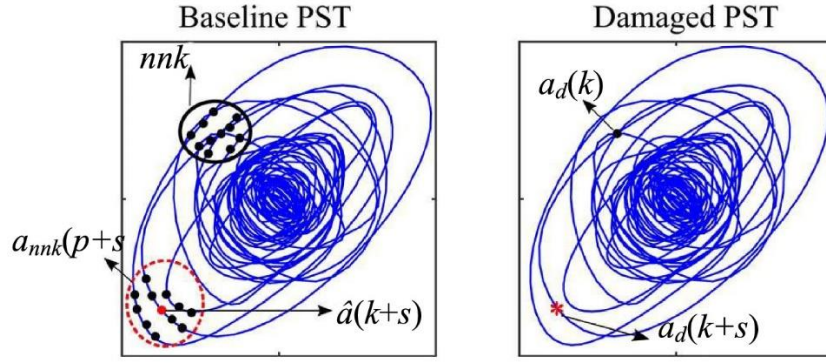


Figure 4-1. Schematic demonstration of CPST calculation

The value of $a_d(k)$ moving ahead some time step s can be forecasted in the baseline trajectory via

$$\hat{a}(k+s) = \frac{1}{p} \sum_{j=1}^p a_{nnk}(p_j+s) \quad (4.9)$$

where the predicted $\hat{a}(k+s)$ is the average of all the evolved values from the neighbors. To ensure the correlation of evolved neighbors in time domain, the time interval s used for prediction is typically selected according to $1 \leq s \leq (1/2)\tau$. Meanwhile, the evolved value on the damaged trajectory after s time step should be $a_d(k+s)$.

The damage index CPST is defined as

$$\text{CPST}(k) = \frac{1}{m} [\|\hat{a}(k+s) - a_d(k+s)\| - \|a(k+s) - \hat{a}(k+s)\|] \quad (4.10)$$

where m is the embedding dimension. $a(k+s)$ represents the evolved value of $a(k)$ on the baseline trajectory after s time steps. The above formula is consisted of two parts: the first part $\|\hat{a}(k+s) - a_d(k+s)\|$ is defined to evaluate Euclidean distance between the trajectories under the baseline and damaged states after moving ahead s time steps; and the second part $\|a(k+s) - \hat{a}(k+s)\|$ is calculated from the baseline state to eliminate the nearest neighbors prediction error introduced in Eq. (4.9) when damage is not occurred. In particular, a fiducial point $a(k)$ and the corresponding nearest p neighbors are selected from the baseline PST. Then the exact value of $a(k)$ moving ahead s time steps $a(k+s)$ as well as the value $\hat{a}(k+s)$ predicted from the nearest p neighbors via Eq. (4.9) can be obtained. CPST value in the selected fiducial point on the damaged state PST with the time index k is calculated based on the difference between the above two parts.

To obtain more stable and reliable damage detection results, a certain number of fiducial points with different time indices are chosen to repeat the calculation procedure illustrated from Eq. (4.7) to Eq. (4.10). It is suggested that the fiducial points N_p should be no less than 5% of the total sample points N [37]. The average of calculated CPST values is given as

$$SSA - CPST_{average} = \sum_{k=1}^{N_p} CPST(k)/N_p \quad (4.11)$$

This will be used as the damage index to detect the damage in structures. The flowchart of the proposed SSA based PST technique for structural damage detection is summarized in Figure 4-2.

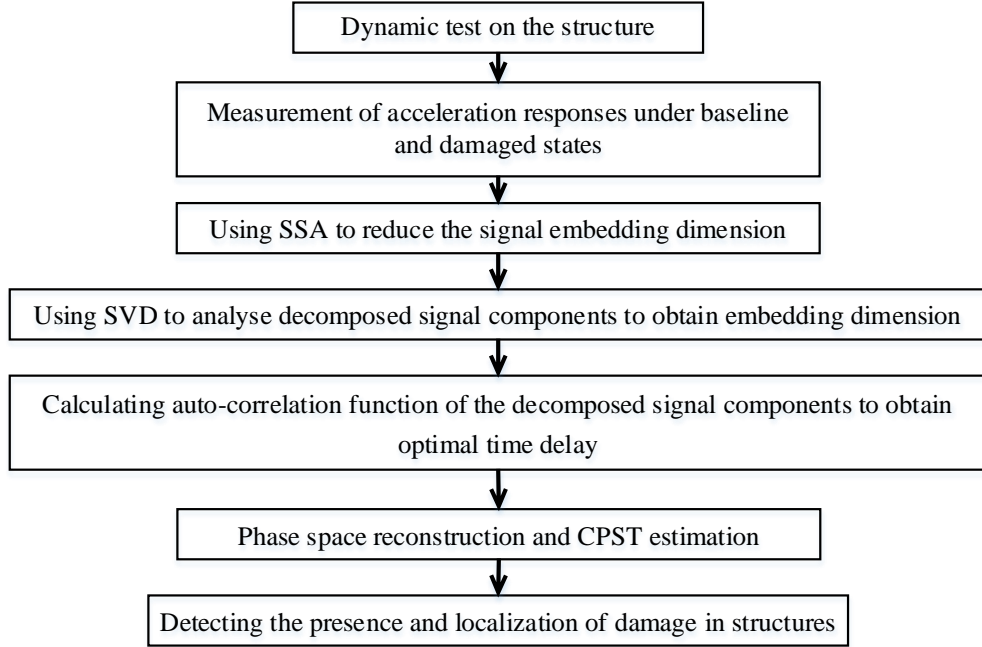


Figure 4-2. Flowchart of the proposed SSA based PST technique for structural damage detection

4.3 Numerical verification

In this section, numerical studies on a plane truss bridge model are conducted to demonstrate the accuracy and improvement of the proposed approach for structural damage detection. The effects of different types of measurement noises, as well as uncertainty in FE model are investigated.

4.3.1 Numerical Model

A simply-supported planar truss bridge model as shown in Figure 4-3 is employed to demonstrate the accuracy of the proposed damage detection approach and verify its effectiveness. There are totally 32 nodes and 61 elements, and all the joint between elements are hinge connections. The length and height of each bay are respectively 0.58 m and 0.38 m, with the same circular cross-section area of $5.65 \times 10^{-4} \text{ m}^2$ for the diagonal and longitudinal bars. The Young's modulus and Poisson's ratio of the material are defined as 90 GPa and 0.3, respectively.

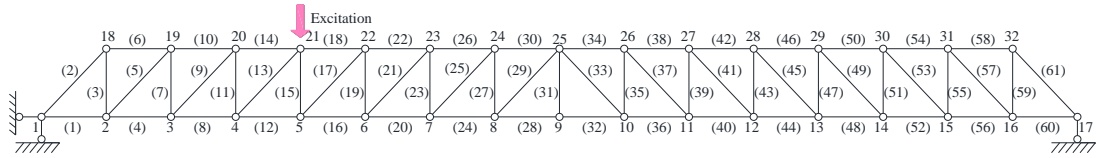


Figure 4-3. Planar truss model used in the numerical study.

100 N vertical impact load is applied on the node #21 of the planar truss model, as shown in Figure 4-3. It should be noted that the impact load is simulated as a triangular load with 20 load sub-steps during 0.1s. The vertical acceleration responses of node #2, #3, ..., #16 under different damage scenarios are collected with a sampling frequency of 2000Hz. Single damage (SD) cases are assumed in the element #21 with different severities, and multiple damages (MD) cases are assumed in the element #21 and #45. The severities are defined by reducing the Young's modulus of damaged elements. The specific locations and severities of single and multiple damage scenarios are listed in Table 4-1. As shown in Table 4-1, the first three order natural frequencies are slightly decreased with the increasing damage extent, indicating that the damage effect is very minor. In addition, the (modal assurance criterion) MAC values between the baseline and damage states are provided in Table 4-2 for understanding the effect of damage on the structural vibration characteristics. As shown in Table 4-2, the MAC values of the first three order mode shapes between the baseline and damage states are very close to 1, which means that the effect of the introduced element level minor damage on the vibration characteristics of the truss model with a high redundancy is not significant.

Table 4-1. Damage scenarios and the first three natural frequencies of the numerical truss model before and after damage.

Damage scenario	Stiffness reduction	1 st order frequency (Hz)	2 nd order frequency (Hz)	3 rd order frequency (Hz)
UD	0% (baseline state)	12.0284	32.8688	69.8015
SD 1	Element #21: 5%	12.0278	32.8651	69.7551
SD 2	Element #21: 10%	12.0272	32.8609	69.7035
SD 3	Element #21: 15%	12.0266	32.8563	69.6458
MD 1	Element #21: 15% & Element #45: 5%	12.0256	32.8558	69.6115
MD 2	Element #21: 15% & Element #45: 10%	12.0245	32.8552	69.5732
MD 3	Element #21: 15% & Element #45: 15%	12.0234	32.8546	69.5304

Table 4-2. MAC values (in %) between the baseline and damage states

UD	SD 3	MD 3
----	------	------

	1	2	3	1	2	3
1	100.0000	0.0000	0.0089	100.0000	0.0000	0.0079
2	0.0000	99.9998	0.0000	0.0000	99.9998	0.0000
3	0.0090	0.0003	99.9966	0.0095	0.0001	99.9961

4.3.2 Single damage detection

4.3.2.1 Determination of embedding dimension and time delay

To evaluate the effectiveness of using the proposed method for detection of single damage scenarios, 5%, 10% and 15% stiffness reductions are simulated respectively and the corresponding acceleration responses at measurement locations are obtained. Figure 4-4 presents the vertical acceleration responses and the frequency spectra of node #7 from the numerical model under healthy state and single damage scenario with different damage severities. It is observed that the acceleration responses of the truss bridge structure excited by the introduced impact load mainly contain four frequency components. Only very minor differences in the time domain acceleration responses and the frequency spectra are observed when the damage occurs, indicating that the presence of damage is difficult to be identified by using the modal information, such as frequency shifts.

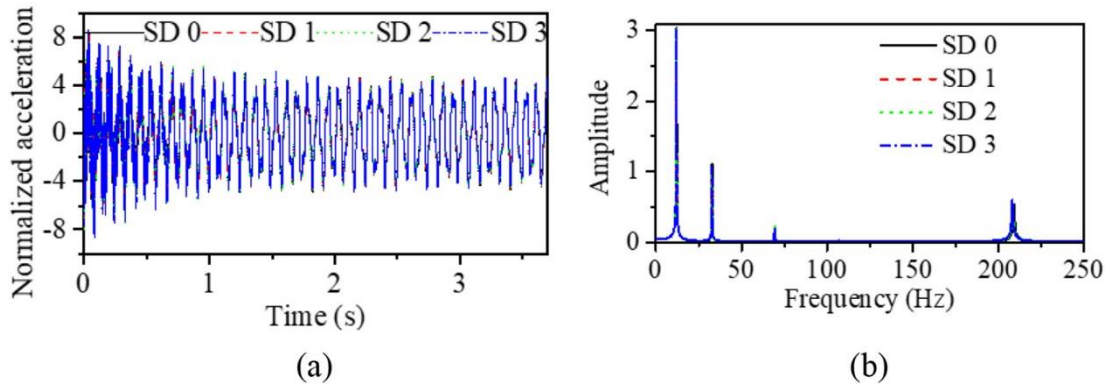


Figure 4-4. Response of node 7 under the impact load: (a) Accelerations; (b) Frequency spectra.

SVD introduced in Section 2.1 is conducted to obtain the dimensionality of the above obtained acceleration responses. Singular values as the diagonal element of matrix \mathbf{Q} are sorted in the descending order and shown in Figure 4-5. It is observed that the SVD results are presented in term of the singular value and embedding dimension. The first 6 singular values account for more than 95% of the sum of all the singular value. This indicates that at least 6 embedding dimensions are required for phase space reconstruction to unfold all the

information hidden in the dynamic response. Since the DI CPST is derived from the geometry of PST in the coordinate system, which pose challenges to calculate the accurate estimation of CPST when the signal is of high dimensionality. This provides the motivation to explore signal decomposition and dimensionality reduction approach to improve the feasibility and accuracy of using PST based damage detection method with high dimensional signals.

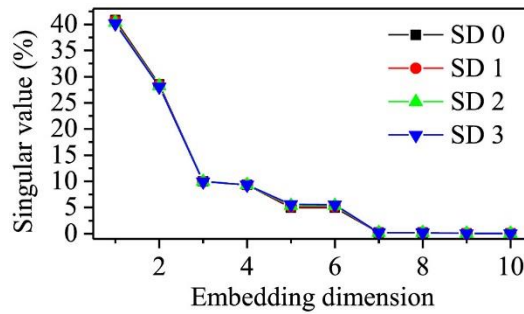


Figure 4-5. Singular values from SVD of acceleration responses at node 7.

In order to maintain the low dimensionality of the reconstructed phase space, the embedding dimension of the input signal should be reduced, ideally no more than three. Hence, SSA introduced in Section 2.1 is used herein for signal dimensionality reduction. The original acceleration response is decomposed into 4 components. It is noteworthy that the grouping step of SSA in this work is guided by frequency distribution, in other words, the elementary matrices with the same frequency distribution are merged into a group. The frequency spectrum of each component as shown in Figure 4-6 demonstrates that 4 main frequency components have been decomposed from the original measured response. These four frequencies correspond to the excited frequency components in the measured acceleration.

Meanwhile, the signal dimensionality of each signal component is calculated by conducting the SVD analysis. Results in Figure 4-7 show that the singular values tend to be zero when the embedding dimension m equals 2. This means that all these four components decomposed from using SSA can be fully unfolded in a 2-D phase space, demonstrating that SSA significantly reduces the signal dimensionality to the required level for PST reconstruction. The phase space of a signal component with the embedding dimension of 2 will be reconstructed in a 2-D coordinate system.

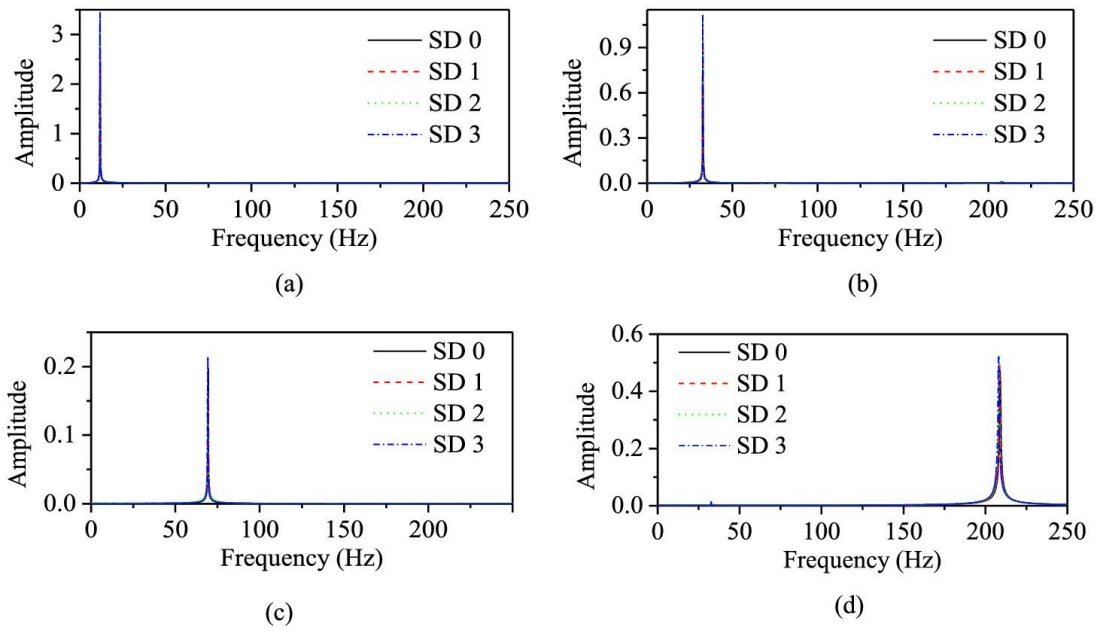


Figure 4-6. Frequency spectra of decomposed components of the response at node 7 by using SSA: (a) 1st; (b) 2nd; (c) 3rd; (d) 4th.

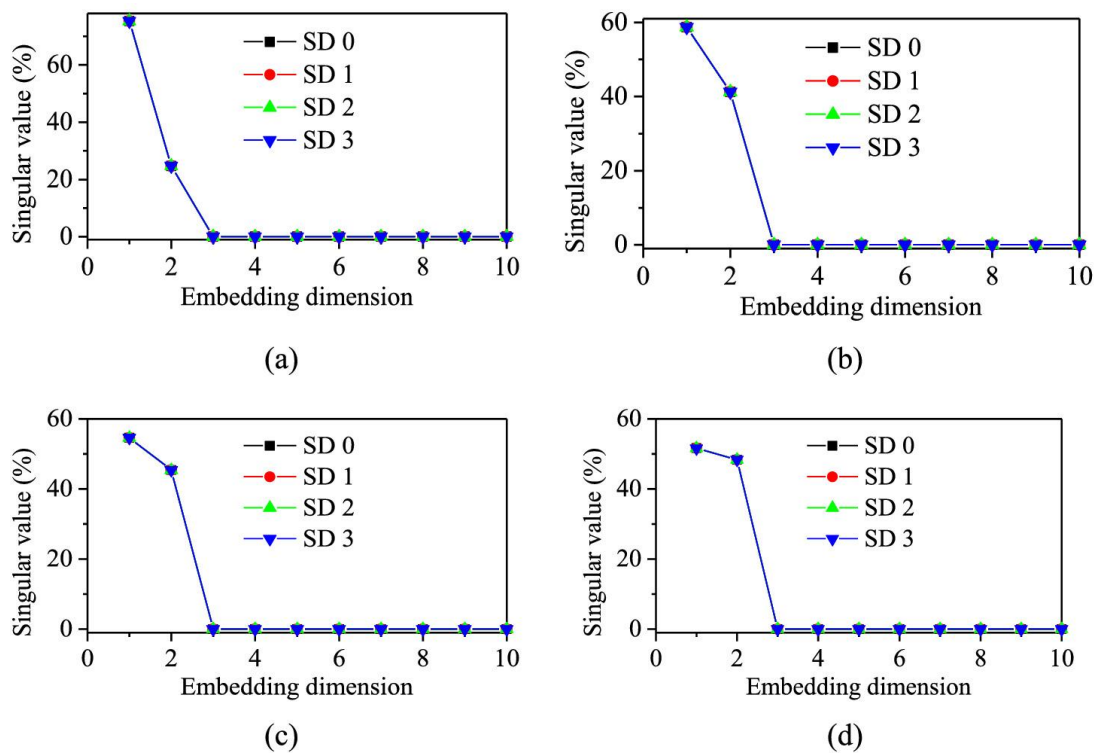


Figure 4-7. Singular values of each decomposed component: (a) 1st; (b) 2nd; (c) 3rd; (d) 4th.

Furthermore, another critical parameter for PST reconstruction, that is the time delay, will be determined by observing the first zero in the respective auto-correlation function described in Eq. (4.6). These four auto-correlations are plotted for each signal component under different

damage scenarios in Figure 4-8. In general, a descending trend in the time delay of the obtained four signal components can be found, which is caused by the difference in its frequency component. Usually, a larger time delay is required for the PST reconstruction of lower frequency signal component, since the period of the decomposed signal is larger. In summary, PST reconstruction parameters of each component under these four damage scenarios are listed in Table 4-3.

Table 4-3. PST reconstruction parameters of each decomposed component

Parameters	First component				Second component			
	SD 0	SD 1	SD 2	SD 3	SD 0	SD 1	SD 2	SD 3
m	2	2	2	2	2	2	2	2
τ	42	42	42	42	16	16	16	16
Parameters	Third component				Fourth component			
	SD 0	SD 1	SD 2	SD 3	SD 0	SD 1	SD 2	SD 3
m	3	3	3	3	2	2	2	2
τ	8	8	8	8	3	3	3	3

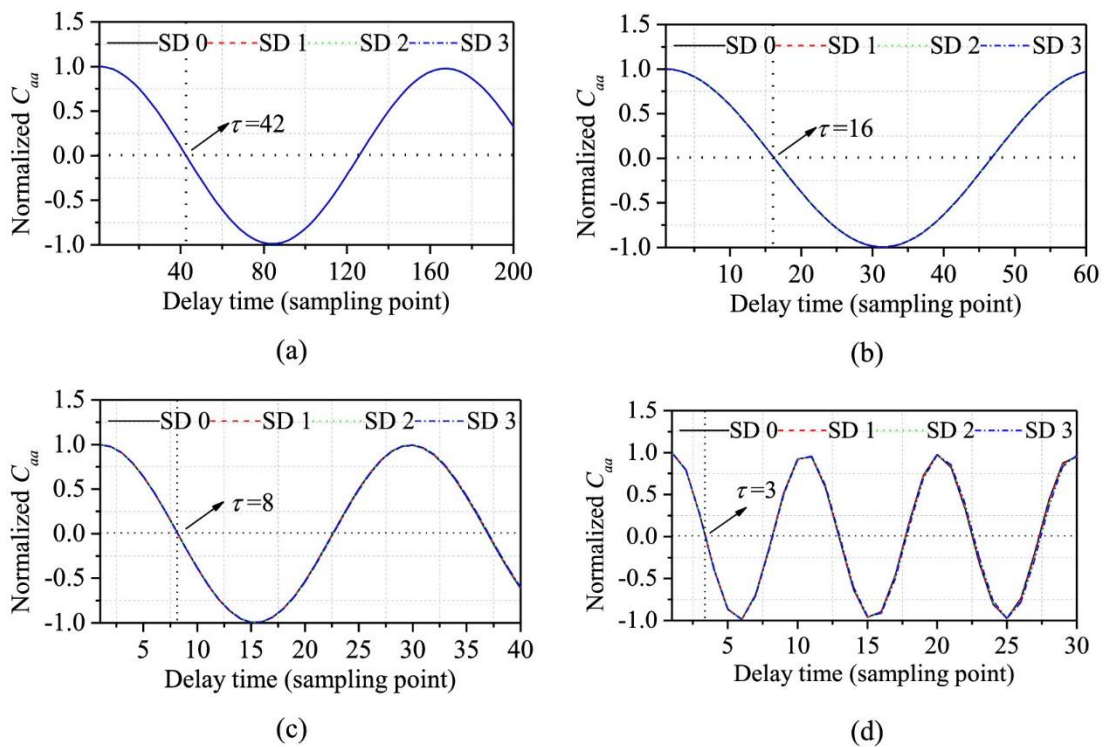


Figure 4-8. Time delay parameters obtained from the normalized auto-correlation functions of each component: (a) 1st; (b) 2nd; (3) 3rd; (4) 4th.

Though the same impact load is used in the above studies, the normalization process can be applied to remove the effect of different impact load levels. When the embedding dimension and time delay are determined, each SSA decomposed component signal is normalized by using the normalization procedure given as

$$\mathbf{a}_{normalized} = \frac{\mathbf{a} - \bar{\mathbf{a}}}{\sigma(\mathbf{a})} \quad (4.12)$$

where $\bar{\mathbf{a}}$ and $\sigma(\mathbf{a})$ denote the mean value and standard deviation of the decomposed acceleration response, respectively. Then, the normalized signal will be embedded in the phase space. The reconstructed PST of each component from the acceleration response of node 7 is shown in Figure 4-9, in which the amplitude of acceleration response is reflected as the radius of a circle in the phase space. It can be observed that the component corresponding to the higher order frequency component decays more quickly than that of the lower order frequency components. Moreover, the difference in the PST reconstructions between undamaged and damaged state is more obvious in the 3rd and 4th components than that of the 1st and 2nd components. These results demonstrate that the higher order frequency response components have a higher sensitivity than lower order frequency components.

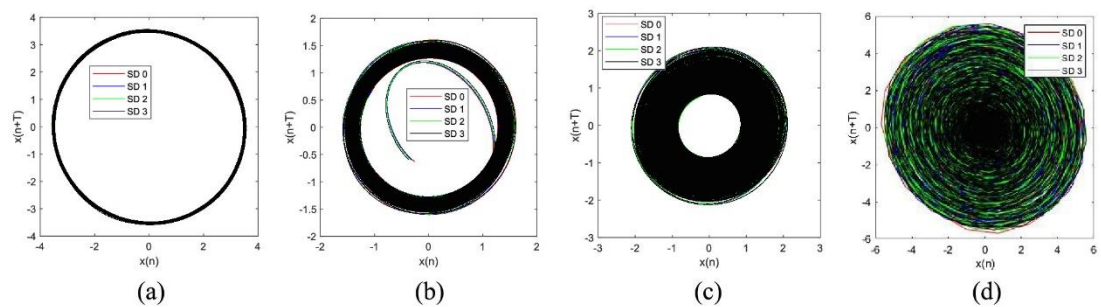


Figure 4-9. Reconstructed PST of: (a) 1st SSA component; (b) 2nd SSA component; (c) 3rd SSA component; (d) 4th SSA component.

4.3.2.2 Sensitivity analysis of the SSA components

To quantitatively compare the sensitivity of using the above obtained SSA components for damage detection, CPST values calculated from the reconstructed PST of each signal component under different damage scenarios are shown in Figure 4-10. It is noted that the first 1000 of the overall 8000 sampling points are used as fiducial points successively to calculate the average CPST value by using Eqs. (10) and (11). It can be observed that the average CPST values increase with the damage level. Besides, the CPST value of the 3rd and 4th components are more sensitive to damage than that of the 1st and 2nd components. These results demonstrate that the high frequency response components that are effectively decomposed by using SSA,

are more sensitive to detect structural damage. Hence, in this numerical study, the 3rd and 4th components are given priority when choosing a component as the input for PST reconstruction and the subsequent damage index calculation for structural damage detection.

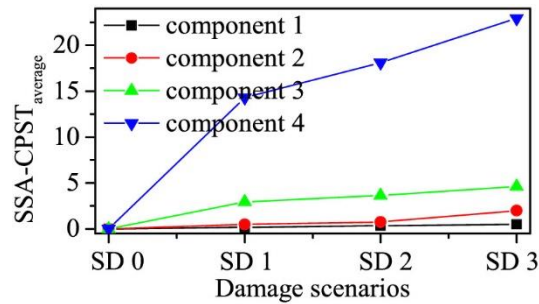


Figure 4-10. Comparison of average CPST value of four decomposed response components by SSA.

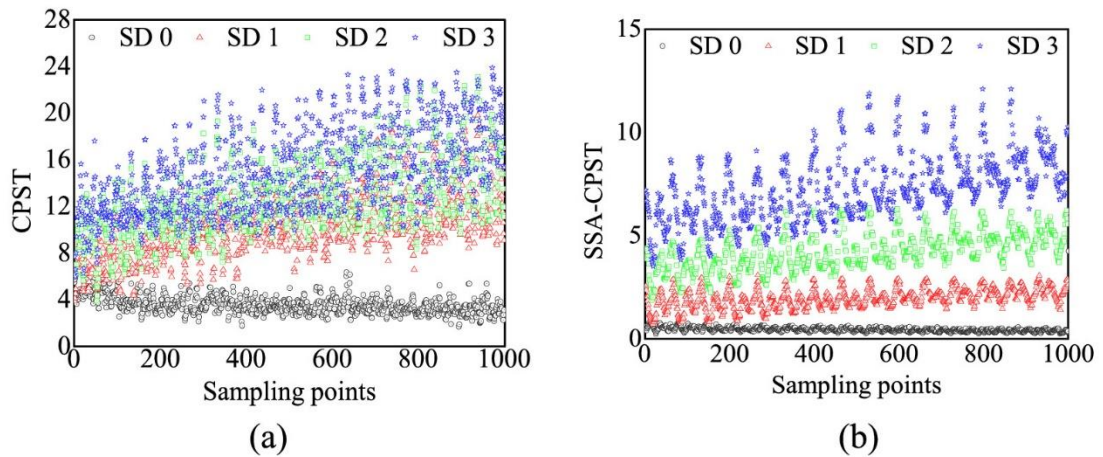


Figure 4-11. Scatterplot for the CPST values under different structural conditions: (a) Original signal; (b) The 4th component.

In order to illustrate the necessity of using low dimensional signal for improving the accuracy and reliability of phase space based technique for structural damage detection, the damage index CPST values calculated from original acceleration response without applying SSA and the 4th component signal decomposed with SSA are compared as scatterplot and shown in Figure 4-11. It is observed from Figure 4-11(a) that the CPST values without using SSA are diverse and the difference between different damage severities are not clearly distinguishable. However, much more consistent results are obtained by using the lower dimensional signal decomposed from SSA, as observed from Figure 4-11(b).

4.3.2.3 Damage detection results

To investigate the effects of different types of measurement noises and modelling errors on the reliability and accuracy of the proposed structural damage detection approach, 10% white noise, 10% pink noise and 1% modelling error are considered in the acceleration responses, respectively. Theoretically the power spectral density (PSD) of white noise in the frequency domain is a constant, which makes it easily be filtered out by applying the auto-correlation analysis. The following equation shows how the white and pink noises are considered.

$$\mathbf{a}_{noise} = \mathbf{a} + N_L N_s \sigma(\mathbf{a}) \quad (4.13)$$

where \mathbf{a}_{noise} is the acceleration response smeared with noise effect; N_L denotes the noise level. 10% white and 10% pink noise levels are considered respectively in this numerical study, therefore $N_L = 0.1$. N_s denotes the generated random white or pink noise. For white noise, it is a zero mean and unit standard deviation vector with the uniform PSD. While for pink noise, the PSD distribution is inversely proportional to $1/\sqrt{f}$ with a frequency f . The finite element modelling errors due to the inhomogeneity of material properties and the measurement errors of geometrical dimensions, inevitably exist. To investigate its influence, 1% variation is assumed in the elemental stiffness parameters as follows

$$E_{uncertainties}(i) = E(i) + U_L U_s E(i) \quad (4.14)$$

where $E_{uncertainties}(i)$ and $E(i)$ denote the Young's modulus of the i -th element with uncertainties and the original value, respectively; U_L is the uncertainty level and is equal to 0.01; and U_s denotes the standard normal distribution vector with zero mean and unit standard deviation.

Figure 4-12(a-d) shows the damage index results calculated with the original decomposed response components by using SSA, without considering measurement noise and modelling error. Figure 4-12(e-h), Figure 4-13(a-d) and Figure 4-13(e-h) show the damage detection results with 10% white noise, 10% pink noise and 1% modelling error, respectively. The true damage is located at the 6th element, marked with a red arrow in the figures. In Figure 4-12, the damage index SSA-CPST_{average} values at each measurement point increase with the damage extent, demonstrating the fact that the phase spaces of structural vibration responses are influenced by the damage in a certain region. Higher damage index values are clearly observed in the #6 measurement node, which is the location of the introduced damage. This shows that the location of the preset single damage is successfully identified.

Comparing the normalized damage index values obtained from the 1st, 2nd, 3rd and 4th decomposed components, it is observed that the values from the 4th component are much higher than those from the other three components. These results are also consistent with the

above analysis, demonstrating that the sensitivity of using the 4th component for damage detection is significantly higher. Regarding the effect of measurement noise and uncertainties, the damage detection results are shown in Figure 4-12(e-h) and Figure 4-13. It is found that the measurement noise and modelling errors only have a slight influence on the performance of damage detection using the proposed approach. In other words, the proposed approach is robust to white noise, pink noise and modelling uncertainties. One possible reason for this good noise immunity of the proposed method is that the principle of the damage index SSA-CPST based on phase space techniques is to evaluate the dissimilarity of reference points in baseline trajectory and its neighbors in the trajectory corresponding to an unknown structural state after several time steps evolution. Therefore this damage index significantly increases the sensitivity to detect the damage in phase space. However, phase-based method evaluates the dissimilarity of PST in baseline and unknown status, the measurement noise and uncertainties affect only the local values of the time series responses that are reflected as the choice of local-scale neighbors in the phase space, while brings a less influence on the free decay period of dynamic responses. Thus, the effects of measurement noise will be submerged in the phase after several time steps evolution. It is noteworthy that the SSA-CPST_{average} value in the 4th SSA component of #9 node (mid-span model node) is null, which is because of the mode shape corresponding to the 4th SSA component cannot be excited on this node. Therefore, the structural damage ought to be evaluated by a combination of several decomposed SSA components to achieve robust damage detection results.

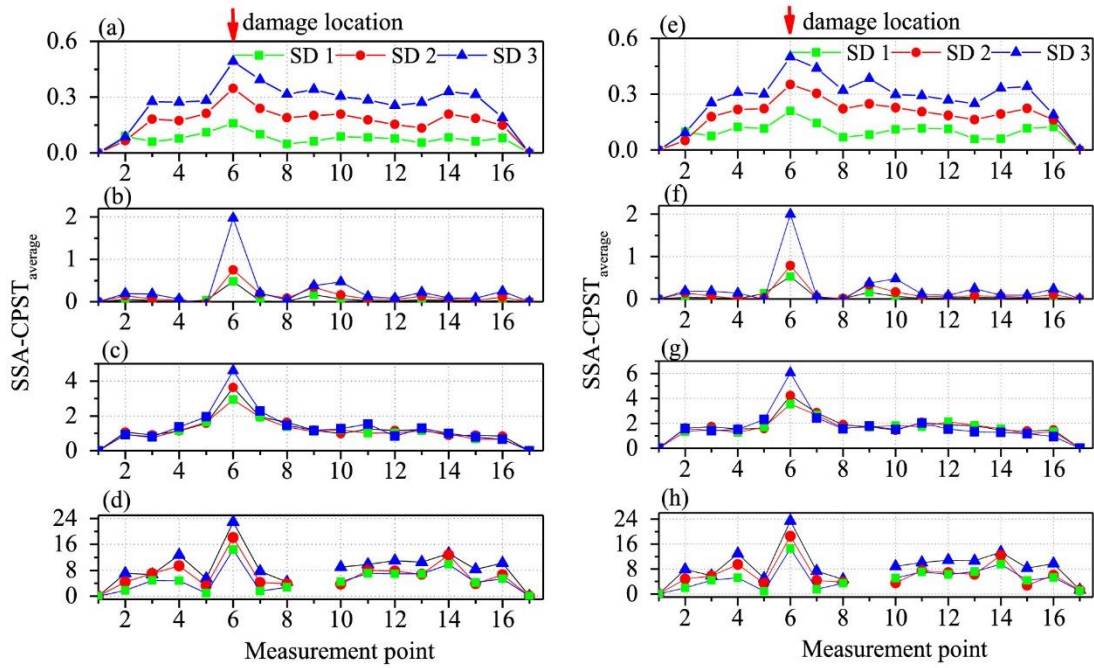


Figure 4-12. Damage detection results for single damage case when using different decomposed components without noise: (a) 1st; (b) 2nd; (c) 3rd; (d) 4th and with 10% white noise: (e) 1st; (f) 2nd; (g) 3rd; (h) 4th.

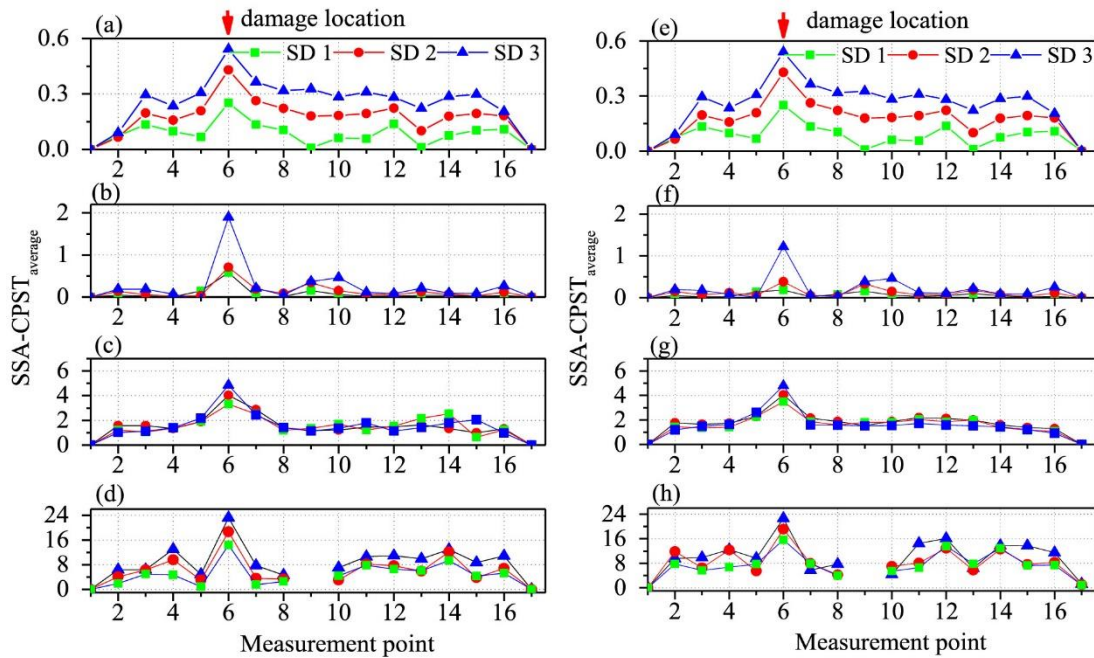


Figure 4-13. Damage detection results for single damage case with 10% pink noise when using different decomposed components: (a) 1st; (b) 2nd; (c) 3rd; (d) 4th and with 1% modelling error when using different decomposed components: (e) 1st; (f) 2nd; (g) 3rd; (h) 4th.

4.3.3 Multiple damage detection

To verify the accuracy of applying the proposed method for identifying multiple damage scenarios, 15% stiffness reduction is defined in element No. 21 and the stiffness reduction in element No. 45 is respectively set as 5%, 10% and 15%, as listed in Table 4-1. The same procedure as the above single damage detection is performed in this section. Figure 4-14(a-d) shows the damage detection results for multiple damage scenarios calculated with the original decomposed response components by using SSA, without both measurement noises and uncertainties. Figure 4-14(e-h), Figure 4-15(a-d) and Figure 4-15(e-h) show respectively the damage detection results for multiple damage case with 10% white noise, 10% pink noise and 1% modelling error. It should be noted that in these detection results, both damage locations could be confidently detected even when the dynamic responses are contaminated with significant white noise, pink noise or uncertainties.

It is worth noting that for most cases, the structural minor damage, i.e. 5% in element No. 45 around measurement location #13 in MD1, is detected accurately, especially when taking noise and uncertainties into consideration. The detection performance is more reliable and sensitive when using higher order frequency responses, as demonstrated by the results using the third and fourth decomposed components from SSA. The damage index values calculated with the fourth component are much higher than those from other three components. This also validates the fact that the fourth component with higher order frequency response is more sensitive and reliable to detect structural damage, even for the minor structural damage, under the significant measurement noise and uncertainty effect.

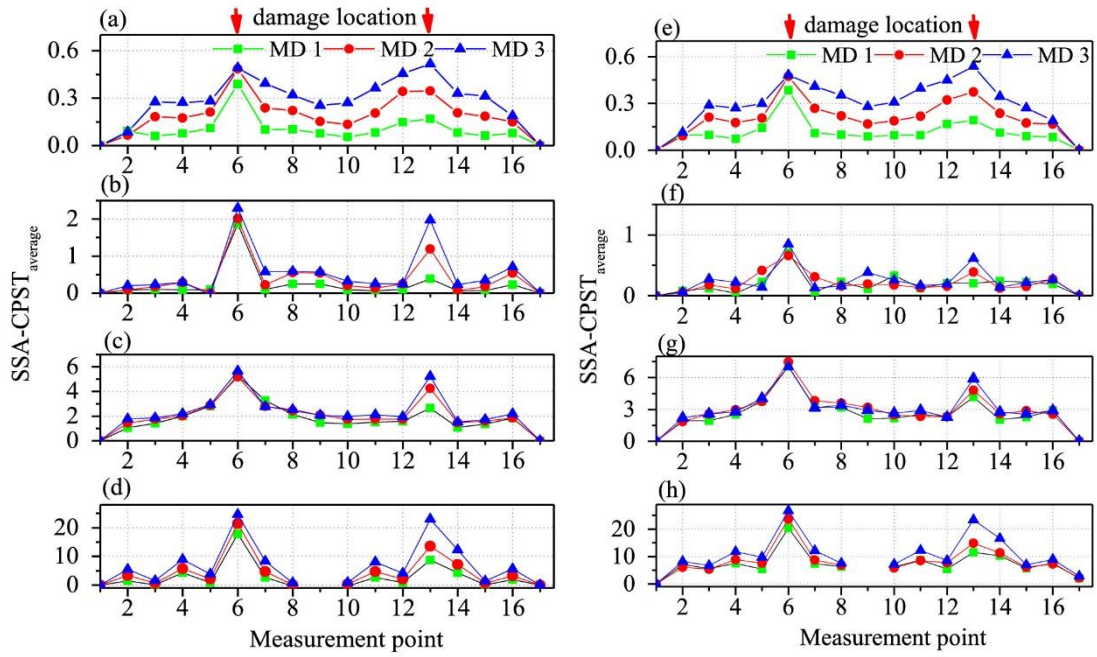


Figure 4-14. Damage detection results for multiple damage case when using different decomposed components: without noise: (a) 1st; (b) 2nd; (c) 3rd; (d) 4th and with 10% white noise: (e) 1st; (f) 2nd; (g) 3rd; (h) 4th.

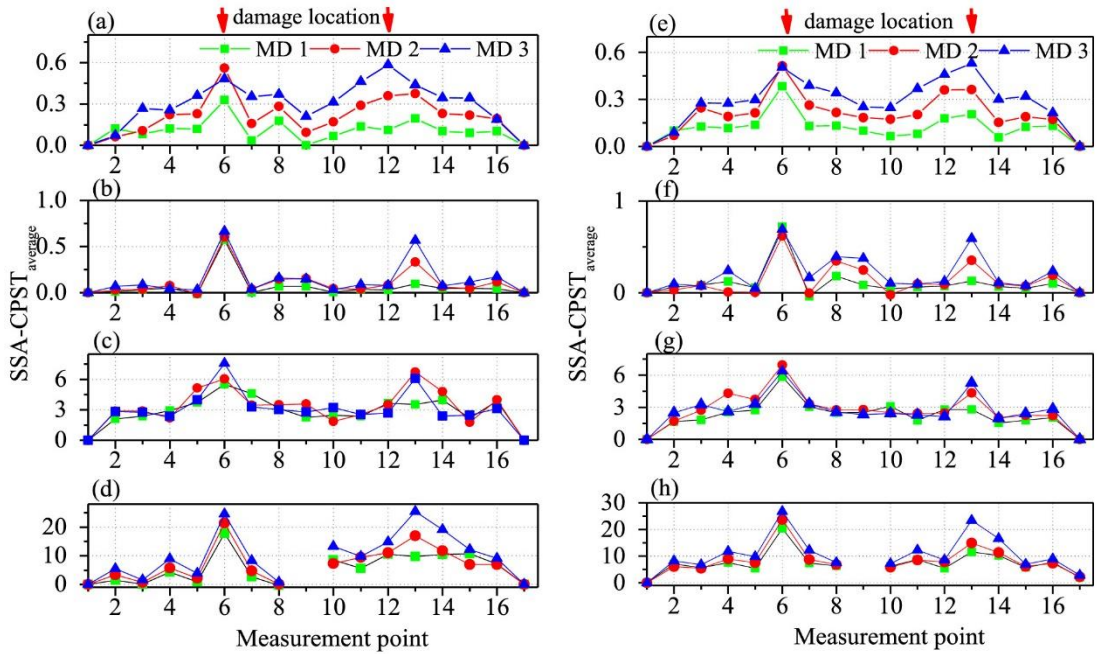


Figure 4-15. Damage detection results for multiple damage case with 10% pink noise when using different decomposed components: (a) 1st; (b) 2nd; (c) 3rd; (d) 4th and with 1% modelling error when using different decomposed components: (e) 1st; (f) 2nd; (g) 3rd; (h) 4th.

4.4 Experimental Application

The performance and reliability of the proposed damage detection method are further verified through the experimental studies on a pre-stressed concrete beam model in the

laboratory. The experiment setup and damage detection results are discussed in this section.

4.4.1 Experiment setup and sensor placement

A Tee-section pre-stressed concrete beam model was constructed in the laboratory to validate the performance and reliability of the proposed damage detection method. Its plan view, cross-section and dimensions are shown in Figure 4-16(a). The Young's modulus and density of concrete are 2.6×10^4 MPa and 2.7077×10^3 kg/m³, respectively. Three pre-stressing tendons with a total pre-stress force of 140 kN was applied on the beam model with the post-tensioning method. The cross-section dimensions and pre-stressing tendon locations at both ends and mid-span are shown in Figure 4-16(b). Seven single-axial sensors numbered from 1 to 7 as shown in Figure 4-16(a), are placed on the top of the T-section beam model for the dynamic vibration tests to measure the accelerations in the vertical direction. Hammer impact loads are applied at the $3L/8$ location to the right end of the beam for the structures under undamaged and damaged states to collect the acceleration vibration responses, which will be used for the damage detection with the proposed approach.

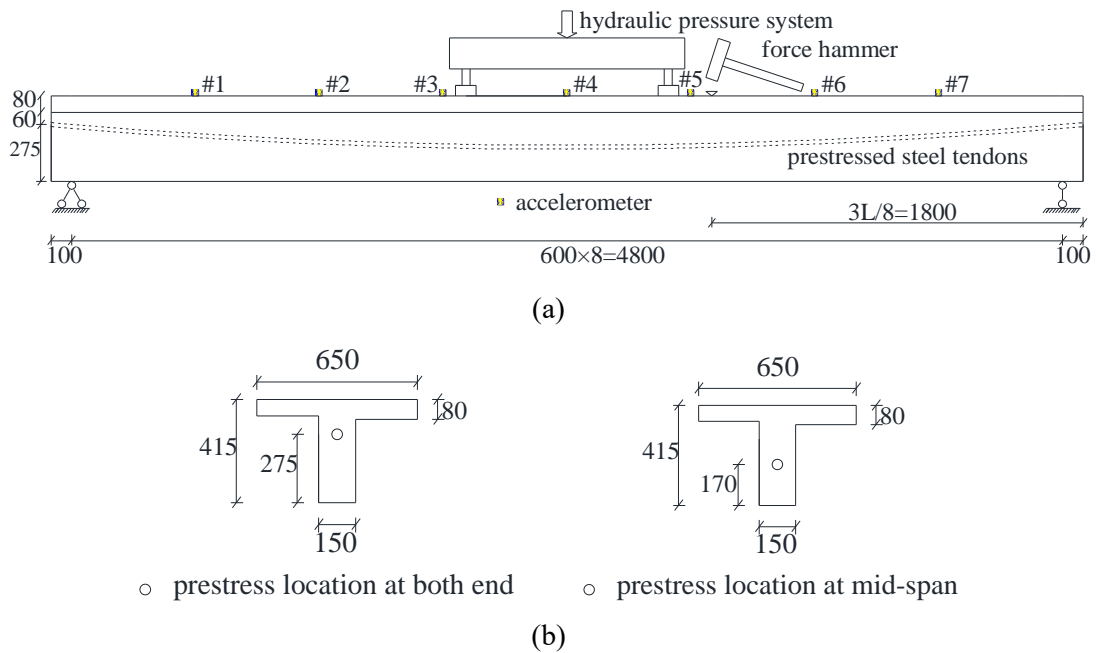


Figure 4-16. The sketch of pre-stressed concrete beam: (a) plan view; (b) cross-sections. (unit: mm).

4.4.2 Loading process to introduce structure damage

Structural damage is introduced by applying three different loading levels on the top of the beam model with hydraulic loading system, as shown in Figure 4-17, to create cracks in the beam. The applied loads of increment 1, increment 2 and increment 3 are 100kN, 180kN and 210kN, respectively.

The crack locations, intensities and distributions under each loading increment are presented in Figure 4-18. The light yellow curve denotes the appeared cracks at the end stage of the applied static load, and the black curve denotes the remaining cracks after unloading for one and a half hours. For the loading increment 1, some small cracks appear in the region from sensors #2 to #6, and only four cracks close to sensors #4 and #5 still remain in the beam model after unloading. The number and severity of cracks such as the depth are further increased when applying loading increment 2. Most of the cracks appeared in the loading increment 1 are not closed after unloading in this case, and some new cracks are developed. The loading increment 3 is applied on the beam structure to further increase the damage extent. It is observed that the depths of most cracks are significantly developed and some cracks are expanding to the flange of Tee-section beam, practically in the region from sensors #2 to #6 in the mid span of the model. Figure 4-19 displays the distribution of cracks observed after the loading increment 3.



Figure 4-17. Experimental setup.

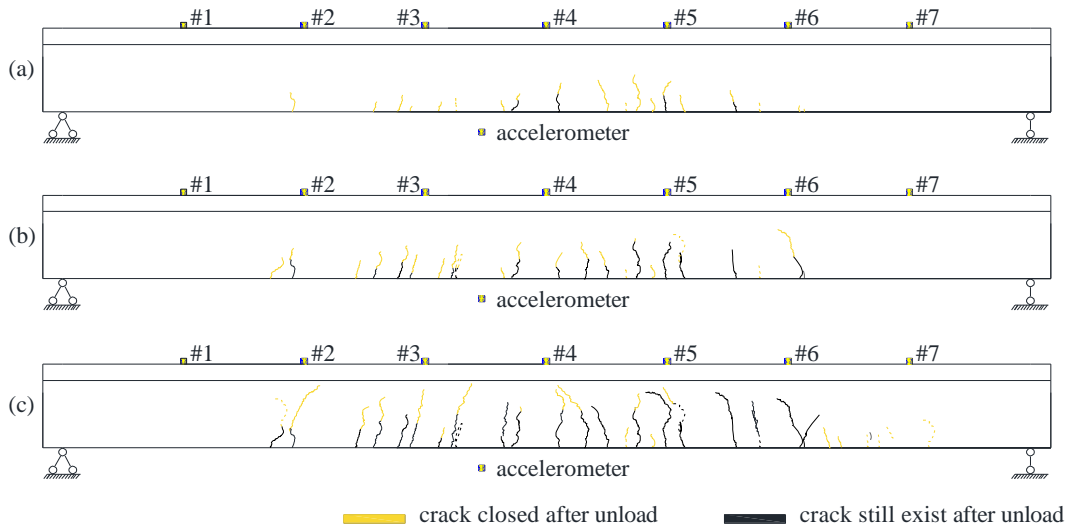


Figure 4-18. The crack distribution pattern in the damaged beam model under different loads: (a) Increment 1; (b) Increment 2; (c) Increment 3.

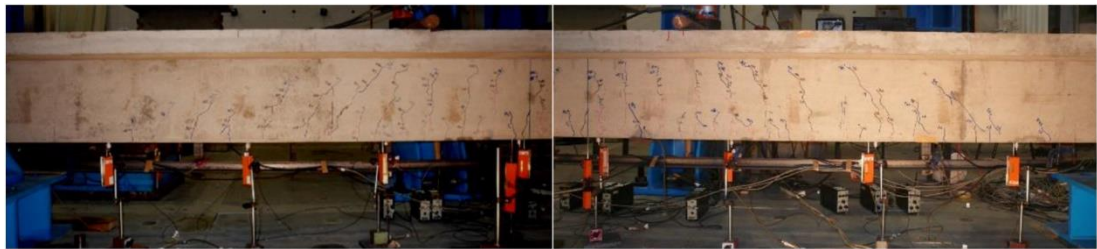


Figure 4-19. Observed crack locations and heights.

4.4.3 Vibration tests and analysis

Dynamic tests were conducted by using a LC-03A hammer with a nylon head and additional weight to make sure that a sufficient amount of energy is applied to excite the structure with a number of vibration modes. Acceleration responses of placed accelerometers under hammer impact tests are acquired from the beam model under the intact and damaged states, after the unloading of each loading increment at a stable state. Figure 4-20 shows the measured acceleration responses from sensor #1 and the corresponding frequency spectra in the healthy and damaged states under the applied incremental loads. It is observed that minor frequency reductions are observed in the low order frequency components, i.e. the fundamental frequency around 40Hz, even for the most significant damage severity under the loading increment 3. However, for the higher order frequency components, for example, those above 400Hz, the resonance frequency shifts are much more prominent, indicating a significantly higher sensitivity to detect the damage. Traditionally natural frequencies and mode shapes of the relatively low frequency components can be more reliably identified. For high frequency components, the excited energy and the participation ratio could be small

compared with those of the first several frequencies. Therefore vibration characteristics of these high frequency components may not be identified confidently. The accuracy of this identification is also susceptible to the effect of various uncertainties, such as measurement noises and other sources of uncertainties etc.

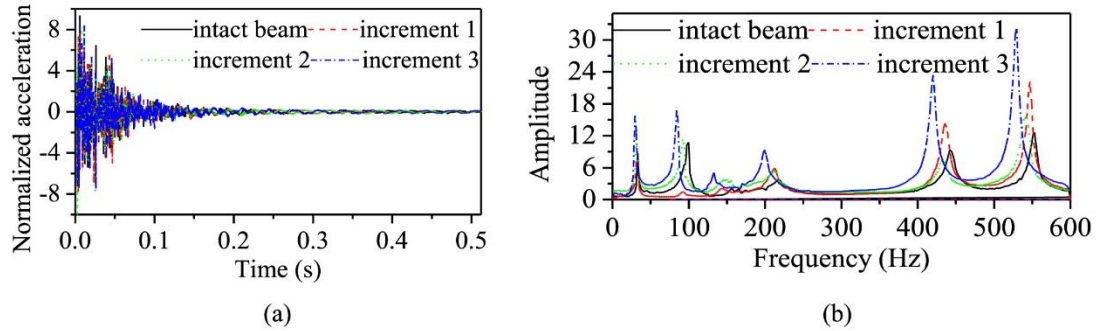


Figure 4-20. Acceleration responses of sensor #1 under hammer loads and different loading increments: (a) Time domain; (b) Frequency spectra.

4.4.4 SSA and phase space reconstruction

Before conducting PST reconstruction and calculating the damage index, SSA is performed to decompose the high dimensional acceleration response into a number of reduced dimensional components, which is more accurate to perform the PST reconstruction and reduces the computational demand as well. Figure 4-21 shows the Fourier spectra of decomposed components from the measured responses of sensor #1. It is clearly observed that the 2nd, 3rd and 4th components obtained by SSA contain only one dominate frequency component, while two frequencies are found in the first component. Besides, the natural frequencies in the 3rd and 4th components are distinctly decreased with the increasing severity of damage from loading increments 1 to 3. As discussed and validated by the results in the numerical studies on the sensitivity analysis of using different decomposed components for damage detection as shown in Figure 4-10 and Figure 4-12, the decomposed component by using SSA corresponding to high order responses is more sensitive to damage. Therefore in this study, the 3rd and 4th components are used herein to reconstruct the PST and evaluate the damage condition by using the proposed approach.

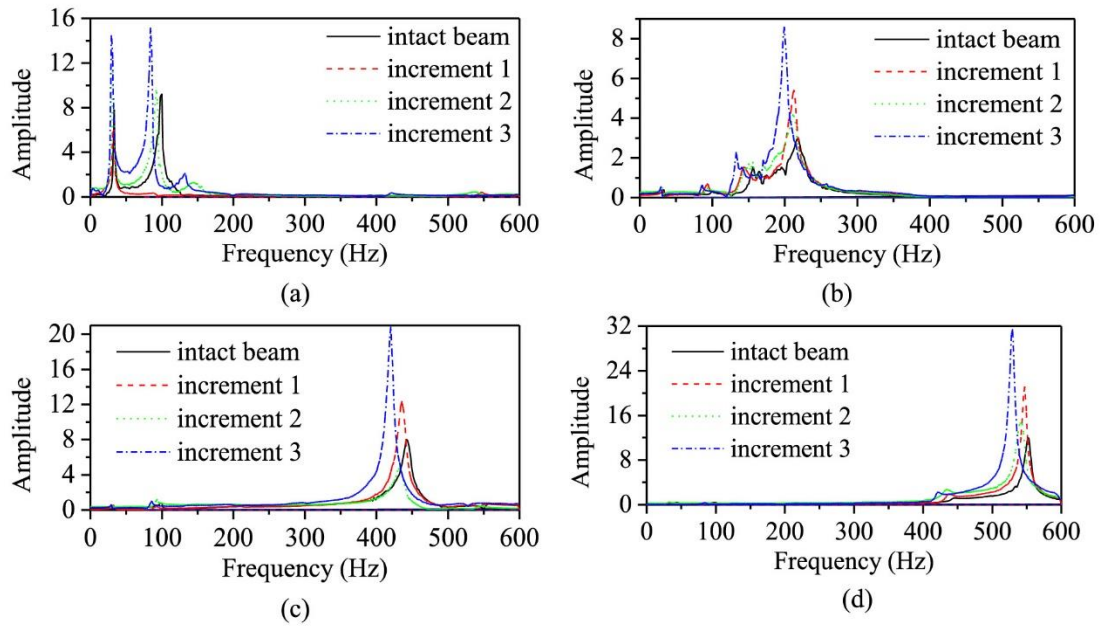


Figure 4-21. Fourier spectra of decomposed components from sensor #1: (a) 1st; (b) 2nd; (c) 3rd; (d) 4th.

SVD and auto-correlation function calculation presented in Section 2.2 are utilized to determine the proper embedding dimension and time delay parameters, respectively. The embedding dimensions of the 3rd and 4th components of the dynamic response measured by sensor #1 are determined as 2. Then, the normalized auto-correlation functions of the 3rd and 4th SSA component of #1 sensor are calculated to find out the optimal choice of delay time parameter. The time delay parameters of the 3rd and 4th components are obtained as 8 and 4, respectively. The process is repeated for the calculation of the embedding dimension and time delay parameters of sensors #1 to #7. With the obtained embedding dimension and time delay parameters, the PST of the 3rd and 4th component by SSA can be reconstructions according to the same procedure described in Section 2.3.

4.4.5 Damage detection results

The obtained PST corresponding to the intact beam is selected as the baseline, and the damage index results, $SSA-CPST_{average}$, are calculated and used to detect structural damage corresponding to the different states of load increment. It is noted that structural damage in this experimental verification is reflected by the number and length of cracks under the applied static loads. With a large number of different cracks observed in the beam model, it is difficult to derive analytically the exact damage extent. Therefore the observed crack pattern is defined as the target to identify in this study. Figure 4-22 shows the obtained $SSA-CPST_{average}$ damage index values depicting the progressive damage evolution for loading increments 1, 2 and 3,

respectively. The magnitudes of SSA-CPST_{average} damage index values in almost all the sensors increase generally with the incremental loads from both the 3rd and 4th components, except the sensor #6 in the load increment 2. The maximum damage index values are observed at the sensor #5 location in all of the three damage scenarios, which means that the region close to sensor #5 sensor has the largest damage severity. The most significant damages are distributed in the region from sensors #2 to #6. These detection results are consistent with the observed crack distribution in Figure 4-19. It is interesting that even though the cracks near sensors #2 and #3 are closed after the unloading of increment 1 for one and a half hour, the calculated damage index values still have a certain level of increase. The reason is that there will be friction in the closed micro cracks of the beam, which will significantly increase the damping ratios of some vibration modes and further affect the duration of free vibrations decay [19]. This observation shows that the damage index used in this study is very sensitive to minor structural damage. Comparing the results in Figure 4-22(a) and Figure 4-22(b) by using the 3rd and 4th components, the detection with the high order responses, i.e. the 4th component, shows a more sensitive and better damage pattern distribution, which matches well with the captured crack images. These results well demonstrate the reliability and sensitivity of using the proposed approach for structural damage detection.

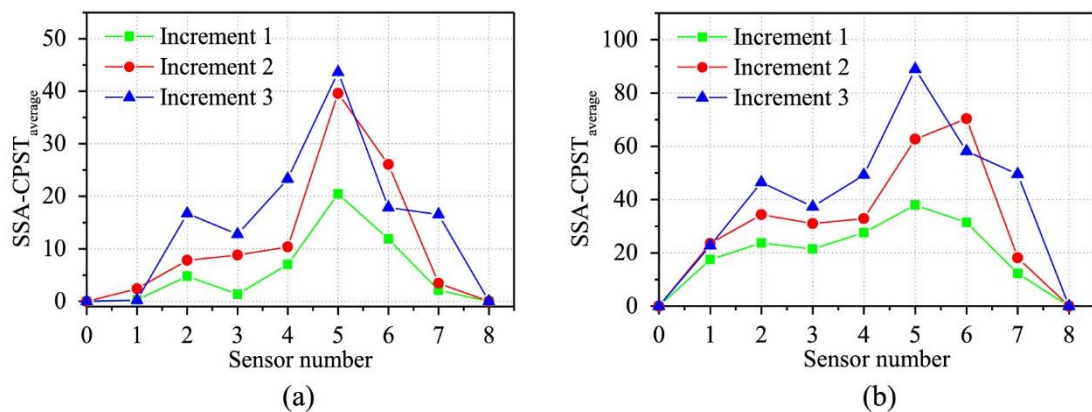


Figure 4-22. Damage detection results by SSA based CPST: (a) 3rd component; (b) 4th component.

To demonstrate the advantage of using the proposed method for structural damage detection in providing a higher sensitivity than the traditional modal information based indices, damage detection results by using the proposed SSA-CPST index are further compared with those from the relative change of other commonly used modal-based indices, i.e. natural frequency, flexibility, COMAC and ECOMAC. The theoretical derivations of the above mentioned DI are summarized by Nie et al. [18]. Figure 4-23 shows the comparison of using

modal-based indices and the proposed SSA-CPST with the 3rd and 4th component at an arbitrary location of measurement (e.g. sensor #5) under different structural conditions, including undamaged and damaged states introduced by different loading increments. It is clearly observed that SSA-CPST is the most sensitive one, followed by the relative change in flexibility. The proposed damage index shows a significantly higher sensitivity than modal based indices in damage detection. Moreover, the values of SSA-CPST show a consistently increasing trend with the damage severity, indicating that this proposed damage index could also be used for structural damage quantification.

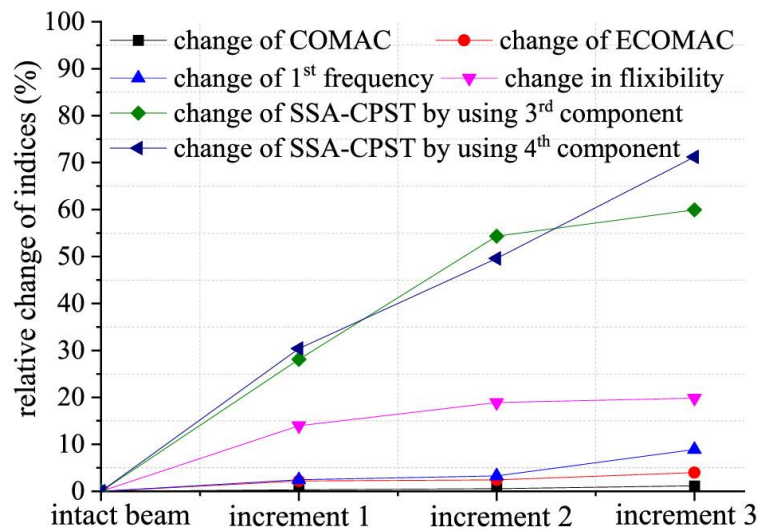


Figure 4-23. Comparison of the proposed damage index and traditional ones.

4.5 Conclusions

This chapter proposes a novel approach to improve the identifiability of structural damage by using higher order responses and SSA based PST technique. It is developed to extend the feasibility of using high dimensional structural responses to achieve the sensitive damage detection, which is essential for effective SHM under a number of uncertainties. The used SSA allows the decomposition of high dimensional structural responses into a number of low dimensional response components with separated vibration frequencies. These components contain sufficient dynamic feature to reflect structural degradation in the phase space. The optimal PST reconstruction parameters, namely, embedding dimension and time delay are determined using SVD analysis and auto-correlation function, respectively. Numerical and experimental studies demonstrate that the presence, location and progressive damage evolution can be identified effectively by the decomposed high order response component with the developed approach. The superiority of using SSA decomposed component corresponding to the higher-order response for damage detection is also demonstrated. Numerical results on

a planar truss model demonstrate that the proposed method is not only sensitive to structural damage, but also tolerant to a significant level of white noise, pink noise and modelling uncertainties. The performance of the proposed method is further verified with experimental investigations on a pre-stressed reinforced concrete beam model. The structure is progressively damaged by applying increasing static loads to develop a series of cracks. Vibration acceleration responses of the testing structure under intact and damaged states are used for SSA and PST reconstruction. The decomposed component with the higher-order response is then used for damage detection. The results show that damage pattern identified by the proposed approach agrees well with the observed crack distribution in the experimental tests.

It should be noted that hammer impact load is applied as excitations in this study. The excitation applied under different conditions is not necessarily the same in the test, but normalization can be conducted to remove the effect of different excitation levels. The flexibility of using the proposed method for scenarios under other forms of external loads, i.e. ambient and seismic excitations could be further investigated. It is also noted that a number of sensors are used to accurately identify damage. This limitation could be overcome by employing the phase space reconstructed from the dynamic responses of a moving vehicle crossing over the bridge, which will be studied in the future work.

References

- [1] K. Worden, C.R. Farrar, J. Haywood, M. Todd, A review of nonlinear dynamics applications to structural health monitoring, *Structural Control and Health Monitoring*, 15 (2008) 540-567.
- [2] Z. Chen, S. Zhu, Y. Xu, Q. Li, Q. Cai, Damage Detection in Long Suspension Bridges Using Stress Influence Lines, *Journal of Bridge Engineering*, 20 (2015) 05014013.
- [3] M.A. Abdo, Parametric study of using only static response in structural damage detection, *Engineering Structures*, 34 (2012) 124-131.
- [4] W. Fan, P. Qiao, Vibration-based damage identification methods: a review and comparative study, *Structural health monitoring*, 10 (2011) 83-111.
- [5] J. Li, H. Hao, A review of recent research advances on structural health monitoring in Western Australia, *Structural Monitoring and Maintenance*, 3 (2016) 33.
- [6] I. Mekjavić, Identification of structural damage in bridges using high-frequency vibrational responses, *Shock and Vibration*, 2015 (2015) 906062.
- [7] C. Yang, S.O. Oyadiji, Damage detection using modal frequency curve and squared residual wavelet coefficients-based damage indicator, *Mechanical Systems and Signal Processing*, 83 (2017) 385-405.
- [8] Y. Xia, H. Hao, G. Zanardo, A. Deeks, Long term vibration monitoring of an RC slab: temperature and humidity effect, *Engineering structures*, 28 (2006) 441-452.
- [9] R. Hou, X. Wang, Q. Xia, Y. Xia, Sparse Bayesian learning for structural damage detection under varying temperature conditions, *Mechanical Systems and Signal Processing*, 145 (2020) 106965.
- [10] R.M. Lin, T.Y. Ng, A new method for the accurate measurement of higher-order frequency response functions of nonlinear structural systems, *Isa Transactions*, 81 (2018) 270-285.
- [11] R. Lin, T. Ng, Applications of higher-order frequency response functions to the detection and damage assessment of general structural systems with breathing cracks, *International Journal of Mechanical Sciences*, 148 (2018) 652-666.
- [12] J.J. Sinou, On the use of non-linear vibrations and the anti-resonances of Higher-Order Frequency Response Functions for crack detection in pipeline beam, *Mechanics Research Communications*, 43 (2012) 87-95.
- [13] L. Chen, L. Yu, Structural Nonlinear Damage Identification Algorithm Based on Time Series ARMA/GARCH Model, *Advances in Structural Engineering*, 16 (2013) 1597-1609.
- [14] J. Li, H. Hao, Z. Chen, Damage identification and optimal sensor placement for structures under unknown traffic-induced vibrations, *Journal of Aerospace Engineering*, 30 (2015) B4015001.
- [15] Y. Xin, H. Hao, J. Li, Time-varying system identification by enhanced empirical wavelet transform based on synchroextracting transform, *Engineering Structures*, 196 (2019) 109313.
- [16] N. Roveri, A. Carcaterra, Damage detection in structures under traveling loads by Hilbert–Huang transform, *Mechanical Systems and Signal Processing*, 28 (2012) 128-144.
- [17] J.P. Amezcua-Sanchez, H. Adeli, Synchrosqueezed wavelet transform-fractality model for locating, detecting, and quantifying damage in smart highrise building structures, *Smart Materials and Structures*, 24 (2015) 065034.
- [18] Z. Nie, H. Hao, H. Ma, Using vibration phase space topology changes for structural

- damage detection, *Structural Health Monitoring: An International Journal*, 11 (2012) 538-557.
- [19] Z. Nie, H. Hao, H. Ma, Structural damage detection based on the reconstructed phase space for reinforced concrete slab: Experimental study, *Journal of Sound and Vibration*, 332 (2013) 1061-1078.
- [20] D.L. Hunt, Application of an enhanced coordinate modal assurance criterion, 10th International modal analysis conference, San Diego, CA, 1992, pp. 66-71.
- [21] M.D. Todd, J.M. Nichols, L.M. Pecora, L.N. Virgin, Vibration based damage assessment utilizing state space geometry changes local attractor variance ratio, *Smart Materials and Structures*, 10 (2001) 1000-1008.
- [22] F. Takens, *Detecting strange attractors in turbulence (Lecture Notes in Mathematics)*, Springer, Berlin, 1981.
- [23] M. Rucka, Damage detection in beams using wavelet transform on higher vibration modes, *Journal of Theoretical and Applied Mechanics*, 49 (2011) 399-417.
- [24] R. Sampaio, N. Maia, J. Silva, Damage detection using the frequency-response-function curvature method, *Journal of Sound and Vibration*, 226 (1999) 1029-1042.
- [25] B. Paul, R.C. George, S.K. Mishra, Phase space interrogation of the empirical response modes for seismically excited structures, *Mechanical Systems and Signal Processing*, 91 (2017) 250-265.
- [26] L. Pamwani, A. Shelke, Damage detection using dissimilarity in phase space topology of dynamic response of structure subjected to shock wave loading, *Journal of Nondestructive Evaluation, Diagnostics and Prognostics of Engineering Systems*, 1 (2018) 041004.
- [27] S. Torkamani, E.A. Butcher, M.D. Todd, G. Park, Hyperchaotic probe for damage identification using nonlinear prediction error, *Mechanical Systems and Signal Processing*, 29 (2012) 457-473.
- [28] S. Kouchaki, S. Sanei, E.L. Arbon, D.-J. Dijk, Tensor based singular spectrum analysis for automatic scoring of sleep EEG, *IEEE Transactions on Neural Systems and Rehabilitation Engineering*, 23 (2014) 1-9.
- [29] H. Jinane, F. Dominique, The Sliding Singular Spectrum Analysis: a Data-Driven Non-Stationary Signal Decomposition Tool, *IEEE Transactions on Signals Processing*, 66 (2017) 1-13.
- [30] S. Xu, H. Hu, L. Ji, P. Wang, Embedding Dimension Selection for Adaptive Singular Spectrum Analysis of EEG Signal, *Sensors*, 18 (2018) 697.
- [31] X. Kong, C. Cai, B. Kong, Damage detection based on transmissibility of a vehicle and bridge coupled system, *Journal of Engineering Mechanics*, 141 (2014) 04014102.
- [32] Y.B. Yang, K.C. Chang, Y.C. Li, Filtering techniques for extracting bridge frequencies from a test vehicle moving over the bridge, *Engineering Structures*, 48 (2013) 353-362.
- [33] J. Li, X. Zhu, S.-s. Law, B. Samali, Drive by Blind Modal Identification with Singular Spectrum Analysis, *Journal of Aerospace Engineering*, 32 (2019) 04019050.
- [34] R. Vautard, M. Ghil, Singular spectrum analysis in nonlinear dynamics, with applications to paleoclimatic time series, *Physica D: Nonlinear Phenomena*, 35 (1989) 395-424.
- [35] Z. Peng, Z. Yang, J. Tu, Genetic Algorithm Based Tikhonov Regularization Method for Displacement Reconstruction, *Journal of Shanghai Jiaotong University (Science)*, 24 (2019) 294-298.
- [36] A.M. Fraser, H.L. Swinney, Independent coordinates for strange attractors from mutual

information, *Physical Review A*, 33 (1986) 1134-1140.

- [37] J.M. Nichols, Structural health monitoring of offshore structures using ambient excitation, *Applied Ocean Research*, 25 (2003) 101-114.
- [38] S. Ørstavik, S. Jaroslav, Reconstruction and cross-prediction in coupled map lattices using spatio-temporal embedding techniques, *Physics Letters*, 247 (1998) 145-160.

CHAPTER 5 DATA DRIVEN STRUCTURAL DAMAGE ASSESSMENT USING PHASE SPACE EMBEDDING AND Koopman OPERATOR UNDER STOCHASTIC EXCITATIONS

ABSTRACT⁴

To address the issue faced by PST based methods for identifying structural damage using high dimensional dynamic responses of structures under stochastic excitations, a novel data driven approach for structural damage assessment based on phase space embedding in conjunction with stochastic Koopman operator, is proposed in this study. Vibration acceleration responses are used to reconstruct the phase space representation of system dynamic attractor using embedding strategy, followed by subspace dynamic mode decomposition (subspace DMD) to estimate the unbiased eigenvalues of the corresponding stochastic Koopman operator. Under the hypothesis that the Koopman operator eigenpairs will vary with structural condition change, the Mahalanobis distance of Koopman operator eigenvalues approximated from healthy state and current testing state is introduced as a DSF to detect structural damage. A planar truss model is adopted in numerical studies to demonstrate the feasibility and applicability of the proposed approach. The robustness of the proposed approach under operational and environmental variations is tested by considering 10% white noise in vibration measurement and six different ambient loading scenarios. Numerical results show that the proposed approach is sensitive to the occurrence and severity of structural damage, and is insensitive to the measurement noise and the variation of stochastic excitation amplitudes. Furthermore, the proposed method is applied to identify damage introduced as the artificially applied settlements of pier in the Z24 benchmark bridge. Results demonstrate that the bridge condition under the reference state and the damage scenarios with different levels of pier settlement are well identified by using the proposed approach with in-field measurement data including different test environment. The defined DSF value can be used to reflect the damage severity in these damage scenarios.

⁴This chapter was published in *Engineering Structures* with the full bibliographic citation as follows: Peng, Z., Li, J., & Hao, H. (2022). Data driven structural damage assessment using phase space embedding and Koopman operator under stochastic excitations. *Engineering Structures*, 255, 113906. <https://doi.org/10.1016/j.engstruct.2022.113906>.

5.1 Introduction

Monitoring infrastructure health condition refers to detecting the structural condition changes by some global or local DSFs extracted from observed vibration responses. In this context, many works have been devoted to deriving features that are sensitive to structural performance degradation, but robust to operational conditions and measurement noise. Comprehensive reviews of vibration based damage detection techniques can be found in Refs. [1, 2]. Without the need to conduct finite element modelling and the requirement of performing model updating, the data driven damage detection methods provide opportunities to assist real-time and long-term condition assessment of large-scale civil engineering structures [3, 4]. Data driven based structural damage detection is usually conducted by statistically comparing the DSFs obtained from possible damage state with those estimated under the reference (healthy) state. However, under certain situations, structures inherently exhibit nonlinearities, owing to the materials with nonlinear constitutive relationship and structural geometric nonlinearity, as well as the damage (crack and bolt loosening, etc.) induced nonlinearity, which result in the presence of nonlinear behavior. This may significantly degrade the performance of using DSFs extracted from modal parameters and its derivatives based on the linear assumption of structures [5, 6] for damage detection. To this end, the ARMA [7, 8], phase space portrait [9], Volterra series [10], autoregressive support vector machines [11], convolutional neural networks and deep learning based techniques [12] have been recently developed to represent the structural nonlinear dynamics with data based models.

In recent years, PST based damage detection methods have received research attention owing to its much higher sensitivity to structural condition change than traditional modal information based damage features, but a significantly less sensitivity to measurement noise. In addition, the nonlinear dynamic behavior can be completely unfolded in phase space with appropriate time delay and embedding dimension parameters [13]. In state-space, a specific mechanical system is deterministic under a steady-state condition. Fortunately, the state-space representation of the dynamic system attractor can be fully reconstructed in phase space using the Taken's embedding theory [14]. Therefore, structural condition changes can be identified by quantifying the PST dissimilarity between the geometric PST under pristine (baseline) and to-be-detected states using DSFs, such as CPST, Mahalanobis distance in phase space trajectory (MDPST) [15, 16], and auto-prediction and cross-prediction errors [17, 18]. More recently, the PST reconstructed by vibration measurements with multiple types of sensors subjected to moving loads has been developed and applied to accurately identify the damage location in bridge structures [19]. Improvement has been made in Ref. [20] by using a single sensor measurement to identify the damage location of a beam subjected to a moving mass. Previous comparative studies shown that the damage sensitivity of PST-based DSFs could be

orders of magnitude higher than that of modal-based DSFs [15, 21]. However, the abovementioned DSFs are extracted from the geometry of low dimensional (usually less than or equal to 3) phase space attractor, which is impractical for structures with high dimensional vibration responses under stochastic excitations. In order to extract DSFs from low-dimensional vibration signals, early attempts were made by applying artificial-made loads with low or narrow band-limited frequency range, i.e. chaotic excitation, to obtain lower-dimensional structural responses. This limited its applicability in practical applications [16, 22]. More recently, signal decomposition techniques, including (but not limited to) EMD, independent component analysis and SSA, have been developed to obtain lower dimensional signal components from high dimensional vibration responses for phase space reconstruction [16, 23]. These signal decomposition techniques successively improved the feasibility of using PST-based methods for structural damage diagnosis to some extent. It is worth noting that the particular signal decomposition method and the appropriate number of components should be carefully selected according to the characteristics of signals. Structural responses under operational and ambient excitations are usually high dimensional. Under this circumstance, the traditional PST based method using low dimensional responses may not be applicable and able to provide reliable damage detection results. For civil engineering structures under operational conditions, the unmeasured ambient excitations are usually considered as stochastic excitations, rather than other artificially-generated deterministic loads, such as multi-frequency sinusoidal wave excitation or chaotic excitation [24, 25]. Therefore, extending the feasibility and accuracy of PST-based methods to monitor and assess the structural performance under operational conditions is significant and remains largely under-explored. In particular, the main obstacle is how to capture the manifold topology of the original attractor with vibration signals subjected to stochastic excitations.

The Koopman operator is a linear but infinite-dimensional operator that can fully capture the dynamic behavior of a nonlinear system through the linear evolution of functions on the state space [26]. Although the concept of Koopman operator was first proposed several decades ago [27], few relevant publications were found in literature, partly owing to the lack of efficient methods in obtaining the Koopman operator itself for a dynamic system without any prior knowledge. Until recently, Schmid [28] proposed the data driven dynamic mode decomposition (DMD) algorithm and proven that the eigenvalues and eigenvectors extracted from DMD is a numerical approximation of Koopman operator. The key strength of DMD is its data driven nature, which does not rely on any prior assumption except using the system responses observed over time. More recently, Tu et al. [29] improved the computational efficiency of DMD algorithm and developed to its current state-of-the-art form. In the last decade, several improvements have been made to enhance the efficiency and accuracy of using

standard DMD for numerically approximating the Koopman operator, the Koopman eigenvalues and eigenvectors. For instance, noise-aware total DMD was developed to eliminate the noise-induced bias description of using dynamic system observations contaminated by noise [30]. For an external force driven system, DMD with control (DMDc) was developed to incorporate the effect of external excitation to extract a low order model from the underlying high dimensional system [31]. Furthermore, the stochastic Hankel DMD and subspace DMD were developed to obtain an accurate estimation of Koopman operator from the random dynamic system (RDS) with observation noise [32, 33]. As a result, Koopman theory and DMD have been recognized as powerful tools for analysing the dynamics of complex nonlinear systems across multiple fields, including complex fluid flows process, computer vision, neuroscience and trends forecasting [34, 35]. Mathematically, Koopman operator and DMD can be viewed as a mapping function acting on the state-space, which builds up a linear representation for the past and current observations of the underlying nonlinear system [36]. For a time-invariant system or linear structures, Koopman operator and DMD enable us to capture the long-term dynamics of observables that appear after the fast unstable transients, and its eigenvalues, eigenfunction and mode will be constant if the system parameters are not changed [34].

This chapter proposes a data driven structural damage assessment approach using phase space embedding strategy in conjunction with Koopman operator under stochastic excitations. The proposed approach consists of three main steps. Firstly, structural vibration responses from a single channel are projected to the dynamic attractor of high dimensional system in phase space using embedding strategy. The second step connects the consecutive embedded Hankel matrix with a mapping matrix, that is, Koopman operator, and obtains the eigenvalues approximation of Koopman operator with subspace DMD. Then, the Mahalanobis distance between the eigenvalue vectors approximated under intact and current testing states is served as DSF to detect the structural condition change. Numerical studies on a truss bridge model are conducted to verify the feasibility and accuracy of the proposed approach. Experimental validations using measurement data from in-field bridge tests are performed to further demonstrate the performance of using the proposed approach for data driven structural damage detection under stochastic ambient excitations.

The remaining sections of this chapter are organised as follows. Section 2 provides a theoretical derivation of embedding alternative view of time-invariant stochastic Koopman operator through single channel measurements. The subspace DMD with the awareness of process noise and observation noise is introduced to obtain the unbiased approximation of Koopman operator eigenvalues. Then, the DSF is extracted from the Mahalanobis distance of the estimated eigenvalues. Section 3 demonstrates the applicability and accuracy of using the

proposed approach for damage detection in a numerical truss model. In Section 4, the proposed approach is applied to evaluate the condition of the Z24 benchmark bridge with different levels of pier settlement. Section 5 provides conclusions of this study, discussions on the limitation and recommendations for future work.

5.2 Theoretical Background and Development

5.2.1 System dynamic attractor reconstruction with phase space embedding strategy

The responses of a discrete-time nonlinear dynamic system can be represented by the following first-order differential equation

$$\dot{\mathbf{x}} = \mathbf{f}(\mathbf{x}, t) \quad \mathbf{x} \in R^d \quad (5.1)$$

where $\mathbf{f}(\cdot)$ is a general, possibly nonlinear and mapping function determined by the underlying system, \mathbf{x} is the state vector with d variables. For a mechanical dynamic system, the state vector \mathbf{x} consists of displacement and velocity. Considering a single degree of freedom (DOF) mechanical system with a cubic nonlinear term (referred to as Duffing-Homels nonlinear oscillator), we have

$$\ddot{x}(t) + c\dot{x}(t) - \alpha x(t) + \beta x^3(t) = F\cos(\omega t) \quad (5.2)$$

in which c denotes the damping coefficient, α and β represent the linear and nonlinear stiffness coefficients, respectively. $F\cos(\omega t)$ is the external driving force with the amplitude F and circular frequency ω . With state vector $\mathbf{x} = [x_1, x_2]^T$, the state space representation of Eq. (5.2) can be expressed as the following first-order equation

$$\begin{cases} \dot{x}_1 = x_2 \\ \dot{x}_2 = F\cos(\omega t) + \alpha x_1 - \beta x_1^3 - c x_2 \end{cases} \quad (5.3)$$

Without loss of generality, the Duffing oscillator parameters are preset as $c = 0.1$, $\alpha = 1$, $\beta = 0.25$, $F = 1.5$ and $\omega = 2$. The fourth-order Runge-Kutta method with a time step of 0.01 s is adopted to obtain the numerical solution of Eq. (5.3). Figure 5-1(a) and Figure 5-1(b) show the displacement time series x_1 and the trajectory of state vector $\mathbf{x} = [x_1, x_2]^T$ in phase space, respectively. When deterministic excitation is applied to a mechanical system, the geometric depiction (also referred to as system dynamic attractor) of state vector is unique under a steady-state condition [37]. The resulting attractor topology will change once the system parameters are slightly disturbed. The manifold topology of any underlying dynamic system can be completely unfolded in phase space to have a better understanding of the state evolution process, when all the state variables are measurable. However, some variables are difficult or even impossible to be accurately observed under actual operations. For instance, owing to the

difficulty to find a fixed reference point, direct measurement of dynamic displacement response is uncommon in bridge health monitoring practices. Fortunately, the original attractor traced out by state vector with all variables can be fully reconstructed with a single variable embedded as follows

$$\mathbf{X}_1^m = [x_1 \ x_2 \ \dots \ x_m] = \begin{bmatrix} x(1) & x(1 + \tau) & \dots & x(1 + (m - 1)\tau) \\ x(1 + \tau) & x(1 + 2\tau) & \dots & x(1 + m\tau) \\ \vdots & \vdots & \ddots & \vdots \\ x(1 + (n - 1)\tau) & x(1 + n\tau) & \dots & x(1 + (m + n - 2)\tau) \end{bmatrix} \quad (5.4)$$

where m and n represent the embedding dimension and the number of samples in each column of the embedding matrix, respectively. Typically, $n \gg m$. τ is the time delay. By introducing an embedding procedure, the single channel vibration response measurement is formed as a higher dimensional attractor in the phase space with more features unfolded [38]. It should be noted that the single response variable in Eq. (5.4) could be displacement or acceleration. The function of embedding strategy is to elevate the single channel response signal to a high dimensional space, where the original dynamic attractor of system traced out by full-state vectors can be fully unfolded by using partial state variable. This is important for civil engineering applications, since the displacement and velocity responses are difficult or expensive to be measured. Figure 5-1 shows an example displacement response, its phase space and reconstructed attractor. For comparison purpose, the attractor reconstructed in the phase space with $m=2$, $\tau=25$ and $n=8000$ is plotted in Figure 5-1(c). Actually, the appropriate selection of embedding dimension and time delay parameters to fully uncover the original attractor is associated with the complexity of the underlying dynamic system. The optimal selection of these parameters is further discussed in Sections 3 and 4. As can be found in Figure 5-1(b) and Figure 5-1(c), apart from that the direction of the attractor is changed in the embedding coordinate, the manifold topology of the original attractor is well reconstructed by using Taken's embedding strategy. For structures under deterministic excitations, the structural condition change can be detected by comparing the dissimilarity between the attractor trajectories reconstructed from vibration responses measured from healthy and damaged states. Nevertheless, most of the up-to-date PST-based structural damage detection methods are only applicable to numerical and experimental structures under user-defined deterministic lower-dimensional loads, which could not meet the requirement of practical SHM applications of civil engineering structures subjected to stochastic ambient excitations. Therefore, extending the feasibility and applicability of PST-based techniques to monitor and assess the structural performance under operational conditions should be further studied.

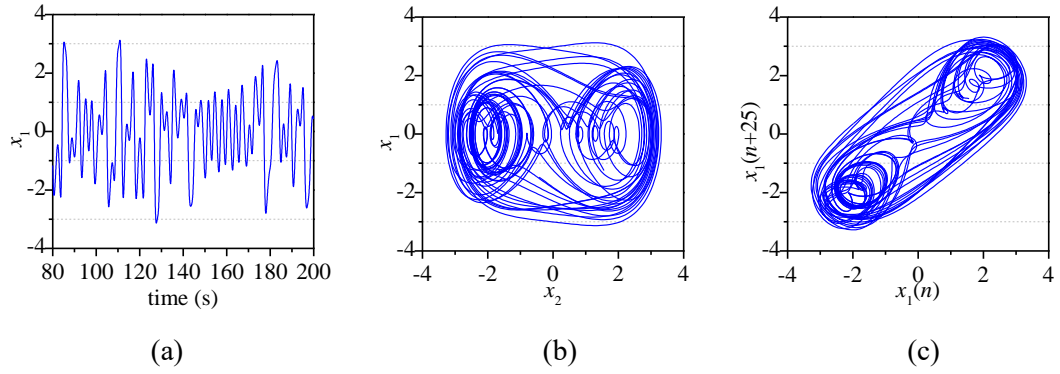


Figure 5-1. An example response of Duffing oscillator: (a) Time series displacement x_1 ; (b) The phase space attractor plotted with state vector \mathbf{x} ; (c) Attractor reconstructed from x_1 with embedding strategy.

5.2.2 Embedding alternative view of data driven Koopman operator

The evolution of a deterministic complex system with unknown underlying dynamic in the phase space can be reorganized as follows

$$\mathbf{x}_{t+1} = f(\mathbf{x}_t), \quad \mathbf{x}_t \in M \quad (5.5)$$

with a measurable map $f: M \rightarrow M$ and a subscript time index $t \in T = \{0\} \cup \mathcal{N}$.

The Koopman operator defines a set of scalar-valued functions (also referred to as observables) $g: M \rightarrow \mathbb{R}^m$ and seeks for the infinite-dimensional linear expression of finite-dimensional nonlinear dynamic system in Hilbert space. The Koopman operator acting on the pre-determined set of observables in Hilbert space is defined as

$$\mathbf{K}g(\mathbf{x}_t) \stackrel{\text{def}}{=} g[f(\mathbf{x}_t)] \quad (5.6)$$

The schematic diagram in Figure 5-2 illustrates the framework of Koopman operator. Figure 5-2 describes how the phase space representation of collected time series from numerical, experimental or real vibration measurements is mapped by the pre-determined set of observables function g . This also indicates the procedure of Koopman operator acting on \mathbb{R}^m propagating the observable y_t to y_{t+1} .

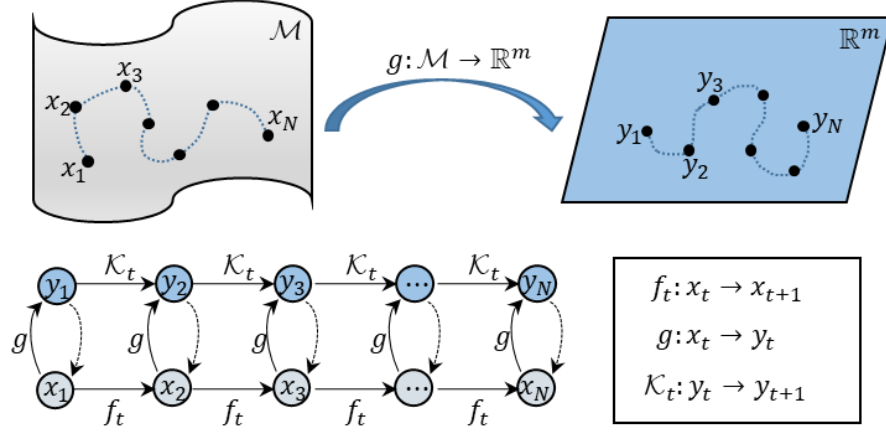


Figure 5-2. Schematic diagram of Koopman operator.

In practical applications, the observable functions need to be manually selected from a library of nonlinear observable dictionary according to the prior knowledge about the nonlinearity sources of the underlying dynamic system, requiring domain-specific knowledge and painstaking parameter tuning [39]. Under this circumstance, neural networks and deep learning techniques that aimed at minimizing the reconstruction residuals were recently found in literature to automatically select the appropriate set of observable functions [40]. DMD is a full data-driven, equation-free alternative algorithm that approximates the Koopman operator from system output only. The dynamic modes and eigenvalues extracted from DMD converge to its corresponding ones obtained from Koopman operator with the assumption of ergodicity, as theoretically demonstrated in Refs. [29, 41]. The algorithm of DMD and the procedure to identify the dynamic modes and eigenvalues of the underlying dynamic system, are briefly reviewed as follows for the completeness of this chapter.

Recalling the Hankel matrix \mathbf{X}_1^m with $n \times m$ elements defined in Eq. (5.4), it can be justified that a mapping matrix \mathbf{A} (a numerical approximation of Koopman operator) exists between consecutive lagged vectors [32]. Those vector spaces span the Krylov subspace

$$\begin{cases} \mathbf{X}_1^m = [\mathbf{x}_1 \ \mathbf{x}_2 \ \mathbf{x}_3 \ \cdots \ \mathbf{x}_m] = [\mathbf{x}_1 \ \mathbf{A}\mathbf{x}_1 \ \mathbf{A}^2\mathbf{x}_1 \ \cdots \ \mathbf{A}^{m-1}\mathbf{x}_1] \\ \mathbf{X}_2^{m+1} = [\mathbf{x}_2 \ \mathbf{x}_3 \ \mathbf{x}_4 \ \cdots \ \mathbf{x}_{m+1}] = [\mathbf{x}_2 \ \mathbf{A}\mathbf{x}_2 \ \mathbf{A}^2\mathbf{x}_2 \ \cdots \ \mathbf{A}^{m-1}\mathbf{x}_2] \end{cases} \quad (5.7)$$

where \mathbf{X}_2^{m+1} denotes the time-shift Hankel matrix. Computationally, the DMD algorithm finds the best-fit operator \mathbf{A} to minimize $\sum_{i=1}^m \|\mathbf{x}_{i+1} - \mathbf{A}\mathbf{x}_i\|$, so that $\mathbf{X}_2^{m+1} \approx \mathbf{A}\mathbf{X}_1^m$. The dimensions of both \mathbf{X}_1^m and \mathbf{X}_2^{m+1} matrices are $n \times m$. Therefore, the size of the mapping matrix \mathbf{A} would be $n \times n$. Since $n \gg m$, it will be computational-intensive to estimate \mathbf{A} directly through $\mathbf{A} = \mathbf{X}_2^{m+1}(\mathbf{X}_1^m)^\dagger$, where $(\mathbf{X}_1^m)^\dagger$ is the Moore–Penrose pseudo-inverse of \mathbf{X}_1^m . Instead, a much more efficient DMD algorithm, termed as standard DMD, developed by Tu et al. [29] has gained wide attention. The Pseudo-code of the standard DMD is detailed in Algorithm 1.

Algorithm 1: standard DMD

Input: Hankel matrix \mathbf{X}_1^m , time-shifted Hankel matrix \mathbf{X}_2^{m+1} and target truncation rank r .

Output: DMD eigenvalues λ , eigenvectors ω and dynamic mode Φ

1: **procedure** standard DMD ($\mathbf{X}_1^m, \mathbf{X}_2^{m+1}, r$)

2: $[\mathbf{U}_{1:r}, \mathbf{S}_{1:r}, \mathbf{V}_{1:r}] \leftarrow$ compact SVD(\mathbf{X}_1^m, r) $> \mathbf{U}_{1:r} \in \mathbf{X}^{n \times r}, \mathbf{S}_{1:r} \in \mathbf{X}^{r \times r}, \mathbf{V}_{1:r} \in \mathbf{X}^{m \times r}, r = \text{rank}(\mathbf{X}_1^m)$

3: $\tilde{\mathbf{A}} \leftarrow \mathbf{U}_{1:r}^* \mathbf{X}_2^{m+1} \mathbf{V}_{1:r} \mathbf{S}_{1:r}^{-1}$ $> \tilde{\mathbf{A}} \in \mathbf{X}^{r \times r}$ is a low-rank with the same eigenvalues to \mathbf{A}

4: $[\tilde{\omega}, \tilde{\lambda}] \leftarrow \text{EIG}(\tilde{\mathbf{A}})$ $>$ eigenvalues $\tilde{\lambda}$ and eigenvector $\tilde{\omega}$

5: $\Phi \leftarrow \mathbf{X}_2^{m+1} \mathbf{V}_{1:r} \mathbf{S}_{1:r}^{-1} \tilde{\omega}$

6: **end procedure**

Algorithm 1 provides accurate eigenvalues approximation for deterministic dynamic systems without external excitations. It is noted that the originality and contribution of this study is to extend the feasibility and applicability of PST based structural damage assessment methods to the scenarios with structures subjected to stochastic loads. For a random dynamical system (RDS) in engineering applications, it should be noted that the process noise and the measurement noise may yield bias eigenvalue estimation using the standard DMD method [30, 42].

The Koopman operator is suitable to construct a linear representation of deterministic nonlinear dynamic systems. In this study, a stochastic Koopman operator is introduced with consideration of process noise and measurement noise. The stochastic Koopman operator extends the feasibility of Koopman operator in generating a linear representation for random dynamic systems, which is better for the analysis of structural vibration responses from stochastic excitations. A subspace DMD algorithm is applied to obtain the unbiased estimation of the stochastic Koopman operator eigenvalues from the RDS responses [32]. A discrete RDS is defined as

$$\mathbf{x}_{t+1} = f_{\Omega}(\mathbf{x}_t, \xi_t), \quad \mathbf{x}_t \in M, \quad \xi \in \Omega \quad (5.8)$$

where $(\Omega, \Sigma_{\Omega}, \mu_{\Omega})$ is a probability space of process noise, ξ_t is a white noise series and is assumed to be independent from \mathbf{x}_t . Similar to Eq. (5.6), the evolution of the RDS can be described using the following stochastic form of Koopman operator

$$\mathbf{K}_{\Omega} g(\mathbf{x}_t) \stackrel{\text{def}}{=} E_{\Omega}[g(f_{\Omega}(\mathbf{x}_t, \xi_t))] \quad (5.9)$$

where E_{Ω} represents the mathematical expectation in space Ω . Setting \mathbf{A}_{Ω} be the finite-

dimension restriction of infinite-dimension invariant stochastic Koopman operator K_Ω , the one step evolution of RDS mapped by \mathbf{A}_Ω can be written as

$$g(\mathbf{x}_{t+1}) = \mathbf{A}_\Omega g(\mathbf{x}_t) + \mathbf{e}_t \quad (5.10)$$

where \mathbf{e}_t represents the process noise owing to the mapping of $g(\mathbf{x}_t)$ to future observation $g(\mathbf{x}_{t+1})$ with finite-dimension operator \mathbf{A}_Ω . The expression of process noise corresponding to the time instant t is

$$\mathbf{e}_t \stackrel{\text{def}}{=} g(f_\Omega(\mathbf{x}_t, \xi_t)) - E_\Omega[g(f_\Omega(\mathbf{x}_t, \xi_t))] \quad (5.11)$$

Further, for a RDS with current state vector \mathbf{x}_t , the evolution of observation of τ steps in the future with the accumulation of process noise satisfies

$$g(\mathbf{x}_{t+\tau}) = \mathbf{A}_\Omega^\tau g(\mathbf{x}_t) + \sum_{i=t}^{t+\tau-1} \mathbf{A}_\Omega^{i-t} \mathbf{e}_i \quad (5.12)$$

Besides the process noise, the observation noise-induced bias is considered as

$$h(\mathbf{x}_t) = g(\mathbf{x}_t) + \mathbf{w}_t \quad (5.13)$$

where $\mathbf{w}_t: S \in X^n$ is assumed to be a uncorrelated Gaussian stationary white noise vector with zero mean and covariance of \mathbf{Q} . $h(\mathbf{x}_t) = g(\mathbf{x}_t)$ when the observation noise is absent.

Similar to the standard DMD, a numerical method called subspace DMD with the considerations of process noise and observation noise developed in Ref. [32], is introduced to capture the unbiased finite-dimension stochastic Koopman operator \mathbf{A}_Ω . For the brevity and clarity of the presentation of this study, the subsequent content of this subsection focuses on introducing the implementation of the subspace DMD. The proofs of using subspace DMD in obtaining unbiased stochastic Koopman operator from process noise and observation noise is attached in the Appendix. The derivation provided in the Appendix I is a supplement of using subspace DMD in obtaining unbiased stochastic Koopman operator with consideration of process noise and observation noise, based on the existing study [32].

To account for the effects of the process noise and observation noise, the Hankel matrix in Eq. (5.7) is rewritten as follows

$$\mathbf{Y}_1^m = [h(\mathbf{x}_1) h(\mathbf{x}_2) h(\mathbf{x}_3) \cdots h(\mathbf{x}_m)] \in X^{n \times m} \quad (5.14)$$

Defining two augmented observation matrices $\mathbf{Y}_p^{aug} = [\mathbf{Y}_1^m; \mathbf{Y}_2^{m+1}]$ and $\mathbf{Y}_f^{aug} = [\mathbf{Y}_3^{m+2}; \mathbf{Y}_4^{m+3}] \in X^{2n \times m}$, the compact SVD of \mathbf{Y}_p with the truncation rank $r = \text{rank}(\mathbf{Y}_p)$ yields

$$\mathbf{Y}_p^{aug} = \mathbf{U}_{1:r} \mathbf{S}_{1:r} \mathbf{V}_{1:r}^* \quad (5.15)$$

where $\mathbf{U}_{1:r} \in X^{2n \times r}$, $\mathbf{S}_{1:r} \in X^{r \times r}$ and $\mathbf{V}_{1:r} \in X^{m \times r}$ denote the left-singular vectors, non-zero

singular values and right-singular vectors of \mathbf{Y}_p , respectively. $\mathbf{V}_{1:r}^*$ is the conjugate transpose of $\mathbf{V}_{1:r}$.

With $\mathbf{O}^{aug} = \mathbf{Y}_f^{aug} (\mathbf{Y}_p^{aug})^* [\mathbf{Y}_p^{aug} (\mathbf{Y}_p^{aug})^*]^{-1} \mathbf{Y}_p^{aug} = \mathbf{Y}_f^{aug} \mathbf{V}_{1:r} \mathbf{V}_{1:r}^* \in X^{2n \times r}$, the compact SVD of \mathbf{O}^{aug} with the truncation rank $q = \text{rank}(\mathbf{O}^{aug})$ is expressed as

$$\mathbf{O}^{aug} = \mathbf{U}_{1:q} \mathbf{S}_{1:q} \mathbf{V}_{1:q}^* = [\mathbf{U}_{1:q1}; \mathbf{U}_{1:q2}] \mathbf{S}_{1:q} \mathbf{V}_{1:q}^* \quad (5.16)$$

where $\mathbf{U}_{1:q1}$ and $\mathbf{U}_{1:q2} \in X^{n \times q}$ represent the first and last n rows of $\mathbf{U}_{1:q}$, respectively; and we have $\mathbf{S}_{1:q} \in X^{q \times q}$ and $\mathbf{V}_{1:q} \in X^{m \times q}$. Further conducting the compact SVD on $\mathbf{U}_{1:q1}$ with the truncation rank $\tilde{r} = \text{rank}(\mathbf{U}_{1:q1})$, we have

$$\mathbf{U}_{1:q1} = \tilde{\mathbf{U}}_{1:\tilde{r}} \tilde{\mathbf{S}}_{1:\tilde{r}} \tilde{\mathbf{V}}_{1:\tilde{r}}^* \quad (5.17)$$

Then, the stochastic Koopman operator \mathbf{A}_Ω can be approximated as

$$\mathbf{A}_\Omega \stackrel{\text{def}}{=} \mathbf{U}_{1:q2} \mathbf{U}_{1:q1}^\dagger = \tilde{\mathbf{U}}_{1:\tilde{r}}^* \mathbf{U}_{1:q2} \tilde{\mathbf{V}}_{1:\tilde{r}} \tilde{\mathbf{S}}_{1:\tilde{r}}^{-1} \quad (5.18)$$

Hereafter, the eigenvalues, eigenvectors and dynamic modes of Koopman operator \mathbf{A}_Ω can be calculated by the same procedures introduced in Steps 4-5 of standard DMD as described in Algorithm 1. Takeishi et al. [32] compared the subspace DMD with standard DMD, total-least-square DMD and optimized DMD (opt-DMD) to demonstrate the superiority of using subspace DMD in accurately estimating the eigenvalues of several numerical examples corrupted by process noise and observation noise. The pseudo-code of subspace DMD based on the procedures introduced in Eqs. (14)-(18) is detailed in Algorithm 2.

Algorithm 2: subspace DMD

Input: augmented Hankel matrix $\mathbf{Y}_p^{aug} = [\mathbf{Y}_1^m; \mathbf{Y}_2^{m+1}]$, $\mathbf{Y}_f^{aug} = [\mathbf{Y}_3^{m+2}; \mathbf{Y}_4^{m+3}]$.

Output: DMD eigenvalues $\tilde{\lambda}_\Omega$, eigenvectors $\tilde{\omega}_\Omega$ and corresponding dynamic mode Φ_Ω .

1: **procedure** subspace DMD ($\mathbf{Y}_p^{aug}, \mathbf{Y}_f^{aug}, r$)

2: $[\mathbf{U}_{1:r}, \mathbf{S}_{1:r}, \mathbf{V}_{1:r}] \leftarrow \text{SVD}(\mathbf{Y}_p^{aug}, r)$ > $\mathbf{U}_{1:r} \in \mathbf{X}^{2n \times r}, \mathbf{S}_{1:r} \in \mathbf{X}^{r \times r}, \mathbf{V}_{1:r} \in \mathbf{X}^{m \times r}, r = \text{rank}(\mathbf{Y}_p^{aug})$

3: $\mathbf{O}^{aug} \leftarrow \mathbf{Y}_f^{aug} \mathbf{V}_{1:r} \mathbf{V}_{1:r}^*$ > $\mathbf{O}^{aug} \in \mathbf{X}^{2n \times r}$

4: $[\mathbf{U}_{1:q1}; \mathbf{U}_{1:q2}] \mathbf{S}_{1:q} \mathbf{V}_{1:q}^* \leftarrow \text{SVD}(\mathbf{O}^{aug}, q)$ > $\mathbf{U}_{1:q1}, \mathbf{U}_{1:q2} \in \mathbf{X}^{n \times q}, \mathbf{S}_{1:q} \in \mathbf{X}^{q \times q}, \mathbf{V}_{1:q} \in \mathbf{X}^{m \times q}$

5: $[\tilde{\mathbf{U}}_{1:\tilde{r}}, \tilde{\mathbf{S}}_{1:\tilde{r}}, \tilde{\mathbf{V}}_{1:\tilde{r}}] \leftarrow \text{SVD}(\mathbf{U}_{1:q1}, \tilde{r})$ > $\tilde{\mathbf{U}}_{1:\tilde{r}} \in \mathbf{X}^{n \times \tilde{r}}, \tilde{\mathbf{S}}_{1:\tilde{r}} \in \mathbf{X}^{\tilde{r} \times \tilde{r}}, \tilde{\mathbf{V}}_{1:\tilde{r}} \in \mathbf{X}^{q \times \tilde{r}}, \tilde{r} = \text{rank}(\mathbf{U}_{1:q1})$

6: $\mathbf{A}_\Omega \stackrel{\text{def}}{=} \tilde{\mathbf{U}}_{1:\tilde{r}}^* \mathbf{U}_{1:q2} \tilde{\mathbf{V}}_{1:\tilde{r}} \tilde{\mathbf{S}}_{1:\tilde{r}}^{-1}$ > \mathbf{A}_Ω is the stochastic Koopman operator

7: $[\tilde{\omega}_\Omega, \tilde{\lambda}_\Omega] \leftarrow \text{EIG}(\mathbf{A}_\Omega)$ > eigenvalues $\tilde{\lambda}$ and eigenvector $\tilde{\omega}$

8: $\Phi_\Omega \leftarrow \mathbf{U}_{1:q2} \tilde{\mathbf{V}}_{1:\tilde{r}} \tilde{\mathbf{S}}_{1:\tilde{r}}^{-1} \tilde{\omega}_\Omega$

9: **end procedure**

5.2.3 DSF extraction

With the subspace DMD algorithm described in Section 2.2, the eigenvalues and eigenvectors of stochastic Koopman operator can be directly estimated from measured system output responses. For a time-invariant system, the eigenvalues of Koopman operator will be constant when the state of dynamic system is not changed. In this study, the Mahalanobis distance is served as DSF to quantify damage level based on the distance between the eigenvectors obtained from a baseline state and current testing state. From the statistical perspective, the Mahalanobis distance is expressed as

$$d_M \left(\text{vec}(\tilde{\lambda}_{\Omega(\text{test})})^i \right) = \sqrt{\text{vec}\{(\tilde{\lambda}_{\Omega(\text{test})})^i - \mu((\tilde{\lambda}_{\Omega(\text{ref})})\})^T [\mathbf{C}_{\text{ref}}]^{-1} \text{vec}\{(\tilde{\lambda}_{\Omega(\text{test})})^i - \mu((\tilde{\lambda}_{\Omega(\text{ref})})\})\}} \quad (5.19)$$

where $\text{vec}(\cdot)$ is a vectorization operator. For example, $\text{vec}(\tilde{\lambda}_\Omega) = \{\tilde{\lambda}_\Omega^1, \tilde{\lambda}_\Omega^2, \tilde{\lambda}_\Omega^3, \dots, \tilde{\lambda}_\Omega^n\}^T$ is a multivariate vector, in which $\tilde{\lambda}_\Omega^i$ denotes the i -th eigenvalue. The subscripts ‘test’ and ‘ref’ represent the statistical samples under the testing and reference (healthy) states, respectively, $\mu((\tilde{\lambda}_{\Omega(\text{ref})})\))$ and \mathbf{C}_{ref} denote the mean and covariance of eigenvalues matrix under the reference state, respectively. $(\tilde{\lambda}_{\Omega(\text{test})})^i$ is the i -th eigenvalue vector sample obtained from acceleration responses under the testing state.

For a better understanding of the procedures, the flowchart of the proposed structural damage assessment approach is summarised in Figure 5-3. Numerical and experimental verifications are presented in the following sections to demonstrate the accuracy and effectiveness of using the proposed approach for structural damage detection.

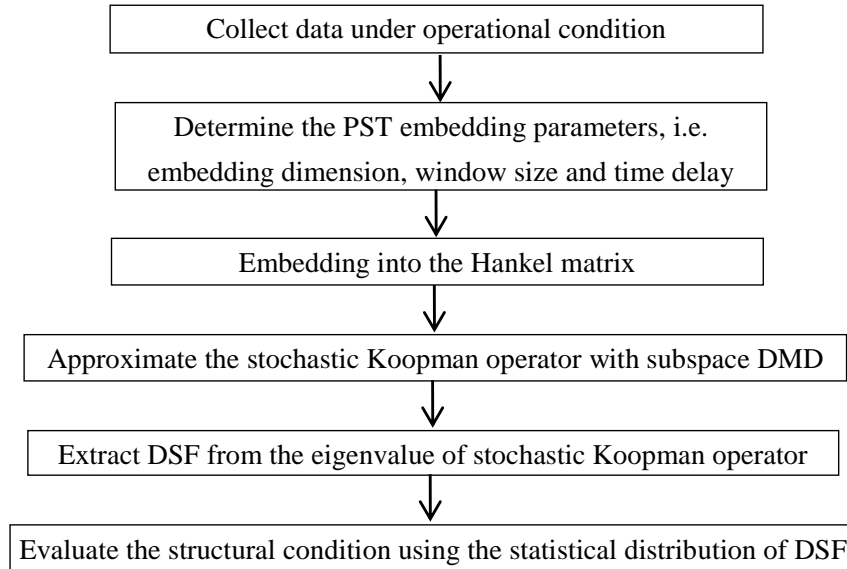


Figure 5-3. The flowchart of the proposed structural damage assessment approach.

In this study, the contribution in methodology development lies on combining the phase space embedding and stochastic Koopman operator to extend the feasibility and accuracy of using PST-based methods for monitoring and assessing the structural performance under operational conditions. Different from the stochastic Koopman operator developed in Ref. [32] using the full-state variables as input, the Hankel matrix reconstructed from phase space embedding is used as the input to Algorithm 2. This means that only partial structural vibration responses are required for obtaining the stochastic Koopman operation. For example, only acceleration responses from a single location is required in this study. The damage feature extracted from the proposed method is sensitive to structural damage, but not sensitive to the measurement noise, stochastic excitation levels and environmental conditions.

5.3 Numerical verifications

5.3.1 FE model description

In this section, the feasibility and accuracy of using the proposed approach with phase space embedding strategy and Koopman operator for damage assessment of structures under

stochastic excitations, are studied. Numerical studies are conducted on a simply supported sixty-one elements planar truss structure subjected to stochastic excitations. As shown in Figure 5-4, the lengths of the horizontal and vertical bar elements are 0.58 m and 0.38 m, respectively. The external and internal radii of circular-shape bars are 18 mm and 12 mm, respectively. Other mechanical parameters, e.g., Young’s modulus, density and Poisson’s ratio are detailed in Figure 5-4. Three severities of single structural damage are simulated by applying 5%, 10% and 15% stiffness degradations in #22 element, marked with a red circle in Figure 5-4. The vertical acceleration responses of node 6 (5/16 span) subjected to stochastic excitations applied in the vertical direction of node 24 are obtained from the finite element analysis with a sampling rate of 400 Hz. Table 5-1 lists the first five natural frequencies of this planar truss structure corresponding to different structural condition states. It can be found that the modal frequencies have been slightly changed with the increasing stiffness reduction in element #22. Owing to the high statically indeterminate characteristic of this truss structure, minor stiffness reduction in a single bar element will not cause a significant influence on the global vibration characteristics. Very minor reductions are observed in the natural frequencies as listed in Table 5-1. These results indicate that modal information based index, e.g. natural frequencies, is not sensitive to the local damage of the truss structure, which motivates the development of damage features that are more sensitive to structural minor damage.

Table 5-1. The first five order natural frequencies of planar truss structure

Structural condition	Modal frequency (Hz)				
	Mode 1	Mode 2	Mode 3	Mode 4	Mode 5
Intact state	12.00	32.15	64.05	89.75	115.80
5% stiffness reduction	12.00	32.15	63.75	89.40	115.80
10% stiffness reduction	12.00	32.05	63.75	89.40	115.10
15% stiffness reduction	11.90	32.05	63.75	89.40	115.10

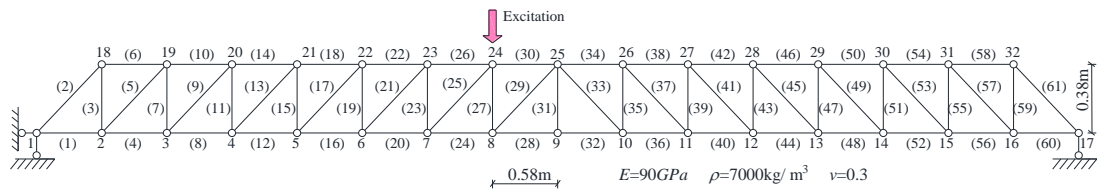


Figure 5-4. Sixty-one elements planar truss structure.

For most data driven damage assessment methods that do not involve the system physical parameters identification process, the measurement noise and the variations of environmental

conditions, including loading properties, temperature and humidity effects, may degrade the damage detection performance to some extent. Therefore, a desirable and effective method should be sensitive to minor structural damage while insensitive to the abovementioned influence factors. In this study, the measurement noise is considered by adding 10% normally distributed white noise to the calculated acceleration response as

$$\ddot{\mathbf{x}}_{measured} = \ddot{\mathbf{x}}_{calculated} + 10\% \times std(\ddot{\mathbf{x}}_{calculated}) \times \mathbf{noise} \quad (5.20)$$

where $\ddot{\mathbf{x}}_{measured}$ and $\ddot{\mathbf{x}}_{calculated}$ represent the measured response with noise effect and the calculated acceleration responses from the numerical finite element analysis, respectively; $std(\ddot{\mathbf{x}}_{calculated})$ and \mathbf{noise} represent respectively the standard deviation of calculated acceleration response and a zero mean and unit variance random measurement white noise vector with the same length as $\ddot{\mathbf{x}}_{calculated}$.

In this study, to investigate the effect of different types of applied stochastic excitations on the effectiveness and performance of the proposed approach, white noise and pink noise with different excitation levels are applied on the structure before and after damage. Table 5-2 lists six loading scenarios considered in this study to simulate the loading effects with different noises. It should be noted that ‘WN’ and ‘PN’ represent white noise excitation and pink noise excitation, respectively; ‘std1’ and ‘std2’ represent that the standard deviations of applied excitations are 1 m/s² and 2 m/s², respectively. For example, PN-std2 denotes pink noise excitation with an excitation amplitude of 2.0 m/s². In Scenarios 1 and 2, white noise of different levels are assumed as the ambient excitations before and after damage. Different excitation level is obtained by applying a scaling factor to the generated stochastic excitation with zero mean value and unit standard deviation. It should be noted that besides the excitation amplitude, the time histories of applied stochastic excitations before and after damage are also different because they are independently generated following the assumed statistical distributions. In Scenario 3, both the white noise excitations are applied on the structure under the healthy and damaged states, but the excitation amplitudes and standard deviations are different. In Scenarios 4 and 5, pink noise of different levels are assumed as the excitations before and after damage. In Scenario 6, the pink noise excitations of different amplitudes are used to excite the healthy and damaged states. These scenarios are assumed to simulate the realistic situation in practical applications with different types of excitations and different excitation levels before and after damage.

Table 5-2. The excitation type and level of each loading scenario

Loading and structural condition	Scenario 1	Scenario 2	Scenario 3	Scenario 4	Scenario 5	Scenario 6
Healthy state	WN-std1	WN-std2	WN-std1	PN-std1	PN-std2	PN-std1
Damage state	WN-std1	WN-std2	WN-std2	PN-std1	PN-std2	PN-std2

5.3.2 Parameters determination and damage detection results

From the formulation of Hankel matrix in Eq. (5.4), the first step of the proposed approach is to reconstruct the Hankel matrix from a single-channel acceleration response with suitable embedding dimension m , time lag τ and window size n . Typically, the optimal embedding dimension is related to the frequency components as well as the noise level [43]. The noise presented in the vibration response is usually associated with the relatively small singular values, after performing SVD. The global attractor of the dynamic system cannot be fully unfolded in the phase space when insufficient dimension m is considered. In literature, SVD technique [21] and false nearest neighbors (FNN) method [13] have been frequently used for the optimal choice of embedding dimension m . The former approach is considered in this study to find an appropriate embedding dimension. In Figure 5-5, the descending singular value calculated from the vertical acceleration responses of node 6 contaminated by 10% white noise are plotted against different dimension m . The slope of decreasing trend tends to be steady when $m \geq 22$. Therefore, it is selected in this study that a suitable embedding dimension for the target structure is equal to 24. For structures with high dimensional responses ($m=24$), the conventional DSFs, e.g. CPST and MDPST extracted from lower dimensional ($m \leq 3$) PST, are not capable of sensitively alarming structural condition change. The time delay is usually determined by the first minima of the average mutual information (AMI) [13] or autocorrelation function [16]. The selection of time lag will influence the reconstructed topological structure of the underlying system in phase space, thus, the optimal time delay is critical for the conventional PST-based damage detection methods. However, the DSF adopted in this study is not extracted from the dissimilarity of trajectories in the embedded phase space. Therefore in this study, the time delay is assumed to be a unit lag for convenience. The same choice of time delay is also found in Refs. [43, 44].

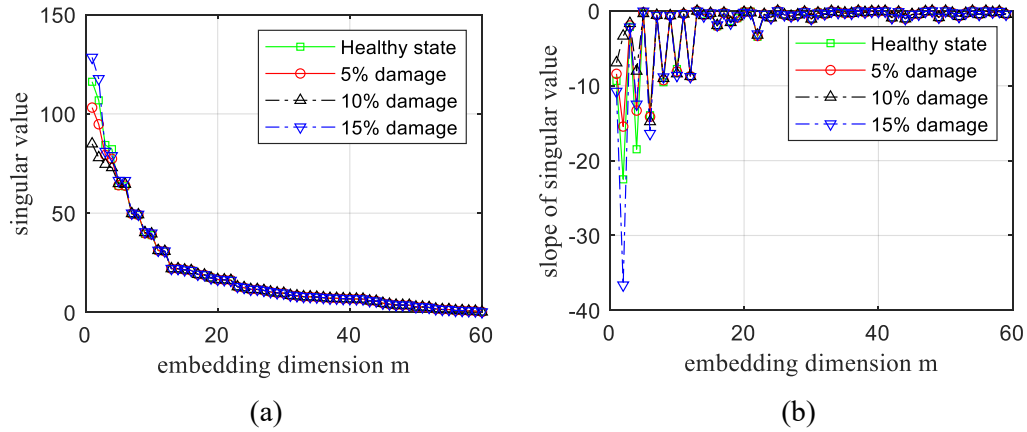


Figure 5-5. Singular values calculated from the acceleration responses at node 6 of the truss structure under reference and damaged states; (b) The slope of singular values.

Besides the embedding dimension and time lag, another parameter that may affect the damage detection results is the window length n . The effect of window size is verified on the simulated panel truss model with different data lengths of $n=1500$, $n=2000$, $n=2500$, $n=3000$, $n=3500$ and $n=4000$, respectively. In particular, the DSF value of each structural condition is estimated with 3000 random trials from structural responses under loading scenario 1, as shown in Table 5-2. The statistical distributions of the calculated DSF values with different window lengths are presented in Figure 5-6. Comparing Figure 5-6(a-f), it can be found that the DSFs estimated from different structural conditions are overlapped and no obvious separation threshold between two adjacent structural states is observed, when a relatively small window size is chosen. In addition, the overlapping area shows a decreasing trend with the increasing window size parameter n , and it finally disappears when $n \geq 3000$. However, the computational demand will be intensive when a large number of samples is involved in each calculation, which may slow the algorithm efficiency and pose challenges to the structural online monitoring. From the parametric analysis results as shown in Figure 6, the window size $n=3500$ is chosen to keep a balance between damage detection performance and computational efficiency.

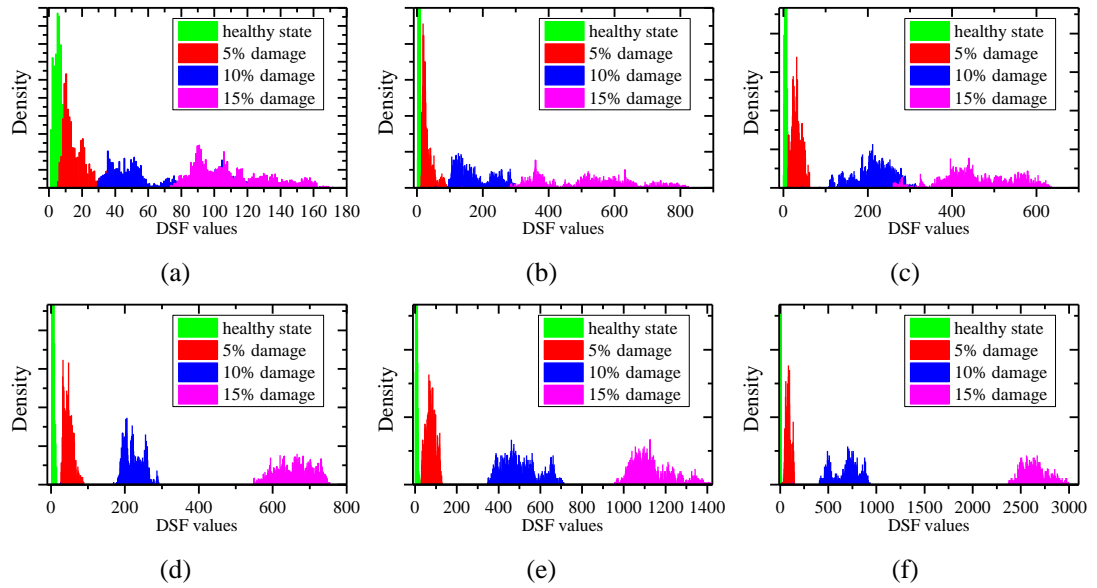


Figure 5-6. Distributions of DSF values obtained by using different window lengths:
 (a) $n=1500$; (b) $n=2000$; (c) $n=2500$; (d) $n=3000$; (e) $n=3500$ and (f) $n=4000$.

With the parameters determined above, structural responses under different loading scenarios and structural conditions listed in Table 5-2 are analysed to verify the effectiveness and robustness of the proposed approach for structural damage detection under different loading effect including the type and level of stochastic excitations. The DSF defined in Eq. (5.19) is calculated for 3000 random trials to obtain the statistical results including the mean and standard deviation under each loading scenario. Figure 5-7 shows the damage detection results of all the loading scenarios. It is observed that the DSF developed in this study can be applied to identify the damage very well. The DSF values from the damaged states, even the excitation levels to the structure before and after damage are different, are significantly larger than those from the healthy state, indicating the sensitivity of the proposed approach to detect minor structural damage. Moreover, for the same type of excitations, consistent results are obtained for loading scenarios with different excitation amplitudes. This means that structural damage can be effectively detected irrespective of the stochastic excitation levels. The DSF values could be used to quantify the damage severity as observed in Figure 5-7(a). It is observed from Figure 5-7(b) that, for those scenarios with pink noise excitations, even with different excitation levels before and after damage (scenario 6), the proposed approach can detect the damage accurately and sensitively. It is also observed the DSF value is proportional to the damage severity in loading scenarios 1, 2, and 3, as well as loading scenarios 4, 5 and 6. This also means that under the same type of stochastic excitations, the used DSF is able to reflect the damage severity.

Nevertheless, it is noted that the average DSF values under white noise excitations

(loading scenarios 1-3) and different damage severities may not be the same as those obtained under pink noise excitations (loading scenarios 4-6). This is because pink noise is not independent and identically distributed in time, with zero mean, time-invariant finite variance and temporally uncorrelated. Therefore, Assumption 1 stated in the Appendix I could not held well. The effect of different types of stochastic excitations is rarely studied. It should be mentioned that normalising the effect of variations in loading distribution characteristics on structural damage detection is still a challenging issue and is a worthwhile research topic for data driven damage assessment methods.

To investigate the accuracy of the proposed method in identifying damage at locations away from the vibration measurement point, one more case is considered. The DSF is calculated by using the vertical acceleration responses of node 15 subjected to those six loading scenarios listed in Table 5-2. The identification results are presented in Figure 5-8. As shown in Figure 5-8, different structural damage conditions can be well separated. It is interesting that the damage detection results by using the vibration responses of node 15 is similar to that of node 6. One reason is that the Koopman operator introduced in this study is a transfer operator, which captures the global evolution of dynamic systems and maps the current state observation to the one-step forward observation. This can be used to indicate the global vibration behavior and health condition of structures. As a result, the eigenvalues of Koopman operator reflect the global condition of structures.

In this study, the single channel vibration responses is used. However, the proposed method is also capable of processing multi-channel vibration responses. In particular, the single channel vibration responses $x(i)$ at the time instant i in Eq. (5.4) is replaced by the multi-channel responses. Other procedures remain unchanged. The performance of using multi-channel responses will be further studied in the future.

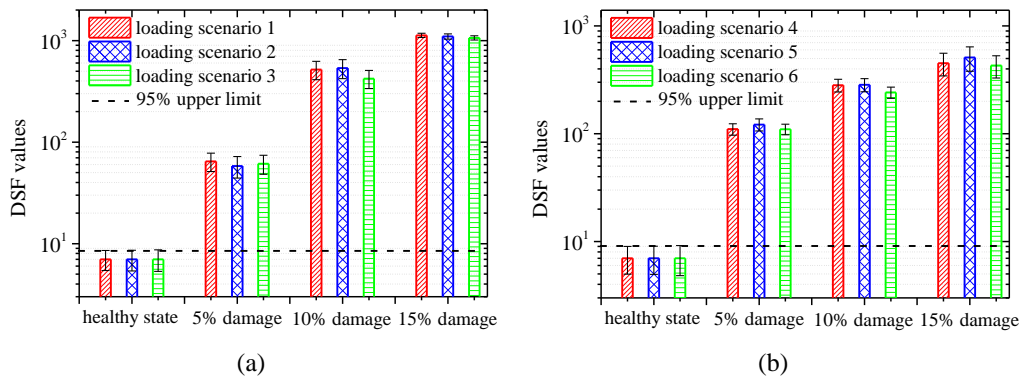


Figure 5-7. Damage identification results by using the vertical acceleration responses of node 6 under six loading scenarios (log-scale).

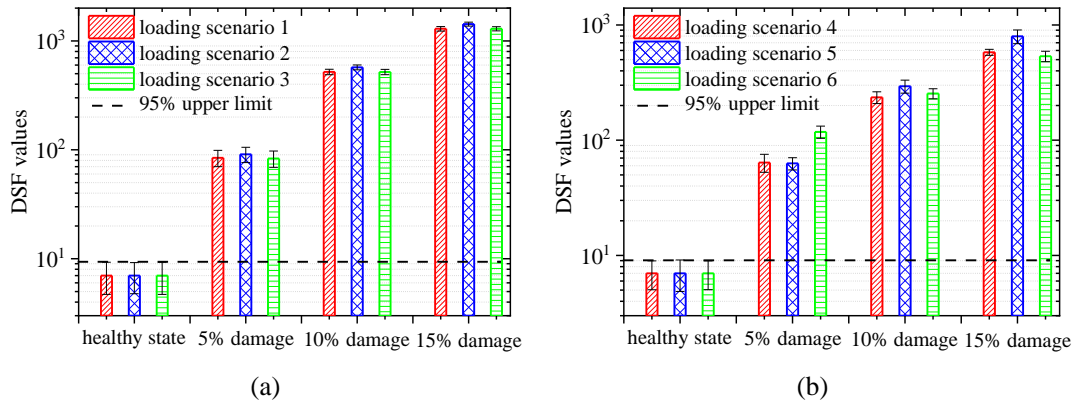


Figure 5-8. Damage identification results by using the vertical acceleration responses of node 15 under six loading scenarios (log-scale).

5.4 Verifications with in-field testing data

5.4.1 Z24 bridge and benchmark data

The Z24 bridge is a commonly used benchmark in the civil engineering community for many vibration-based SHM studies including environmental effect analysis [45], system identification and condition assessment [46, 47]. The front view and top view of the Z24 Bridge are shown in Figure 5-9(a). Detailed descriptions of SHM system setup, sensor locations and introduced damage scenarios can be found in Ref. [48] and other reports attached in the data package, which is available via <https://bwk.kuleuven.be/bwm/z24>. Within the framework of System Identification to Monitor Civil Engineering Structures project, a series of artificially introduced progressive damage tests, including settlements of pier, tilt of foundation, spalling of concrete, failure of concrete hinges at abutments of piers, failure of anchor heads of post-tensioning cables and rupture of tendons were sequentially conducted before its demolition in 1998. Before and after each test, vibration acceleration responses subjected to external forced and ambient excitations are respectively recorded. Figure 5-9(b) shows the deployment locations of five installed accelerometers during the tests.

Compared with settlements of pier, other types of damages mentioned-above cause very minor or less degradation of bending stiffness. Therefore, the vertical acceleration responses at location V2, as shown in Figure 5-9(b), under ambient excitations from the reference state and damage scenarios with different levels of settlement of pier, are analysed in this study. The acceleration responses were recorded with a sampling rate of 100 Hz and a duration of 655.3 seconds for each damage scenario. Table 5-3 lists the mean values and standard deviations of the first four identified natural frequencies obtained by Stochastic Subspace Identification method [48], for the reference states and damaged states with pier settlements. Overall, the identified natural frequencies show a slowly decreasing trend with an increasing settlement,

under a certain level of uncertainties in the environmental conditions.

Table 5-3. Natural frequencies of Z24 bridge with different pier settlements under different damage scenarios

No.	Implementation date	Damage scenario	Natural frequency (Hz) [48] (Mean + Standard Deviation)			
			Mode 1	Mode 2	Mode 3	Mode 4
1	04/08/1998	First reference measurement	3.92±0.02	5.12±0.02	9.93±0.02	10.52±0.08
2	09/08/1998	Second reference measurement	3.89±0.03	5.02±0.04	9.80±0.03	10.30±0.05
3	10/08/1998	Lowering of pier, 20 mm	3.87±0.01	5.06±0.02	9.80±0.04	10.33±0.05
4	12/08/1998	Lowering of pier, 40 mm	3.86±0.01	4.93±0.04	9.74±0.03	10.25±0.03
5	17/08/1998	Lowering of pier, 80 mm	3.76±0.01	5.01±0.03	9.37±0.04	9.90±0.15
6	18/08/1998	Lowering of pier, 95 mm	3.67±0.02	4.95±0.03	9.21±0.04	9.69±0.04

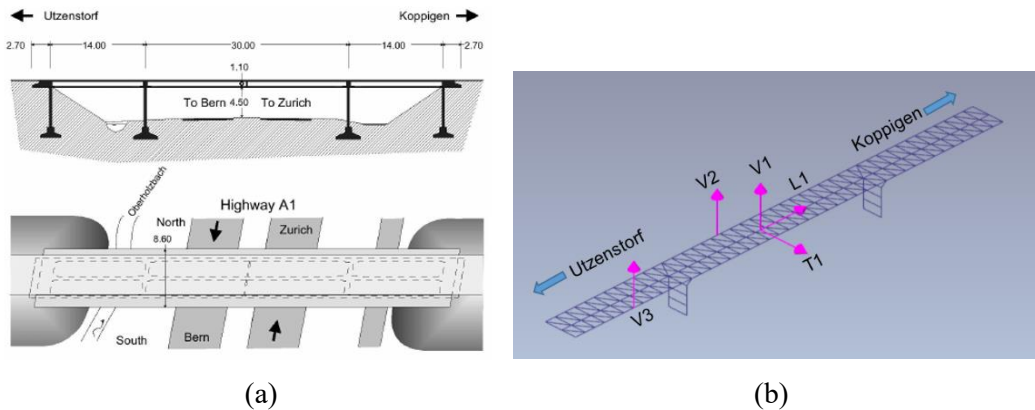


Figure 5-9. The Z24 bridge and its sensor locations: (a) Front and top views; (b) Installed accelerometer locations.

5.4.2 Parameters determination and damage detection results

For the illustration purpose, the acceleration responses from the sensor location V2 measured under damage scenarios listed in Table 5-3, are shown in Figure 5-10. Singular value spectrum of the bridge under different structural conditions are obtained by applying SVD method to the corresponding data measurement, and the results are shown in Figure 5-11. The decreasing trend of singular value spectrum gradually converges when $m \geq 40$. Hence, the embedding dimension parameter is set as 40 in this study.

In order to formulate the Hankel matrix with the suitable window size, a total of 2000 damage identification trials are conducted for each structural condition with a window size of $n=3000$, $n=4000$ and $n=5000$, respectively. Results are shown in Figure 5-12. It is observed that the distribution of DSF values corresponding to the lowering of pier of 40 mm is mixed with that from lowering of pier of 80 mm, when the window size $n \leq 4000$. Good separation results between any two adjacent scenarios are obtained when the window size $n = 5000$. Therefore, a sample window size of 5000 is chosen in this study.

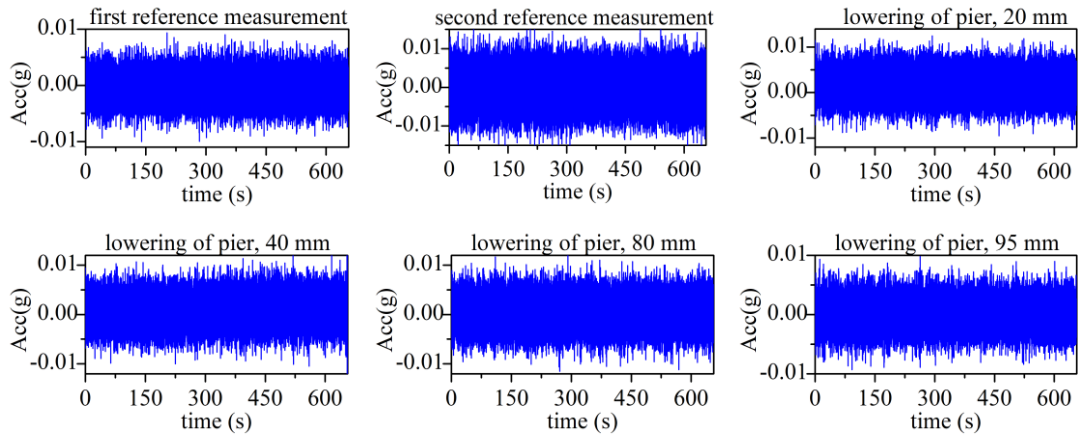


Figure 5-10. Measured acceleration responses at V2 from reference state and each damage scenario.

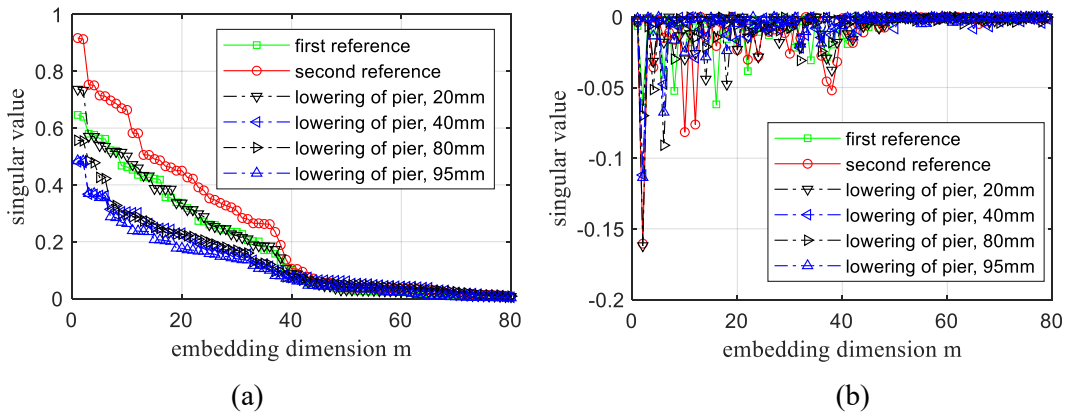


Figure 5-11. Singular values calculated from the acceleration responses of Z24 bridge under reference and damage states, (b) the slope of singular value.

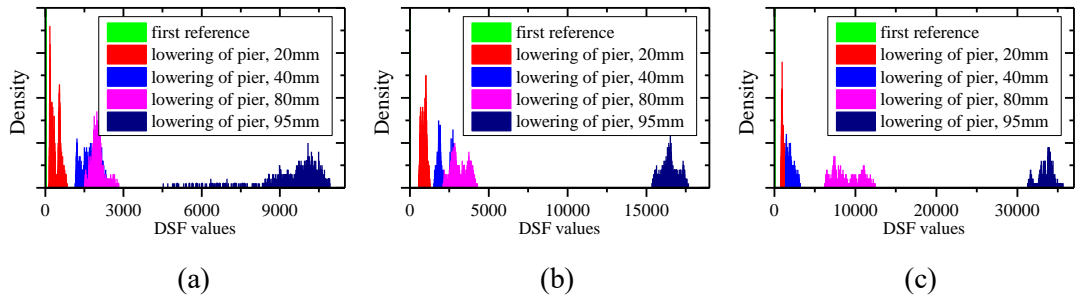


Figure 5-12. Distribution of DSF values identified with different window size parameters: (a) $n=3000$; (b) $n=4000$; (c) $n=5000$.

Vibration measurement datasets with embedding dimension $m=40$, window size $n=5000$ and unit time lag are analysed for 2000 random trials to statistically obtain the means and standard deviations of DSF values of the bridge under the reference and damaged states. During the test implementation and vibration measurement, the variation in environment effects, e.g. temperature, wind, traffic under the bridge and measurement noise may cause a certain level of uncertainties in the measured structural dynamic responses. The effect of those factors is not quantitatively investigated, but is included in this study, since the experimental measurement data before and after the damage have different environmental conditions. Damage assessment results obtained by the proposed approach are presented in Figure 5-13(a). The DSF values under the reference states from Scenarios 1 and 2 have almost the same values, indicating structural condition is the same. From the results for damage scenarios with settlements of pier, the proposed approach is sensitive to detect the lowering of pier and the corresponding DSF value is obviously increased with the degradation of structural condition. The magnitude of the defined DSF can be used to reflect the severity of the introduced damage. Figure 5-13(b) compares the relative change of the proposed DSF and the first four order natural frequencies. It is observed that the proposed DSF is much more sensitive (several order of magnitudes) to detect structural damage than using natural frequencies, even the higher order frequencies. Overall, the bridge condition under the reference state and damage scenarios with different settlements of pier can be well identified by the proposed approach under the test environment, using the real in-field testing data from a real bridge under different environmental conditions.

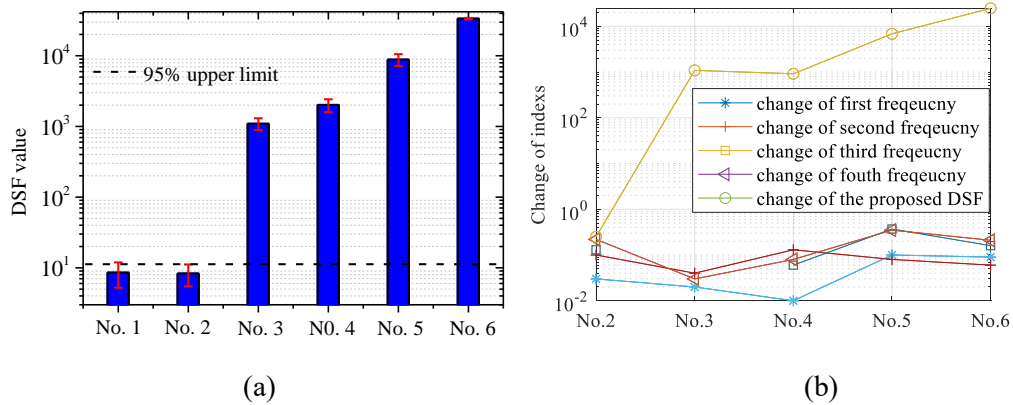


Figure 5-13. (a) Damage identification results (log-scale) under the reference state and different damage scenarios, (b) Sensitivity analysis and comparison.

In the numerical and experimental verifications, the selection of phase space reconstruction parameters like embedding dimension and window length is discussed. The general mechanism for the optimal selection of these two parameters is further provided. For deterministic dynamic systems, there are several existing methods that can be used for the optimal selection of embedding dimension. This is because the dimension of deterministic dynamic systems in phase space is finite. However, the dimension of random dynamic systems in the phase space is infinite. In this study, the singular value spectrum is applied to determine a suitable embedding dimension. In the singular value spectrum, larger singular values appear in pairs, and each pair corresponds to a frequency component of the vibration responses. The vibration responses are dominated by the first several frequency components with larger singular values. The noise is mainly distributed in the components with lower singular values. There is a sudden drop between each singular value pair, which is manifested as a large slope in the singular value spectrum curve. Therefore, the slope of singular values spectrum is utilized for optimal selection of the embedding dimension. It should be noted that the embedding dimension used for analysing structural vibration responses before and after damage should be the same.

The effect of window size on the DSF value presented in Figure 5-6 and Figure 5-12 shows that better separation results between different damage scenarios can be obtained when a larger window size is selected. However, the computational demand increases when a large number of samples are involved in each calculation. Therefore, the window size can be chosen based on the balance between damage detection performance and computational efficiency.

5.5 Conclusions

Motivated by the infeasibility of using conventional PST-based methods in extracting

damage features from high dimensional structural dynamic responses, this chapter proposes a novel data driven approach using phase space embedding strategy and Koopman operator for the health monitoring and condition assessment of structures subjected to stochastic excitations. The main contribution of this study is to obtain the time-invariant stochastic Koopman operator from the phase space representation of observable vibration responses, e.g. a single channel acceleration response, which is subsequently used for damage assessment. In contrast to many of the existing PST-based methods by extracting DSFs from the manifold topology of the original attractor in low dimensional phase space representations, the DSF developed in this chapter is derived from the eigenvalues of the corresponding Koopman operator. As a result, the high sensitivity of using high dimensional phase space to detect the structural damage is obtained to conduct structural condition assessment with observations measured under operational conditions, e.g. stochastic ambient excitations instead of artificially generated excitations including chaotic, impulse or limited band swept-sine, etc. The feasibility and accuracy of the proposed approach are validated using acceleration responses obtained from numerical FE model of a truss bridge subjected to stochastic excitations, as well as in-field monitoring data from a real bridge under ambient loads. In numerical studies, minor structural damage simulated as stiffness reductions is detected effectively and accurately. For the in-field studies on a bridge, the introduced damage in the form of settlement is also identified effectively and reliably. Different forms of structural damage are identified in numerical and experimental studies. The results from both numerical and in-field studies reveal that the proposed method is sensitive to structural condition change, but insensitive to environmental condition and measurement noise. In particular, the statistical distribution of the obtained DSF values of each scenario is concentrated and well distinguished, supporting a reliable condition assessment result.

The effect of stochastic loading amplitude and distribution properties is numerically investigated. Results demonstrate that the proposed approach is robust to change in excitation amplitudes, however, the damage detection performance may be influenced at a certain level when the excitation type is not the same before and after damage. Therefore, in the future study, a better normalisation method could be further investigated to eliminate the effect of load conditions and detect the damage in structures under different types of stochastic excitations before and after damage.

References

- [1] S. Das, P. Saha, S. Patro, Vibration-based damage detection techniques used for health monitoring of structures: a review, *Journal of Civil Structural Health Monitoring*, 6 (2016) 477-507.
- [2] J. Li, H. Hao, A review of recent research advances on structural health monitoring in Western Australia, *Struct Monit Maint*, 3 (2016) 33-49.
- [3] M. Cerrada, R.-V. Sánchez, C. Li, F. Pacheco, D. Cabrera, J.V. de Oliveira, R.E. Vásquez, A review on data-driven fault severity assessment in rolling bearings, *Mechanical Systems and Signal Processing*, 99 (2018) 169-196.
- [4] F. Cavadas, I.F. Smith, J. Figueiras, Damage detection using data-driven methods applied to moving-load responses, *Mechanical Systems and Signal Processing*, 39 (2013) 409-425.
- [5] S.B. Shiki, S. da Silva, M.D. Todd, On the application of discrete-time Volterra series for the damage detection problem in initially nonlinear systems, *Structural Health Monitoring*, 16 (2017) 62-78.
- [6] C. Cheng, Z. Peng, W. Zhang, G. Meng, Volterra-series-based nonlinear system modeling and its engineering applications: A state-of-the-art review, *Mechanical Systems and Signal Processing*, 87 (2017) 340-364.
- [7] L. Chen, L. Yu, Structural Nonlinear Damage Identification Algorithm Based on Time Series ARMA/GARCH Model, *Advances in Structural Engineering*, 16 (2013) 1597-1609.
- [8] C. Bao, H. Hao, Z.-X. Li, Integrated ARMA model method for damage detection of subsea pipeline system, *Engineering Structures*, 48 (2013) 176-192.
- [9] Z. Nie, H. Hao, H. Ma, Structural damage detection based on the reconstructed phase space for reinforced concrete slab: Experimental study, *Journal of Sound and Vibration*, 332 (2013) 1061-1078.
- [10] L.G. Villani, S. da Silva, A. Cunha, M.D. Todd, On the detection of a nonlinear damage in an uncertain nonlinear beam using stochastic Volterra series, *Structural Health Monitoring*, (2019) 1475921719876086.
- [11] L. Bornn, C.R. Farrar, G. Park, K. Farinholt, Structural health monitoring with autoregressive support vector machines, *Journal of Vibration and Acoustics*, 131 (2009).
- [12] C.S.N. Pathirage, J. Li, L. Li, H. Hao, W. Liu, P. Ni, Structural damage identification based on autoencoder neural networks and deep learning, *Engineering Structures*, 172 (2018) 13-28.
- [13] G. Liu, Z. Mao, M. Todd, Damage detection using transient trajectories in phase-space with extended random decrement technique under non-stationary excitations, *Smart Materials and Structures*, 25 (2016) 115014.
- [14] F. Takens, *Detecting strange attractors in turbulence (Lecture Notes in Mathematics)*, Springer, Berlin, 1981.
- [15] Z. Nie, H. Hao, H. Ma, Using vibration phase space topology changes for structural damage detection, *Structural Health Monitoring: An International Journal*, 11 (2012) 538-557.
- [16] L. Pamwani, A. Shelke, Damage detection using dissimilarity in phase space topology of dynamic response of structure subjected to shock wave loading, *Journal of Nondestructive Evaluation, Diagnostics and Prognostics of Engineering Systems*, 1 (2018) 041004.

- [17] J. Nichols, M. Todd, M. Seaver, L. Virgin, Use of chaotic excitation and attractor property analysis in structural health monitoring, *Physical Review E*, 67 (2003) 016209.
- [18] M. Todd, K. Erickson, L. Chang, K. Lee, J. Nichols, Using chaotic interrogation and attractor nonlinear cross-prediction error to detect fastener preload loss in an aluminum frame, *Chaos: An Interdisciplinary Journal of Nonlinear Science*, 14 (2004) 387-399.
- [19] W. Zhang, J. Li, H. Hao, H. Ma, Damage detection in bridge structures under moving loads with phase trajectory change of multi-type vibration measurements, *Mechanical Systems and Signal Processing*, 87 (2017) 410-425.
- [20] Z. Nie, T. Ngo, H. Ma, Reconstructed phase space-based damage detection using a single sensor for beam-Like structure subjected to a moving mass, *Shock and Vibration*, 2017 (2017).
- [21] R.C. George, S.K. Mishra, M. Dwivedi, Mahalanobis distance among the phase portraits as damage feature, *Structural Health Monitoring*, 17 (2018) 869-887.
- [22] B. Paul, R.C. George, S.K. Mishra, Phase space interrogation of the empirical response modes for seismically excited structures, *Mechanical Systems and Signal Processing*, 91 (2017) 250-265.
- [23] L. Pamwani, A. Shelke, Damage quantification in moment resisting frame using phase space reconstructed from independent component sources, *Structural Control and Health Monitoring*, 26 (2019) e2438.
- [24] Z. Chen, Y. Bao, H. Li, B.F. Spencer Jr, A novel distribution regression approach for data loss compensation in structural health monitoring, *Structural Health Monitoring*, 17 (2018) 1473-1490.
- [25] Y. Bao, Z. Chen, S. Wei, Y. Xu, Z. Tang, H. Li, The state of the art of data science and engineering in structural health monitoring, *Engineering*, 5 (2019) 234-242.
- [26] A. Salova, J. Emenheiser, A. Rupe, J.P. Crutchfield, R.M. D'Souza, Koopman operator and its approximations for systems with symmetries, *Chaos: An Interdisciplinary Journal of Nonlinear Science*, 29 (2019) 093128.
- [27] B.O. Koopman, Hamiltonian systems and transformation in Hilbert space, *Proceedings of the national academy of sciences of the united states of america*, 17 (1931) 315.
- [28] P.J. Schmid, Dynamic mode decomposition of numerical and experimental data, *Journal of fluid mechanics*, 656 (2010) 5-28.
- [29] J.H. Tu, C.W. Rowley, D.M. Luchtenburg, S.L. Brunton, J.N. Kutz, On dynamic mode decomposition: theory and applications, *Journal of Computational Dynamics*, 1 (2014) 391-421.
- [30] M.S. Hemati, C.W. Rowley, E.A. Deem, L.N. Cattafesta, De-biasing the dynamic mode decomposition for applied Koopman spectral analysis of noisy datasets, *Theoretical and Computational Fluid Dynamics*, 31 (2017) 349-368.
- [31] J.L. Proctor, S.L. Brunton, J.N. Kutz, Dynamic mode decomposition with control, *SIAM Journal on Applied Dynamical Systems*, 15 (2016) 142-161.
- [32] N. Takeishi, Y. Kawahara, T. Yairi, Subspace dynamic mode decomposition for stochastic Koopman analysis, *Physical Review E*, 96 (2017) 033310.
- [33] N. Črnjarić-Žic, S. Maćešić, I. Mezić, Koopman operator spectrum for random dynamical systems, *Journal of Nonlinear Science*, (2019) 1-50.
- [34] J.L. Proctor, S.L. Brunton, J.N. Kutz, Generalizing Koopman theory to allow for inputs and control, *SIAM Journal on Applied Dynamical Systems*, 17 (2018) 909-930.
- [35] J.N. Kutz, X. Fu, S.L. Brunton, N.B. Erichson, Multi-resolution dynamic mode

- decomposition for foreground/background separation and object tracking, in: 2015 IEEE International Conference on Computer Vision Workshop (ICCVW), IEEE, 2015, pp. 921-929.
- [36] M.O. Williams, I.G. Kevrekidis, C.W. Rowley, A data-driven approximation of the koopman operator: Extending dynamic mode decomposition, *Journal of Nonlinear Science*, 25 (2015) 1307-1346.
- [37] L. Overbey, C. Olson, M. Todd, A parametric investigation of state-space-based prediction error methods with stochastic excitation for structural health monitoring, *Smart Materials and Structures*, 16 (2007) 1621.
- [38] D. García, D. Tcherniak, An experimental study on the data-driven structural health monitoring of large wind turbine blades using a single accelerometer and actuator, *Mechanical Systems and Signal Processing*, 127 (2019) 102-119.
- [39] N. Takeishi, Y. Kawahara, T. Yairi, Learning Koopman invariant subspaces for dynamic mode decomposition, in: *Advances in Neural Information Processing Systems*, 2017, pp. 1130-1140.
- [40] E. Yeung, S. Kundu, N. Hodas, Learning deep neural network representations for Koopman operators of nonlinear dynamical systems, in: *2019 American Control Conference (ACC)*, IEEE, 2019, pp. 4832-4839.
- [41] H. Arbabi, I. Mezić, Ergodic theory, dynamic mode decomposition, and computation of spectral properties of the Koopman operator, *SIAM Journal on Applied Dynamical Systems*, 16 (2017) 2096-2126.
- [42] S.T. Dawson, M.S. Hemati, M.O. Williams, C.W. Rowley, Characterizing and correcting for the effect of sensor noise in the dynamic mode decomposition, *Experiments in Fluids*, 57 (2016) 42.
- [43] E. Figueiredo, M.D. Todd, C.R. Farrar, E. Flynn, Autoregressive modeling with state-space embedding vectors for damage detection under operational variability, *International Journal of Engineering Science*, 48 (2010) 822-834.
- [44] D.S. Broomhead, G.P. King, Extracting qualitative dynamics from experimental data, *Physica D: Nonlinear Phenomena*, 20 (1986) 217-236.
- [45] B. Peeters, G. De Roeck, One - year monitoring of the Z24 - Bridge: environmental effects versus damage events, *Earthquake engineering & structural dynamics*, 30 (2001) 149-171.
- [46] J. Kullaa, Damage detection of the Z24 bridge using control charts, *Mechanical Systems and Signal Processing*, 17 (2003) 163-170.
- [47] J. Maeck, B. Peeters, G. De Roeck, Damage identification on the Z24 bridge using vibration monitoring, *Smart materials and structures*, 10 (2001) 512.
- [48] J. Maeck, G. De Roeck, Description of Z24 benchmark, *Mechanical Systems and Signal Processing*, 17 (2003) 127-131.

CHAPTER 6 STRUCTURAL DAMAGE DETECTION VIA PHASE SPACE BASED MANIFOLD LEARNING UNDER CHANGING ENVIRONMENTAL AND OPERATIONAL CONDITIONS

ABSTRACT⁵

The feasibility and performance of existing vibration-based damage detection methods to real world civil engineering structures are inevitably affected by the varying environmental and operational conditions. Reliable damage detection methods with damage features that are sensitive to structural condition change but robust to environmental and loading effects are desirable for practical applications. This chapter proposes a novel structural damage detection approach based on manifold learning for the effective condition assessment of real-world structures under environmental and operational conditions. The phase space representation of the vibration characteristics is reconstructed using the identified natural frequencies of structures. Then, the intrinsic nonlinear manifold between the environmental variables and natural frequencies in the high dimensional phase space is projected to a low-dimensional representation via manifold learning. The Gaussian process regression technique is introduced to extract reliable damage index from the learned manifold structure. The effectiveness and superiority of the proposed approach are demonstrated by two real-world engineering structures, that is, the Dowling Hall Footbridge and Z24 bridge. Damage detection results obtained from the proposed approach are compared with those from the current state-of-the-art Kernel PCA method, which is a representative nonlinear dimensionality reduction method to alleviate the environmental effects. The results demonstrate that the proposed approach is sensitive to structural damage but insensitive to changes in environmental and operational conditions. More importantly, the nonlinear environmental effects can be efficiently characterized by the proposed approach, using only partial datasets with environmental variations in the training datasets.

6.1 Introduction

Existing infrastructure, such as bridges and buildings exposed to the operational

⁵Peng, Z., Li, J., Hao, H. (2022) Structural damage detection via phase space based manifold learning under changing environmental and operational conditions, *Engineering Structures*. 263, 114420. <https://doi.org/10.1016/j.engstruct.2022.114420>.

environment for long service life, are prone to performance degradation, owing to the material deterioration, natural hazards and human-made loading conditions. The wide applications of SHM systems accumulate massive real measured structural long-term vibration responses as well as environmental condition measurements. Similarly, vibration-based structural damage detection and condition assessment methods have been extensively developed over the last several decades for monitoring the conditions of civil engineering structures. A comprehensive review of the new development in the vibration-based damage identification methods for civil infrastructure over the past decades is recently provided in Ref. [1]. Apart from the traditional modal parameter-based methods and FE model updating based methods, machine learning and deep learning techniques have also been extensively studied for damage identification in recent years. Generally speaking, the damage detection problem can be viewed as a pattern recognition process, which transfers the observable variables in the time domain, frequency domain or time-frequency domain into DSF. The ultimate goal of damage diagnosis is to extract damage features that are sensitive to structural condition change, but robustness to external loading and environmental conditions, and measurement noise [2].

Modal parameters are directly related to structural properties, but independent to the applied loads. Thus, modal information, such as natural frequency, mode shape and FRF, etc., has been served as the input of many newly developed damage detection methods, including the machine learning/deep learning based methods. A major challenge is that modal parameters can also be significantly affected by the environmental conditions, i.e. temperature, wind characteristics and humidity that the structures faced with [3]. Temperature effects have been reported to be the primary influential factor in the variation of modal parameters than other environmental effects [4]. Temperature affects structural properties in a complicated manner. The variations in the thermal coefficient of Young's modulus and the thermal expansion coefficient will directly or indirectly vary the stiffness, geometric dimension and boundary condition of structures. The mechanism how temperature affects the structural vibration characteristics could be more complicated when the spatial temperature distribution inside the structures as well as the seasonally frozen soil effects are considered [5-7]. Owing to the uniqueness of different structural styles and designs, construction material properties and construction process are different from case to case, it is almost impossible to deduce a generally applicable formula to quantify the temperature effects on the mechanical properties of different structures. In most long term SHM applications, vibration measurements from the in-service structures under varying operational conditions are massively available, which provides opportunities to statistically evaluate the dissimilarity in the defined DSF between baseline (healthy) and the currently inspected states.

The damage detection methods considering the environmental and operational conditions

can be classified into two main categories, according to the situation whether the environmental effects and operational loads, such as temperature, humidity, wind characteristics and traffic flow are simultaneously monitored along with vibration responses or not. For the former case, the environmental effects can be eliminated by conducting the correlation analysis between the environmental variable and the developed DSF. Most of the existing studies focus on analysing the correlation between structural modal parameters and the air temperature. Limited studies considered the thermal gradient distribution in structures and thermal time lags effect, owing to the limitation of deploying a very spatially dense network of thermometers [8, 9]. Therefore, methods developed towards separating the temperature effects and structural damage without the environmental measurements have a more practical significance. When the environmental measurements are not available, research efforts have been devoted to distinguishing the environmental effect, based on the assumption that the variations in the obtained vibration characteristics induced by structural damage behaves differently from those due to the change in operational and environmental conditions. In this regards, various methods, including the Kernel principle component analysis (PCA) [10], co-integration analysis [11] and auto-associative neural networks [12] have been recently developed for extracting reliable damage features.

For dynamic systems, all the observable variables span a phase space. Each possible state of a system corresponds to one unique point in the phase space [13, 14]. It is noted that the dimension of the spanned phase space is equal to the number of independent observable variables that are used. All the possible states will form a unique topology trajectory (also referred to as manifold in data science) in the high-dimensional phase space. The locally nearby points in the phase space correspond to similar structural conditions. For instance, a healthy structure exposed to similar operational conditions at two different time instants will be embodied as neighbors in the high dimensional phase space. The influential external factors will be manifested as a distribution in a specific region of the phase space. When the structural condition changes, the PST corresponding to the new structural condition no longer returns to the original distribution, even though the external influential factors remain unchanged. The unmeasured variables, such as environmental conditions and traffic loads, can be viewed as latent variables (also referred to as hidden variables), which can be fully unfolded in the defined high dimensional phase space. It is noted that phase space technique is known for its capability in effectively representing both linear and nonlinear dynamic features, which has a great potential in expressing the nonlinear relationship between the environmental variables and structural modal parameters. Different combinations of structural states and operational conditions will formulate a unique trajectory or distribution in a phase space with a sufficiently high dimension. Structural damage detection can be achieved by projecting the observations

in high dimensional phase space to low dimensional feature space. PCA is a representative linear dimensionality reduction technique. However, PCA is not applicable to variables with a nonlinear mutual relationship. For example, Reynders et al. [15] pointed out that PCA can fail to distinguish the structural damage condition from the healthy state, when the temperature is below 0°C. Under this circumstance, Kernel PCA with Gaussian kernel was introduced to alleviate the false-positive alarms owing to the nonlinear effects of temperature on natural frequencies. The capacity of using Kernel PCA for structural damage detection has been verified on a benchmark Z24 bridge using the first four order natural frequencies under different environmental conditions to train the model. It should be noted that a broader range of temperature conditions, including the period when the temperature is below -5°C should be covered in the training datasets.

Manifold learning is a promising nonlinear dimensionality reduction technique that seeks low-dimensional visualization of the inherent structure of original datasets embedded in high-dimensional phase spaces. The hypothesis of manifold learning is that the phase space attractor of real-world systems spanned by the observable state variables is expected to evolve in a much low-dimensional manifold. The most remarkable feature of manifold learning is that the local topological and neighborhood information of the original datasets is preserved in the low dimensional graph representation [16]. An illustrative example is presented in Figure 6-1 for better understanding the mechanism of manifold learning in dimensionality reduction. Figure 6-1(a) visualizes the original data with a Swiss roll-like topologic inherent structure, the corresponding low dimensional embedding as shown in Figure 6-1(b) is unfolded via a specific manifold learning method called Isomap [17]. It can be found that the neighborhoods in the original data with the similar color have been mapped close to each other in the unfolded 2D manifold, which demonstrates the ability of manifold learning in preserving the consistency of the neighborhood structure. In literature, locally linear embedding (LLE) [18], Isomap [17], Laplacian eigenmaps [19] are some of the most representative manifold learning methods for nonlinear dimensionality reduction. Features extracted from the manifold learning have been successfully applied for early warning of the financial market [20], hyperspectral image classification [21], machinery fault diagnosis [22] and structural damage classification [23], etc. For SHM, rare work has been conducted in order to characterize the nonlinear manifold of monitoring data of civil engineering structures subjected to operational conditions, and to further develop DSF that is robust to environmental and operational conditions for structural condition assessment.

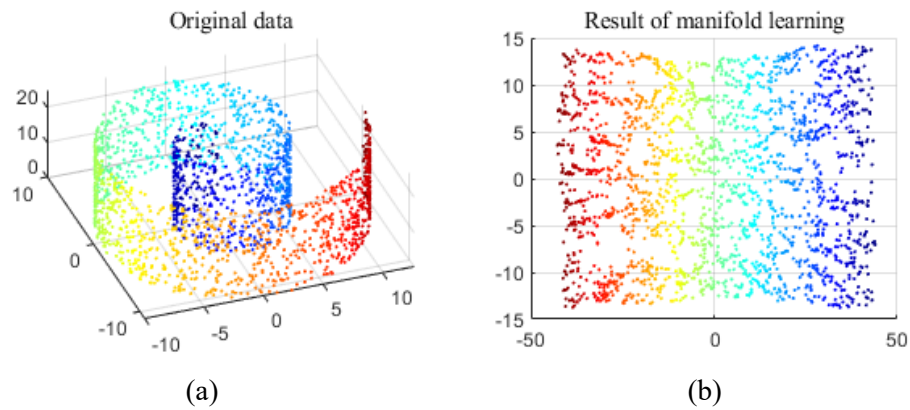


Figure 6-1. An illustrative example of manifold learning: (a) Original data in a high dimensional phase space with a Swiss roll-like topologic inherent structure; (b) 2D embedding via manifold learning.

This chapter proposes a novel approach based on manifold learning to develop a DI for structural damage detection, taking into account the environmental and operational conditions. The feasibility and superiority of using manifold learning for revealing the inherent topological structure of the underlying systems subjected to operational conditions with the long-term vibration monitoring responses are demonstrated. DSF that is sensitive to damage but insensitive to environmental effects is developed via the multivariate Gaussian process regression model. Gaussian process regression is a robust nonparametric, Bayesian-based probabilistic model for regression and classification tasks in machine learning. In particular, partial of the samples under the healthy state are used as the input to the Gaussian process regression model for learning the environmental effects induced nonlinear relationship. Then, the trained Gaussian process regression model is used to predict the future responses and the absolute prediction residual is served as DSF, which is used for structural damage detection considering environmental and operational conditions. It is noted that the damage features extracted from phase space based manifold learning on the measurement data under the initial stage (baseline) and the current stage are compared to detect possible structural condition change. The closely spaced modes can be extracted by using the improved modal identification methods [24]. However, this is not within the scope of this study.

The remaining sections of the chapter are organized as follows. In Section 2, the theoretical background of phase space reconstruction, manifold learning and Gaussian process regression is briefly reviewed. In Sections 3 and 4, the long term SHM data of Dowling Hall footbridge and the Z24 bridge are utilized to demonstrate the feasibility and superiority of the proposed method in sensitively detecting the structural condition change while remaining robust to operational condition variations. Comparisons with other state-of-the-art data-driven damage detection methods are also conducted and the results are discussed. Finally, the

conclusion is provided in Section 5.

6.2 Theoretical Background and Development

6.2.1 Phase space reconstruction

For a civil engineering structure, structural natural frequency is a function of its geometry, boundary condition and material properties, which can be expressed as follows

$$f_n = \mathcal{F}_n(\lambda_n, G, K, M) \quad (6.1)$$

where the subscript n represents the n -th order natural frequency. The dimensionless parameters λ_n and G are functions of the boundary constraint conditions and geometric properties of the structure, respectively; K and M denote the stiffness and mass matrices, respectively. As can be found in Eq. (6.1), the mapping function \mathcal{F}_n from structural variables to natural frequency is deterministic. However, the boundary condition, geometric dimension and elastic modulus can be directly or indirectly affected by the material thermal coefficient of modulus and the thermal coefficient of linear expansion in a complicated manner, considering the temperature is the major factor that affects structural vibration characteristics. As a result, Eq. (6.1) can be rewritten as

$$f_n = \mathcal{F}_n[\lambda_n(T), G(T), K(T), M, T] + e \quad (6.2)$$

where T represents the non-uniform temperature distribution along the structure, e represents the uncertainties caused by measurement noise and modelling errors. For small scale structures, the air temperature or temperatures at a few critical points of the structure are sufficiently accurate to quantify the relationship between the temperature and natural frequency. However, the accuracy of frequency calculation can be significantly affected for large-scale structures without installing a dense set of thermometers to obtain the thermal distribution of the entire structure [25]. Owing to the budget constraints, only partial measurements of temperatures and vibration responses at some crucial locations can be made by sensor networks installed in SHM applications. In the theory of phase space, the unavailable temperature spatial distribution can be viewed as a hidden variable, which is manifested as a specific trajectory or distribution in the phase space spanned by partial observable variables. For this purpose, in this study, the identified natural frequencies are selected as the observed variables. The phase space spanned by the first n natural frequencies with a window size of m samples, can be defined as

$$\Phi_{n,m} = \begin{bmatrix} \mathbf{f}_1 \\ \mathbf{f}_2 \\ \vdots \\ \mathbf{f}_n \end{bmatrix} = \begin{bmatrix} f_1(t_1) & f_1(t_2) & \cdots & f_1(t_m) \\ f_2(t_1) & f_2(t_2) & \cdots & f_2(t_m) \\ \vdots & \vdots & \ddots & \vdots \\ f_n(t_1) & f_n(t_2) & \cdots & f_n(t_m) \end{bmatrix} \quad (6.3)$$

The dimension of the phase space defined in Eq. (6.3) is n . The topologic structure traced out by the PST of the underlying system can be visualized when $n \leq 3$. For phase space based methods, in general, the more variables used to span the phase space, the better the dynamic attractor of underlying system obtained and the more accurate the unmeasurable latent variables represented. The higher order vibration modes may not be well excited for bridge structures under operational conditions. Therefore, to improve the performance of damage pattern recognition, the several low order modal frequencies that are reliably identified from the vibration responses are used to construct a high dimensional phase space [26]. In particular, the first four and the first five order natural frequencies are used for the studies on Dowling Hall footbridge and Z24 bridge, respectively.

6.2.2 Manifold learning

In practice, it is challenging to extract interpretative features from a high dimensional phase space. To this end, deriving a low-dimensional projection of a given high-dimensional trajectory that preserves the equivalent intrinsic manifold structure and maintains the local neighborhood information is of great significance [27]. Owing to the fact that most of the real-world dynamic systems exhibit the nonlinearity to a certain extent, the nonlinear dimensionality reduction algorithm, such as kernel PCA and other manifold learning methods, i.e. Laplacian eigenmaps, Isomap and LLE have been developed in existing works. In this study, the Laplacian eigenmaps is adopted to extract the inherent nonlinear relationship between natural frequencies and environmental variables, by taking advantages of its locality preserving characteristics [28]. The Laplacian eigenmaps method is mainly consisted of two steps, namely, constructing the similarity graph from high dimensional data points and projecting points into a low-dimensional space using eigenvectors of the graph.

Supposing that the n -dimensional frequency observation vector at time instant t_i is $\mathbf{x}(t_i) = [f_1(t_i) f_2(t_i) \cdots f_n(t_i)]^T$, the corresponding low-dimensional representation is $\mathbf{y}(t_i) = [y_1(t_i) y_2(t_i) \cdots y_m(t_i)]^T$, where $m < n$. The premise of Laplacian eigenmaps is that the neighborhood information should be preserved, in other words, nearby points on the original graph stay as close as possible after dimensionality reduction projection. To this end, the following cost function is defined

$$Loss(\mathbf{y}) = \min \sum_{i,j} \|\mathbf{y}(t_i) - \mathbf{y}(t_j)\|^2 w_{i,j} \quad (6.4)$$

where $w_{i,j}$ represents the weighting coefficient determined by the similarity score between two observations $\mathbf{x}(t_i)$ and $\mathbf{x}(t_j)$, $\mathbf{W} = (w_{i,j})$ of dimension $n \times n$ is the weight matrix. In Laplacian eigenmaps, the weight matrix \mathbf{W} is calculated using the Gaussian kernel function, which is expressed as

$$w_{i,j} = e^{-\frac{\|\mathbf{x}(t_i) - \mathbf{x}(t_j)\|^2}{2\sigma^2}} \quad (6.5)$$

As can be found in Eq. (6.5), the closer two points is in the original high dimensional phase space, the larger the weighting coefficient is. The Gaussian kernel function is used to ensure that neighboring points $\mathbf{x}(t_i)$ and $\mathbf{x}(t_j)$ have a heavy penalty when they are mapped far away in the low-dimensional space. The diagonal degree matrix \mathbf{D} of the weight matrix \mathbf{W} is introduced, and the diagonal element is obtained as $D_{i,i} = \sum_j w_{i,j}$. The Laplacian graph \mathbf{L} is calculated by $\mathbf{L} = \mathbf{D} - \mathbf{W}$. The cost function in Eq. (6.4) can be expanded as

$$\begin{aligned} \mathcal{L}oss(\mathbf{y}) &= \sum_i \mathbf{y}(t_i)^T \mathbf{y}(t_i) D_{i,i} + \sum_j \mathbf{y}(t_j)^T \mathbf{y}(t_j) D_{j,j} - 2 \sum_{ij} \mathbf{y}(t_i)^T \mathbf{y}(t_j) w_{i,j} \\ &= 2\mathbf{Y}^T \mathbf{D} \mathbf{Y} - 2\mathbf{Y}^T \mathbf{W} \mathbf{Y} = 2\mathbf{Y}^T \mathbf{L} \mathbf{Y} \end{aligned} \quad (6.6)$$

From Eq. (6.6), the optimization problem is converted to minimise $\mathbf{Y}^T \mathbf{L} \mathbf{Y}$. The low-dimensional data representation \mathbf{Y} can thus be found by solving the following generalized Eigen analysis problem [19, 29]

$$\mathbf{L} \mathbf{v} = \lambda \mathbf{D} \mathbf{v} \quad (6.7)$$

With Eq. (6.6) defined as the loss function for a minimization problem, the eigenvalues and the corresponding eigenvectors solved from Eq. (6.7) are sorted based on the order from the smallest to the largest eigenvalues [19, 28]. The low-dimensional projection \mathbf{Y} is consisted of the eigenvectors corresponding to the m smallest eigenvalues.

6.2.3 DSF extraction based on Gaussian process regression

Gaussian process regression models are nonparametric kernel-based probabilistic models within the machine learning community. In this study, the Gaussian process regression will be used to estimate the nonlinear relationship between the components of \mathbf{Y} obtained from Laplacian Eigenmaps. In particular, the first two Laplacian components $\mathbf{y}_{1,2} = [\mathbf{y}_1; \mathbf{y}_2]$ of dimension $2 \times n$ are used as the input to predict the third Laplacian component \mathbf{y}_3 of dimension $1 \times n$. A Gaussian process model is defined by its mean function $m(\mathbf{y}_{1,2})$ and covariance function $k(\mathbf{y}_{1,2}, \mathbf{y}'_{1,2})$, that is

$$\hat{\mathbf{y}}_3 \sim GP[m(\mathbf{y}_{1,2}), k(\mathbf{y}_{1,2}, \mathbf{y}'_{1,2})] \quad (6.8)$$

A Gaussian process regression model can be trained using Matlab inbuilt function ‘fitrgp’. The alternative options of the prior mean function include zero (default), linear and polynomial functions. The covariance function defines the covariance of neighboring data points as a function of the corresponding distance, which governs the smoothness of a process. Dozens of specific covariance functions, i.e., squared exponential kernel (default), exponential kernel, Matern kernel are provided to optimize the regression performance. In this study, the default mean function and covariance function are adopted to train the Gaussian process regression model. Empirical experiments conducted by the authors indicate that the accuracy of Gaussian process regression model with default setting is desirable. In practical applications, part of the observations corresponding to the healthy state will be used to train the model, and then the remaining datasets are employed for monitoring structural condition change. The Gaussian process regression model may not provide accurate prediction results when the structural damage occurs and structural condition changes. Therefore, the residual in the absolute prediction is defined as a damage index (DI)

$$DI = |\mathbf{y}_3 - \hat{\mathbf{y}}_3| = |\mathbf{y}_3 - GP[m(\mathbf{y}_{1,2}), k(\mathbf{y}_{1,2}, \mathbf{y}'_{1,2})]| \quad (6.9)$$

in which $\hat{\mathbf{y}}_3$ denotes the prediction of the third Laplacian component via the trained Gaussian process regression model. It should be noted that only the structural long-term vibration responses under different environmental conditions are used in the proposed damage detection approach. The environmental conditions, such as temperature measurements are not required, and the robustness of the proposed method to environmental effects will be demonstrated in the following sections.

This study proposes a data-driven structural damage detection method. One of the main challenges of data-driven SHM methods is to understand and eliminate the environmental effects on structural vibration characteristics or responses. To this end, most of the existing methods, such as PCA and more recently developed cointegration method, aim at separating the environmental effect on vibration characteristics with structural damage effect. This chapter develops a novel approach from a new perspective by visualizing the manifold structure of environmental effects via phase space technique. Different environment conditions correspond to specific points in the reconstructed phase space. The manifold structure of a real engineering structure can be viewed as a data-driven model. The occurrence of structural damage, i.e., boundary condition change or stiffness reduction, is detected by quantifying the dissimilarity of manifold topological structures. This study develops a damage feature that is sensitive to structural damage, but insensitive to changes in environmental and operational

conditions. The environmental and loading conditions affect the structural vibration characteristics in a complicated manner. For example, the Young's modulus, thermal stress and boundary conditions will be affected by air temperature and the thermal gradings in the entire structure, etc. It is difficult to numerically simulate realistic environmental and loading conditions on real bridge structures. However directly using the in-field vibration measurement data of structures is considered as the best way to validate the effectiveness and performance of the proposed approach. Therefore, the long-term SHM data measured from the two in-situ bridges are employed to verify the performance of proposed method. Figure 6-2 shows the flowchart of the proposed approach for structural damage detection from data obtained with varying environmental conditions.

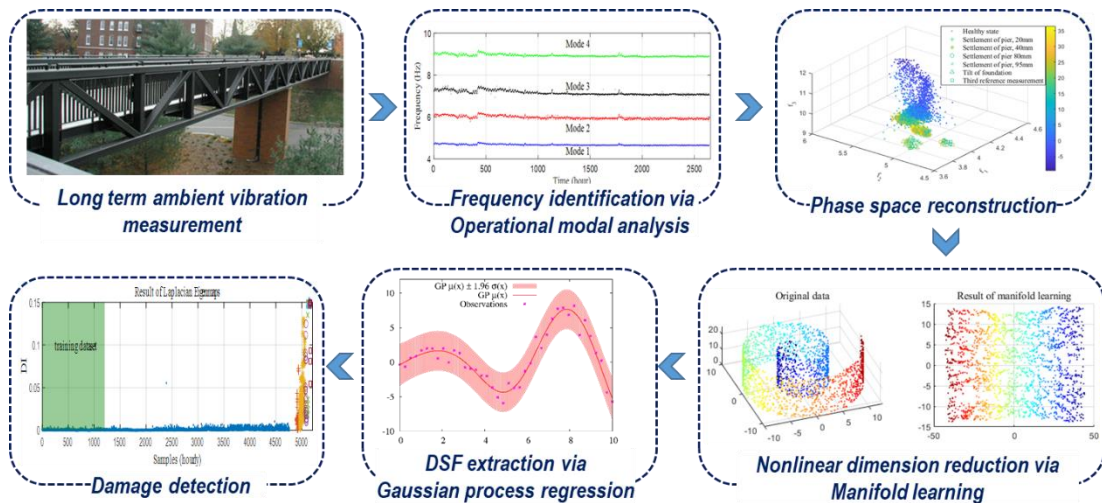


Figure 6-2. Flowchart of the proposed approach for structural damage detection from data obtained with varying environmental conditions.

6.3 Real-world Application 1: Dowling Hall Footbridge

In this section, about 16 weeks continuously monitored vibration responses of Dowling Hall Footbridge are utilized to verify the effectiveness and performance of using the proposed approach for structural condition monitoring. The Dowling Hall footbridge, as shown in Figure 6-3, is a two-span continuous steel frame structure located at the Medford campus of Tufts University, Massachusetts. The length and width of each span are about 22 m and 3.7 m, respectively. A vibration-based long term SHM system was designed and installed on this bridge in 2009 to measure the acceleration and strain responses as well as the temperature at different locations. The locations of installed sensors are shown in Figure 6-3(b). Vibration modes of this footbridge can be easily excited by the pedestrian and/or wind loads. During the monitoring period, no structural damage was observed. More details about the design and the

implementation of this SHM system are described in Ref. [30-32].

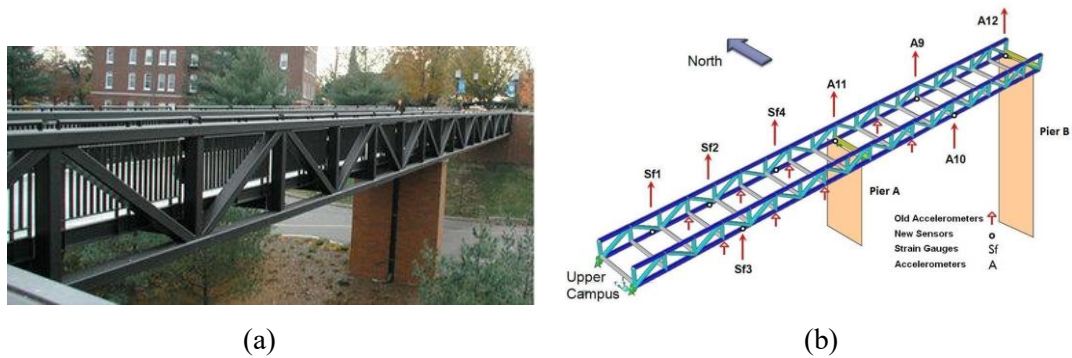


Figure 6-3. (a) Overview of the Dowling Hall footbridge; (b) Locations of installed sensors [32].

In this study, the first four natural frequencies of Dowling Hall footbridge during this 16 weeks are identified by using the poly-reference least squares complex frequency method (p-LSCF) [33, 34], which is one of the current widely used methods for operational modal analysis methods in the frequency domain. The identification results based on acceleration measurements in every hour are presented in Figure 6-4. The frequency variations in the first four natural frequencies owing to environmental and operational effects are 4.18%, 7.02%, 7.34% and 4.16%, respectively. As reported in an existing study [31], the first two mode shapes are bending modes in the vertical direction, and the third and fourth mode shapes of the bridges are torsional modes. The corresponding air temperature measurements in every hour during this 16 weeks are shown in Figure 6-5. The environmental temperature varies from $-11.5\text{ }^{\circ}\text{C}$ to $30\text{ }^{\circ}\text{C}$, and the lowest temperature is observed at 9.00 am, January 30, 2010 (sample 457 in Figure 6-4). Owing to the temperature difference between day and night time, a clear pattern of daily variation in the natural frequency is observed in Figure 6-4. Besides, the first four frequencies are obviously increased when the bridge experiences the lowest temperature.

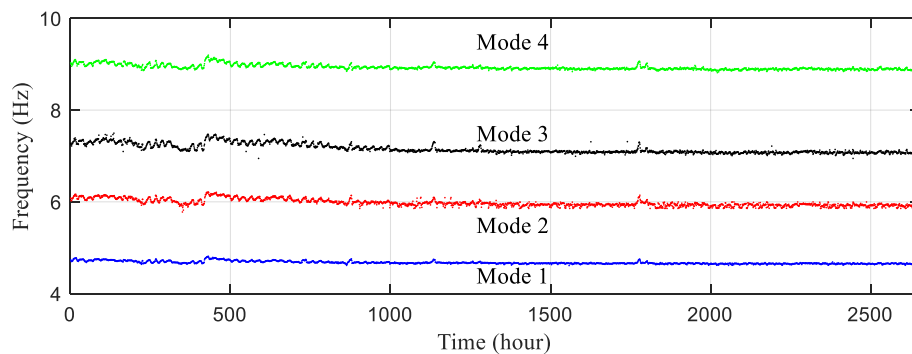


Figure 6-4. The identified first four natural frequencies during the monitored period.

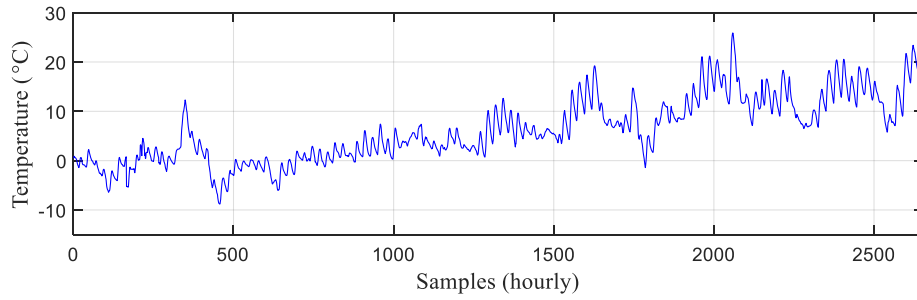


Figure 6-5. Air temperature variations during the monitored period.

Figure 6-6 shows the paired relationships between any two of the obtained natural frequencies. Overall, the natural frequencies raise with the decrease of environmental temperature. Curve-like topologic structures are observed in frequency pairs, i.e., f_1 vs f_2 , f_2 vs f_4 and f_3 vs f_4 . Linear relationship is observed in other frequency pairs. The 2D phase space topologic structures as shown in Figure 6-6 indicate that the temperature effect on each order frequency is different. To further visualize the temperature effect on a higher dimensional phase space, the first three natural frequencies are used to form a three-dimensional (3D) phase space. In Figure 6-7, the frequency observations form a spatial curve, and no distinct outlier cluster is observed in the 3D phase space.

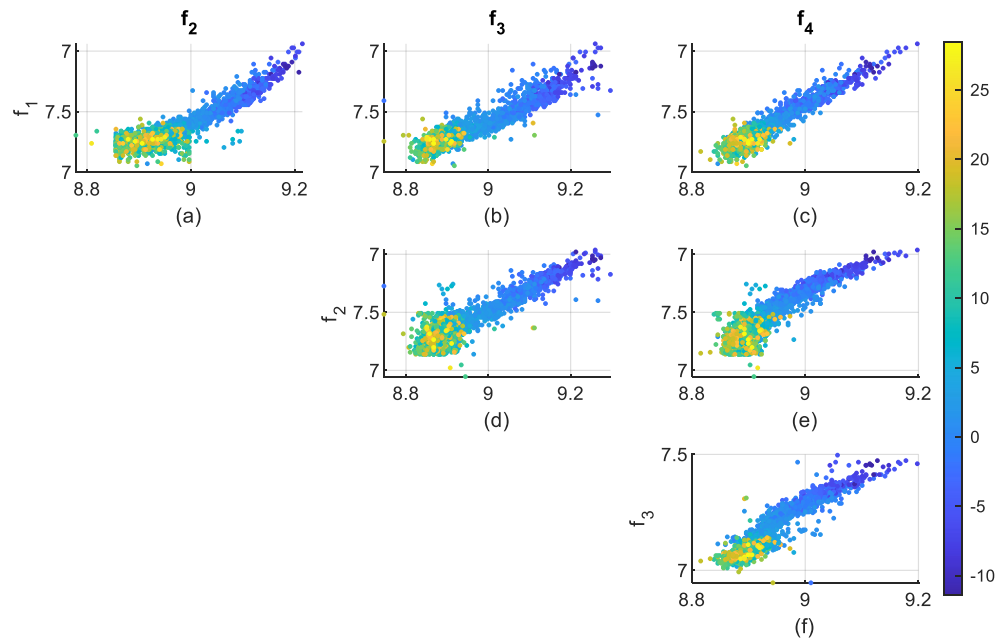


Figure 6-6. Visualisation of the relationships between the pairs of the first four natural frequencies. (The color bar denotes the environmental temperature).

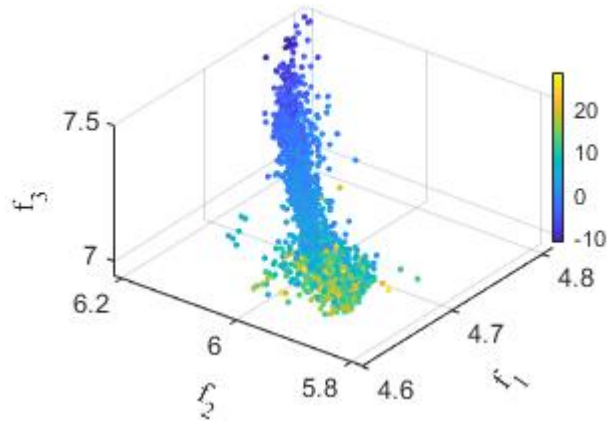


Figure 6-7. Visualisation of the nonlinear manifold of the Dowling Hall footbridge in the phase space spanned by the first three natural frequencies. (The color bar denotes the environmental temperature).

Generally speaking, the natural frequencies of bridge structures subjected to the operational condition are mainly affected by the temperature and loading conditions. The live loads applied on structures introduce additional mass and interaction effects to the bridge and thus induce frequency variations [35]. For a footbridge located on the campus, the pattern of live pedestrian loads on the bridge has periodically changes, which allows to understand the frequency variations attributed to live loads. In this study, the root mean square (RMS) of the acceleration responses is calculated to approximately evaluate the living load effects. Figure 6-8(a) and 8(c) statistically show the weekly and daily RMS variations within 16 weeks. It can be found that the RMS acceleration in weekday and the daytime (between 9 to 20 o'clock) are significantly higher than that of weekend and nighttime. The reason is that most of the pedestrians cross the bridge during the daytime in weekdays. The corresponding weekly and daily frequency variations are presented in Figure 6-8(b) and (d), respectively. As shown in Figure 6-8(b), the weekly variation of the mean value of the first-order frequency is about 0.3%. Compared with the overall temperature effect on the variation of the first-order natural frequency (4.18%), the live load effect on frequency is negligible.

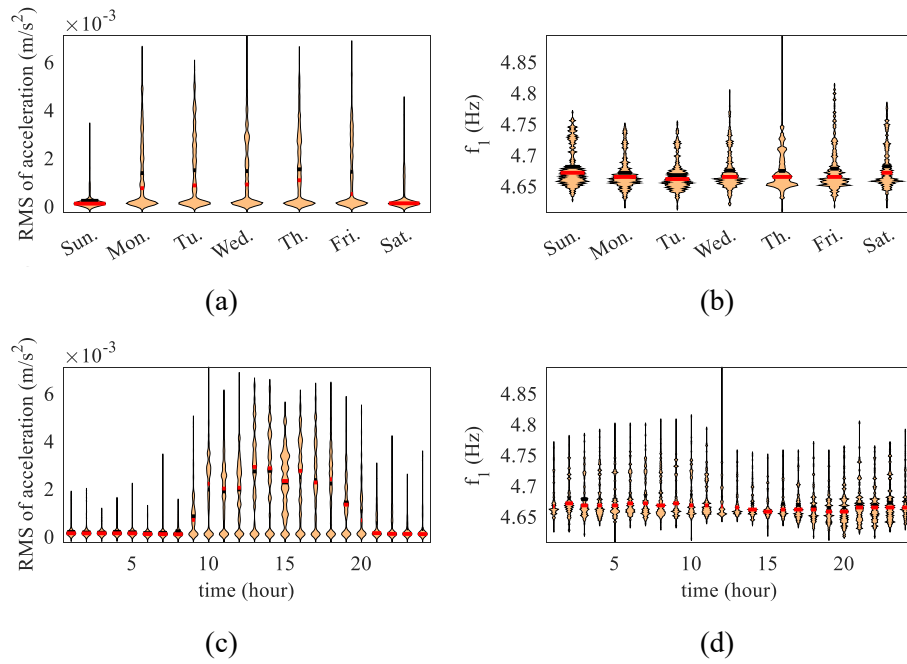


Figure 6-8. Effect of live load on natural frequency: (a) weekly RMS variation; (b) weekly frequency variation; (c) daily RMS variation; (d) daily frequency variation.

The first four natural frequencies of Dowling Hall footbridge shown in Figure 6-4 are utilized as input to the Laplacian Eigenmaps method and Kernel PCA method to project the manifold structure from four-dimensional observation space into 3D feature space. In the Laplacian Eigenmaps method, the number of nearest neighbors is set as 6. In the Kernel PCA method, the Gaussian kernel is used. The intrinsic structure of the underlying dynamic discovered by both nonlinear dimensionality reduction methods are visualized in Figure 6-9. The manifold identified by the Laplacian Eigenmaps is distributed along with the temperature. A better converged pattern is observed by using Laplacian Eigenmaps as shown in Figure 6-9(a) than that of the Kernel PCA method in Figure 6-9(b).

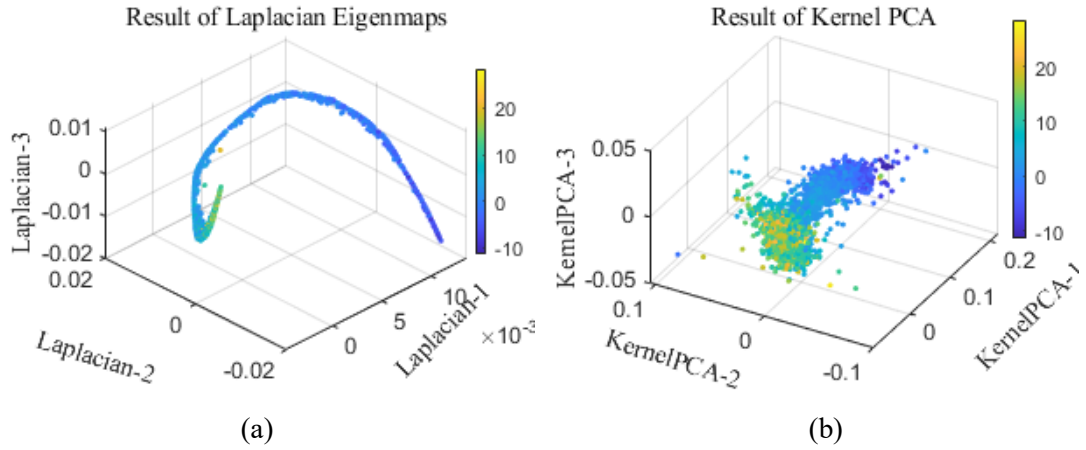


Figure 6-9. Manifold structures of the Dowling Hall Footbridge discovered by: (a) Laplacian Eigenmap method; (b) Kernel PCA method. (The color bar denotes the environmental temperature).

As mentioned in Section 2.3, a multivariate Gaussian process regression model is trained using the first two Laplacian components to predict the third Laplacian component. With the consideration that the extreme environment condition may not be experienced by the structure at the early stage of an installed SHM system, in this case study, only the first 400 samples are used to train the Gaussian process regression model. The air temperature measurements of Dowling Hall Footbridge are shown in Figure 6-5, and the temperature variation of the first 400 samples is between -7.5°C to 12.9°C , which only covers partial of overall temperature variations. The absolute prediction error of Gaussian process regression is used as DI to alarm the structural condition change, as described in Eq. (6.9). The DI obtained from the Laplacian Eigenmap and Kernel PCA with the training datasets of 400 samples are shown in Figure 6-10(a) and Figure 6-10(b), respectively. The DI of the proposed Laplacian Eigenmaps based Gaussian process regression method is very stable and remains at the same level even though the temperature exceeds the range of the training datasets. Meanwhile, significant fluctuation is observed in the DI calculated from Kernel PCA based Gaussian process regression method at the sample intervals from 416 to 449, when the structure experiences the lowest temperature. These errors are observed since the data under corresponding environmental conditions are not included in the training datasets.

To further investigate the effect of training dataset size on the environmental robustness of Kernel PCA based Gaussian process regression method and examine whether the performance can be improved, the first 1500 samples are utilized to fit the Gaussian process regression model. The false positive alarms appeared in Figure 6-10(b) owing to the extreme cold temperature, which, however, no longer exist in the results with more training samples as shown in Figure 6-10(c). In addition, the overall amplitude of DI is also slightly decreased,

which means that the environmental effects can be alleviated by including a wider range of temperature variations into the training datasets. However, it can be observed that larger damage index values are obtained for the testing sample, even when 1500 samples are used for training the Kernel PCA based method. Overall, no damage-induced outlier and very minor values are observed in the DI results calculated from the proposed approach, which is consistent with the ground truth. This demonstrates that using the proposed approach for damage detection is not subjected to environmental and operational conditions. Phase space based manifold learning method proposed in this study is robust to the environmental effects when measurement samples with only partial temperature variations are included in the training datasets. One possible reason is that nonlinear characteristics induced by temperature variations are captured by the phase space based manifold learning method. Therefore, the false alarm related to the extreme environmental condition is minimized. The damage feature extracted from the nonlinear regression tool such as Gaussian process regression, is directly related to the structural condition change and can be used as a reliable DSF for long term health monitoring.

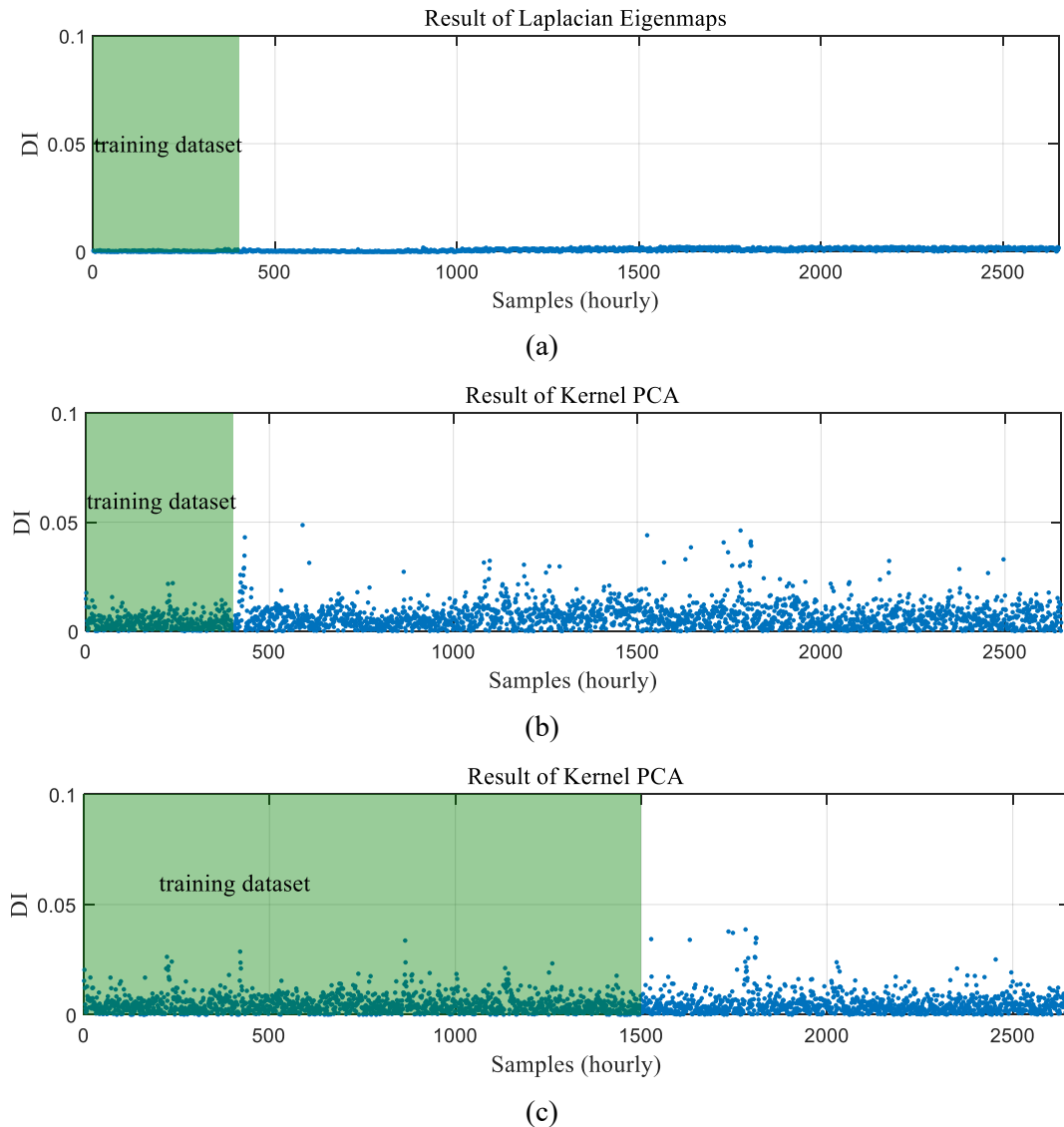


Figure 6-10. DI results of Dowling Hall footbridge: (a) Laplacian Eigenmaps with 400 training data; (b) Kernel PCA with 400 samples; and (c) Kernel PCA with 1500 samples.

6.4 Real-world Application 2: Z24 Bridge

In this section, a widely used benchmark structure, namely, Z24 bridge, is adopted to further verify the environmental robustness and sensitivity of using the proposed approach for damage detection. The Z24 bridge is a post-tensioned concrete box-girder bridge, which has been serviced as a full-scale benchmark to test the applicability of new developed long-term health monitoring and damage detection methods with the consideration of environmental and operational effects. Before the demolition in the 1990s, a SHM system has been installed to measure nearly one-year vibration responses and environmental variables, such as temperature, humidity, wind characteristic and traffic flow under operational conditions. At

the end stage of health monitoring, a series of progressive damage scenarios described in Table 6-1 [15] are artificially applied. A detailed description of the SHM system configuration, the introduced damage scenarios and implemented vibration tests can be found in Refs. [36-38]. System identification and damage detection methods have been developed in the past decades, for extracting DSFs that can be used to detect structural damage under the environmental conditions.

Table 6-1. Z24 progressive damage test scenarios

Sequence	Date	Description	Samples No.
D0	11-Nov-1997 to 4-Aug-1998	Baseline state	1~6393
D1	10-Aug-1998	Settlement of pier, 20mm	6514~6557
D2	12-Aug-1998	Settlement of pier, 40mm	6572~6671
D3	17-Aug-1998	Settlement of pier, 80mm	6682~6705
D4	18-Aug-1998	Settlement of pier, 95mm	6726~6745
D5	19-Aug-1998	Tilt of foundation	6745~6765
D6	20-Aug-1998	New Reference Measurement	6769~6788
D7	25-Aug-1998	Spalling of Concrete (12 m ²)	6874~6897
D8	26-Aug-1998	Spalling of Concrete (24 m ²)	6898~6921
D9	28-Aug-1998	Landslide of 1 m at abutment	6962~6993
D10	31-Aug-1998	Failure of concrete hinges at abutment pier	7019~7028
D11	02-Sep-1998	Failure of anchor heads of post tensioning cables (1 head)	7066~7089
D12	03-Sep-1998	Failure of anchor heads of post tensioning cables (4 heads)	7090~7113
D13	07-Sep-1998	Rupture of tendons #1	7186~7209
D14	08-Sep-1998	Rupture of tendons #2	7210~7233
D15	09-Sep-1998	Rupture of tendons #3	7234~7257

Figure 6-11 shows the hourly variations of the first five natural frequencies during the entire monitoring period identified by the p-LSCF method mentioned in Section 3. The first 4912 samples belong to the healthy state, the samples from 4913 to 5638 correspond to the progressive damage tests listed in Table 6-1. It should be mentioned that some samples with sensor fault or being unable to identify the first five modal frequencies have been removed. The environmental effects induced frequency variations of the first five natural frequencies under the healthy state are 17.22%, 20.34%, 14.69% 15.34% and 22.09%, respectively. The corresponding air temperature measurements of the bridge are shown in Figure 6-12. The temperature variation during the monitoring period is ranged from -9.6 °C to 35.7 °C. The time

scales between Figure 6-11 and Figure 6-12 are the same. Generally, the natural frequency is negatively correlated with the air temperature. Significant frequency fluctuations are observed in the samples from 1650 to 2300, owing to stiffness hardening caused by the soil-frozen effects, which is more obvious than the damage-induced frequency reduction in the first five natural frequencies [15, 39]. The performance of damage detection can be adversely affected, when the effect of environmental and operational conditions could not be eliminated. This is the reason that the nonlinear manifold learning is introduced in this study to alleviate the false-positives obtained in damage identification results due to the environmental and loading effects.

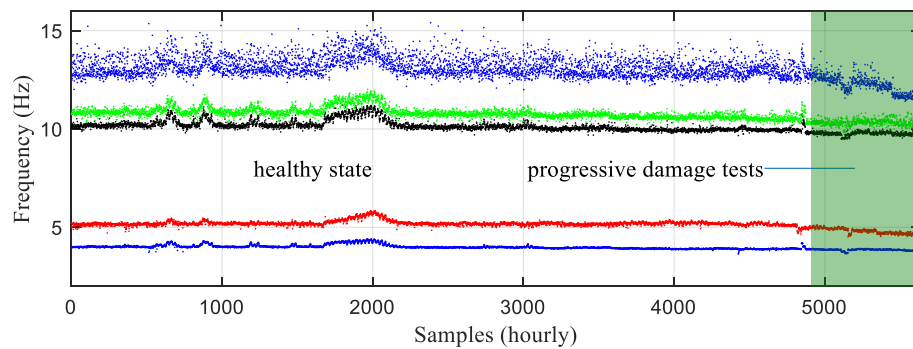


Figure 6-11. The first five natural frequencies during the monitoring period (the progressive damage scenarios are denoted by green background color).

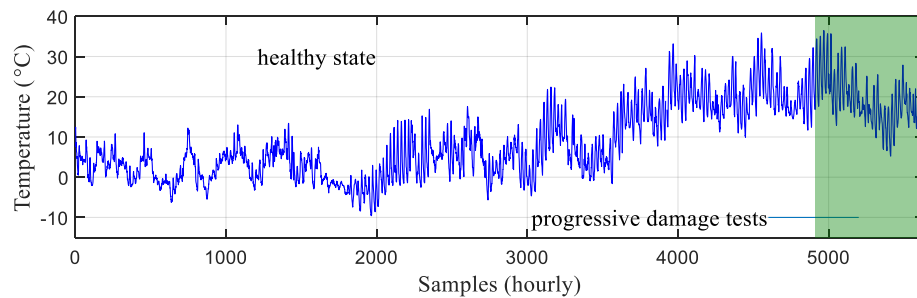


Figure 6-12. Air temperature measurements during the monitoring period.

In most previous studies, the relationships between natural frequency and temperature are derived. In this study, a pair of modal frequencies can be plotted to visualize the temperature effect. The relationship between a pair of natural frequencies can be viewed as the manifold of natural frequencies visualized in 2D phase space. In this study, both 2D and 3D phase spaces are respectively visualized in Figure 6-13 and Figure 6-14 to demonstrate that the underlying nonlinear manifold structure and structural condition can be better unfolded and classified in a higher dimensional phase space. In Figure 6-13, the natural frequencies under the healthy state are marked with the temperature-related color dots. The black dots represent the

observations under the damaged states. As shown in Figure 6-13, the frequency observations corresponding to similar temperature conditions are distributed closely with each other. Besides, the distribution of damaged states is overlapped with that of the healthy state, which means that the 2D phase space spanned by any two of the first five frequencies is unable to separate the damage states with healthy states. It is noted that the second natural frequency f_2 is nonlinearly (bilinear) correlated with f_1, f_3, f_4 and f_5 , while the natural frequencies f_1, f_3 and f_4 appear to be nearly linearly related with each other. One possible reason is that the second mode is transverse bending combined with the torsion of the girder, while the other four mode shapes are either vertical bending modes or vertical bending coupled with torsion [40]. Therefore, it can be preliminarily concluded that the extent of temperature effects on the modal parameter in different directions of the structure is different. This phenomenon is understandable since the mechanical properties such as boundary condition stiffness and cross-sectional moment of inertia are different in vertical, transverse and torsional directions. The correlation relationship between natural frequencies of Z24 bridge is quite different from that of Dowling Hall Footbridge, indicating that the temperature effects on natural frequencies are structure dependent. It is reasonable to see different relationships between vibration characteristics and temperature conditions on different structures.

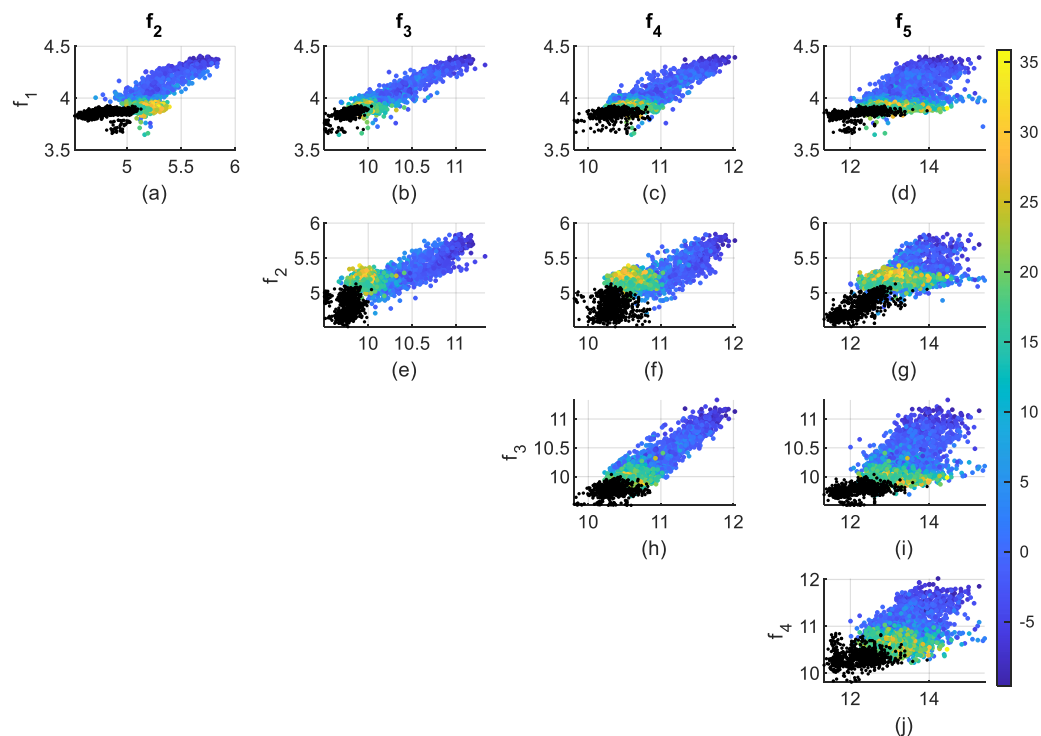


Figure 6-13. Visualisation of the relationships between any two of the first five natural frequencies. (Colored dots: the healthy state; Black dots: the damage state).

Following the same procedure in Section 3, the 3D nonlinear manifold structure of Z24

bridge is visualized in the phase space spanned by the first three order frequencies. Figure 6-14 presents the nonlinear manifold in the phase space using the measurements of the first three natural frequencies of Z24 bridge under the healthy state and the first 6 damage scenarios as listed in Table 6-1 with different environmental conditions. Compared with Figure 6-13, the distribution of damage states is well separated with that of the undamaged state in the 3D phase space, which means that the classification performance of structural condition changes can be improved in a higher dimensional observation space. In particular, the first six damage scenarios forms three distinct clusters (cluster 1: Damage scenarios D1~D3; cluster 2: Damage scenarios D4~D5; cluster 3: Damage scenario D6). The distributions of early damage scenarios D1~D3 are close to that of the structure under the healthy state corresponding to relatively high temperatures. In the third reference measurement (scenario D6), the foundation and pier were raised to the original position under the healthy state. It is reported in Ref. [40] that the bridge suffered an amount of cracks after damage scenario D5, but the reinforcement steel was still within the elastic range. However, the frequency distribution of the third reference measurement (D6) in the defined phase space cannot return to the original distribution corresponding to the healthy state. This means that the structural condition is irretrievable even though the deflection is within elastic stage and the settlement has been lifted to the original position. It is likely that the boundary condition has been changed during the implementation of settlements of pier and tilt of foundation in those damage scenarios. Therefore the new reference state in scenario D6 is different from the original healthy state.

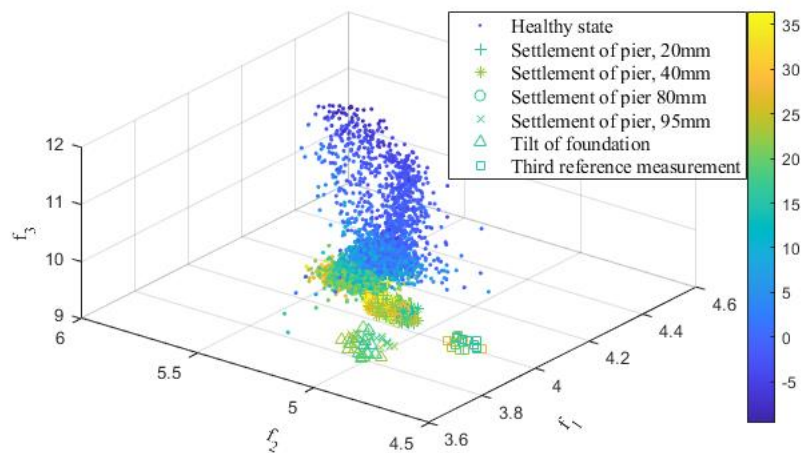


Figure 6-14. Visualisation of the nonlinear manifold of Z24 bridge in the phase space spanned by the first three natural frequencies.

Based on the visualisation of nonlinear manifold of Z24 bridge with operational condition changes as presented in Figure 6-13 and Figure 6-14, it is reasonable to consider that the accuracy of the manifold characteristics can be further improved when more observables are

used. In the higher dimensional phase space, the separation of different damage scenarios is more feasible. The phase space dimensions used for the Dowling Hall Footbridge and Z24 bridge are 4 and 5, respectively. The main purpose of using Laplacian eigenmap is to identify the low-dimensional (3D used in this study) manifold from the original high-dimensional phase space reconstructed from bridge natural frequencies. Furthermore, a manifold structure with dimensions higher than three could not be visualized effectively. Figure 6-15 shows a 3D scatter plot with a Laplacian Eigenmaps projection for the first five order natural frequencies presented in Figure 6-11. The manifold as shown in Figure 6-15(a) reveals two distinctive distributions of the obtained frequency datasets. The first one shows the curved surface-like manifold of the bridge under the healthy state with different environmental temperatures, and the other one presents the trajectory of damage scenarios. For comparison, the 3D scatter plot of the manifold obtained using the kernel PCA algorithm is presented in Figure 6-15(b). The observables corresponding to those damaged cases in the manifold learned by kernel PCA are overlapped with the healthy observables measured under high temperature conditions. This may cause some false damage identification results.

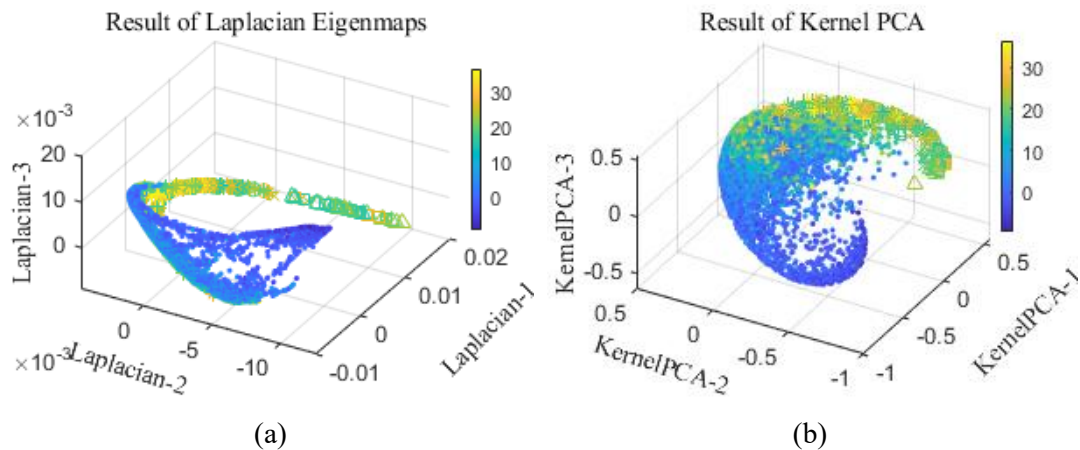


Figure 6-15. Manifold structures of the Z24 bridge discovered by: (a) Laplacian Eigenmap method; and (b) Kernel PCA method. (The symbols shown in this figure are the same as those defined in Figure 6-14).

The relationship between environmental temperature and the third Laplacian component predicted by the Gaussian process regression model is shown in Figure 6-16 to explain the underlying principles that the proposed damage feature is able to minimize the influences of temperature variations. As observed in Figure 6-16(a), the third Laplacian component predicted by the Gaussian process regression model under the damaged state is far away from that under the health state, which means that the proposed damage feature is more sensitive to damage while insensitive to temperature variation. In Figure 6-16(b), the samples corresponding to the hot and cold temperature conditions are distributed in two distinctive

directions, which means that the proposed approach learns the nonlinear characteristics of temperature effect on the vibration characteristics. Under the cold temperature conditions, the third Laplacian component value in the training dataset shows a decreasing trend with the decreasing temperature. It is noted that the results predicted by the Gaussian process regression model under the extreme cold temperature conditions, which are not within the temperature range of training datasets, are broadly consistent with the major trend obtained from the training datasets. The third Laplacian component values corresponding to the high temperatures that are not included in the training dataset (15°C to 35°C), are at the similar level as those in the training dataset from temperature 5°C to 15°C. The damaged state can be obviously separated from the healthy state even when samples under different environmental conditions are used for training.

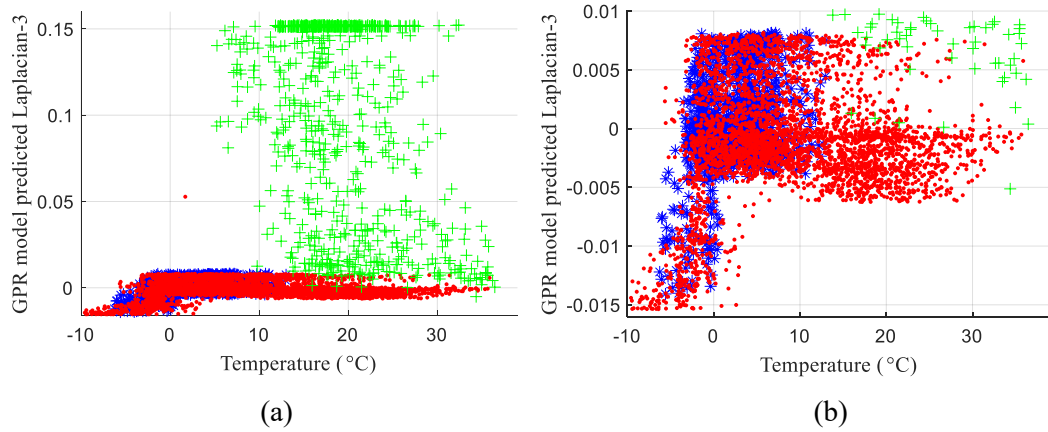


Figure 6-16. (a) The relationship between environmental temperature and the Gaussian process regression model predicted third Laplacian component; and (b) zoom in view of the samples corresponding to health state. Symbol *: training dataset (samples 1-1200); symbol • : Gaussian process regression model predicted samples corresponding to health state and symbol +: Gaussian process regression model predicted samples corresponding to damage state.

To investigate the sensitivity of using the proposed approach to detect structural damage and the robustness of environmental conditions, a predictive multivariate Gaussian process regression model is trained by using the first two components and the third component of Laplacian eigenmaps as input and output, respectively. With the consideration that the extreme environment conditions may not be experienced by the structure at the early stage when a SHM system is installed, only the first 1200 samples are served as the training datasets. It should be noted that the training data cover only partial of the environmental variations from -6.3 °C to 13.0 °C. In particular, the extremely low temperature samples during the sample intervals from 1650 to 2300 as well as the relatively high temperature region from 3500 to 4500 are not covered. The absolute prediction error defined in Eq. (6.9) is used as the DI to

alarm the structural condition change. The DI obtained from the Laplacian Eigenmap is presented in Figure 6-17(a). The DI is very stable in the healthy states, and no visible false-positive alarm is observed under sub-zero and high temperature conditions. The DI values increase significantly when the progressive damage scenarios are applied to the bridge, demonstrating that the introduced damage can be detected effectively, even though different environmental conditions are considered. The encouraging results indicate that the mechanism of temperature-induced nonlinearity is acquired accurately by the proposed approach with a limited training dataset. Furthermore, the DI defined based on the proposed approach is sensitive to structural condition change while insensitive to operational condition changes. For comparison, Figure 6-17(b) provides the damage detection results of using Kernel PCA with a training dataset size of 1200 samples. As observed, there is an obvious peak around the sample 2000, when the temperature is colder than the lowest temperature used in the training data. The amplitude of false positive detection results is at the same level or even higher than that of the introduced damaged cases, indicating that the performance of using Kernel PCA for damage detection could be comprised. To alleviate the potential false identification, the number of samples in Gaussian process regression modal training datasets is increased to 3000 for Kernel PCA, which covers a wider range of environmental conditions under the healthy state. In Figure 6-17(c), no visible peak is observed in the low temperature region, which indicates that the damage detection capacity of using Kernel PCA-based Gaussian process regression model could be significantly enhanced by increasing the size of training dataset.

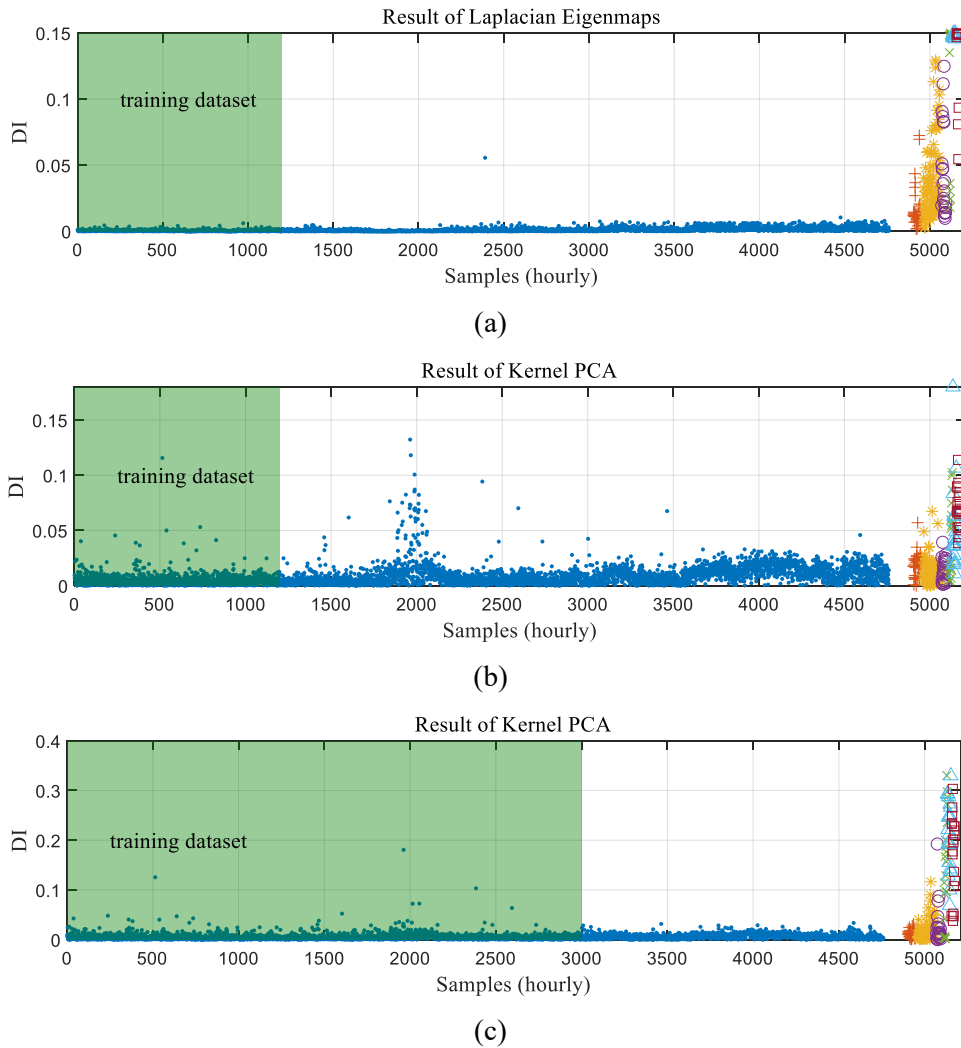
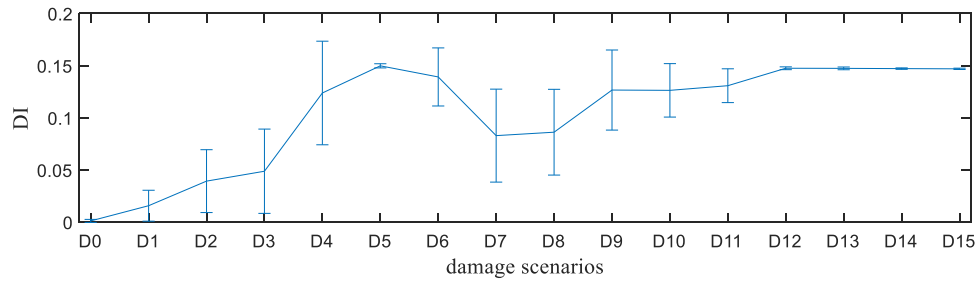


Figure 6-17. Comparison of damage detection results: (a) The proposed approach with training datasets of 1200 samples; (b) Kernel PCA with 1200 samples; and (c) Kernel PCA with 3000 samples.

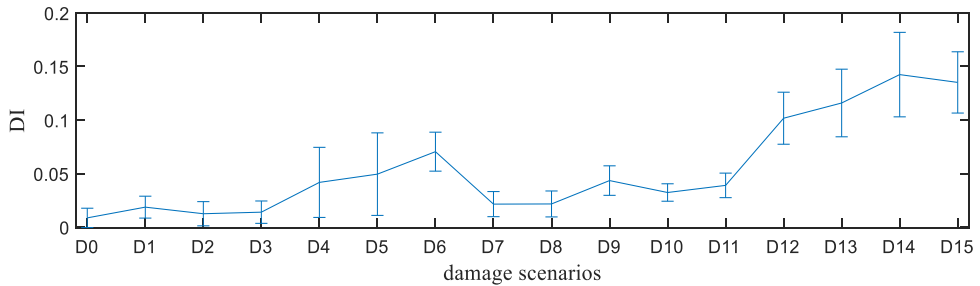
In order to compare the sensitivity of using the proposed approach for detecting damage with Kernel PCA, DI values under the healthy (D0) and damaged states (D1-D15) are calculated and listed in Table 6-1. Figure 6-17(a) and (b) compare the mean values and standard deviations of DI values by using both methods with a training dataset size of 1200. Under the healthy state D0, the amplitude of DI in Figure 6-18(a) obtained by the proposed approach is obviously smaller than those of other damage scenarios. This indicates that the damage introduced in those damage scenarios can be well detected. The DI values of the introduced damage scenarios by using the proposed approach are generally larger than those by using Kernel PCA. On the other hand, for the results obtained with Kernel PCA, similar DI values between D0 and D1~D3 are observed as shown in Figure 6-18(b), which means that the DI calculated from Kernel PCA based method may introduce false identification results. When more samples are included in the training datasets of using Kernel PCA method, a better

performance is obtained. No false identification is obtained. It should be noted that the results of using the Kernel PCA-based method presented in Figure 6-17(c) already outperform most of the data-driven damage detection methods applied to the Z24 bridge benchmark during the past decade [15, 41, 42]. Comparison results show that the proposed approach can be used to alarm structural condition change with a higher confidence and sensitivity, especially when only a limited number of training data are available. In conclusion, the applicability and performance of the proposed approach developed in this study are superior than those of the existing state-of-the-art Kernel PCA-based methods in accurately detecting structural damage.

However, since the DI defined in this study is calculated from the prediction residual, it is unable to generate a linear relationship between the DI value and the structural stiffness reduction induced by structural damage. In the progressive damage tests, different types and extents of damage are artificially applied. Therefore, the damage scenarios fall into a multiple damage feature space, with different types of damage and different damage extents. It is unrealistic to quantify the damage extent using the one-dimensional DI defined in this study without errors. However, there are some impressive results that can be extracted from Figure 6-18. For example, before introducing the damage scenario D6 as a new reference state, an upward trend of the mean values of DI is observed from D1 to D5. This is evident by the introduced increasing settlement of bridge piers. Another increasing trend in the DI values is observed from the damage scenarios D7 to D15, as observed in Figure 6-17(a) and (b), since further progressive damage is introduced in the bridge. These results demonstrate that the DI values obtained from the proposed approach can reliably detect the structural damage and have the potential to indicate the development of damage severity in structures. It should be noted that only the measurements under the healthy states are included in the training and calculating the defined DI, and no measurements under the damaged states are required in prior for the training.



(a)



(b)

Figure 6-18. Damage detection results of using: (a) The proposed approach with 1200 training samples; and (b) Kernel PCA with 1200 training samples.

In this study, the phase space representation of vibration characteristics is reconstructed by using the identified natural frequencies of structures. The adjacent points in the phase space correspond to similar structural conditions. For example, as shown in Figure 6-14, the samples corresponding to similar temperature and structural condition are close to each other. Both the Laplacian eigenmaps from manifold learning method used in this study and kernel PCA are representative nonlinear dimension reduction methods. As indicated in Eqs. (4-5), the Laplacian eigenmap based on manifold learning method constructs the adjacency graph from the high dimension phase space. The node and edge in the adjacency graph represent a sample and the similarity between two nodes. The weighting coefficient is large when two samples are very close. By this way, the low dimension projection has locality-preserving properties. However, Kernel PCA fails to consider the locality preserving constraint.

6.5 Conclusions

This chapter proposes a novel damage detection approach based on the phase space based manifold learning technique, for the reliable assessment of the healthy condition of real-world civil engineering structures subjected to environmental and operational conditions. The inherent nonlinear relationship between temperature variation and structural vibration properties is unfolded in the high-dimensional phase space spanned by the identified natural frequencies. Then the topological structure of the underlying system is projected into a low-

dimensional space via manifold learning. Gaussian process regression model is then applied to the low-dimensional manifold to extract DSF for structural damage detection. Vibration responses measured from two in-situ bridges, namely Dowling Hall Footbridge and Z24 bridge are utilized to validate the applicability and performance of the proposed approach for structural damage detection under ambient operation conditions. In summary, the proposed approach is sensitive to structural damage but not sensitive to environmental and loading conditions, even when only observations from the healthy state under partial environmental and operational variations are available and included in the training datasets. This shows a promising performance of using the proposed approach for damage detection of structures based on long term SHM data.

References

- [1] R. Hou, Y. Xia, Review on the new development of vibration-based damage identification for civil engineering structures: 2010–2019, *Journal of Sound and Vibration*, (2020) 115741.
- [2] A. Deraemaeker, E. Reynders, G. De Roeck, J. Kullaa, Vibration-based structural health monitoring using output-only measurements under changing environment, *Mechanical systems and signal processing*, 22 (2008) 34-56.
- [3] Y. Xia, B. Chen, S. Weng, Y.-Q. Ni, Y.-L. Xu, Temperature effect on vibration properties of civil structures: a literature review and case studies, *Journal of civil structural health monitoring*, 2 (2012) 29-46.
- [4] Y. Xia, H. Hao, G. Zanardo, A. Deeks, Long term vibration monitoring of an RC slab: temperature and humidity effect, *Engineering structures*, 28 (2006) 441-452.
- [5] J. Teng, D.-H. Tang, W.-H. Hu, W. Lu, Z.-W. Feng, C.-F. Ao, M.-H. Liao, Mechanism of the effect of temperature on frequency based on long-term monitoring of an arch bridge, *Structural Health Monitoring*, (2020) 1475921720931370.
- [6] V. Meruane, W. Heylen, Structural damage assessment under varying temperature conditions, *Structural Health Monitoring*, 11 (2012) 345-357.
- [7] S. Pereira, F. Magalhães, J.P. Gomes, Á. Cunha, J.V. Lemos, Vibration-based damage detection of a concrete arch dam, *Engineering Structures*, 235 (2021) 112032.
- [8] Y. Cao, J. Yim, Y. Zhao, M.L. Wang, Temperature effects on cable stayed bridge using health monitoring system: a case study, *Structural Health Monitoring*, 10 (2011) 523-537.
- [9] N. de Battista, J.M. Brownjohn, H.P. Tan, K.-Y. Koo, Measuring and modelling the thermal performance of the Tamar Suspension Bridge using a wireless sensor network, *Structure and Infrastructure Engineering*, 11 (2015) 176-193.
- [10] A. Santos, E. Figueiredo, M. Silva, C. Sales, J. Costa, Machine learning algorithms for damage detection: Kernel-based approaches, *Journal of Sound and Vibration*, 363 (2016) 584-599.
- [11] H. He, W. Wang, X. Zhang, Frequency modification of continuous beam bridge based on co-integration analysis considering the effect of temperature and humidity, *Structural Health Monitoring*, 18 (2019) 376-389.
- [12] J. Gu, M. Gul, X. Wu, Damage detection under varying temperature using artificial neural networks, *Structural Control and Health Monitoring*, 24 (2017) e1998.
- [13] Z. Nie, H. Hao, H. Ma, Using vibration phase space topology changes for structural damage detection, *Structural Health Monitoring*, 11 (2012) 538-557.
- [14] Z. Peng, J. Li, H. Hao, Z. Nie, Improving identifiability of structural damage using higher order responses and phase space technique, *Structural Control and Health Monitoring*, (2021) e2808.
- [15] E. Reynders, G. Wursten, G. De Roeck, Output-only structural health monitoring in changing environmental conditions by means of nonlinear system identification, *Structural Health Monitoring*, 13 (2014) 82-93.
- [16] Y. Bengio, A. Courville, P. Vincent, Representation learning: A review and new perspectives, *IEEE transactions on pattern analysis and machine intelligence*, 35 (2013) 1798-1828.
- [17] M. Balasubramanian, E.L. Schwartz, J.B. Tenenbaum, V. de Silva, J.C. Langford, The isomap algorithm and topological stability, *Science*, 295 (2002) 7-7.

- [18] S.T. Roweis, L.K. Saul, Nonlinear dimensionality reduction by locally linear embedding, *science*, 290 (2000) 2323-2326.
- [19] M. Belkin, P. Niyogi, Laplacian eigenmaps for dimensionality reduction and data representation, *Neural computation*, 15 (2003) 1373-1396.
- [20] Y. Huang, G. Kou, Y. Peng, Nonlinear manifold learning for early warnings in financial markets, *European Journal of Operational Research*, 258 (2017) 692-702.
- [21] D. Lungu, S. Prasad, M.M. Crawford, O. Ersoy, Manifold-learning-based feature extraction for classification of hyperspectral data: A review of advances in manifold learning, *IEEE Signal Processing Magazine*, 31 (2013) 55-66.
- [22] Y. Wang, G. Xu, L. Liang, K. Jiang, Detection of weak transient signals based on wavelet packet transform and manifold learning for rolling element bearing fault diagnosis, *Mechanical Systems and Signal Processing*, 54 (2015) 259-276.
- [23] J.X. Leon-Medina, M. Anaya, D.A. Tibaduiza, F. Pozo, Manifold Learning Algorithms Applied to Structural Damage Classification, *Journal of Applied and Computational Mechanics*, (2020).
- [24] Y. Xin, H. Hao, J. Li, Operational modal identification of structures based on improved empirical wavelet transform, *Structural Control and Health Monitoring*, 26 (2019) e2323.
- [25] Y. Xia, Y.-L. Xu, Z.-L. Wei, H.-P. Zhu, X.-Q. Zhou, Variation of structural vibration characteristics versus non-uniform temperature distribution, *Engineering structures*, 33 (2011) 146-153.
- [26] B. Bayik, P. Omenzetter, E. Pavlovskaja, Experimental modelling of a top-tensioned riser for vibration-based damage detection, *Engineering Structures*, 223 (2020) 111139.
- [27] W. Wang, Y. Yan, F. Nie, S. Yan, N. Sebe, Flexible manifold learning with optimal graph for image and video representation, *IEEE Transactions on Image Processing*, 27 (2018) 2664-2675.
- [28] M. Belkin, P. Niyogi, Laplacian eigenmaps and spectral techniques for embedding and clustering, in: *Nips*, 2001, pp. 585-591.
- [29] S.T. Tu, J.Y. Chen, W. Yang, H. Sun, Laplacian eigenmaps-based polarimetric dimensionality reduction for SAR image classification, *IEEE Transactions on Geoscience and Remote Sensing*, 50 (2011) 170-179.
- [30] B. Moaveni, I. Behmanesh, Effects of changing ambient temperature on finite element model updating of the Dowling Hall Footbridge, *Engineering Structures*, 43 (2012) 58-68.
- [31] P. Moser, B. Moaveni, Environmental effects on the identified natural frequencies of the Dowling Hall Footbridge, *Mechanical Systems and Signal Processing*, 25 (2011) 2336-2357.
- [32] P. Moser, B. Moaveni, Design and deployment of a continuous monitoring system for the Dowling Hall Footbridges, *Experimental Techniques*, 37 (2013) 15-26.
- [33] S. Diord, F. Magalhães, Á. Cunha, E. Caetano, N. Martins, Automated modal tracking in a football stadium suspension roof for detection of structural changes, *Structural Control and Health Monitoring*, 24 (2017) e2006.
- [34] W.-H. Hu, S. Thöns, R.G. Rohrmann, S. Said, W. Rücker, Vibration-based structural health monitoring of a wind turbine system. Part I: Resonance phenomenon, *Engineering Structures*, 89 (2015) 260-272.
- [35] H. Moghimi, H.R. Ronagh, Development of a numerical model for bridge-vehicle interaction and human response to traffic-induced vibration, *Engineering Structures*, 30

(2008) 3808-3819.

- [36] B. Peeters, G. De Roeck, One - year monitoring of the Z24 - Bridge: environmental effects versus damage events, *Earthquake engineering & structural dynamics*, 30 (2001) 149-171.
- [37] J. Maeck, B. Peeters, G. De Roeck, Damage identification on the Z24 bridge using vibration monitoring, *Smart materials and structures*, 10 (2001) 512.
- [38] W.S.L. Wah, Y.-T. Chen, J.S. Owen, A regression-based damage detection method for structures subjected to changing environmental and operational conditions, *Engineering Structures*, 228 (2021) 111462.
- [39] S. Zhou, W. Song, Environmental - effects - embedded model updating method considering environmental impacts, *Structural Control and Health Monitoring*, 25 (2018) e2116.
- [40] R. Brincker, P. Andersen, R. Cantieni, Identification and level I damage detection of the Z24 highway bridge, *Experimental techniques*, 25 (2001) 51-57.
- [41] W.S.L. Wah, J.S. Owen, Y.-T. Chen, A. Elamin, G.W. Roberts, Removal of masking effect for damage detection of structures, *Engineering Structures*, 183 (2019) 646-661.
- [42] W. Soo Lon Wah, Y.-T. Chen, G.W. Roberts, A. Elamin, Separating damage from environmental effects affecting civil structures for near real-time damage detection, *Structural Health Monitoring*, 17 (2018) 850-868.

CHAPTER 7 FINITE LINEAR REPRESENTATION OF NONLINEAR STRUCTURAL DYNAMICS USING PHASE SPACE EMBEDDING COORDINATE

ABSTRACT⁶

Modelling of structural nonlinear dynamic behavior is a central challenge in civil and mechanical engineering communities. The phase space embedding of response time series has been demonstrated to be an efficient coordinate basis for data-driven approximation of the modern Koopman operator, which can fully capture the global evolution of nonlinear dynamics by a linear representation. This study demonstrates that linear and nonlinear structural dynamic vibrations can be represented by a universal forced linear model in a finite dimension space projected by time-delay coordinates. Compared to the existing methods, the proposed approach improves the performance of finite linear representation of nonlinear structural dynamics on two essential issues including the robustness to measurement noise and applicability to multi-degree-of-freedom (MDOF) systems. For linear structures, the dynamic mode shapes and the corresponding natural frequencies can be accurately identified by using the time-delay DMD algorithm with acceleration response data experimentally measured from an eight-story shear-type linear steel frame. Modal parameters extracted from the time-delay DMD match well with those identified from traditional modal identification methods, such as frequency domain decomposition (FDD) and complex mode indicator function (CMIF). In addition, numerical and experimental studies on nonlinear structures are conducted to demonstrate that the finite dimensional DMD based on the discrete Hankel SVD coordinate is highly symmetrically structured, and is able to accurately obtain a linear representation of structural nonlinear vibration. The resulting linearized data-driven equation-free model can be used to accurately predict the responses of nonlinear systems with limited training datasets.

7.1 Introduction

The geometric, material, boundary and structural damage-induced nonlinearities exist widely in civil/mechanical structures or components, which are frequently manifested by complex nonlinear behaviors, i.e. nonlinear harmonic generation and/or nonlinear attenuation in observed vibration responses [1, 2]. The state-of-the-art experimental and analytical modal

⁶ Peng, Z., Li, J., Hao, H. Finite linear representation of nonlinear structural dynamics using phase space embedding coordinate. (Under review).

analysis involves methods using a small set of parameters to describe the dynamic behavior of structures [3]. In reality, most structures are subjected to a certain extent of nonlinear and non-stationary vibration behavior, therefore, modal analysis techniques based on linearity assumption may fail to provide accurate estimation or prediction of nonlinear problems [4]. A variety of data-driven methods and mathematical models, such as ARMA, Kalman filter, Volterra series, machine learning, deep learning and its derived methods, are extensively developed to discover and describe nonlinear behavior of structures [5]. Despite its long success, lack of direct physical interpretability is increasingly recognised as one of the main obstacles of machine learning/deep learning and similar data-driven techniques. Alternatively, a nonlinear structural system can be generally considered as a linear system with the nonlinearity induced restoring force along with the external excitation based on an underlying linear system [6, 7]. Consequently, state space models based on linear theory can be used to estimate, predict and control the dynamic behavior of nonlinear systems in many diverse engineering fields. For civil and mechanical engineering structures, the full measurement of the governing variables, namely, displacement, velocity and acceleration responses are required to construct the equation of motion of interest. In practice, only partial measurements, i.e. acceleration responses at a limited number of locations are usually available and the corresponding velocities and displacements are obtained through numerical integration. The measurement noise along with the integration error may degrade the accuracy of state space model. In this regards, advanced signal processing techniques in conjunction with partially measurable state information are constantly reported to reconstruct the full state variables of dynamic systems [8].

For a dynamic system with incomplete observations, time-delay embedding is a promising technique to augment the information contained in the system state by constructing PST from univariate measurement with suitable embedding dimension and time lag [9]. Takens' embedding theorem reveals that the reconstructed PST can be diffeomorphic to the original system attractor traced out by full state variables [10]. Two manifolds are said to be diffeomorphic if there exists a diffeomorphism between them, which is an isomorphism of smooth manifolds. It is an invertible function that maps one differentiable manifold to another such that both the functions and its inverse are smooth. The phase space reconstruction of well-known chaos systems, such as Duffing oscillator and Lorenz attractor, is commonly used to intuitively interpret the definition of diffeomorphic [11]. For deterministic system, each possible state corresponds to one unique point in the phase space. Signal processing techniques developed based on time delay embedding, such as Eigensystem realization algorithm (ERA) [12], SSA [13] and nonlinear Laplacian spectral analysis [14], have been widely applied to system identification, spectral estimation as well as nonstationary signal prediction. Hankel

alternative view of Koopman (HAVOK) analysis is a recently developed data-driven framework, which combines the time delay embedding strategy with modern Koopman operator theory to represent nonlinear systems from a linearized perspective for nonlinear dynamics analysis [15]. The central principle of Koopman operator is to map the time series measurements into a new coordinate system, where nonlinear manifold can be reproduced by linear evolution on the newly-defined coordinate system space [16, 17]. Nonlinear linearization model is desirable because it allows using many efficient estimation, prediction and control methods based on linear theory for nonlinear systems. In practice, the proper choice of appropriate coordinate basis is crucial to characterise the underlying dynamic, but is often difficult to evaluate without domain-specific knowledge.

To this end, a variety of approaches have been developed. For example, extended dynamic mode decomposition (EDMD) [18] and kernel DMD have been recently proposed by potentially augmenting a boarder set of observables, i.e. polynomial kernel, radial basis functions and sigmoid kernel [19] to the conventional linear coordinate system. Besides, machine learning methods, such as manifold learning and dictionary learning, have also been integrated to address this issue [20]. The HAVOK framework conducts SVD and uses the right-singular vectors of time-delay embedding matrix as observables (hereafter refers to as Hankel SVD coordinate) to approximate the Koopman operator. This framework has been successfully applied to a series of well-known nonlinear dynamic examples including Lorenz attractor, Duffing oscillator and Van der Pol oscillator as well as real-world examples like data from Earth's magnetic field reversal, electrocardiogram, electroencephalogram, measles outbreaks and power grid load, etc. [21]. Results demonstrated that the space of observables spanned by Hankel SVD coordinate is admitted as a faithful linear representation of nonlinear dynamics. Kamb et al. [22] and Lusch et al. [23] theoretically proofed that the time-delay coordinate forms an optimal finite-dimensional basis for representing the time-invariant Koopman operator. However, the feasibility of using HAVOC framework for analysing the dynamic vibration responses of civil/mechanical structures is still unexplored. Typically, using the HAVOC framework for processing the structural vibration responses faces two potential challenges. Firstly, the response signals of the above-mentioned nonlinear dynamic examples are from a single channel. Extension should be made to process the multi-channel vibration responses recorded from MDOF structures. Secondly, continuous Hankel SVD coordinate is used in the original HAVOC framework to approximate the Koopman operator. The measurement noise effect might be amplified to calculate the derivative of the Hankel SVD coordinate. Therefore, the effect of inevitable measurement noise should be carefully considered.

The proposed approach in this study is built on the HAVOK framework by including the

spatially distributed structural vibration responses, which allows for finding spatiotemporal linear representation of MDOF nonlinear structures. Two main improvements are made in this study. Firstly, the multi-channel phase space embedding is introduced to accommodate the vibration responses recorded from MDOF structure. Secondly, apart from the original HAVOC framework with continuous Hankel SVD coordinate, the HAVOC framework based on discrete Hankel SVD coordinate is introduced to alleviate the noise effect. The prediction performance of using HAVOC framework based on discrete Hankel SVD coordinate is demonstrated to be better than the original continuous form. It is noteworthy that the proposed method is fully data-driven, which learns a forced linear model in Hankel SVD coordinate in an unsupervised manner. The proposed method has the following advantages: (1) Only partial system state information (acceleration or displacement responses) is required, thus, the non-negligible errors in full-state variables reconstruction introduced from integration or differentiation procedure are avoided; (2) The proposed method based on the Hankel SVD coordinate can be used to obtain a linear model and Koopman invariant measurement system that nearly perfectly captures the dynamics of nonlinear quasiperiodic systems; (3) The proposed method is feasible for both linear and nonlinear dynamic systems. For linear systems, the computed Hankel SVD coordinate matches with that extracted via time-delay DMD algorithm. The corresponding modal parameters, such as natural frequencies and modal shapes, can be accurately identified.

The layout of this chapter is organised as follows. Section 2 summarises the process, where the phase space representation is obtained from MDOF state variable measurement. The regression of linear DMD with three types of coordinate basis, namely, the time-delay coordinate, continuous Hankel SVD coordinate and discrete Hankel SVD coordinate are presented. Section 3 experimentally demonstrates the feasibility and efficiency of using time-delay DMD in modelling the linear systems and extracting modal parameters from acquired vibration responses of an eight-story shear-type linear steel frame subjected to hammer loads. Section 4 reveals the applicability of continuous and discrete Hankel SVD coordinate systems on linearising the structural nonlinear vibrations acquired from numerical and experimental structures. The presented method is successful in discovering finite dimension predictive linearization representation of structural nonlinear vibrations in a fully unsupervised manner. In Section 5, concluding remarks are provided.

7.2 Data-driven decomposition of nonlinear dynamic into forced linear model

7.2.1 Time-delay embedding and DMD for linear systems

Generally speaking, a forced nonlinear dynamic system can be expressed as follows

$$\begin{cases} \dot{\mathbf{z}}(t) = f(\mathbf{z}(t), \mathbf{u}(t)) \\ \mathbf{z}(t) = [\mathbf{x}(t) \ \dot{\mathbf{x}}(t)]^T \end{cases} \quad (7.1)$$

in which $\mathbf{z}(t) = [\mathbf{x}(t) \ \dot{\mathbf{x}}(t)]^T$ denotes the state space vector. For a discrete n DOFs nonlinear dynamic system, $\mathbf{x}(t) = [x_1(t), x_2(t), \dots, x_n(t)]^T$ and $\dot{\mathbf{x}}(t) = [\dot{x}_1(t), \dot{x}_2(t), \dots, \dot{x}_n(t)]^T$ represent the displacement vector and velocity vector at the time instant t , respectively. $\mathbf{u}(t)$ is the external loading vector applied on each DOF. $f(\cdot)$ is a general, possibly nonlinear mapping function of the underlying system. An alternative way to visualize the system dynamics is to build the state-space dynamic attractor from all the state variables [24]. In practice, only partial state variable, i.e. acceleration or displacement responses of structures are directly measured from instrumented sensors. Thus, the time-delay embedding of partially observed state information is implemented to reconstruct the PST. Under a certain condition, the full dynamics of a system as complicated as a turbulent fluid could be unfolded from a phase space embedding of a single point measurement [15]. The reconstructed PST can be diffeomorphic to the original state space attractor.

For an acceleration time series $a(t) \in \mathbb{R}$ measured from a specific location of the structure, it is possible to transform it to higher embedding dimension via time-shift copies of itself. The resulted Hankel matrix \mathbf{H} is expressed as follows

$$\mathbf{H} = \begin{bmatrix} a(t_1) & a(t_2) & \cdots & a(t_m) \\ a(t_2) & a(t_3) & \cdots & a(t_{m+1}) \\ \vdots & \vdots & \ddots & \vdots \\ a(t_d) & a(t_{d+1}) & \cdots & a(t_{d+m-1}) \end{bmatrix} \quad (7.2)$$

where m and d represent the window size and embedding dimension, respectively. The extension of phase space embedding procedure to the case of MDOF system is straightforward. For a vector $(t) \in \mathbb{R}^n$, the resulted Hankel matrix \mathbf{H} in Eq. (7.2) becomes

$$\mathbf{H} = \begin{bmatrix} \mathbf{a}(t_1) & \mathbf{a}(t_2) & \cdots & \mathbf{a}(t_m) \\ \mathbf{a}(t_2) & \mathbf{a}(t_3) & \cdots & \mathbf{a}(t_{m+1}) \\ \vdots & \vdots & \ddots & \vdots \\ \mathbf{a}(t_d) & \mathbf{a}(t_{d+1}) & \cdots & \mathbf{a}(t_{d+m-1}) \end{bmatrix}, \mathbf{H}' = \begin{bmatrix} \mathbf{a}(t_2) & \mathbf{a}(t_3) & \cdots & \mathbf{a}(t_{m+1}) \\ \mathbf{a}(t_3) & \mathbf{a}(t_4) & \cdots & \mathbf{a}(t_{m+2}) \\ \vdots & \vdots & \ddots & \vdots \\ \mathbf{a}(t_{d+1}) & \mathbf{a}(t_{d+2}) & \cdots & \mathbf{a}(t_{d+m}) \end{bmatrix} \quad (7.3)$$

where $\mathbf{a}(t_i) = [a_1(t_i), a_2(t_i), \dots, a_n(t_i)]^T$ represents the acceleration response vector measured from each DOF at time instant t_i . When the acceleration response $\mathbf{a}(t)$ is the free decay response subjected to an impulse load, modal frequencies, damping ratios and mode shapes of the studied structure can be identified by using ERA. \mathbf{H}' is a Hankel matrix of the same size to \mathbf{H} and is shifted with a single step forwarded in time domain. Two tunable parameters, namely the delay embedding dimension d and the window size m , determine the size of Hankel matrix \mathbf{H} . In literature, the lowest delay embedding dimension value is dependent on the complexity of vibration responses, and is usually approximated by using

AMI [25], FNN analysis [26], SVD or the optimal hard threshold of Gavish and Donoho [27]. In this study, SVD is implemented to extract a rank-reduced basis. Therefore it is not very essential to perform a very careful selection of the parameter d . Existing studies suggest that the observed dynamic can be faithfully unfolded in phase space when the embedding dimension is larger than two times of the distinct frequency components [22]. Another parameter that needs to be selected carefully is the window size m , which is related to the sampling rate, the fundamental frequency as well as the time scale of the dynamic system of interest. A detailed discussion of appropriate selection criterion is given in Ref. [28]. A further error analysis of the window size on the performance of the proposed approach will be conducted in Section 4.1.

For linear and weak nonlinear deterministic systems, Hankel matrix \mathbf{H} and \mathbf{H}' in Eq. (7.3) can be connected by a best linear regression operator \mathbf{A} , which is given as

$$\mathbf{H}' \approx \mathbf{A}\mathbf{H} \quad (7.4)$$

where the transfer operator \mathbf{A} is the finite-dimensional approximation of infinite-dimensional time-invariant Koopman operator as mentioned above. The recently developed DMD has been demonstrated as an accurate and time-efficient algorithm to obtain \mathbf{A} by solving the optimization of the objective difference function $\|\mathbf{H}' - \mathbf{A}\mathbf{H}\|_F$. The subscript F denotes the Frobenius norm. When further conducting the eigen-decomposition on \mathbf{A} , the consequent DMD eigenvectors and DMD eigenvalues offer a great deal of interpretability in terms of the coherent spatiotemporal structures. For linear dynamic systems, these eigenvalues and eigenvectors are as the same as natural frequencies and mode shape obtained by using ERA. The applicability and interpretation of using DMD to extract the experimental modal parameters of linear structures have been recently provided in Refs. [29, 30]. In these two studies, DMD algorithm is combined with computer vision method to extract full-field, spatially dense vibration modes of experimental and real-world cable stayed bridges. For weak nonlinear dynamics with sparse power spectra, the DMD exhibits its superiority in representing the spatiotemporal behavior associated with each dynamic mode. A more detailed discussion of the DMD theory and its application to process real-world nonlinear dynamic process can be found in Ref. [31]. For the sake of brevity, the procedure of using time-delay DMD for modal analysis of structures is summarized in Algorithm 1.

Algorithm 1: Structural modal analysis by time-delay DMD

Input: Hankel matrix \mathbf{H} , time-shifted Hankel matrix \mathbf{H}' and target truncation rank r .

Output: modal frequency \mathbf{f} , mode shape Φ

1: **procedure** time-delay DMD ($\mathbf{X}_1^m, \mathbf{X}_2^{m+1}, r$)

2: $[\mathbf{U}_{1:r}, \mathbf{S}_{1:r}, \mathbf{V}_{1:r}] \leftarrow$
compact SVD(\mathbf{X}_1^m, r)

$> \mathbf{U}_{1:r} \in \mathbf{X}^{n \times r}, \mathbf{S}_{1:r} \in \mathbf{X}^{r \times r}, \mathbf{V}_{1:r} \in \mathbf{X}^{m \times r}, r$
 $= \text{rank}(\mathbf{X}_1^m)$

3: $\tilde{\mathbf{A}} \leftarrow \mathbf{U}_{1:r}^* \mathbf{X}_2^{m+1} \mathbf{V}_{1:r} \mathbf{S}_{1:r}^{-1}$

$> \tilde{\mathbf{A}} \in \mathbf{X}^{r \times r}$ is a low-rank with the same
eigenvalues to \mathbf{A}

4: $[\tilde{\omega}, \tilde{\lambda}] \leftarrow \text{EIG}(\tilde{\mathbf{A}})$

$>$ eigenvalues $\tilde{\lambda}$ and eigenvector $\tilde{\omega}$

5: $\mathbf{f} = \ln[\text{imag}(\tilde{\lambda}^j)] / (2\pi\Delta t)$

$>$ modal frequency \mathbf{f}

6: $\Phi = \text{real}(\mathbf{U}_{1:r} \tilde{\omega})$

$>$ modal shape Φ

7: **end procedure**

7.2.2 Linearized representation of nonlinear dynamic system using Hankel SVD coordinate

For many real-world nonlinear dynamic systems without exhibiting sparse discrete power spectra, time-delay DMD introduced in Section 2.1 may fail to build a finite-dimensional linear predictive model. In literature, modifications have been made on the DMD architectures, such as extended DMD and kernel DMD, to linearize the underlying system with a specific type of nonlinearity. The basic principle is to augment a broader set of nonlinear coordinate basis, i.e., polynomial kernel, radial basis functions and sigmoid kernel to the linear basis based on domain-specific prior knowledge. As has been repeatedly stated, an accurate representation of the Koopman operator exclusively relies on the good choice of nonlinear coordinate basis. Alternatively, Brunton et al. [15] obtained intrinsic coordinates basis from the right-singular vector of Hankel matrix defined in Eq. (7.3). This perspective is fully data-driven, without relying on prior knowledge about the nonlinearity of underlying dynamic. The Hankel SVD coordinate is obtained by conducting compact SVD on the time-delay embedding matrix \mathbf{H}

$$\mathbf{H} \approx \mathbf{U}_r \mathbf{S}_r \mathbf{V}_r^* \quad (7.5)$$

where $r \ll d$ denotes the truncation order. The obtained left singular vector \mathbf{U}_r , singular value \mathbf{S}_r and right singular vector \mathbf{V}_r from the compact SVD of \mathbf{H} , are of the dimensions $d \times r$, $r \times r$ and $r \times m$, respectively. The Hankel SVD coordinate basis is proven to be effective in producing approximate linear model accurately, even for strongly nonlinear dynamic system. Then, linear predictive Koopman operator \mathbf{A} can be least-square regressed using data from the first r rows of the right singular vector \mathbf{V}_r as

$$\dot{\mathbf{V}}_r \approx \mathbf{A} \mathbf{V}_r \quad (7.6)$$

where $\dot{\mathbf{V}}_r$ is the derivative of \mathbf{V}_r . The fourth-order central difference method is adopted to approximate the derivative. Eq. (7.6) defines the DMD based on the continuous Hankel SVD coordinate basis to extract linear Koopman operator \mathbf{A} . By integrating this discrete differential equation, the resultant model is able to reproduce the dynamic behavior in the space of the Hankel SVD coordinate and to predict the evolution of state variables.

It should be noted that measurement noise inevitably exists in real measured data and its influence will be magnified in the numerical differentiation calculation to compute $\dot{\mathbf{V}}_r$. Consequently, the accuracy of linear predictive Koopman operator \mathbf{A} approximation will be significantly degraded. Under this circumstance, this study presents the following formulation of DMD with discrete Hankel SVD coordinate

$$\hat{\mathbf{V}}_r = \begin{bmatrix} | & | & \cdots & | \\ \mathbf{v}(t_2)\mathbf{v}(t_3)\cdots\mathbf{v}(t_{m+1}) \\ | & | & \cdots & | \end{bmatrix} \approx \mathbf{A} \begin{bmatrix} | & | & \cdots & | \\ \mathbf{v}(t_1)\mathbf{v}(t_2)\cdots\mathbf{v}(t_m) \\ | & | & \cdots & | \end{bmatrix} \quad (7.7)$$

In the HAVOC framework proposed in Ref. [15], the last row of the right singular vectors \mathbf{V}_r is recognised as the discovered force. Improvement is made in this study by performing one-step forward forecasting, and the residual between the prediction and ground truth is extracted as the discovered force

$$\mathbf{F} = \mathbf{V}_r - \hat{\mathbf{V}}_r = \begin{bmatrix} | & | & \cdots & | \\ \mathbf{v}(t_2)\mathbf{v}(t_3)\cdots\mathbf{v}(t_{m+1}) \\ | & | & \cdots & | \end{bmatrix} - \mathbf{A} \begin{bmatrix} | & | & \cdots & | \\ \mathbf{v}(t_1)\mathbf{v}(t_2)\cdots\mathbf{v}(t_m) \\ | & | & \cdots & | \end{bmatrix} \quad (7.8)$$

where $\hat{\mathbf{V}}_r$ denotes the predicted right singular vectors. With the exogenous control force \mathbf{F} been simultaneously discovered, the forced linear model defined by $\hat{\mathbf{v}}_r(t_{j+1}) = \mathbf{A}\mathbf{v}_r(t_j) + \mathbf{F}(t_j)$ can accurately capture the evolution of observed nonlinear dynamic dominated by near-periodic mode. The aperiodic dynamic component, such as external force and abrupt change lying beyond the reach of DMD mode, will be relegated to the discovered force. The Hankel matrix in Eq. (7.3) constructed by the embedding of measured dynamic responses can be reconstructed using the predicted $\hat{\mathbf{V}}_r$ via the following matrix multiplication

$$\hat{\mathbf{H}} = \mathbf{U}_r \mathbf{S}_r \hat{\mathbf{V}}_r^* \quad (7.9)$$

It should be noted that each ascending skew-diagonal element of the Hankel matrix displayed in Eq. (7.3) is constant. However, no such property is guaranteed for the reconstructed $\hat{\mathbf{H}}$. Acceleration response vector \mathbf{a} can be obtained from the diagonal averaging procedure typically used in SSA. In Refs. [15] and [32], the focus is on the chaotic system, and an additional nonlinear force term is included in the HAVOK model to account for chaotic switching or bursting phenomena. This study focuses on structural nonlinear vibration analysis and demonstrates that the linearized model obtained by HAVOK is sufficient to reconstruct

and predict the free decay or sinusoidal-wave forced vibration responses of nonlinear structures in the numerical and experimental studies. This framework provides a more physical interpretable approach to nonlinear systems than many existing methods, and its linear intrinsic dynamic enables spectrum analysis through eigenvalue decomposition. In addition, the discovered force signal offers diagnostic insight into anomalous events. For instance, the HAVOC framework has been applied to construct a linear control model to reconstruct and forecast time series with almost-periodic dynamics of the real-world power grid load [21]. The schematic procedure of using the proposed data-driven approach to transform a nonlinear dynamic system into a linearized model is summarized in Figure 7-1. The multi-channel vibration responses measured from MDOF structure are embedded by using Eq. (7.3). Then the compact SVD is conducted on the time-delay embedding matrix to obtain the Hankel SVD coordinate. DMD regression is subsequently applied to the Hankel SVD coordinate to approximate finite dimension Koopman operator. Eventually the resulting Koopman operator can be used to predict the future responses of state variable with a desirable accuracy. DMD regression performed on the right singular vector \mathbf{V} matrix yields a forced linearized model to capture the dominate evolution of dynamic behavior in the discrete time Hankel SVD coordinate basis. The stepwise prediction residual is interpreted as the discovered force.

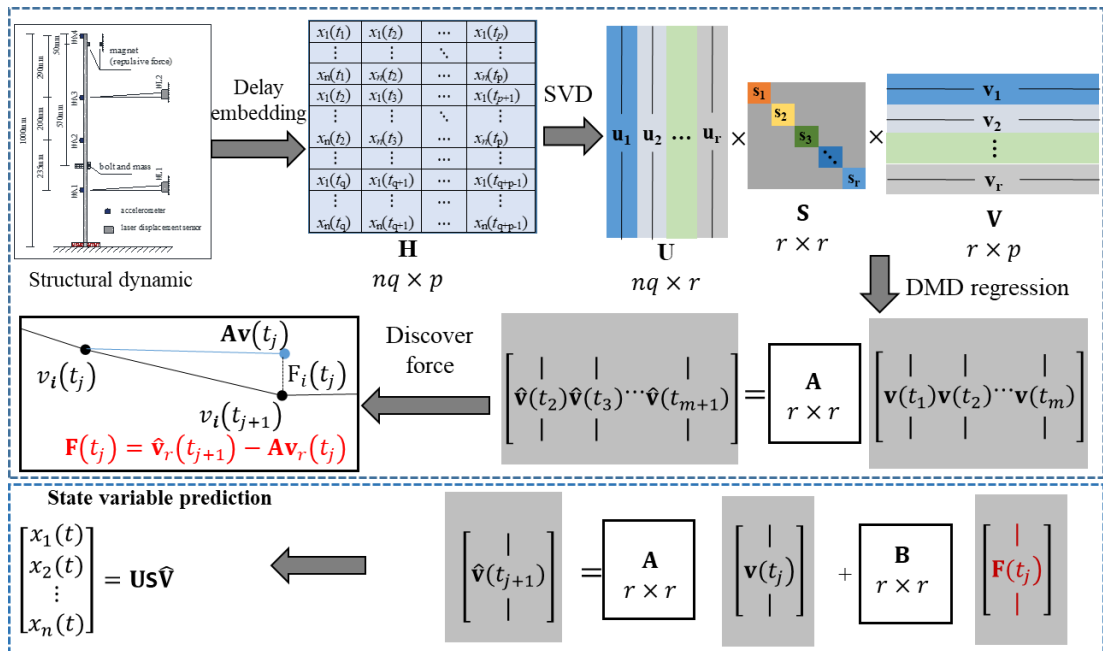


Figure 7-1. Procedure for representing nonlinear dynamic system as a forced linearized model using the DMD based on discrete Hankel SVD coordinate.

7.2.3 Contribution of this study

This study improves the original HAVOC framework and investigates the applicability of using the proposed method for generating a finite linear representation of nonlinear structural vibration. In particular, the main contributions of this study are clarified as follows:

1) The phase space embedding of multi-channel responses is introduced to extend the feasibility of using the original HAVOC framework to process the vibration signals measured from MDOF structures.

2) When structural vibration responses are contaminated with measurement noise, the continuous Hankel SVD coordinate utilized in the original HAVOC framework may significantly affect the nonlinear vibration prediction accuracy. Therefore, the DMD with discrete Hankel SVD coordinate is introduced to improve the noise tolerance.

The introduced linearization framework is applicable to structural systems with discrete frequency spectrum and one equilibrium position (fixed point) in steady state. The vast majority of civil engineering structures subjected to operational condition falls into this category.

7.3 Experimental verification with a linear structure

Before considering nonlinear systems, the vibration responses experimentally measured from a MDOF linear structure are used to illustrate how the predictive model as well as modal parameters, such as mode shape and natural frequencies can be extracted by using the time-delay DMD introduced in Section 2.1. In particular, vibration responses of an eight-storey shear-type steel frame structure as shown in Figure 7-2 subjected to hammer impact excitations are used in this study. The frame structure is fixed at the base, and the geometric dimension and material properties are reported in Ref. [33]. Eight KD-1300 accelerometers with a sampling rate of 1024 Hz are respectively attached at each floor to measure the horizontal acceleration responses. The hammer impact excitation is applied at the first floor by using a SINOCERA LC-04A hammer with a rubber tip. The applied force is simultaneously acquired along with the acceleration responses for identifying the FRF. However, only the raw measured acceleration data are selected to construct the Hankel matrix in Eq. (7.3). A low-pass filter with a cutoff frequency of 100 Hz is applied to preserve the first eight modes. Time-delay DMD presented in Algorithm 1 is applied to the first 10s free decay responses. Figure 7-3(a) compares the power spectrum and the eigen-frequencies from time-delay DMD. The eigen frequencies obtained from DMD match with the peaks in the power spectrum of the used acceleration responses, which means that the time-delay DMD converges to a sparse sinusoidal basis that is strongly represented in the data observed from linear systems. Figure 7-3(b) shows

the structure of the Koopman operator \mathbf{A} estimated by Eq. (7.4). It can be found that the Koopman operator extracted from time-delay coordinate is highly symmetrically structured. In particular, the diagonal elements are approximately equivalent to 1, whereas the off-diagonal element away from the diagonal tends to zero. As previously stated in Algorithm 1, modal parameters of linear systems can be obtained from time-delay DMD algorithm. For comparison purpose, all the eight natural frequencies and mode shapes of the eight-story shear-type linear steel frame identified by time-delay DMD, FDD [34] and CMIF method [35] are presented in Table 7-1 and Figure 7-4, respectively. As can be found in the identification results, the mode shapes and natural frequencies obtained by time-delay DMD agree well with those from FDD and CMIF methods.

To quantitatively evaluate the accuracy of the mode shapes predicted by the time-delay DMD method, modal assurance criterion (MAC) values for these eight modes are computed. MAC values between the mode shapes obtained by time-delay DMD and FDD as well as those values between mode shapes from time-delay DMD and CMIF are provided in

Table 7-2 and Table 7-3, respectively. The diagonal terms of both MAC matrices are larger than 99.8%, whereas the off-diagonal elements are less than 2.5%. The MAC values further indicate that the mode shapes extracted from the time-delay DMD method are reliable and the orthogonality of the modes are guaranteed. In fact, the time-delay DMD method is easy to connect with vision-based techniques to extract the full-field temporal-spatial dense dynamic modes from experimental and real-world structures [29].

Table 7-1. Comparison of natural frequencies obtained by time-delay DMD, FDD and CMIF

Method	Mode order							
	Mode 1	Mode 2	Mode 3	Mode 4	Mode 5	Mode 6	Mode 7	Mode 8
Time-delay DMD	4.6650	13.7058	22.5549	30.6968	38.2429	44.4365	48.8286	52.3084
FDD	4.6617	13.7086	22.5580	30.6963	38.2420	44.4444	48.8296	52.3062
CMIF	4.6563	13.7187	22.5625	30.6875	38.2500	44.4375	48.8437	52.3125

Table 7-2. MAC (in %) between the modes obtained by time-delay DMD and FDD

Time-delay DMD	FDD							
	1	2	3	4	5	6	7	8
1	99.815	0.002	0.029	0.015	0.085	0.219	0.020	0.049
2	0.029	99.998	0.095	0.064	0.004	0.086	0.076	0.001
3	0.000	0.040	99.901	0.005	0.090	0.002	0.043	0.000
4	0.056	0.056	0.053	100.000	0.065	0.000	0.007	0.016
5	0.213	0.003	0.039	0.037	99.989	0.000	0.000	0.035
6	0.019	0.121	0.000	0.016	0.004	99.943	0.009	0.006
7	0.044	0.032	0.058	0.058	0.023	0.021	99.900	0.006
8	0.024	0.002	0.002	0.069	0.093	0.000	0.011	99.928

Table 7-3. MAC (in %) between the modes obtained by time-delay DMD and CMIF

Time-delay DMD	CMIF							
	1	2	3	4	5	6	7	8
1	99.904	0.002	0.029	0.015	0.085	0.220	0.020	0.048
2	0.045	99.998	0.096	0.064	0.004	0.086	0.076	0.001
3	0.006	0.049	99.898	0.006	0.091	0.002	0.042	0.000
4	0.024	0.056	0.062	100.000	0.069	0.000	0.008	0.018
5	0.141	0.003	0.040	0.042	99.987	0.001	0.000	0.037
6	0.061	0.122	0.000	0.014	0.003	99.936	0.004	0.010
7	0.051	0.033	0.059	0.058	0.021	0.017	99.891	0.014
8	0.019	0.002	0.002	0.069	0.092	0.000	0.012	99.921



Figure 7-2. Laboratory steel frame model.

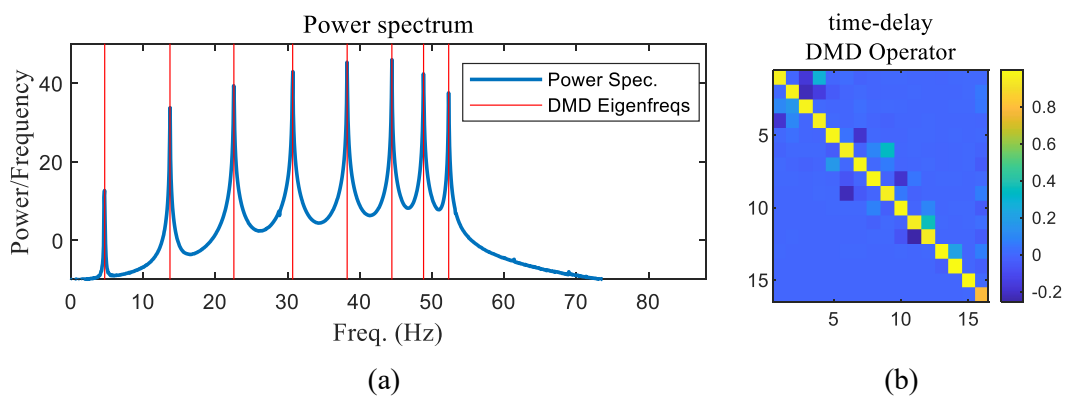


Figure 7-3. (a) Comparison of power spectrum and eigen-frequencies obtained from time-delay DMD; (b) Visualization of the structure of the time-delay DMD.

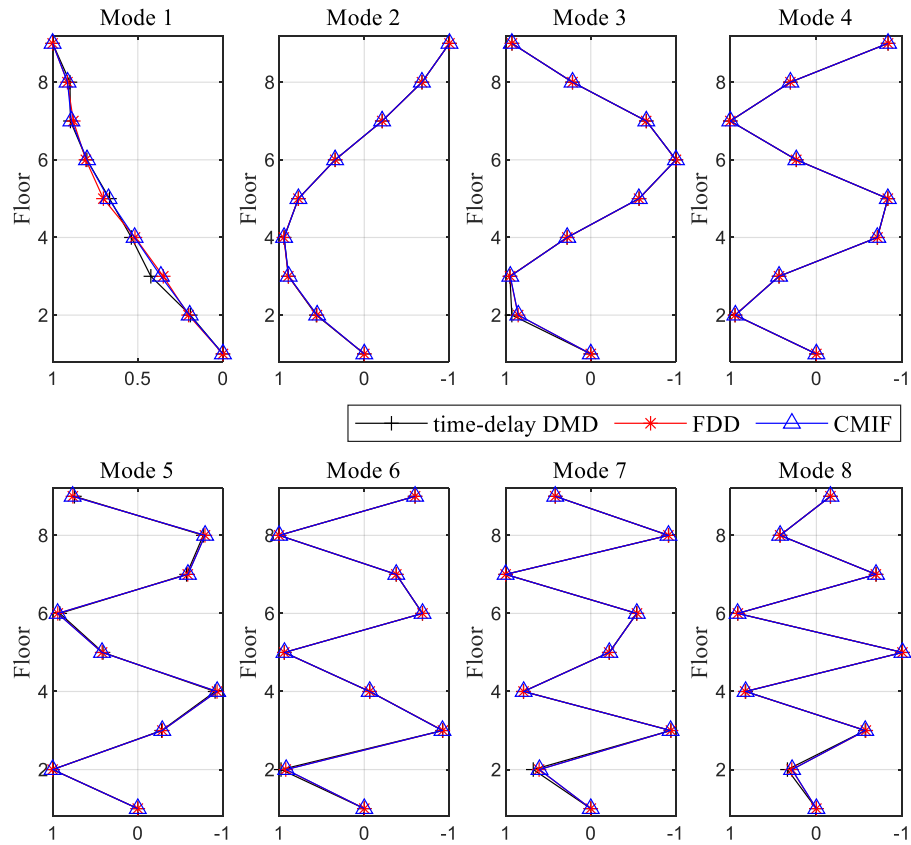


Figure 7-4. Comparison of the mode shapes obtained by time-delay DMD, FDD and CMIF.

For validating the accuracy of Koopman operator approximated from the time-delay DMD algorithm, the performance of using time-delay DMD to predict the state variables is tested. In particular, the acceleration data measured from $t=0$ s to $t=10$ s are set as training datasets to obtain the regressed finite-dimensional approximation of Koopman operator A . Then, the future state variables that are not used to train the model are set as variables in the prediction datasets. Figure 7-5 presents the response forecasting of each DOF by using the time-delay DMD. The Y -axis on the right-hand side shows the absolute prediction error. Response prediction results demonstrate that the presented model accurately captures the evolution of linear structural vibrations, although the prediction error slightly increases at the end of responses owing to the errors in the accumulated integration process.

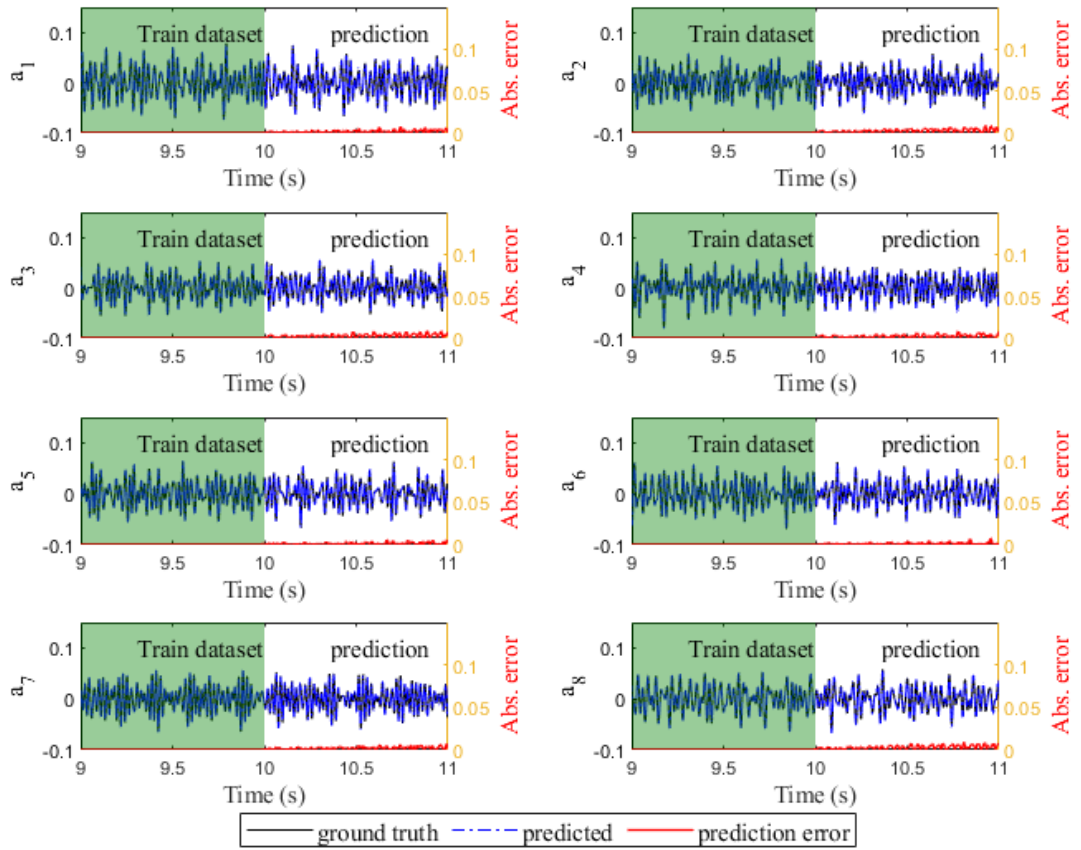


Figure 7-5. Prediction performance of time-delay DMD algorithm.

The time-delay DMD algorithm can be applied to both single DOF and MDOF linear structural systems exhibiting discrete spectrum characteristics, as shown in Figure 7-3. This is a restrictive condition, since many structures of interest may present nonlinear behavior and do not exhibit fully discrete power spectra. As a result, the method introduced in Section 2.1 may fail to build a linear model using the time-delay coordinate. The remainder of this chapter is devoted to developing a new coordinate basis that the nonlinear dynamic system can be linearly represented by using the proposed approach.

7.4 Nonlinear structures

Numerical and experimental verifications are conducted in this section to demonstrate the applicability of using the proposed approach in discovering a finite dimensional linear representation of dynamic behavior of nonlinear structures. In particular, three types of DMD algorithms introduced in Section 2, namely, time-delay DMD, DMD with continuous and discrete Hankel SVD coordinate bases are tested. Then, the DMD with discrete Hankel SVD coordinate will be applied to construct the linearized model for state variable prediction.

7.4.1 6-DOF nonlinear structural system with a hardening Adjustable Template Stiffness Device (ATSD)

Before conducting experimental verifications, a six DOFs mass-spring-damper system with a hardening adjustable template stiffness device (ATSD) installed at the second DOF, as shown in Figure 7-6, is designed to evaluate the feasibility and accuracy of the proposed method. The ATSD was firstly proposed in Ref. [36] and has been used as a nonlinear stiffness modification device for structural vibration mitigation. The mechanical model of ATSD and several curved templates designed for the realization of stiffness hardening, softening and negative stiffness are detailed in Refs. [36, 37]. Assuming that the surface of ATSD and the curved template block is smooth, therefore, the friction force between the ATSD and curved template block is neglected. The restoring force F_{ATSD} provided by the ATSD in the motion direction is given as

$$F_{ATSD}(x) = k_{ATSD} \frac{f'(x)}{1+f'(x)^2} [\Delta L + f(x)] \quad (7.10)$$

where k_{ATSD} and ΔL represent the stiffness and the initial compression length of the pre-compressed spring, respectively, $f(x)$ is the shape function of template block surface. A variety of force-displacement relationships $F_{ATSD}(x)$ can be achieved by changing the design of shape function and specification of pre-compressed spring. In this study, the spring stiffness is $k_i = 15 \text{ N/m}$ ($i=1, \dots, 6$), damping coefficient is $c_i = 0.01$ ($i=1, \dots, 6$) and mass value is $m_i = 1 \text{ kg}$ ($i=1, \dots, 6$). The stiffness and initial compression length of the pre-compressed spring are $k_{ATSD}=150 \text{ N/m}$ and $\Delta L = 1 \text{ m}$, respectively. $F(t)$ is the external force applied on the 6th DOF. In particular, the excitation is considered as a sinusoidal force with an excitation frequency of 3 Hz and an amplitude of 10 N, respectively. The shape function $f(x)$ is chosen as a 4th order polynomial function to increase the stiffness of the original structure in the direction of structural motion, which is expressed as

$$f(x) = 0.1x^4 \quad (7.11)$$

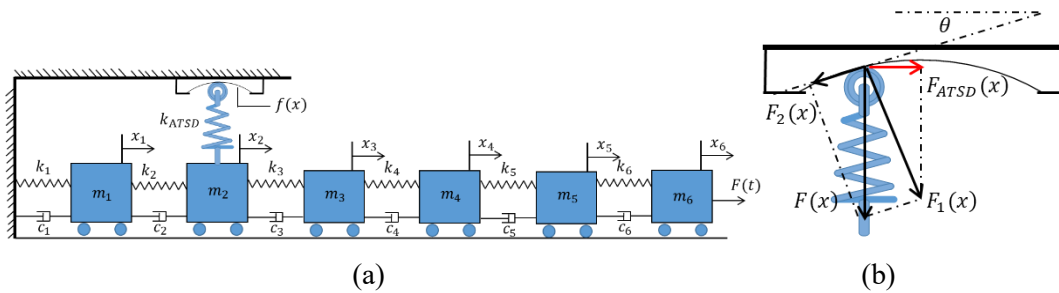


Figure 7-6. (a) A six DOFs nonlinear system with ATSD and (b) mechanical modeling of the ATSD.

The equation of motion of the nonlinear structural system illustrated in Figure 7-6 is given as follows

$$\begin{cases} m_1\ddot{x}_1 + (k_1 + k_2)x_1 - k_2x_2 + (c_1 + c_2)\dot{x}_1 - c_2\dot{x}_2 = 0 \\ m_2\ddot{x}_2 + (k_2 + k_3)x_2 - k_2x_1 - k_3x_3 + (c_2 + c_3)\dot{x}_2 - c_2\dot{x}_1 - c_3\dot{x}_3 + F_{ATSD}(x_2) = 0 \\ m_3\ddot{x}_3 + (k_3 + k_4)x_3 - k_3x_2 - k_4x_4 + (c_3 + c_4)\dot{x}_3 - c_3\dot{x}_2 - c_4\dot{x}_4 = 0 \\ m_4\ddot{x}_4 + (k_4 + k_5)x_4 - k_4x_3 - k_5x_5 + (c_4 + c_5)\dot{x}_4 - c_4\dot{x}_3 - c_5\dot{x}_5 = 0 \\ m_5\ddot{x}_5 + (k_5 + k_6)x_5 - k_5x_4 - k_6x_6 + (c_5 + c_6)\dot{x}_5 - c_5\dot{x}_4 - c_6\dot{x}_6 = 0 \\ m_6\ddot{x}_6 - k_6x_5 + k_6x_6 - c_6\dot{x}_5 + c_6\dot{x}_6 = -F(t) \end{cases} \quad (7.12)$$

with Eq. (7.10) and the above pre-defined parameters, $F_{ATSD}(x_2)$ can be expressed as

$$F_{ATSD}(x_2) = 150 \frac{0.4x_2^3}{1+(0.4x_2^3)^2} [1 + 0.1x_2^4] \quad (7.13)$$

With parameter and excitation defined above, the nonlinear structural system defined in Eq. (7.12) is integrated to steady-state using the fourth-order Runge–Kutta scheme with a randomly generated initial condition. The numerical acceleration responses of each DOF are obtained with a sampling rate of 100 Hz. Figure 7-7(a) and (b) show the acceleration responses of the 1st DOF and the restoring force-displacement loop, respectively. As can be found in Figure 7-7(b), the curve slope gradually increases with displacement, which brings a stiffness hardening effect to the structure.

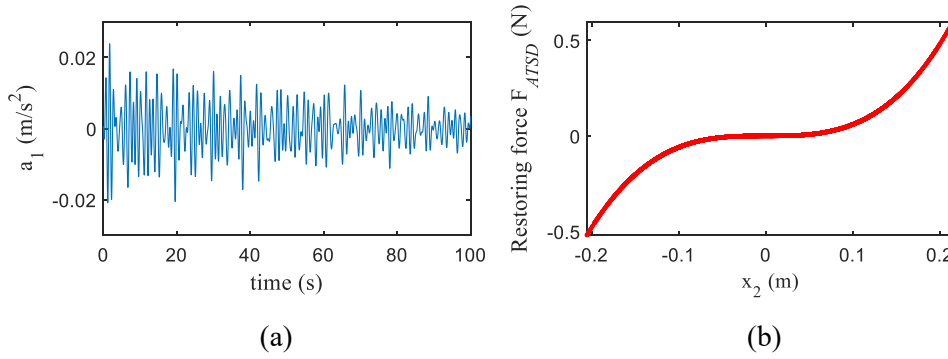


Figure 7-7. (a) Acceleration time history of the 1st DOF; and (b) the restoring force-displacement curve.

In literature, attempt has been made in Ref. [37] to solve the governing equation of nonlinear behavior defined in Eq. (7.12) by using the algorithm for sparse identification of nonlinear dynamical systems (SINDy) recently proposed by Brunton et al. [31]. This method builds up a dictionary of possible candidate functions and uses sparse symbolic regression to obtain a parsimonious model, which is the most accurate representative to the underlying system. Lai et al. [37] constructed the candidate function dictionary with the polynomials of state variables and the external excitation term. The derived governing equation matches well

with the third-order Taylor expansion of theoretic formula. However, full state information, i.e. displacement, velocity and acceleration time series are required in SINDy framework. In the present work, a data-driven equation-free framework is introduced to obtain linearized representation of nonlinear dynamics with partial state information.

For nonlinear structures, the time-delay DMD with a finite dimension introduced in Section 2.1 is not expected to perform well, since system with nonlinear components will not exhibit a fully discrete power spectra, and a finite number of discrete frequencies cannot densely cover a continuous interval on the frequency space. In this section, the time-delay DMD is extended to model nonlinear dynamic system as a forced linear system acting on the SVD vectors of Hankel matrix. The Hankel matrix is constructed from the acceleration responses of each DoF with an embedding dimension of 100. The Hankel SVD coordinate is directly obtained from the data and a wide range of nonlinear systems could be well-approximated by applying DMD to these coordinates [22]. Following the procedure illustrated in Figure 7-1, a standard DMD working in the space of Hankel SVD coordinate $\mathbf{v}(t_{i+1}) \approx \mathbf{A}\mathbf{v}(t_i)$ using the full duration of training dataset yields the best-fit approximation of linear operator \mathbf{A} . The resulting model is then used for stepwise forward prediction. The prediction residual out of the reach of the above mentioned linear model will be considered as simultaneously obtained force term. The forced linear model defined by $\mathbf{v}(t_{i+1}) = \mathbf{A}\mathbf{v}(t_i) + \mathbf{F}(t_i)$ fits the observed data perfectly.

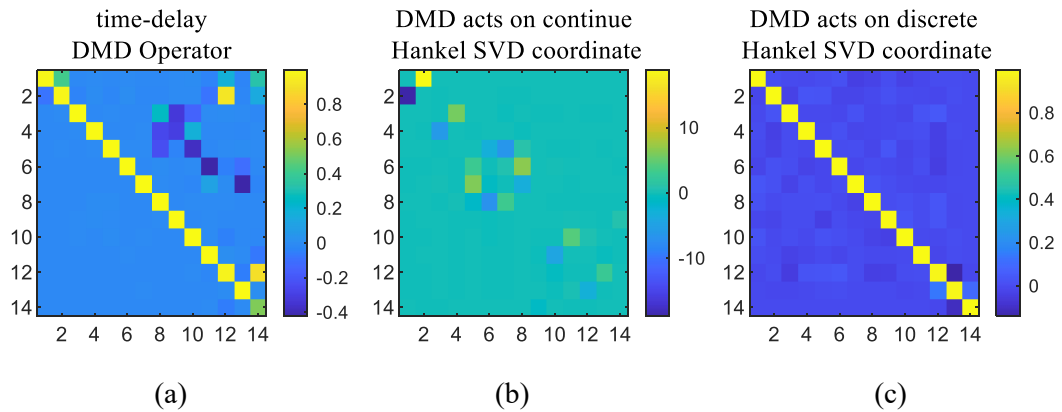


Figure 7-8. Visualization of Koopman operator approximated from: (a) Time-delay DMD; (b) DMD with continuous Hankel SVD coordinate; and (c) DMD with discrete Hankel SVD coordinate.

For comparison, the time-delay DMD, DMD with continuous Hankel SVD coordinate and discrete Hankel SVD coordinate are respectively best fitted by Eq. (7.4), Eq. (7.6) and Eq. (7.7) using the first 10 s acceleration measurements. The structures of Koopman operators estimated from three different formulas are illustrated in Figure 7-8. As can be observed in Figure 7-8(a), the time-delay DMD-based Koopman operator estimated from a nonlinear

system is an upper triangular matrix, which is quite different from the highly symmetrical structured operator for linear dynamic systems presented in Figure 7-3(b). In contrast, the Koopman operators based on the continuous Hankel SVD coordinate and discrete Hankel SVD coordinate appear to be symmetric. In particular, the continuous SVD coordinate operator displayed in Figure 7-8(b) is nearly skew-symmetric and most of the nonzero matrix elements are distributed in the first off-diagonals region. This particular structure means that the derivative $\dot{v}_{i,j}$ can be well-approximated by $\mathbf{A}_{i,j-1}v_{i-1,j} + \mathbf{A}_{i,j+1}v_{i+1,j}$. The subscripts i and j represent the i -th row and j -th column of the matrix defined in Eq. (7.6). In Figure 7-8(c), the Koopman operator with discrete Hankel SVD coordinate presents distinct diagonal structure, which is similar as the time-delay DMD-based Koopman operator of linear dynamic systems shown in Figure 7-3(b). Further theoretical demonstration and explanation about these particular operator structures can be found in Refs. [38, 39]. Alternatively, a good linearized Koopman operator should be able to capture the evolution of the underlying dynamic behavior of nonlinear systems, therefore three resulting Koopman operators are illustrated in Figure 7-8 by comparing the prediction performance. The first 4000 sampling points are used as training dataset to obtain the best fitted Koopman operator using the above-mentioned method. Then, the obtained Koopman operators can be utilized to predict the future responses. Here, the subsequent 4000 sampling point responses of each DOF are compared with the ground truth. The prediction performance is evaluated by using the NRMSE, which is defined as follows

$$NRMSE = \frac{\sqrt{\frac{\sum_{i=1}^N (\hat{a}(t_i) - a(t_i))^2}{N}}}{\max(\mathbf{a}) - \min(\mathbf{a})} \quad (7.14)$$

where $\hat{a}(t_i)$ and $a(t_i)$ are the predicted and ground truth acceleration time series, respectively. $\max(\mathbf{a})$ and $\min(\mathbf{a})$ denote the maximum and minimum value of \mathbf{a} , respectively. $N=4000$ is the number of sampling points. The prediction errors of three different types of DMD algorithm are presented in Figure 7-9. Overall, the time-delay DMD yields the highest NRMSE, which further verifies that DMD based on the conventional time-delay coordinate is not suitable to model the dynamics of nonlinear structures. Moreover, the prediction performance of DMD with discrete Hankel SVD coordinate is consistently better than that calculated from continuous one. One possible reason is that the differential procedure is conducted in Eq. (7.6) to obtain the derivative of \mathbf{V}_r . Thus, the inevitable measurement noise will affect the accuracy of $d\dot{\mathbf{V}}_r$ and further influence the approximation of DMD with continuous Hankel SVD coordinate.

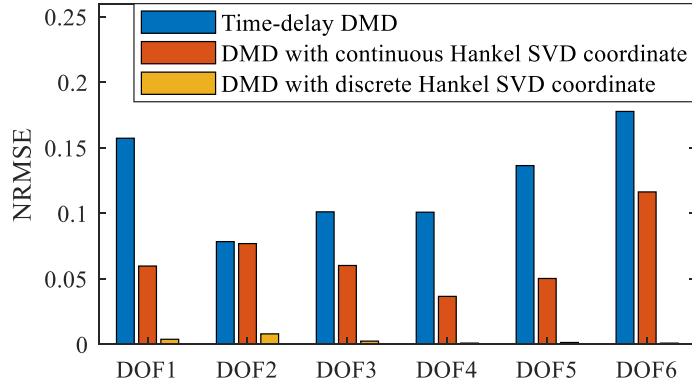


Figure 7-9. Comparison of prediction errors by using different DMD algorithm.

In this nonlinear numerical example, the prediction results shown in Figure 7-9 demonstrate that the DMD with discrete Hankel SVD coordinate operator introduced in Section 2.2 is able to correctly capture the dynamic evolution and predict the future responses with an improved accuracy than time-delay DMD and DMD with continuous Hankel SVD coordinate. It is interesting to investigate the necessary amount of data to train the DMD with discrete Hankel SVD coordinate and correctly identify a given nonlinear system. To this end, the number of training sampling points varying from 1000 to 10000 with an interval of 1000 points are tested. For each sampling duration, the procedure introduced in Figure 7-1 is repeated 50 times with a randomly generated initial condition. The resulting mean value, median as well as the statistical distribution of NRMSE is presented in the Violin graph as shown in Figure 7-10. With few exceptions, most of the NRMSE values are below 0.1, even when only 1000 sampling points are used as the training datasets. Overall, the prediction error shows a decreasing trend with an increasing number of sampling points. The mean values and variations of the prediction errors tend to converge when the length of training datasets is larger than 2000 points. It should be noted that the first-order frequency of the studied structure is about 0.1495 Hz (a period of the oscillation is $T \approx 6.689$ s). For a sampling rate of 100 Hz used in this example, the number of sampling points corresponds to a period of the oscillation is about 669 points. To further test the noise effects on the proposed method, 5% white noise is added to the training dataset. Comparing the violin plot of NRMSE shown in Figure 7-10 and Figure 7-11, it can be found that the effect of measurement noise is not significant on the prediction performance. Therefore, it can be preliminarily concluded that the DMD with the discrete Hankel SVD coordinate can be used to rapidly discover the underlying dynamics of the nonlinear system with confidence, even when only 3 periods of oscillation sampling data are available to train the model.

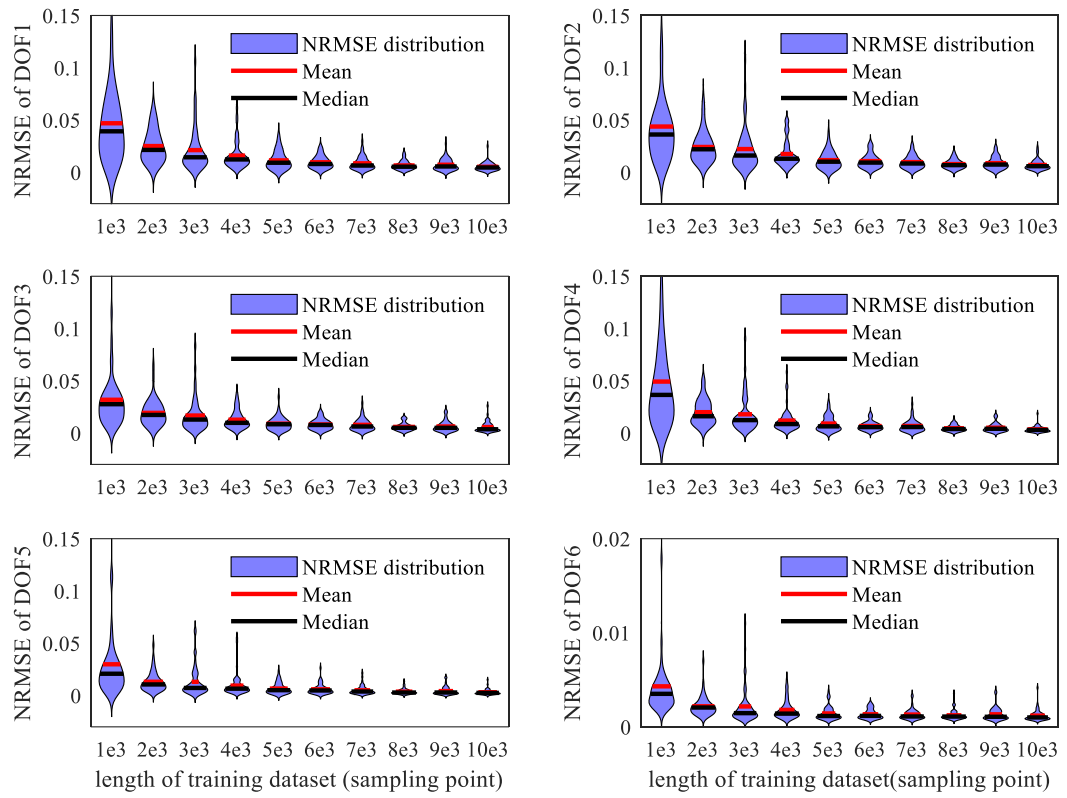


Figure 7-10. Violin plot of NRMSE of each DOF corresponding to different lengths of training dataset.

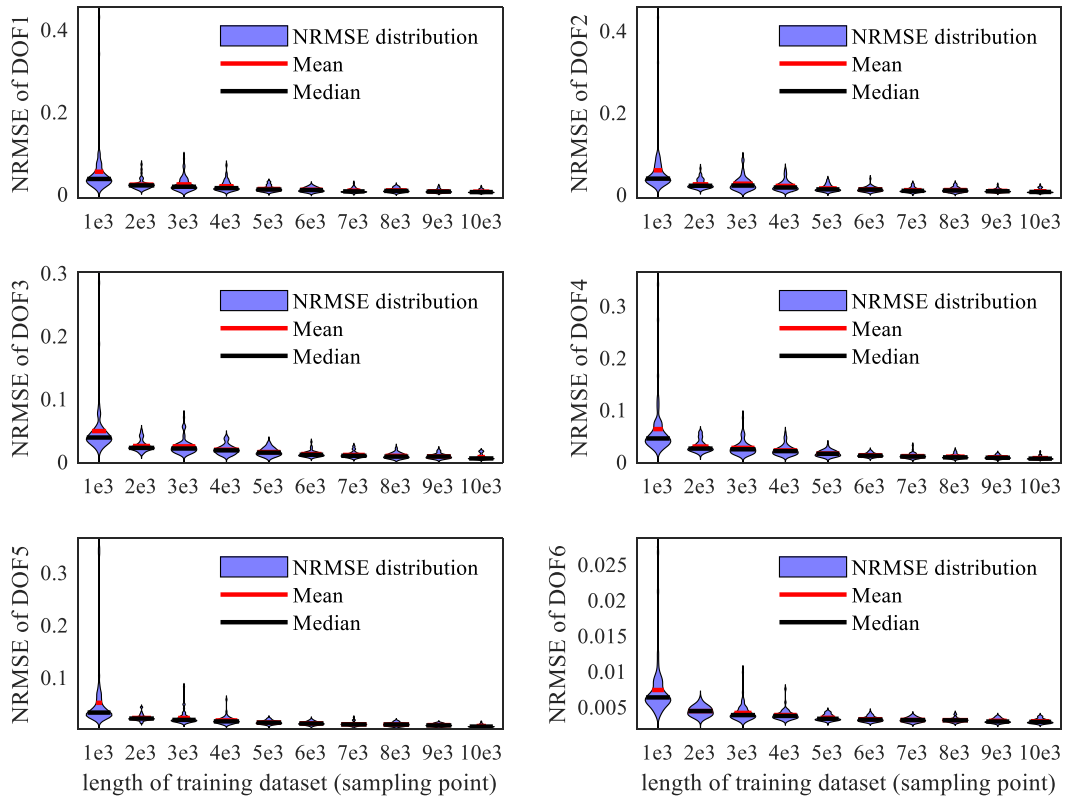


Figure 7-11. Violin plot of NRMSE of each DOF corresponding to different lengths of training dataset with 5% measurement noise.

For illustration purpose, the dynamic response forecasting results from the learned Koopman operator are shown in Figure 7-12. This model is trained on 5000 sampling points (50 seconds), and the dynamic responses of the next 50 seconds are predicted to analyse the accuracy of the obtained linear model to represent the nonlinear system. Since the external force is applied to DOF 6, the vibration response of a_6 is significantly different from the other DOFs. The predicted responses match well with the ground truth throughout this duration and the absolute error shown in the right y-axis is very small.

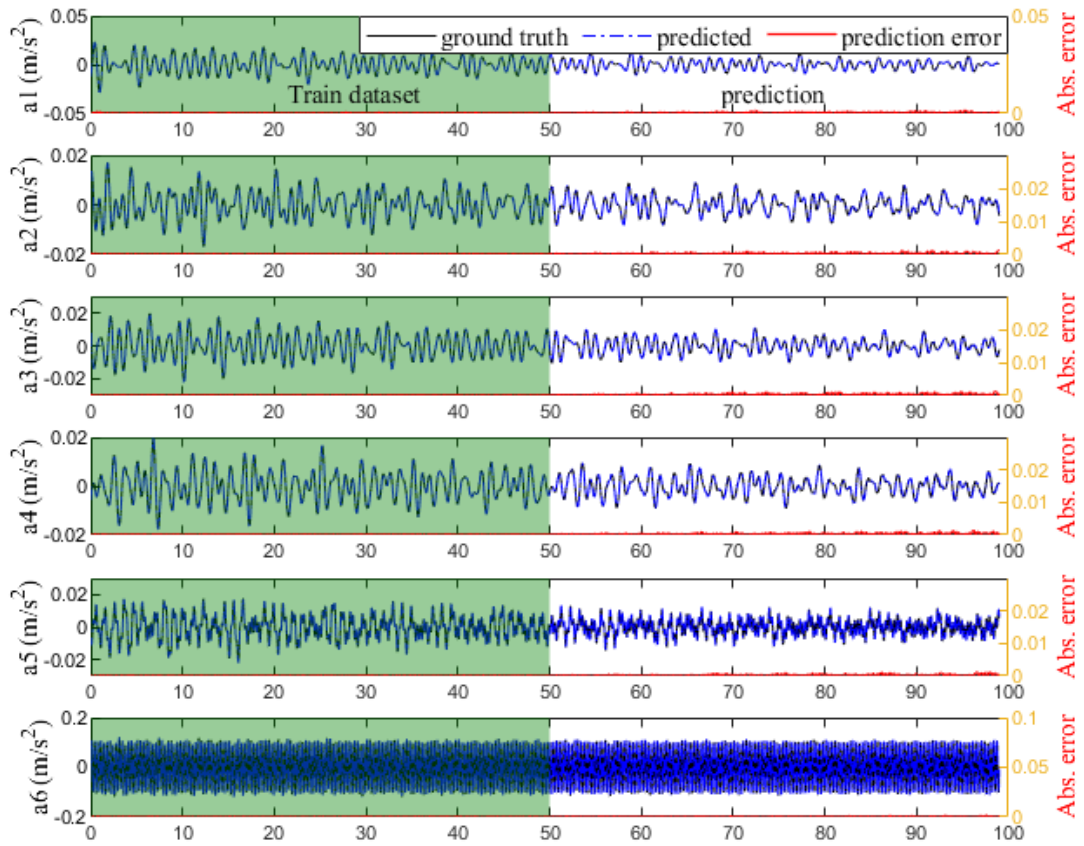


Figure 7-12. Using the DMD with discrete Hankel SVD coordinate to forecast the future 50 s of the vibration data.

7.4.2 An aluminum column with magnet induced nonlinearity in laboratory test

In this section, a nonlinear system consisting of an aluminum column with magnet induced nonlinearity is designed to further validate the feasibility of the proposed method. The experimental setup is shown in Figure 7-13. An aluminum flat bar with dimensions of 40 mm (Width)×3 mm (Depth)×1000 mm (Length) is used as the testing specimen. One end of the specimen is clamped to a strong base connected to a shaking table. As shown in Figure 7-13(b), one round rare earth magnet with a diameter of 18 mm is attached to the free end of the column specimen and another one is attached to a still stand at the same elevation. The still stand is fixed to the strong floor on the right side of the column. This setup is used to introduce a nonlinear force by using these two magnets. Four accelerometers #A1~#A4 are installed along the height of the column with locations specified in the schematic diagram. The sampling rate is set as 300 Hz. The nonlinear behavior in this structure comes from the repulsive force between two magnets. The repulsive force generated by the magnets is not only related to the properties, i.e. the residual flux density, geometric shape, common area of magnet, but also is a complex nonlinear function of the distance between two magnets [40, 41]. Figure 7-13(c) illustrates a nonlinear spring equivalent model to describe the magnet induced nonlinearity.

The repulsive magnetic force will dramatically increase when these two magnets move closer, which causes a stiffness hardening effect to the column when a large displacement occurs at the free end. It is noted that this structure does not represent a scale model of any particular “real-world” structure, but is made to simulate a structural system with stiffness hardening nonlinear behavior owing to larger displacement responses and magnet induced nonlinearity.

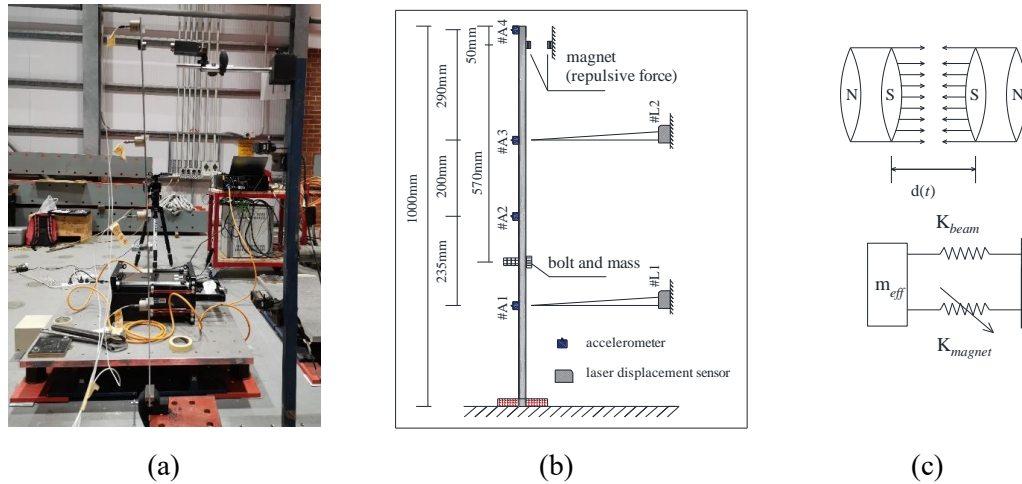


Figure 7-13. The experimental setup: (a) Layout of the aluminum specimen with a tip magnet; (b) schematic diagram; and (c) spring equivalents for the magnet induced repulsive force, resulting in stiffness hardening.

The free decay vibration tests are performed three times on the specimen, and the time domain and frequency domain responses are presented in Figure 7-14. As can be found in Figure 7-14(b), 7 peaks appear in the frequency spectrum. Therefore, the phase space embedding dimension is set as 14. The time varying instantaneous frequency presented in Figure 7-14 (c) verified the existence of nonlinearity in the vibration responses.

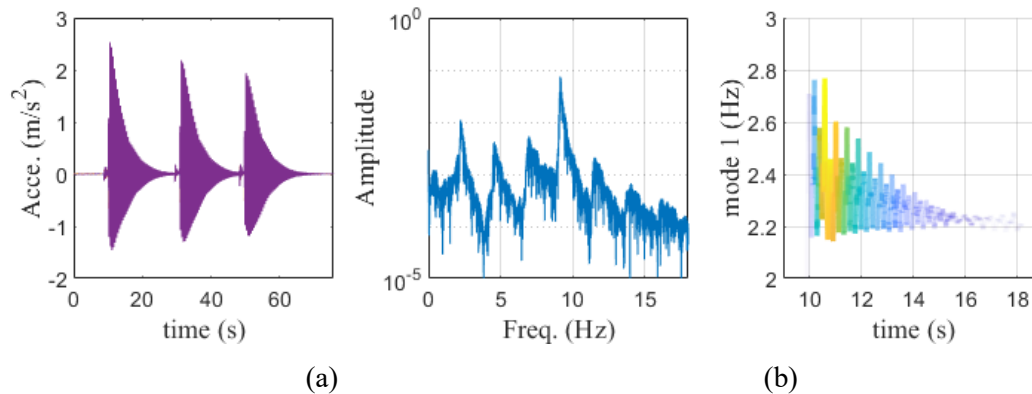


Figure 7-14. The free decay vibration responses in: (a) Time domain; and (b) Frequency domain and (c) time-frequency representation of mode 1.

Performing the same procedure described in the above numerical studies in Section 4.1,

three types of Koopman operators are respectively obtained using the structural free vibration responses. Similar to Figure 7-8, the diagonal symmetrical structure is also observed in the Koopman operator as shown in Figure 7-15 based on continuous and discrete Hankel SVD coordinate systems. It has been demonstrated in the above numerical example that the DMD with discrete Hankel SVD coordinate has the best accuracy. Owing to the space limitation, only the DMD with discrete Hankel SVD coordinate is used to conduct response prediction to verify the accuracy of the finite linearized representation of this nonlinear system. The first 2000 sampling points of the first free decay test are used as training datasets to predict the future responses of duration with 1000 sampling points. The prediction errors of three different types of DMD algorithm are presented in Fig. 16. The prediction performance of DMD with discrete Hankel SVD coordinate is significantly better than that calculated from other two, which is consistent with the results obtained from the numerical case study. The prediction results of all the four acceleration responses are presented in Figure 7-16. Overall, the prediction accuracy is very good.

Furthermore, the phase angle of the predicted trajectory always matches well with the ground truth. It should be noted that the focus of this study is to demonstrate the feasibility of using DMD based on Hankel SVD coordinate system to yield a predictive linear model and represent the nonlinear structural vibration behavior. The deterministic sinusoidal wave excitation or free vibration under an initial displacement are used to excite the numerical and experimental structures. In the numerical studies, the excitation force is periodic. Thus, the Koopman operator includes the frequency component of the applied external periodic force. For the free-decay or periodic load-induced responses of nonlinear structures, the force component will not be discovered by using Eq. (7.8). This is because the frequency component corresponding to the periodic excitation will be included in the DMD mode. Therefore, accurate prediction performance can be achieved in all the case studies introduced in this study without periodic force. However, it is noteworthy that the proposed method is applicable to the vibration of nonlinear systems with arbitrarily applied forces.

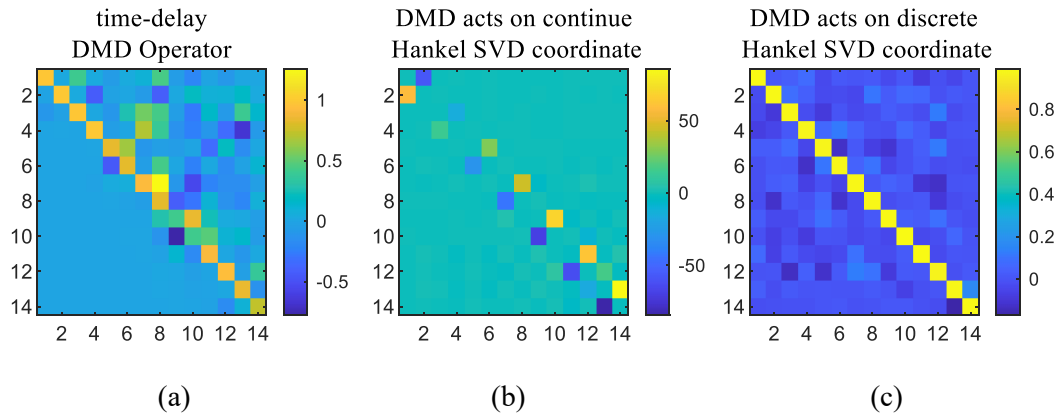


Figure 7-15. Visualizing the structure of: (a) Time-delay DMD; (b) DMD with continuous Hankel SVD coordinate; and (c) DMD with discrete Hankel SVD coordinate.

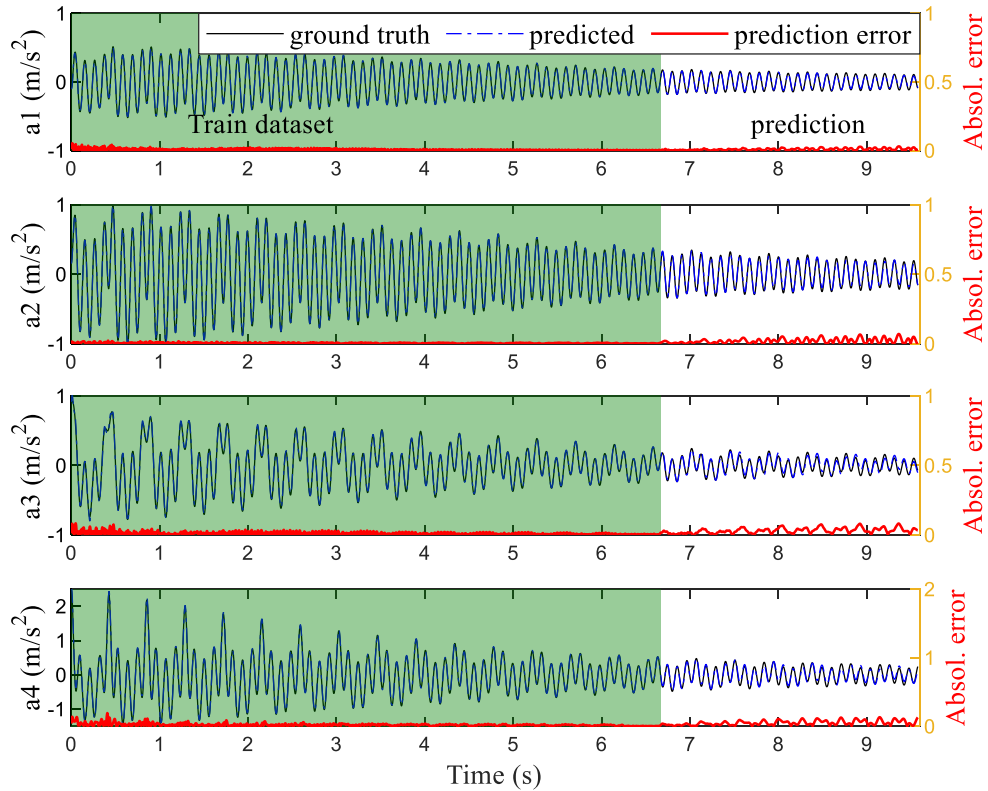


Figure 7-16. Response forecasting results of a nonlinear structure by using DMD with discrete Hankel SVD coordinate.

7.5 Conclusions

Phase space embedding has been recognized as a representative technique for analysing the vibration of nonlinear systems, which enriches the partially measured state information with time-shifted copies of itself. Under a certain condition, the reconstructed phase space attractor in delay coordinate can be up to diffeomorphic to the original attractor traced out by full-state variables. This study demonstrates that the HAVOC framework based on time-delay

DMD can be used to generate a linear representation of MDOF nonlinear structures with the consideration of measurement noise. The evolution of underlying nonlinear system can be linearly represented in the coordinate system spanned by singular vectors of the phase space embedded Hankel matrix. On this basis, a data-driven equation-free procedure to derive a linearized system representation of structural nonlinear vibrations is presented. This proposed approach is based on phase space embedding, regression of DMD and Koopman operator. Numerical and experimental vibration response measurements from both linear and nonlinear structural systems are utilized to validate the feasibility and accuracy of the presented method. For linear systems, the DMD based on the time-delay coordinate accurately captures the evolution of linear structural vibration. Natural frequencies and mode shapes are accurately extracted from the eigenvalues and eigenvectors of Koopman operator. For free vibration and forced vibration of nonlinear structures subjected to sinusoidal excitations, the proposed approach exhibits highly predictive performance. This study examines DMD regression acting on continuous and discrete Hankel SVD coordinate systems and demonstrates that the prediction performance of the latter is consistently better than the former. In addition, error analysis is conducted to clarify the effect of training dataset length on the response prediction performance. The results indicate that DMD with discrete Hankel SVD coordinate can very rapidly establish the relationships of the underlying dynamics with limited data. In conclusion, the proposed approach is efficient to generate linearized representation of deterministic nonlinear systems, which is useful in understanding and predicting structural nonlinear dynamics.

References

- [1] J.-P. Noël, G. Kerschen, Nonlinear system identification in structural dynamics: 10 more years of progress, *Mechanical Systems and Signal Processing*, 83 (2017) 2-35.
- [2] M. Hong, Q. Wang, Z. Su, L. Cheng, In situ health monitoring for bogie systems of CRH380 train on Beijing–Shanghai high-speed railway, *Mechanical Systems and Signal Processing*, 45 (2014) 378-395.
- [3] D. Giagopoulos, A. Arailopoulos, Computational framework for model updating of large scale linear and nonlinear finite element models using state of the art evolution strategy, *Computers & Structures*, 192 (2017) 210-232.
- [4] E. Reynders, System identification methods for (operational) modal analysis: review and comparison, *Archives of Computational Methods in Engineering*, 19 (2012) 51-124.
- [5] M. Cerrada, R.-V. Sánchez, C. Li, F. Pacheco, D. Cabrera, J.V. de Oliveira, R.E. Vásquez, A review on data-driven fault severity assessment in rolling bearings, *Mechanical Systems and Signal Processing*, 99 (2018) 169-196.
- [6] G. Kerschen, K. Worden, A.F. Vakakis, J.-C. Golinval, Past, present and future of nonlinear system identification in structural dynamics, *Mechanical Systems and Signal Processing*, 20 (2006) 505-592.
- [7] B. Xu, J. He, R. Rovekamp, S.J. Dyke, Structural parameters and dynamic loading identification from incomplete measurements: approach and validation, *Mechanical Systems and Signal Processing*, 28 (2012) 244-257.
- [8] H.S. Lee, Y.H. Hong, H.W. Park, Design of an FIR filter for the displacement reconstruction using measured acceleration in low - frequency dominant structures, *International Journal for Numerical Methods in Engineering*, 82 (2010) 403-434.
- [9] W. Zhang, J. Li, H. Hao, H. Ma, Damage detection in bridge structures under moving loads with phase trajectory change of multi-type vibration measurements, *Mechanical Systems and Signal Processing*, 87 (2017) 410-425.
- [10] A. Eftekhari, H.L. Yap, M.B. Wakin, C.J. Rozell, Stabilizing embedology: Geometry-preserving delay-coordinate maps, *Physical Review E*, 97 (2018) 022222.
- [11] T. Buzug, G. Pfister, Optimal delay time and embedding dimension for delay-time coordinates by analysis of the global static and local dynamical behavior of strange attractors, *Physical review A*, 45 (1992) 7073.
- [12] C.X. Qu, T.H. Yi, H.N. Li, Mode identification by eigensystem realization algorithm through virtual frequency response function, *Structural Control and Health Monitoring*, 26 (2019) e2429.
- [13] E.G. Plaza, P.N. López, Surface roughness monitoring by singular spectrum analysis of vibration signals, *Mechanical Systems and Signal Processing*, 84 (2017) 516-530.
- [14] C. Sabeerali, R. Ajayamohan, D. Giannakis, A.J. Majda, Extraction and prediction of indices for monsoon intraseasonal oscillations: An approach based on nonlinear Laplacian spectral analysis, *Climate Dynamics*, 49 (2017) 3031-3050.
- [15] S.L. Brunton, B.W. Brunton, J.L. Proctor, E. Kaiser, J.N. Kutz, Chaos as an intermittently forced linear system, *Nature communications*, 8 (2017) 1-9.
- [16] I. Mezić, Analysis of fluid flows via spectral properties of the Koopman operator, *Annual Review of Fluid Mechanics*, 45 (2013) 357-378.
- [17] M.O. Williams, I.G. Kevrekidis, C.W. Rowley, A data-driven approximation of the koopman operator: Extending dynamic mode decomposition, *Journal of Nonlinear Science*, 25 (2015) 1307-1346.

- [18] M. Korda, I. Mezić, On convergence of extended dynamic mode decomposition to the Koopman operator, *Journal of Nonlinear Science*, 28 (2018) 687-710.
- [19] P. Héas, C. Herzet, B. Combes, Generalized Kernel-Based Dynamic Mode Decomposition, *ICASSP 2020-2020 IEEE International Conference on Acoustics, Speech and Signal Processing (ICASSP)*, IEEE, 2020, pp. 3877-3881.
- [20] N. Takeishi, Y. Kawahara, T. Yairi, Learning Koopman invariant subspaces for dynamic mode decomposition, *Advances in Neural Information Processing Systems*, 30 (2017) 1130-1140.
- [21] D. Dylewsky, D. Barajas-Solano, T. Ma, A.M. Tartakovsky, J.N. Kutz, Dynamic mode decomposition for forecasting and analysis of power grid load data, *arXiv preprint arXiv:2010.04248*, (2020).
- [22] M. Kamb, E. Kaiser, S.L. Brunton, J.N. Kutz, Time-delay observables for koopman: Theory and applications, *SIAM Journal on Applied Dynamical Systems*, 19 (2020) 886-917.
- [23] B. Lusch, J.N. Kutz, S.L. Brunton, Deep learning for universal linear embeddings of nonlinear dynamics, *Nature Communications*, 9 (2018) 1-10.
- [24] M. Todd, J. Nichols, L. Pecora, L. Virgin, Vibration-based damage assessment utilizing state space geometry changes: local attractor variance ratio, *Smart Materials and Structures*, 10 (2001) 1000.
- [25] A.-H. Jiang, X.-C. Huang, Z.-H. Zhang, J. Li, Z.-Y. Zhang, H.-X. Hua, Mutual information algorithms, *Mechanical Systems and Signal Processing*, 24 (2010) 2947-2960.
- [26] Z. Liao, L. Song, P. Chen, Z. Guan, Z. Fang, K. Li, An effective singular value selection and bearing fault signal filtering diagnosis method based on false nearest neighbors and statistical information criteria, *Sensors*, 18 (2018) 2235.
- [27] M. Gavish, D.L. Donoho, The optimal hard threshold for singular values is $\sqrt{3}$, *IEEE Transactions on Information Theory*, 60 (2014) 5040-5053.
- [28] K.P. Champion, S.L. Brunton, J.N. Kutz, Discovery of nonlinear multiscale systems: Sampling strategies and embeddings, *SIAM Journal on Applied Dynamical Systems*, 18 (2019) 312-333.
- [29] S. Bhowmick, S. Nagarajaiah, Identification of full-field dynamic modes using continuous displacement response estimated from vibrating edge video, *Journal of Sound and Vibration*, 489 (2020) 115657.
- [30] A. Saito, T. Kuno, Data-driven experimental modal analysis by Dynamic Mode Decomposition, *Journal of Sound and Vibration*, (2020) 115434.
- [31] S.L. Brunton, J.L. Proctor, J.N. Kutz, Discovering governing equations from data by sparse identification of nonlinear dynamical systems, *Proceedings of the national academy of sciences*, 113 (2016) 3932-3937.
- [32] D. Dylewsky, E. Kaiser, S.L. Brunton, J.N. Kutz, Principal Component Trajectories (PCT): Nonlinear dynamics as a superposition of time-delayed periodic orbits, *arXiv preprint arXiv:2005.14321*, (2020).
- [33] P. Ni, Y. Xia, J. Li, H. Hao, Improved decentralized structural identification with output-only measurements, *Measurement*, 122 (2018) 597-610.
- [34] R. Brincker, L. Zhang, P. Andersen, Modal identification of output-only systems using frequency domain decomposition, *Smart Materials and Structures*, 10 (2001) 441.
- [35] C. Shih, Y. Tsuei, R. Allemang, D. Brown, Complex mode indication function and its

applications to spatial domain parameter estimation, *Mechanical Systems and Signal Processing*, 2 (1988) 367-377.

- [36] Z. Lai, T. Sun, S. Nagarajaiah, Adjustable template stiffness device and SDOF nonlinear frequency response, *Nonlinear Dynamics*, 96 (2019) 1559-1573.
- [37] Z. Lai, S. Nagarajaiah, Sparse structural system identification method for nonlinear dynamic systems with hysteresis/inelastic behavior, *Mechanical Systems and Signal Processing*, 117 (2019) 813-842.
- [38] A. Salova, J. Emenheiser, A. Rupe, J.P. Crutchfield, R.M. D'Souza, Koopman operator and its approximations for systems with symmetries, *Chaos: An Interdisciplinary Journal of Nonlinear Science*, 29 (2019) 093128.
- [39] S. Pan, K. Duraisamy, Physics-informed probabilistic learning of linear embeddings of nonlinear dynamics with guaranteed stability, *SIAM Journal on Applied Dynamical Systems*, 19 (2020) 480-509.
- [40] V.R. Challa, M. Prasad, Y. Shi, F.T. Fisher, A vibration energy harvesting device with bidirectional resonance frequency tunability, *Smart Materials and Structures*, 17 (2008) 015035.
- [41] Y. Leng, D. Tan, J. Liu, Y. Zhang, S. Fan, Magnetic force analysis and performance of a tri-stable piezoelectric energy harvester under random excitation, *Journal of Sound and Vibration*, 406 (2017) 146-160.

CHAPTER 8 PHASE SPACE RECONSTRUCTION AND Koopman OPERATOR BASED LINEARIZATION OF NONLINEAR MODEL FOR DAMAGE DETECTION OF NONLINEAR STRUCTURES

ABSTRACT⁷

Vibration responses of structures with inherent nonlinear behaviors can degrade the performance of linear theory based damage detection methods. This chapter integrates the phase space reconstruction and Koopman operator to provide a linear representation of strongly nonlinear systems. Similar to the modal analysis of linear systems, the linearized model allows for handling nonlinear vibration responses as a superposition of the discovered nonlinear coordinate basis. This property provides opportunities to identify the structural condition change of structures with initial nonlinearity. The eigen-frequencies extracted from the Koopman operator are served as damage features. The performance of using the eigen-frequencies from DMD for nonlinear structural damage detection is compared with the natural frequencies obtained from FFT and the time-frequency analysis method to emphasize the superiority of the proposed approach. Two experimental structures exhibiting inherent nonlinearity, namely a magneto-elastic system and a precast segment beam, are employed to demonstrate the feasibility and effectiveness of using the proposed method for identifying condition change of nonlinear structures. Results demonstrate that the presented nonlinearity linearization framework and the damage feature defined in this study are suitable for reliably identifying the occurrence of structural damage and condition change in structures with inherent nonlinearities.

8.1 Introduction

Over the past decades, structural damage detection has been widely recognized as one of the most crucial aspects of SHM. In literature, damage detection methods can be divided into two main categories, namely, NDT-based and vibration-based methods [1]. The vibration-based methods have attracted considerable attention due to their unique ability to detect minor

⁷ Peng, Z., Li, J. (2022). Phase space reconstruction and Koopman operator based linearization of nonlinear model for damage detection of nonlinear structures. *Advances in Structural Engineering*, 25(7), 1652-1669. <https://doi.org/10.1177/13694332221082729>.

structural condition changes inside the structures that are invisible via regular inspection. The fundamental principle of vibration-based damage detection methods is to extract reliable features including structural vibration characteristics, such as modal information and its variants from vibration responses, to distinguish the healthy and damage states of structures. It is assumed in most of the vibration-based damage detection methods that the structural dynamics are governed by linear theory. This means that structures are assumed as linear before and after damage, and vibration characteristics of structures with linear vibration behavior are used for damage detection. These traditional and well-developed methods have been successfully applied to identify the presence, location, and even the extent of damage in linear structures with the assistance of an accurate FE model and model updating techniques.

However, structures may exhibit nonlinear behaviors due to the accumulation of structural damage (e.g., breathing crack, plastic deformation and joint looseness) [2-5]. Under these circumstances, damage detection methods based on the linear structural assumption could not be accurate for structures with nonlinear behavior. The well-established time-frequency analysis, PST and higher order spectra methods can be employed to identify the damage-induced nonlinearity [6-10]. Besides, the real-world structures are inherently nonlinear to a certain extent, because of the geometric nonlinearities, materials with nonlinear constitutive relationships, complex boundary conditions and joint interfaces [11]. Under this situation, linear theory based system parameter identification or modal analysis methods might result in biased parameter estimation results and fail to accurately detect structural damage. Focus has been increasingly turned from linear theory based methods to nonlinear damage detection methods [12, 13].

Most types of inherent structural nonlinearities are nonlinear functions of the displacement responses and can be visualized via the restoring force-displacement curve. For instance, the stiffness hardening, softening and piecewise linear stiffness nonlinearity are represented as functions of displacement responses. Other nonlinearity sources, such as nonlinear damping and Coulomb friction, are related to the velocity responses. Owing to the complexity of nonlinearity, prior knowledge on the nonlinearity type and function form is required for selecting reasonable nonlinear system identification and damage detection methods. In literature, time-frequency analysis, nonlinear FE model updating, extended Kalman filter and Bayesian inference-based methods have been extensively developed to identify nonlinear structural parameters [10, 14, 15]. Another common type of methods constructs a mathematic alternative model to describe the possible nonlinear feature of the underlying system [16, 17]. Although a considerable number of techniques have been developed for nonlinear system identification and damage detection, a generalized model that is able to characterize structural nonlinear behaviors has not well established partially due to

the following challenges:

- 1) Nonlinear dynamics do not satisfy the linear superposition principle, therefore the well-characterized system identification and modal analysis methods are not applicable;
- 2) The nonlinear function may be governed by a hidden variable, i.e. the hysteretic displacement $z(t)$ of Bouc-wen model is non-observable; and
- 3) In practical SHM applications, only partial state variables can be measured at a limited number of spatial locations. Furthermore, the external excitations applied to actual structures are difficult or expensive to be accurately measured.

Koopman operator is an infinite-dimensional linear operator, seeking a new coordinate system where the nonlinear dynamic behavior can be linearly represented [18]. The Koopman operator enables globally linear representation of nonlinear dynamical models, which can be used to predict the future responses by using the current measurements. This property has been confirmed by the author's previous study [19]. Linearized models are desirable since many powerful linear algebraic methods, such as the ERA, can be extended to the nonlinear systems. DMD has been demonstrated to be an effective algorithm for estimating the finite-dimensional eigenvalues and eigenvectors of Koopman operator [20]. However, to accurately approximate the eigenfunction of Koopman operator, prior knowledge on the type of nonlinearity is required to judiciously choose the nonlinear coordinate basis vectors. To alleviate this issue, the EDMD has been established, which augments a broader set of nonlinear coordinate basis, i.e. polynomial kernel, Fourier modes, radial basis functions or discontinuous spectral elements to the classic DMD according to domain-specific prior knowledge [21]. The sparse identification and dictionary-learning algorithm have been commonly used to select a small number of representative nonlinear coordinate basis from a set of nonlinear candidate observations [22].

Phase space embedding is a classical technique to enrich the information, when only partial state measurement is available. According to Taken's embedding theorem, the PST reconstructed by the time-shift copy of a single state variable can be up to diffeomorphic to the original dynamic attractor traced out by full-state observations. Recently, Brunton et al. [23] developed a HAVOK approach and demonstrated that the Koopman operator approximated by DMD on delay embedding coordinate provides a linear representation of strongly nonlinear systems. Unlike EDMD, HAVOK does not require the explicit use of a pre-determined basis dictionary, the right singular vector of Hankel matrix provides a coordinate that converges to the true Koopman eigenfunction and eigenvalue of nonlinear systems [24]. Therefore, HAVOC framework can be used on highly chaotic nonlinear systems, for the scenarios when approximations of the underlying near-periodic dynamics are completely

unknown. However, it should be noted that the HAVOC framework is also applicable to linear structures, since the HAVOC discovers a sparse Fourier basis made of sinusoids that match well with the Fourier spectrum [24, 25]. According to the author's previous study [19], the eigenvalue and eigenvector of a linear steel frame approximated by HAVOC framework agree well with the natural frequency and mode shape obtained from FDD and CMIF methods [26-28]. In literature, the HAVOC framework has been applied to construct a linear control model to reconstruct and forecast the real-world power grid load [29]. The control force discovered by the HAVOC framework matches well with the electricity usage of public holiday, i.e. new year, super bowl, labor day with respect to unusual electricity usage, which means that the learned external force can offer interpretative insight into anomalous events occurred in the operational condition. The comparison results show that the prediction performance of HAVOC method is superior than other leading data-driven methods, such as long short-term memory (LSTM), recurrent neural networks, auto regressive integrated moving average (ARIMA) and ensemble Gaussian process regression [29]. The convergence of HAVOC model to the true Koopman eigenfunction and eigenvalues are theoretically discussed in Refs. [18, 24, 30]. HAVOC framework can be potentially developed and applied for analysing the vibration responses of civil engineering structures mainly due to the following two reasons. Firstly, the delay embedding of partial variables are serviced as the input, which motivates the applications to civil engineering structures where only partial state variables are measurable. Secondly, the nonlinear linearization model obtained by HAVOC model offers many desirable properties. For example, the analogous concept of natural frequency of linear structures can be extended to nonlinear structures by calculating the eigenvalues of Koopman operator, which will be demonstrated in the subsequent study and following sections.

This chapter aims to validate the feasibility of using the Koopman operator identified from the HAVOC framework to conduct the damage detection of nonlinear structures. It should be clarified that the framework of discovering the nonlinear coordinate to linearize the nonlinear systems is developed in the authors' previous study [19]. The main contribution of this study is to extract the damage feature from the linearization framework to identify structural damage of nonlinear structures. As an early attempt in this study, the eigenvalues (or understood as eigen-frequencies) of Koopman operator are approximated from the nonlinear vibration responses corresponding to different structural conditions using the HAVOC model. The extracted eigen-frequencies of Koopman operator are compared with the vibration frequencies obtained from FFT and the time-frequency analysis method, such as variational mode decomposition-Hilbert transform (VMD-HT) [31], to emphasize the superiority of the proposed approach. The focus of this study is extracting the damage-sensitive features by developing Nonlinear Linearization Model for damage detection of nonlinear structures. This

research contributes to providing an equivalent nonlinearity linearization framework and extending the feasibility of generalized eigen-frequencies for nonlinear structural damage detection. It should be highlighted that the process of discovering the linearized model is fully data-driven and unsupervised, which means that prior knowledge on the source and type of nonlinearity is not necessary. This is an essential advantage of using the proposed approach for laboratory and real applications.

The outline of this study is described as follows: Section 2 will briefly introduce the theoretical derivation of extracting the eigen-frequencies of DMD obtained from the HAVOC framework. In addition, using the DMD eigen-frequencies as damage features for nonlinear structural damage detection is discussed. In Sections 3 and 4, two experimental structures with inherent nonlinearities, namely a magneto-elastic system and a precast segment beam, are employed to demonstrate the feasibility and effectiveness of the proposed method to identify condition change of nonlinear structures. In Section 5, the conclusions and future studies for further improvement are provided.

8.2 Data-driven decomposition of nonlinear dynamic system into linear model

8.2.1 Theoretical derivation

For the sake of completeness, theoretical derivation of three main components of the developed nonlinearity linearization method [19], including the phase space reconstruction, SVD and DMD, are briefly introduced in this section. Phase space reconstruction (sometimes referred to as time-delay embedding) is a process of lifting a single column time series into a higher dimensional attractor by stacking it with time-delay embedding of itself. Phase space embedding technique possesses a crucial benefit. In particular, the phase space attractor reconstructed from partial state variables can be up to diffeomorphic to the original attractor spanned by the full-state observation. This is of great practical significance to dynamic system, when full-state variable is impossible or expensive to measure. In literature, a single-channel signal is often used to reconstruct the PST. More generally, the time delay embedding procedure can be extended to multi-channel signals. For a structure attached with n accelerometers, the acceleration responses vector $\mathbf{a}(t) \in \mathbb{R}^n$ can be embedded as

$$\mathbf{H} = \begin{bmatrix} | & | & \cdots & | \\ \mathbf{a}(t_1) & \mathbf{a}(t_2) & \cdots & \mathbf{a}(t_m) \\ | & | & \cdots & | \\ \mathbf{a}(t_2) & \mathbf{a}(t_3) & \cdots & \mathbf{a}(t_{m+1}) \\ | & | & \ddots & | \\ \vdots & \vdots & \ddots & \vdots \\ | & | & \cdots & | \\ \mathbf{a}(t_d) & \mathbf{a}(t_{d+1}) & \cdots & \mathbf{a}(t_{d+m-1}) \\ | & | & \cdots & | \end{bmatrix} \quad (8.1)$$

where \mathbf{H} is a vectorized Hankel matrix with a dimension of $nd \times m$. d and m represent the embedding dimension and the embedding length, respectively. For structural vibration test or in-situ measurement, the number of samples m is sufficient. Previous studies suggest that the embedding dimension d should be larger than two times of the distinct frequency components that appear in the Fourier spectrum, to ensure that the dynamic responses can be fully unfolded in the phase space. Further parameter analysis is conducted in Section 3 to demonstrate the effect of embedding dimension on the estimation of Koopman operator. Figure 8-1 provides a schematic diagram of Koopman operator. As shown in this figure, the original dynamic system $f(x_t)$ evolving on a nonlinear manifold \mathcal{M} is transformed to a linear dynamic system $\mathcal{K}(y_t)$ in the space spanned by $g: x_t \rightarrow y_t$.

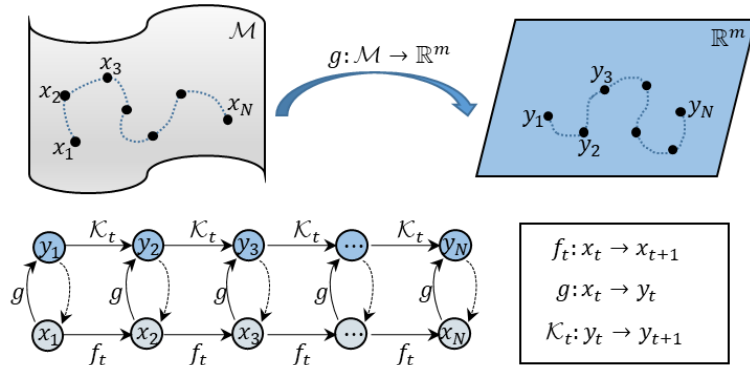


Figure 8-1. Schematic diagram of Koopman operator.

For linear or weak nonlinear systems, DMD can be applied to the Hankel matrix defined in Eq. (8.1) to obtain a set of modes that are representatives of the underlying dynamic systems with the most accuracy. However, DMD acting on the time-delay coordinates is unable to approximate the time-invariant Koopman operator for strong nonlinear dynamic systems accurately. This is because DMD seeks a best-fit linear model of the dynamic system. SVD is one of the most popular methods to provide a unitary orthogonal basis for the row and columns of data matrix. Given the Hankel matrix $\mathbf{H} \in \mathbb{R}^{nd \times m}$, the SVD decomposes \mathbf{H} into the product of three matrices

$$\mathbf{H} \approx \mathbf{U}_r \mathbf{S}_r \mathbf{V}_r^* \quad (8.2)$$

where $\mathbf{U}_r \in \mathbb{R}^{nd \times r}$ and $\mathbf{V}_r^* \in \mathbb{R}^{r \times m}$ are the left and right singular vectors of \mathbf{H} , respectively. r is the truncation order, which can be determined as two times of the number of observed distinct frequency components from the singular value spectrum. In the HAVOK framework, Brunton et al. [23] proved that the DMD which acts on the coordinate system consisting of the first r rows of \mathbf{V}_r^* , yields accurate linear representation of strong nonlinear systems. For consistence, this coordinate system is referred to as Hankel SVD coordinate.

DMD is applied on the Hankel SVD coordinate to discover the following linearized model

$$\dot{\mathbf{V}}_r^* \approx \mathbf{A} \mathbf{V}_r^* \quad (8.3)$$

where $\dot{\mathbf{V}}_r$ is the derivative of \mathbf{V}_r . \mathbf{V}_r^* denotes the complex conjugate transpose of \mathbf{V}_r . In this study, the 4th order central difference is used to calculate $\dot{\mathbf{V}}_r$. In the simplest implementation, the Koopman operator \mathbf{A} can be approximated via the standard DMD algorithm by solving the following optimization

$$\mathbf{A} = \min_{\mathbf{A}} \|\dot{\mathbf{V}}_r^* - \mathbf{A} \mathbf{V}_r^*\|_F \quad (8.4)$$

where the solution is $\mathbf{A} = \dot{\mathbf{V}}_r^* (\mathbf{V}_r^*)^\dagger$, where \dagger represents the pseudo-inverse and the subscript F denotes the Frobenius norm. Instead of using the standard DMD, an alternative formulation known as opt-DMD proposed in Ref. [32] is used throughout this study to estimate the Koopman operator \mathbf{A} . The opt-DMD obtains less bias in Koopman operator estimation in the presence of measurement noise than the standard DMD algorithm. Eigenvalues λ and eigenvector φ of the HAVOC model can be obtained using the eigendecomposition of matrix \mathbf{A}

$$[\lambda, \varphi] = \text{eig}(\mathbf{A}) \quad (8.5)$$

For linear structures, the imaginary and real parts of the obtained eigenvalues are the same as the natural frequency and damping ratio, respectively. The opt-DMD eigenvector is the same as the mode shape. For nonlinear dynamic structures, the eigenvalue (also referred to as eigen-frequency) identified from the HAVOC nonlinear linearization framework are used as the damage feature to indicate the presence of structural condition change. The pseudocode for estimating the opt-DMD eigen-frequency via HAVOC framework is presented in Algorithm 1. The process by performing the HAVOC framework to extract the opt-DMD eigen-frequency for damage detection of nonlinear structures is shown in Figure 8-2. The multi-channel vibration responses are embedded by using Eq. (8.1). Then, the truncated SVD is applied on the time-delay embedded matrix \mathbf{H} to obtain the Hankel SVD coordinate. The

opt-DMD algorithm is applied to the Hankel SVD coordinate to approximate the koopman operator \mathbf{A} . It should be noted that the eigenvalue λ of koopman operator \mathbf{A} is used as damage feature for the damage identification of structure with initial nonlinearity.

Algorithm 1: Estimation of the opt-DMD eigen-frequency via HAVOC framework

Input: measured vibration responses $\mathbf{a}(t)$ and target truncation rank r .

Output: Koopman operator \mathbf{A} and opt-DMD eigen-frequency λ

1: $\mathbf{H} = \text{Hankel}(\mathbf{a}(t), r)$

2: $[\mathbf{U}_{1:r}, \mathbf{S}_{1:r}, \mathbf{V}_{1:r}^*] = \text{SVD}(\mathbf{H}, r)$ $\mathbf{U}_{1:r} \in \mathbb{R}^{nd \times r}, \mathbf{S}_{1:r} \in \mathbb{R}^{r \times r}, \mathbf{V}_{1:r}^* \in \mathbb{R}^{r \times m}$

3: $\dot{\mathbf{V}}_r^* \approx \mathbf{A} \mathbf{V}_r^*$ $\mathbf{A} \in \mathbb{R}^{r \times r}$

4: $\mathbf{A} = \text{opt-DMD}(\min_{\mathbf{A}} \|\dot{\mathbf{V}}_r^* - \mathbf{A} \mathbf{V}_r^*\|_F)$ $\gg \text{opt-DMD}$

$\mathbf{A} \mathbf{V}_r^*\|_F)$

5: $[\lambda, \varphi] = \text{eig}(\mathbf{A})$ $\gg \text{eigenvalues } \lambda \text{ and eigenvector } \varphi$

6: end procedure

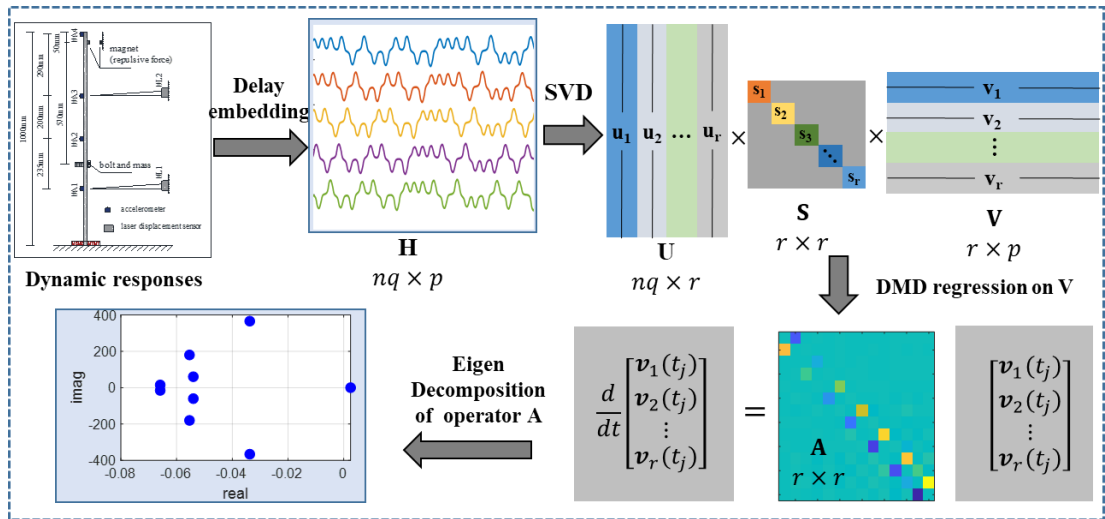


Figure 8-2. The procedure of obtaining the damage feature from the nonlinear linearization framework.

8.2.2 Remarks on the proposed approach

In this study, the HAVOC framework is introduced to generate a linearized representation of structural nonlinear vibration responses and extract damage feature. It will be demonstrated that the obtained opt-DMD eigen-frequency could be used as a reliable DI for the condition

assessment of structure with inherent nonlinearity. The proposed method is driven by the following aspects and advantages:

1) HAVOC discovers a nonlinear coordinate basis that most represent the underlying system in an unsupervised way without prior knowledge on the specific type of nonlinearity. This method allows for handling nonlinear vibration responses as a superposition of the discovered coordinate basis, which is impossible to be represented by the Fourier basis-based linear system modal analysis method [19, 23].

2) The opt-DMD eigen-frequency approximated from the linearization model is robust to external excitation and yields reliable clustering performance under different structural conditions [32].

3) The proposed method is easy to implement. Two parameters, namely the embedding dimension d and the SVD truncation rank r , should be predetermined to implement the proposed method. Parameter sensitivity analysis will be conducted in Section 3 to demonstrate that the embedding dimension brings ignorable influence to the extraction of opt-DMD eigen-frequencies. Clear criterion is provided in Section 2 to determine the truncation rank r .

However, a main limitation is that the introduce linearization framework is not applicable to vibration responses without discrete frequency spectral peaks. This is because singular value spectrum of a signal with a continuous spectrum is not dominated by several distinct frequency component, and thus cannot be fully reproduced by the opt-DMD with a limited truncation order. As a result, the proposed method is not suitable for systems with a strong hysteresis effect without discrete frequency spectrum.

8.3 Experimental verifications on an aluminum beam with magnet induced nonlinearity

8.3.1 Experimental setup

To validate the feasibility and accuracy of using the proposed method for the damage detection of a system with an inherent nonlinearity, an aluminum beam with the magnet-induced nonlinearity is used in this study. The experimental setup is shown in Figure 8-3(a). The dimension of the cantilever aluminum beam is 1000 mm \times 40 mm \times 3 mm. A bolt connected with different numbers of nuts is used to simulate the structure condition changes, by changing the weight of added mass at a specific location. Hexagon steel bolts with a diameter of 8mm and a length of 40mm are used in the first experimental tests. The weights of bolt and each nut are about 29 grams and 10 grams, respectively. The specimen is excited by a shaking table system. Four accelerometers and two laser displacement sensors are installed to measure the vibration responses with a sampling rate of 300 Hz. Two round

magnets with a diameter of 18 mm are respectively mounted on the supporting frame and the free end of the aluminum beam at the same height. The locations of sensors and magnets are shown in Figure 8-3(b).

The repulsive magnetic force changes nonlinearly with the relative distance between two magnets, which causes a stiffness hardening effect in the system when the free end of the cantilever beam moves towards the supporting frame. An equivalent spring diagram is presented in Figure 8-4 to explain the stiffness hardening effects induced by the magnet induced repulsive force. The closer of two magnets will results in the increase of the nonlinear repulsive force, vice versa. The application of magnetic force to simulate stiffness nonlinearity is also found in Refs. [17, 33]. It is noted that this structure does not represent a scaled model of a particular real-world structure, but is rather constructed to simulate a structural system with nonlinear behavior. Therefore, the measured responses from free vibration tests with an initial introduced displacement and seismic load tests with two levels of PGA values are obtained to validate the robustness and performance of using the proposed method for nonlinear structural damage detection. The applied ground motion excitations are generated by a shake table according to Australian Standard AS 1170.4-2007 and scaled to PGA values of 0.05 g and 0.1 g, respectively.

As shown in Figure 8-5, one nut is installed on the bolt for the baseline state. The number of nuts is set as two, three, and four, respectively, to simulate three levels of structural condition change for damage detection investigations. The dynamic tests are repeated three times for each structural state condition subjected to a specific loading scenario. Figure 8-6 shows the time domain and frequency domain responses of the magneto-elastic system under the baseline state subjected to free vibration and seismic tests, respectively. As can be observed in the Fourier spectra, the first three order natural frequencies of the aluminum beam are around 2.4 Hz, 9.09 Hz and 27.86 Hz, respectively.

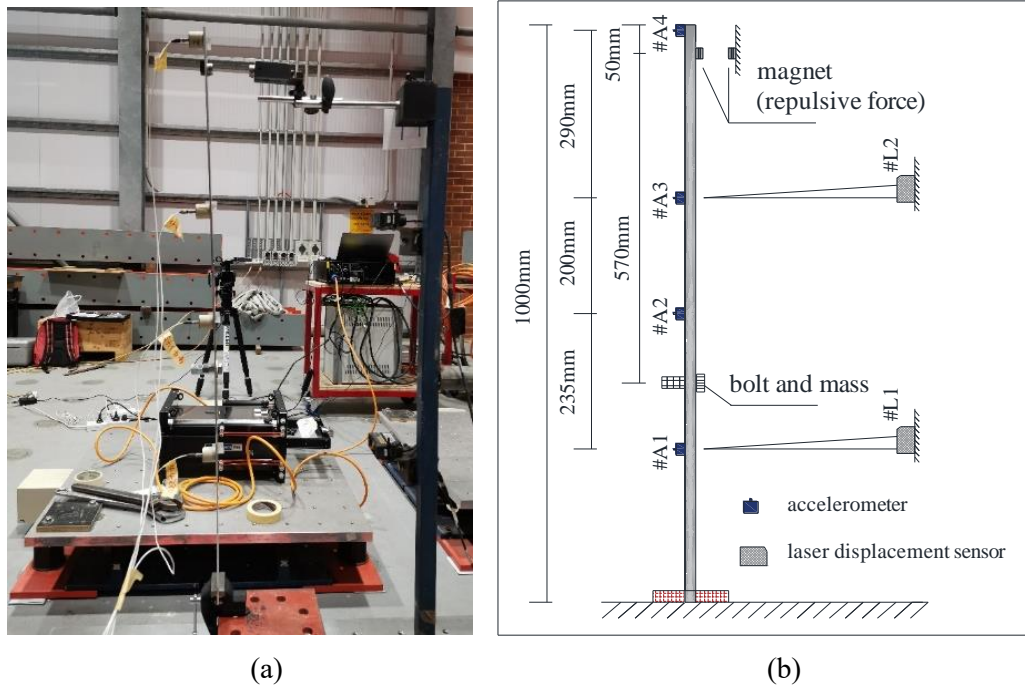


Figure 8-3. The experimental setup: (a) Layout of the aluminum specimen with magnet installed at the top tip; (b) Schematic diagram of experimental setup.

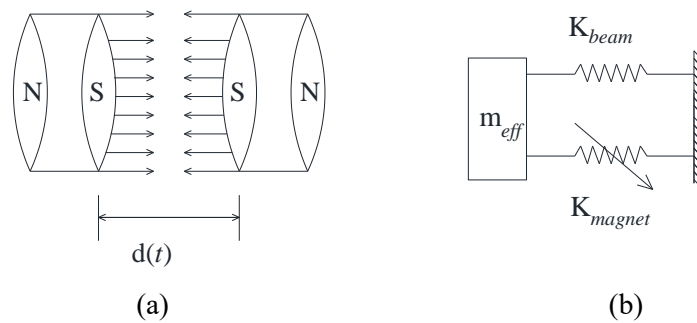


Figure 8-4. Spring equivalents for the magnet induced repulsive force resulting in stiffness hardening effect: (a) Magnet induced repulsive force; (b) Equivalent spring model.

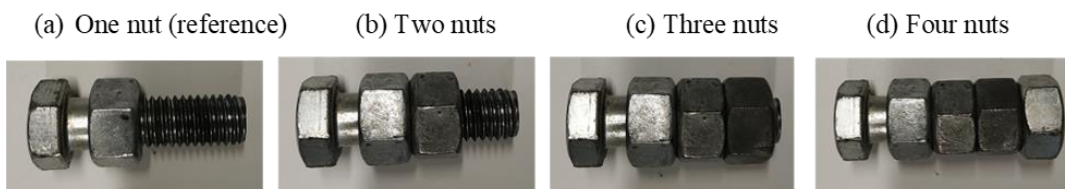


Figure 8-5. Use of nuts to simulate the structural condition change.

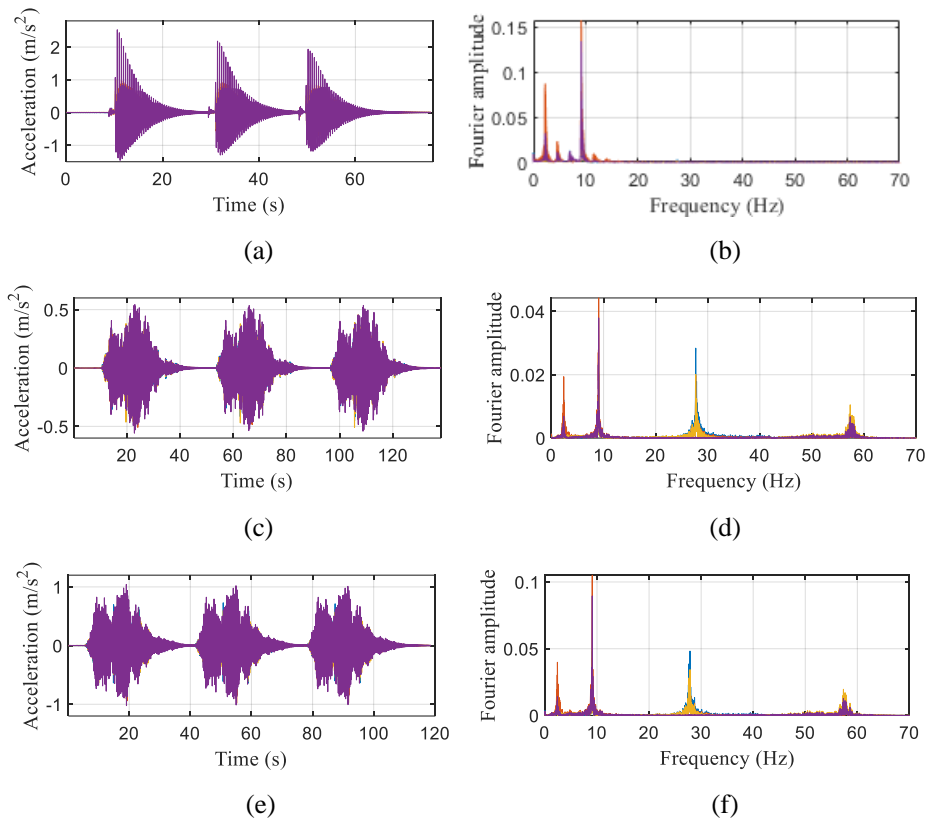


Figure 8-6. The measured acceleration responses and obtained frequency spectra from the specimen subjected to free vibration (a-b), seismic excitation with a GPA of 0.05g (c-d) and seismic excitation with a GPA of 0.1g (e-f).

To detect and visualize the magnetic force induced nonlinear effect in the structure, the VMD-HT method is adopted to extract the time-frequency representation of free vibration responses. As shown in the time-frequency analysis results presented in Figure 8-7(a), the first two order instantaneous frequencies are time-varying. The variation of instantaneous frequencies decrease with the amplitude of vibration responses. Figure 8-7(b) shows the scatter plot of dynamic displacement responses measured by LVDT #L2 and the corresponding instantaneous frequencies. A strong correlation is found in the mutual relationship between the displacement and the first-order instantaneous frequency. The correlation coefficient between displacement and the first order natural frequency is 0.9338. The magnet induced repulsive force intensifies and results in stiffness hardening, when the aluminum beam moves towards to the magnet attached on the supporting frame. This intrinsically nonlinear behavior negatively affects the detectability of the simulated structural condition change by using the existing frequency domain or time frequency analysis based damage detection methods, since the system is nonlinear and traditional linear methods may not be applicable.

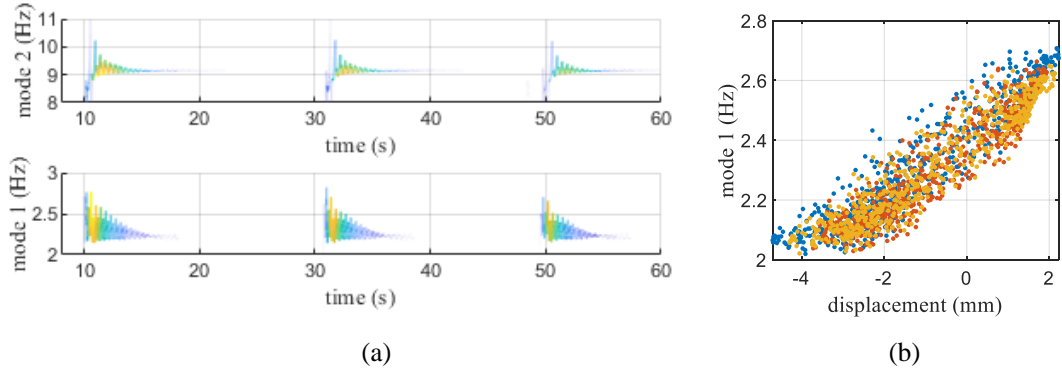


Figure 8-7. (a) Time frequency representation of the free vibration responses of specimen; (b) the relationship between the dynamic displacement measured by LVDT #L2 and the first order natural frequency.

The acceleration responses $\mathbf{a}(t)$ measured from the first repeated tests of the structure under the baseline state subjected to the ground motion excitation with a GPA of 0.05g, are used to demonstrate the procedure of obtaining the Koopman operator and extracting the corresponding opt-DMD eigen-frequencies. $\mathbf{a}(t)$ is of size 4×13117 , which consists of 4 channels acceleration responses with a length of 13117 sampling points. The Hankel matrix \mathbf{H} of size 512×12990 can be reconstructed by using the multivariate phase space embedding with the number of delay predetermined as 128. The effect of delay embedding dimension on the identification of opt-DMD eigen-frequency is further analysed and the results are shown in Table 8-1. Then, the truncated SVD is applied to perform $\mathbf{H} \approx \mathbf{USV}^*$. Figure 8-8 shows the first eight columns of the matrix $\mathbf{U} \in \mathbb{R}^{512 \times 8}$ and the corresponding Fourier spectrum of right-singular vector. u_i represents the i -th column of the left-singular vector \mathbf{U} , which is referred to as SVD modes in this chapter. Several key features are observed in Figure 8-8. Firstly, the frequencies of SVD modes are consistent with the natural frequencies presented in the Fourier spectrum of the acceleration responses shown in Figure 8-6(d), which means that the SVD applied on the time delay matrix discovers a sparse and nearly sinusoidal basis that is most representative coordinate of the nonlinear vibration responses. For instance, the frequencies of the first two SVD modes are approaching to the second order modal frequency presented in Figure 8-6(d). Secondly, the SVD modes self-organize into pairs (e.g. u_1 and u_2), which share the same frequency and different phase angle. Thirdly, the sequence of SVD modes is associated with the singular values. For example, the first two singular values shown in the singular value spectrum correspond to SVD modes u_1 and u_2 , which indicates that these two SVD modes contribute most to the signal. The frequency of right-singular vector v_1 and v_2 are corresponding to the second order natural frequency, with the highest Fourier amplitude.

Table 8-1. The effect of delay number on the estimation of DMD eigen-frequencies

Delay number	12	24	48	72	96	128
1 st DMD Eigenfreqs	2.3609	2.3611	2.3610	2.3609	2.3610	2.3611
2 nd DMD Eigenfreqs	9.0722	9.0722	9.0722	9.0722	9.0723	9.0723
3 rd DMD Eigenfreqs	27.6861	27.6862	27.6860	27.6858	27.6857	27.6857
4 th DMD Eigenfreqs	57.3691	57.3691	57.3691	57.3691	57.3692	57.3693

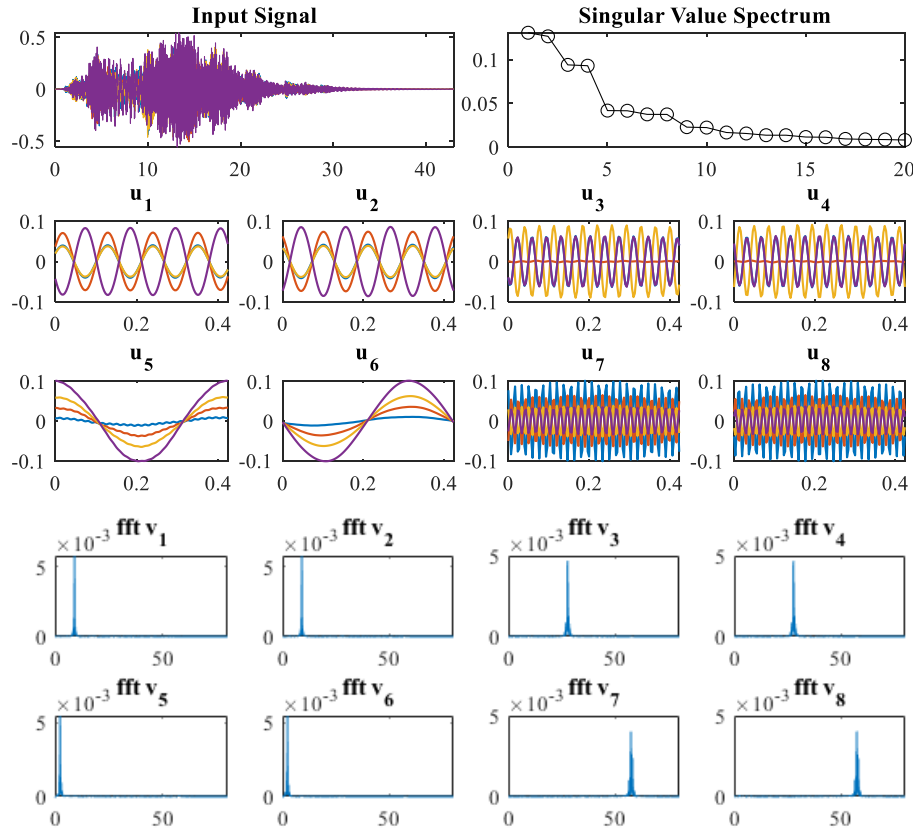


Figure 8-8. The singular value spectrum, SVD modes and the corresponding Fourier spectrum of right-singular vector of the considered nonlinear system subjected to ground motion excitation with a PGA of 0.05g.

Following the HAVOC procedure defined in Figure 8-2, the finite-dimension Koopman operator \mathcal{A} can be regressively approximated by applying the opt-DMD to the right-singular vector \mathbf{V} . In this study, the Opt-DMD developed in Ref. [34] is introduced to estimate the Koopman operator \mathcal{A} . Finally, the eigen-decomposition can be applied to the Koopman operator \mathcal{A} to obtain the opt-DMD eigen-frequencies. In practical applications, the delay number may affect the approximation of Koopman operator \mathcal{A} and further the accuracy of opt-DMD eigen-frequencies. The number of delay used to construct the Hankel matrix \mathbf{H} varies from 12 to 128 with an interval of 24 to illustrate the effects of delay number. Results listed in Table 8-1 indicate that the variation of the first four DMD eigen-frequencies caused by the

change of delay number is negligible. Therefore it can be concluded that reliable damage feature can be obtained via HAVOC framework without rigorous tuning delay number parameter. It is suggested that the delay number should be greater than or equal to two times of the number of peaks observed in the Fourier spectrum. In this experimental case, four frequency peaks are clearly observed in Figure 8-6, therefore, the delay number should be no less than 8.

Figure 8-9 compares the resonance frequencies in the Fourier spectrum and the opt-DMD eigen-frequencies using the vibration responses measured under the ground motion with a PGA of 0.05g. It can be observed that the DMD spectrum is sparse and the opt-DMD eigen-frequencies match well with the first four order frequencies. However, the exact opt-DMD eigen-frequencies are slightly different from the peaks of Fourier spectrum.

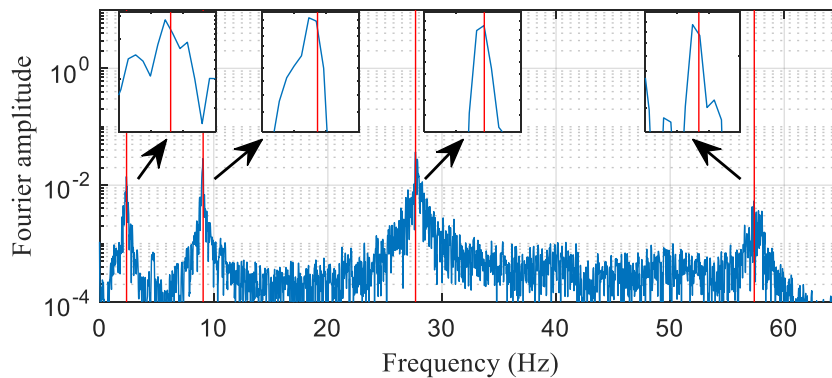


Figure 8-9. Comparison of Fourier spectrum and the DMD eigen-frequencies (The Fourier spectrum is plotted in blue and the vertical red line represents the opt-DMD eigen-frequencies).

8.3.2 Structural condition change identification results

For comparison, the time-varying instantaneous frequency, Fourier frequency and the opt-DMD eigen-frequency of each structural condition using the vibration responses acquired from different loading scenarios are identified to illustrate the superiority of the proposed nonlinear structural damage detection method. The instantaneous frequencies are identified by using the VMD-HT based method. The accuracy of time-frequency analysis could be deficient in the lower amplitude region, therefore, the instantaneous frequencies are discarded when the corresponding amplitude is less than 20% of its maxima value. The Fourier frequency is determined as the peaks appeared in the Fourier spectrum. Figure 8-10 shows the violin plot of the first two order instantaneous frequencies subjected to different excitations by using the VMD-HT method. Owing to the nonlinear stiffness effect, a certain level of variation is observed in the first two instantaneous frequencies. In particular, the frequency variation range under seismic excitation of PGA 0.1 g is larger than that of PGA 0.05 g. The mean value and medium value of instantaneous frequencies are stably decreased with the increasing number

of nuts. This is because increasing the added mass on the testing system results in a decrease in the natural frequencies. In Figure 8-10, the trend of mean values of instantaneous frequency is consistent with the severity of preset damage scenarios. However, significant variation of instantaneous frequency is observed.

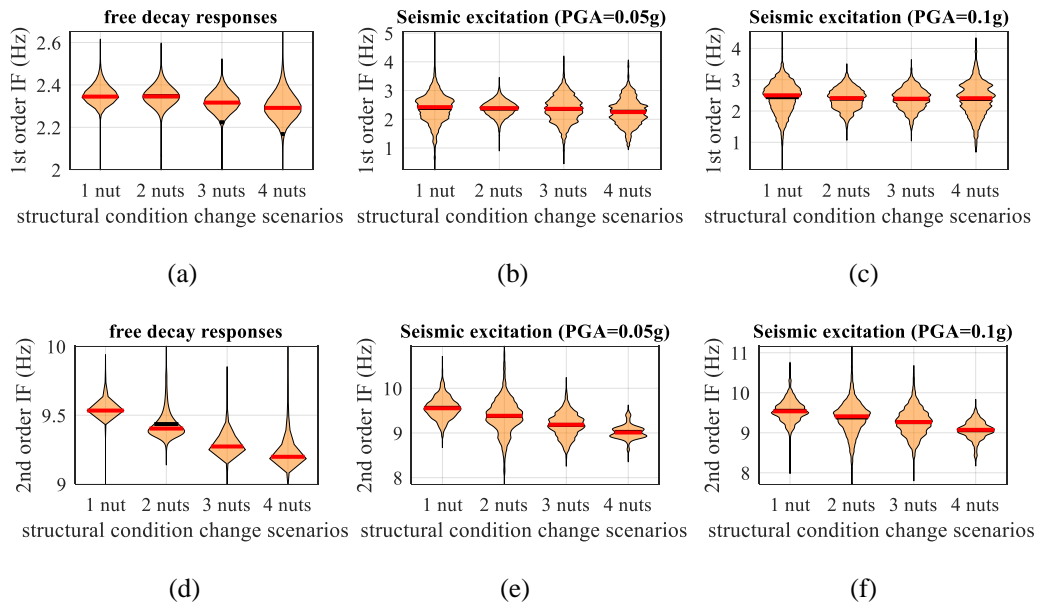


Figure 8-10. The distributions of the first two order instantaneous frequencies under different structural conditions. Red and black lines represent the mean value and medium of instantaneous frequencies, respectively. IF means instantaneous frequency.

Figure 8-11, Figure 8-12 and Figure 8-13 show the FFT, time-frequency analysis and opt-DMD eigen-frequencies of the aluminum beam subjected to free vibration, ground motion excitations with two levels of PGA values, respectively. The FFT frequencies is defined as the peaks that are observed in the Fourier spectrum. The IF mean values in these figures represent the mean values of instantaneous frequency corresponding to each repeat test. Comparison results presented in these figures indicate that the opt-DMD eigen-frequencies obtained from the proposed method are more converged than those of FFT frequencies and time-frequency analysis results. In particular, in Figure 8-13(b), 2 nuts and 3 nut states are not able to be separated by using FFT frequencies. The results of DMD eigen frequencies are better than those obtained from FFT and time-frequency analysis for all the cases. The opt-DMD eigen-frequencies as DSF show excellent clustering results for each structural condition, which demonstrates the advantage of using the proposed method in generating a linearization model and improving the damage detectability for nonlinear structures. In this experimental verification, both the opt-DMD eigen-frequencies and the mean values of instantaneous frequencies can be used to evident the structure condition change. Using opt-DMD eigen-frequencies as damage-sensitive features outperforms the FFT and time-frequency analysis

based methods in terms of the effectiveness and accuracy for detecting the damage in structures with inherent nonlinearities. It should be noted that the main advantage of the proposed approach is to linearize nonlinear systems into linear ones, and then the obtained eigenvalues can be used for damage detection of nonlinear structures effectively. However, Different from linear structure, the external loading amplitude and type will affect the nonlinearity level of the vibration responses of nonlinear structures. As a result, the vibration frequency, instantaneous frequency and the developed opt-DMD eigen-frequency extracted from the vibration responses of nonlinear structures subjected to different loading conditions are different. Therefore, it is not suitable to compare the proposed damage feature for nonlinear structures under different loading conditions in one figure.

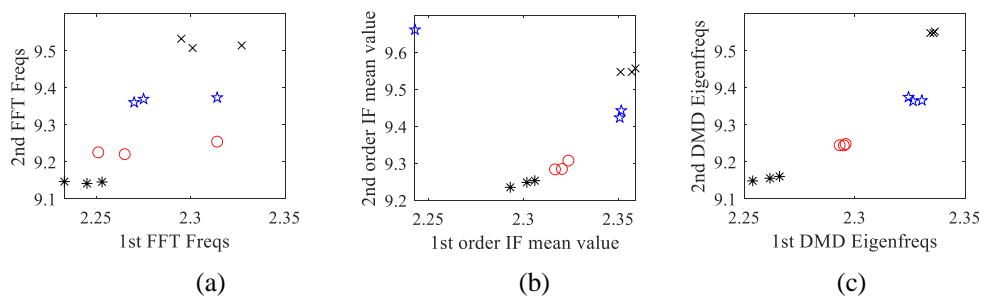


Figure 8-11. The first two order natural frequencies identified from free vibration responses: (a) FFT frequencies; (b) mean values of time-varying instantaneous frequencies; (c) opt-DMD eigen-frequencies. The symbols ×, ☆, ○ and * represent structural states with one nut, two nuts, three nuts and four nuts, respectively.

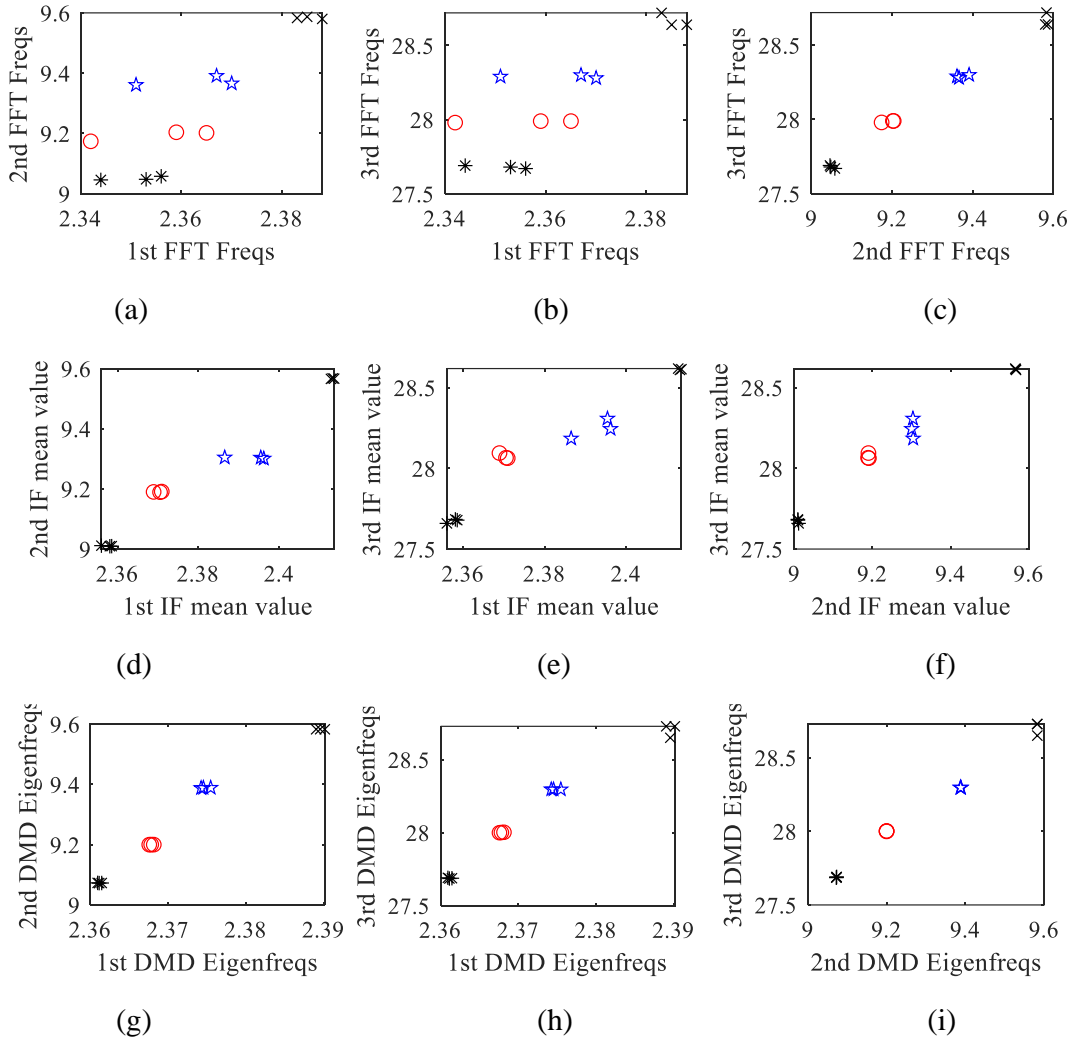


Figure 8-12. Comparison among the first three order eigen-frequencies identified from the structural responses subjected to seismic excitation of PGA 0.05g: (a) 1st and 2nd, (b) 1st and 3rd and (c) 2nd and 3rd FFT frequencies; (d) 1st and 2nd, (e) 1st and 3rd and (f) 2nd and 3rd mean values of time-varying instantaneous frequencies; (g) 1st and 2nd, (h) 1st and 3rd and (i) 2nd and 3rd opt-DMD eigen-frequencies. The symbols \times , \star , \circ and \star represents the one nut, two nuts, three nuts and four nut state, respectively.

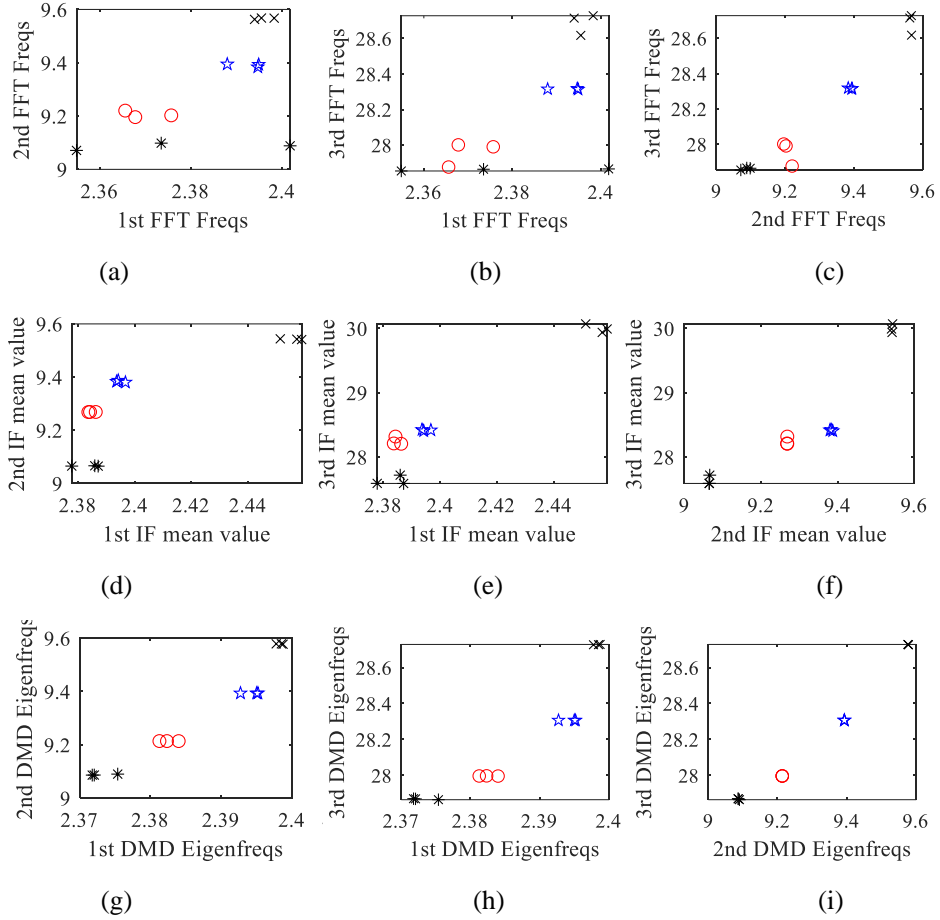


Figure 8-13. Comparison among the first three order eigenfrequency identified from structural responses subjected to seismic excitation of PGA 0.1g: (a) 1st and 2nd, (b) 1st and 3rd and (c) 2nd and 3rd FFT frequencies; (d) 1st and 2nd, (e) 1st and 3rd and (f) 2nd and 3rd mean values of time-varying instantaneous frequencies; (g) 1st and 2nd, (h) 1st and 3rd and (i) 2nd and 3rd opt-DMD eigen-frequencies. The symbols ×, ☆, ○ and * represents the 1nut, two nuts, three nuts and four nut state, respectively.

8.3.3 Noise effect analysis

In actual SHM applications, the measurement noise inevitably exists in the vibration responses. A reliable structural damage detection method should have excellent noise tolerance [35]. It should be noted that the measurements used in this study already includes the measurement noise in the laboratory experimental. However, to investigate the noise effect, in this section, 10% white noise is additionally added to the measured acceleration responses. The noise level is defined as

$$\text{Noise Level (\%)} = \frac{\text{var}(\text{Noise})}{\text{var}(\text{Signal})} \times 100\% \quad (8.6)$$

Figure 8-14 and Figure 8-15 show the first three-order opt-DMD eigen-frequencies identified from the structural responses subjected to ground motion excitations with PGA values of 0.05g and 0.1g, respectively. Comparing the identification results with Figure

8-12(g-h) and Figure 8-13(g-h), it can be found that four structural conditions are well separated when 10% white noise is considered. The data points under the same structural condition are all grouped together with a small standard deviation. Therefore, the proposed approach with the defined damage feature is robust to the presence of measurement noise and can be used to indicate the structural condition change reliably.

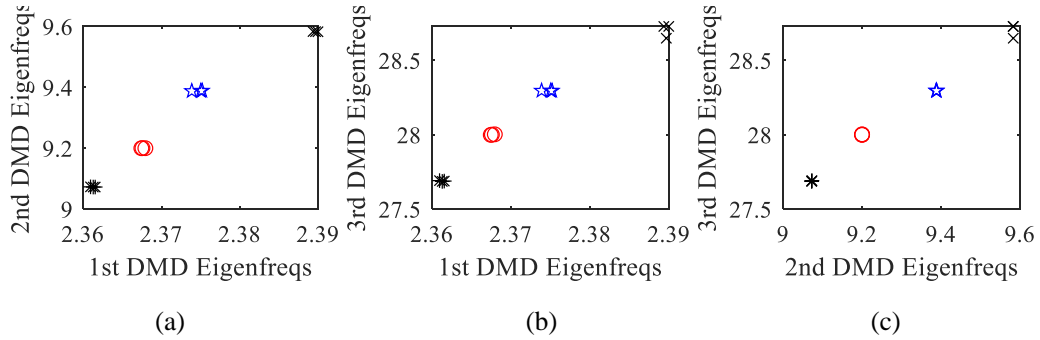


Figure 8-14. The first three order opt-DMD eigen-frequencies identified via the proposed method using the structural responses subjected to ground motion excitation of PGA 0.05g with 10% noise. The symbols \times , \star , \circ and $*$ represents the states with one nut, two nuts, three nuts and four nuts, respectively.

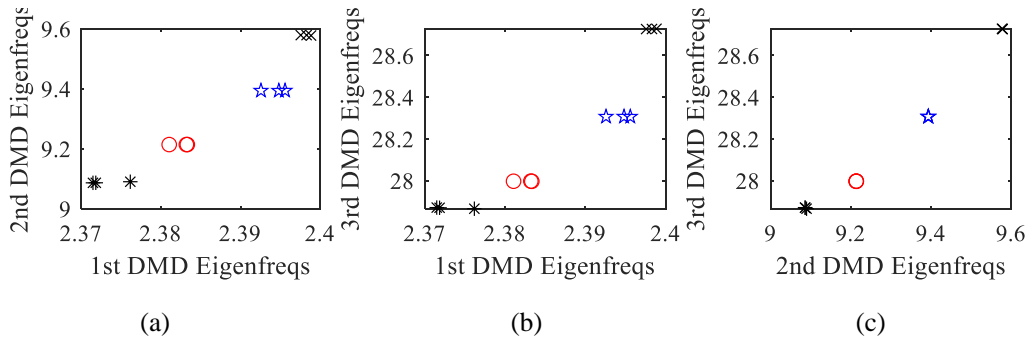


Figure 8-15. The first three order opt-DMD eigen-frequencies identified via the proposed method using the structural responses subjected to ground motion excitation of PGA 0.1g with 10% noise. The symbols \times , \star , \circ and $*$ represents the states with one nut, two nuts, three nuts and four nuts, respectively.

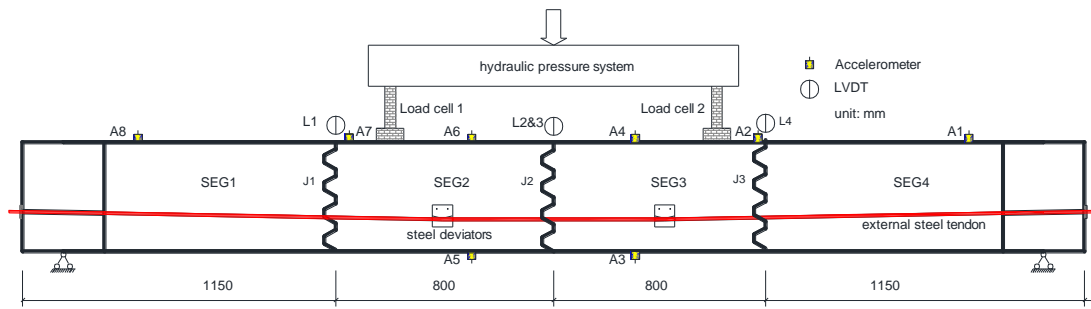
8.4 Experimental verifications on a precast segmental concrete beam

The precast prestressed segmental beam has been widely used for highway bridges, owing to its time-saving in construction and economic benefits. Different from the monolithic beam, the vibration behavior of the prestressed segmental concrete beams is inherently nonlinear, due to the joint contact and interaction between adjacent segments. Few studies has been conducted on the vibration-based condition monitoring and assessment of precast segmental structures. In this study, a precast segmental concrete beam prestressed with

external steel tendons is used to further validate the feasibility of the proposed method for nonlinear structural condition assessment.

The schematic diagram of experimental setup as well as the configuration of accelerometers and Linear Variable Differential Transformer (LVDT) sensors are presented in Figure 8-16. Detailed description of the material, specimen fabrication, post-tensioning procedure and experimental test setup are elaborated in Refs. [36, 37]. Four point static loads are cyclically applied with an increment of 20 kN until structural failure to introduce different structural states and simulate different extents of structural damage. Figure 8-17(a) and Figure 8-17(b) show the progressive loading increment intervals and the load-deflection curve at each loading level, respectively. Two loading cycles are performed at each loading increment level. In particular, the hydraulic static loading system gradually increases the load at a rate of 3-5 kN/min to the designed loading level and then decreases to around 5 kN before starting the next cycle.

Six progressive structural damage scenarios from DS0 (baseline), DS1 to DS5 represented by the blue lines in Figure 8-17(a) are defined. Ten repeats of hammer impact load tests are conducted under the baseline and damage states to acquire the acceleration responses for vibration-based condition assessment of this nonlinear structure. It should be noted that the hydraulic pressure system is unloaded to the untouched state between the loading system and the specimen during the hammer load tests to avoid the coupling effect and boundary condition change of the testing specimen. In the first three loading intervals, no visible damage is observed at the joint and surface of the testing beam. Structural damage evident as the concrete crushing on the top surface of joint 2 (J2) is observed when the applied load reached to 80kN, followed by the yielding of the external steel tendons when the applied load reached to 100kN. A linear relationship between the applied load and mid-span deflection is observed in Figure 8-17 (b) when the applied load is less than 50kN. The slope of the load-deflection curve between 10 kN to 20 kN is extracted in Figure 8-17(c) to show the accumulation of structural damage. There might be initial slip between the joints interface at the early loading stage, therefore, it is noted that load-deflection curve between 0-10kN is not included in the estimation of slope. As shown in Figure 8-17(c), the slope subjected to the increasing incremental loading persistently decreases, which means that the bending stiffness degradation in each damage scenario is well observed. Therefore structural damage are introduced under different structure states.

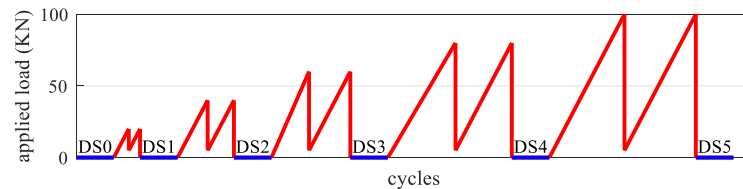


(a)

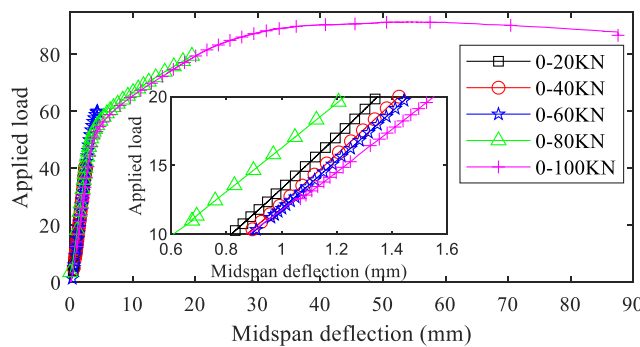


(b)

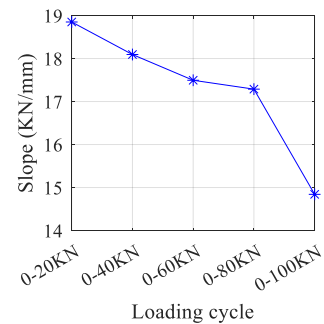
Figure 8-16. Experimental setup: (a) Schematic diagram of experimental setup and sensor configuration; and (b) Experiment testing specimen.



(a)



(b)



(c)

Figure 8-17. (a) Progressive loading intervals to simulate structural damage accumulation. Blue lines represents the damage scenarios. (b) load-deflection curves of the beam. The load-deflection curve in the region of 10-20 kN is highlighted. (c) The slope of load-deflection curve in the load range 10-20 kN for each structural state.

Figure 8-18 shows the acceleration responses, Fourier spectrum and the identified instantaneous frequencies of the intact prestressed segment beam subjected to hammer loads. It can be observed that the vibration of the precast segment beams is predominantly observed at its fundamental frequency. Owing to the inherent nonlinearity generated by the interface of adjacent joints surface, as shown in Figure 8-18(c), the first order instantaneous frequencies are oscillating over the period of hammer impact excitation, and are gradually converged to the fundamental frequency, since the nonlinear structural behavior contributes less to the vibration.

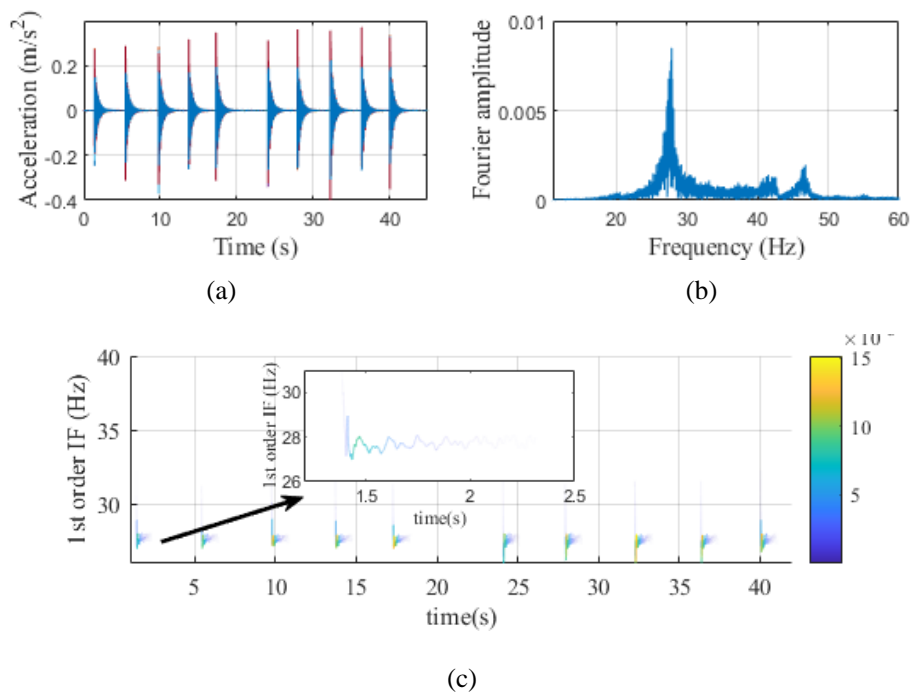


Figure 8-18. Time frequency analysis results: (a) Measured acceleration responses; (b) Fourier spectrum; and (c) The instantaneous frequency of hammer load induced vibration.

The statistical distributions of the first two instantaneous frequencies under six structural conditions are estimated in the same way as the first experiment and are depicted in Figure 8-19. As observed, the mean values of the first two order instantaneous frequencies present a monotonically decreasing trend with the accumulation of structural damage. The decrease in the mean values of the instantaneous frequencies agree well with the bending stiffness reductions observed in Figure 8-17(c). However, significant variation are observed in the identified instantaneous frequencies (especially the second order instantaneous frequency), which means that the time-frequency analysis is not sufficiently robustness to the damage detection of the segmental beam with the higher order responses. Following the HAVOC framework introduced in Figure 8-2, the opt-DMD eigen-frequencies of vibration responses measured from each hammer load test can be estimated. Figure 8-20 shows the obtained

Fourier frequencies, mean values of instantaneous frequencies and opt-DMD eigen-frequencies corresponding to each damage scenario. It is observed that the obtained opt-DMD eigen-frequencies from the proposed approach under each structural condition are more concentrated than those Fourier frequencies. Clear separations are observed among the obtained opt-DMD eigen-frequencies for five different damage scenarios. Furthermore, statistical properties including the mean values and standard deviations (STD) of instantaneous frequencies obtained from the time-frequency analysis, Fourier transform and the proposed approach under each damage scenario are listed in Table 8-2. It should be noted that the mean values and STD of the Fourier frequencies and the opt-DMD eigen-frequencies from the proposed approach corresponding to each structural condition are calculated from ten repeat tests. In Table 8-2, the relative changes of mean values of instantaneous frequencies estimated from the time-frequency analysis and the opt-DMD eigen-frequencies are consistent with the damage-induced bending stiffness reduction, as shown in Figure 8-17(c). Besides, the STD value of the proposed method corresponding to each of the six damage scenarios is superior than that approximated from the Fourier analysis and time frequency analysis. These results clearly show that the nonlinearity linearization framework and the opt-DMD eigen-frequencies proposed in this study are suitable for reliably identifying the presence of structural condition change in the system with inherent nonlinearity.

Table 8-2. Comparison of the first order frequency identified from time frequency analysis, Fourier frequency and the proposed DMD Eigen frequency.

	Instantaneous frequency			Fourier frequency			The proposed DMD eigen-frequencies		
	Mean (Hz)	Relative change (%)	STD	Mean (Hz)	Relative change (%)	STD	Mean (Hz)	Relative change (%)	STD
DS0	27.5582	0	0.1473	27.6272	0	0.0832	27.6325	0	0.0458
DS1	26.9854	2.0785	0.1460	27.2036	1.5333	0.1315	27.132	1.8113	0.0310
DS2	26.8627	2.5237	0.1024	26.9376	2.4961	0.0673	26.8918	2.6810	0.0155
DS3	26.775	2.8420	0.0910	27.0054	2.2507	0.0888	26.8876	2.6957	0.0344
DS4	26.5255	3.7473	0.0835	26.8113	2.9532	0.063	26.6932	3.3992	0.0227
DS5	26.328	4.4640	0.2179	26.5308	3.9685	0.0822	26.4779	4.1784	0.0181

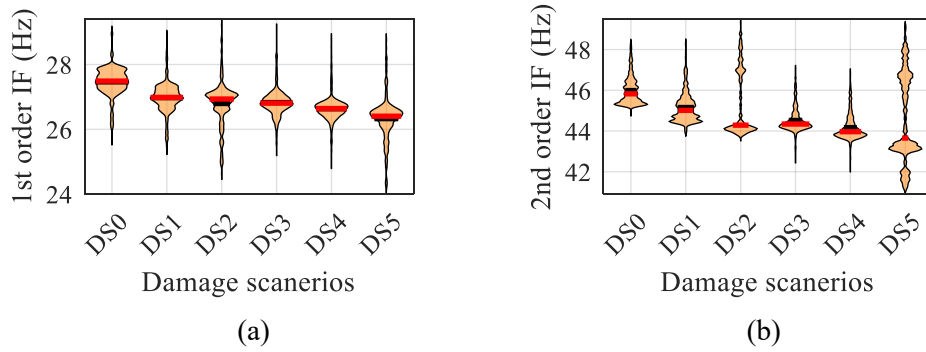


Figure 8-19. Statistical distributions of the identified instantaneous frequencies by VMD-HT method: (a) The first order; and (b) The second order. Red and black lines represent the mean value and median, respectively.

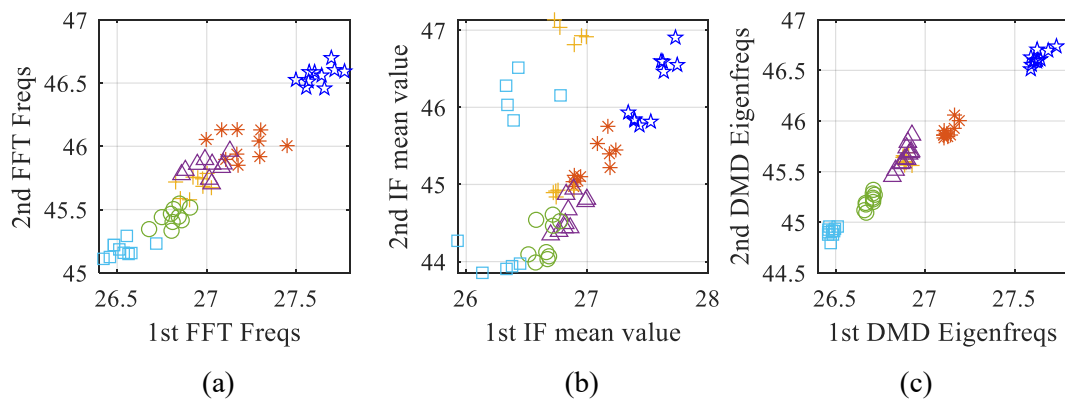


Figure 8-20. (a) Frequencies from Fourier spectrum analysis; (b) IF mean values ; (c) DMD eigen-frequencies under different damage scenarios. The symbols \star , $*$, Δ , $+$, \circ and \square represent the damage scenarios DS0, DS1, DS2, DS3, DS4 and DS5, respectively.

8.5 Conclusions

The effect of inherent nonlinear behavior in structures on the vibration responses can mask the effect of structural damage, when using the damage feature extracted from those methods based on linearity assumption. This chapter introduces a nonlinear linearization method by integrating the phase space embedding and the Koopman operator for damage detection of nonlinear structures. A DI based on the eigenvalues of Koopman operator is used to monitor structural condition change with initial nonlinear behavior. The applicability of the proposed damage feature is verified through two experimental structures exhibiting inherent nonlinearity, namely, a magneto-elastic system and a precast prestressed segmental beam. These results demonstrate that the proposed approach identifies correctly the structural condition changes in different damage scenarios. Furthermore, the introduced opt-DMD eigen-frequencies provide a reliable damage detection performance, when the influence factors such as loading effect and measurement noise are considered. However, it should be noted that the vibration responses of both experimental structures utilized in this study exhibit discrete

frequency spectral peaks. The finite dimension Koopman operator for vibration signals with continuous spectrum cannot be accurately approximated using the coordinate basis discovered by SVD. As a result, the proposed method may not suitable for a system that does not exhibit a discrete frequency spectrum.

References

- [1] R. Hou, Y. Xia, Review on the new development of vibration-based damage identification for civil engineering structures: 2010–2019, *Journal of Sound and Vibration*, (2020) 115741.
- [2] S. Voggu, S. Sasmal, Dynamic nonlinearities for identification of the breathing crack type damage in reinforced concrete bridges, *Structural Health Monitoring*, 20 (2021) 339-359.
- [3] F. Wang, G. Song, Bolt early looseness monitoring using modified vibro-acoustic modulation by time-reversal, *Mechanical Systems and Signal Processing*, 130 (2019) 349-360.
- [4] A. Kampitsis, E. Sapountzakis, Dynamic analysis of beam-soil interaction systems with material and geometrical nonlinearities, *International Journal of Non-Linear Mechanics*, 90 (2017) 82-99.
- [5] Y. Li, W. Sun, R. Jiang, Y. Han, Signal-segments cross-coherence method for nonlinear structural damage detection using free-vibration signals, *Advances in Structural Engineering*, 23 (2020) 1041-1054.
- [6] Z. Feng, M. Liang, Fault diagnosis of wind turbine planetary gearbox under nonstationary conditions via adaptive optimal kernel time–frequency analysis, *Renewable Energy*, 66 (2014) 468-477.
- [7] G. Liu, Z. Mao, M. Todd, Damage detection using transient trajectories in phase-space with extended random decrement technique under non-stationary excitations, *Smart Materials and Structures*, 25 (2016) 115014.
- [8] J. Nichols, M. Seaver, S. Trickey, A method for detecting damage-induced nonlinearities in structures using information theory, *Journal of Sound and Vibration*, 297 (2006) 1-16.
- [9] Z. Peng, J. Li, H. Hao, Z. Nie, Improving identifiability of structural damage using higher order responses and phase space technique, *Structural Control and Health Monitoring*, (2021) e2808.
- [10] Z. Peng, J. Li, H. Hao, Y. Xin, High - resolution time - frequency representation for instantaneous frequency identification by adaptive Duffing oscillator, *Structural Control and Health Monitoring*, 27 (2020) e2635.
- [11] N. Jamia, H. Jalali, J. Taghipour, M. Friswell, H.H. Khodaparast, An equivalent model of a nonlinear bolted flange joint, *Mechanical Systems and Signal Processing*, 153 (2021) 107507.
- [12] K. Worden, C.R. Farrar, J. Haywood, M. Todd, A review of nonlinear dynamics applications to structural health monitoring, *Structural Control and Health Monitoring: The Official Journal of the International Association for Structural Control and Monitoring and of the European Association for the Control of Structures*, 15 (2008) 540-567.
- [13] L. Chen, L. Yu, Structural nonlinear damage identification algorithm based on time series ARMA/GARCH model, *Advances in Structural Engineering*, 16 (2013) 1597-1609.
- [14] H. Ebrahimian, R. Astroza, J.P. Conte, R.A. de Callafon, Nonlinear finite element model updating for damage identification of civil structures using batch Bayesian estimation, *Mechanical Systems and Signal Processing*, 84 (2017) 194-222.
- [15] Y. Lei, F. Chen, H. Zhou, An algorithm based on two - step Kalman filter for intelligent structural damage detection, *Structural Control and Health Monitoring*, 22 (2015) 694-706.
- [16] Z. Peng, J. Li, H. Hao, C. Li, Nonlinear structural damage detection using output - only

- Volterra series model, *Structural Control and Health Monitoring*, (2021) e2802.
- [17] L.G. Villani, S. Da Silva, A. Cunha Jr, M.D. Todd, Damage detection in an uncertain nonlinear beam based on stochastic Volterra series: an experimental application, *Mechanical Systems and Signal Processing*, 128 (2019) 463-478.
- [18] H. Arbabi, I. Mezic, Ergodic theory, dynamic mode decomposition, and computation of spectral properties of the Koopman operator, *SIAM Journal on Applied Dynamical Systems*, 16 (2017) 2096-2126.
- [19] Z. Peng, J. Li, H. Hao, Finite Linear Representation of Nonlinear Structural Dynamics using Phase Space Embedding Coordinate, *Journal of Sound and Vibration*, (2021) (under review).
- [20] C.W. Rowley, I. MEZI?, S. Bagheri, P. Schlatter, D. Henningson, Spectral analysis of nonlinear flows, *Journal of Fluid Mechanics*, 641 (2009) 115-127.
- [21] M.O. Williams, I.G. Kevrekidis, C.W. Rowley, A data-driven approximation of the koopman operator: Extending dynamic mode decomposition, *Journal of Nonlinear Science*, 25 (2015) 1307-1346.
- [22] E. Yeung, S. Kundu, N. Hodas, Learning deep neural network representations for Koopman operators of nonlinear dynamical systems, in: 2019 American Control Conference (ACC), IEEE, 2019, pp. 4832-4839.
- [23] S.L. Brunton, B.W. Brunton, J.L. Proctor, E. Kaiser, J.N. Kutz, Chaos as an intermittently forced linear system, *Nature Communications*, 8 (2017) 1-9.
- [24] M. Kamb, E. Kaiser, S.L. Brunton, J.N. Kutz, Time-delay observables for koopman: Theory and applications, *SIAM Journal on Applied Dynamical Systems*, 19 (2020) 886-917.
- [25] D. Dylewsky, E. Kaiser, S.L. Brunton, J.N. Kutz, Principal Component Trajectories (PCT): Nonlinear dynamics as a superposition of time-delayed periodic orbits, arXiv preprint arXiv:2005.14321, (2020).
- [26] H. Li, J. Liu, W. Chen, Z. Lu, Y. Xia, Y. Ni, Analysis of dynamic characteristics of the Canton tower under different earthquakes, *Advances in Structural Engineering*, 18 (2015) 1087-1100.
- [27] Z. Hu, J. Li, L. Zhi, X. Huang, Modal Identification of damped vibrating systems by iterative smooth orthogonal decomposition method, *Advances in Structural Engineering*, 24 (2021) 755-770.
- [28] Q. Wen, X. Hua, Z. Chen, J. Guo, H. Niu, Modal parameter identification of a long-span footbridge by forced vibration experiments, *Advances in Structural Engineering*, 20 (2017) 661-673.
- [29] D. Dylewsky, D. Barajas-Solano, T. Ma, A.M. Tartakovsky, J.N. Kutz, Dynamic mode decomposition for forecasting and analysis of power grid load data, arXiv preprint arXiv:2010.04248, (2020).
- [30] S.M. Hirsh, S.M. Ichinaga, S.L. Brunton, J.N. Kutz, B.W. Brunton, Structured Time-Delay Models for Dynamical Systems with Connections to Frenet-Serret Frame, arXiv preprint arXiv:2101.08344, (2021).
- [31] P. Ni, J. Li, H. Hao, Y. Xia, X. Wang, J.M. Lee, K.H. Jung, Time - varying system identification using variational mode decomposition, *Structural Control and Health Monitoring*, 25 (2018) e2175.
- [32] T. Askham, J.N. Kutz, Variable projection methods for an optimized dynamic mode decomposition, *SIAM Journal on Applied Dynamical Systems*, 17 (2018) 380-416.

- [33] V.R. Challa, M. Prasad, Y. Shi, F.T. Fisher, A vibration energy harvesting device with bidirectional resonance frequency tunability, *Smart Materials and Structures*, 17 (2008) 015035.
- [34] P. Héas, C. Herzet, Optimal low-rank dynamic mode decomposition, in: 2017 IEEE International Conference on Acoustics, Speech and Signal Processing (ICASSP), IEEE, 2017, pp. 4456-4460.
- [35] C. Liu, J. Teng, Z. Peng, Optimal sensor placement for bridge damage detection using deflection influence line, *Smart Struct. Syst*, 25 (2020) 169-181.
- [36] T.D. Le, T.M. Pham, H. Hao, H. Li, Behavior of Precast Segmental Concrete Beams Prestressed with External Steel and CFRP Tendons, *Journal of Composites for Construction*, 24 (2020) 04020053.
- [37] T.D. Le, T.M. Pham, H. Hao, Y. Hao, Flexural behaviour of precast segmental concrete beams internally prestressed with unbonded CFRP tendons under four-point loading, *Engineering structures*, 168 (2018) 371-383.

CHAPTER 9 CONCLUSIONS AND RECOMMENDATIONS

9.1 Main conclusions

This thesis focuses on addressing three main issues namely, operational condition change, nonlinearities and measurement noise that adversely affect the feasibility and accuracy of vibration-based SHM techniques for civil engineering structures. The major conclusions and findings in this thesis are summarized below:

Chapter 2 proposes a novel high resolution time-frequency analysis approach based on an adaptive Duffing oscillator array to identify the instantaneous frequency of nonstationary signals under strong noise. To avoid the use of a large array of oscillators, improvement is made by recursively adjusting the central reference frequency in each time window according to the frequency estimated in the previous time window. The proposed method is compared with EWT-HT based time frequency analysis method. The numerical and experimental validation results reveal that a more stable and clear time-frequency transient feature and instantaneous frequency can be estimated by using the proposed method than the EWT-HT based method.

Chapter 3 proposes an output-only Volterra series model to identify structural nonlinear effects by quantifying the nonlinear contribution in structural vibration responses. Compared with the conventional input-output based Volterra series model-based methods, the proposed method does not require the measurement of external excitation. Numerical and experimental results demonstrate that the nonlinear behavior can be modelled qualitatively by using the proposed method with the optimally selected parameters. The proposed method can accurately locate the nonlinear structural damage by using measurement data under different structural conditions. Furthermore, the damage extent can be estimated by comparing the evolution of nonlinearity contribution index value obtained in each structural region.

Chapter 4 proposes a novel SSA-based PST technique to improve the identifiability of structural damage by using higher order responses. The proposed method extends the feasibility of PST method to high dimensional structural responses. Numerical and experimental studies demonstrate that the occurrence, location and progressive damage evolution can be detected effectively by the decomposed high order response component with the developed approach. Numerical results on a planar truss model demonstrate that the proposed method is not only sensitive to structural damage, but also robust to a significant level of white noise, pink noise and modelling uncertainties.

Chapter 5 proposes a novel data driven approach, which combines the phase space

embedding strategy and Koopman operator for the damage detection of structure subjected to stochastic excitation. The proposed method extends the feasibility of PST-based damage detection method by using the structural responses under ambient load. The numerical study on a truss bridge with minor damage and experimental study on an in-field bridge reveals that the proposed method is sensitive to structural condition change, but insensitive to environmental conditions and measurement noise.

Chapter 6 proposes an innovative approach based on the phase space based manifold learning technique for the damage detection of in-situ civil engineering structures subjected to operational conditions. The natural frequencies identified from operational modal analysis are used to span a high-dimensional phase space that can unfold the inherent nonlinear relationship between temperature variation and structural vibration properties. Then, manifold learning is introduced to project the high-dimensional PST to the low-dimensional topological structure of the underlying system. DSF is extracted from the low-dimensional manifold structure via Gaussian process regression model. The applicability and performance of the developed method are demonstrated by using vibration responses measured from two real-world bridges. Results verify that the proposed approach is sensitive to structural damage but not sensitive to environmental and loading conditions, even when only observations from the healthy state under partial environmental and operational variations are available and included in the training datasets.

Chapter 7 proposes a data-driven finite linear representation of nonlinear structural dynamics using phase space embedding technique with the consideration of measurement noise. The evolution of underlying nonlinear system can be linearly represented in the coordinate system spanned by singular vectors of the phase space embedded Hankel matrix. Numerical and experimental studies are conducted to validate the feasibility and accuracy of the presented method by using vibration responses measured from linear and nonlinear structure systems. For linear structures, the proposed method can accurately identify the modal parameters, namely natural frequencies and mode shapes. For nonlinear structures, the proposed method exhibits highly predictive performance with limited training dataset. In conclusion, the proposed method is efficient to generate a linearized representation of deterministic nonlinear systems, which is useful in understanding and predicting structural parameter nonlinear variations during dynamic responses.

Chapter 8 proposed a damage detection approach for structures that exhibit inherent nonlinearities based on the nonlinear dynamic linearization model presented in Chapter 7. The eigen-frequencies extracted from the finite linearization model (Koopman operator) are used as damage features, which provide a new perspective to conduct nonlinear structural damage

detection in a linear manner. The superiority of the proposed method is verified by comparing the damage detection performance with the natural frequencies obtained from FFT and the time-frequency analysis methods. The feasibility and effectiveness of the proposed method are validated by using two experimental structures exhibiting inherent nonlinearities. Results prove that the developed nonlinearity linearization framework and the damage feature defined in this study are applicable for reliably identifying the condition change in structures with inherent nonlinearities.

9.2 Recommendations for future works

The research that has been undertaken for this thesis has highlighted several topics that can be further studied.

1. In Chapter 2, the measurement noise is considered as Gaussian white noise with constant power spectral density at different frequencies. However, the distribution of actual noise may not strictly satisfy this assumption. Therefore, the superiority of the proposed high resolution time-frequency analysis method subjected to pink noise and other types of strong noise and system uncertainties should be further investigated.

2. The basic principle of the proposed output-only Volterra series model based method is based on the nonlinearity contribution in structural vibration responses. Many nonlinear sources, such as geometric nonlinearity, nonlinear boundary conditions, joints of prefabricated structures and material nonlinearity, etc., may complicate the damage detection performance. Therefore, how to distinguish different sources of nonlinear characteristics could be further investigated.

3. The methods presented in Chapter 4 and Chapter 5 focus on extending the feasibility of PST technique to high dimensional vibration responses and stochastic excitations, respectively. However, the damage detection performance may be influenced when the excitation type is not the same before and after damage. Therefore, in the future study, a better normalisation method could be further developed to eliminate the effect of load conditions and detect the damage in structures under different types of stochastic excitations before and after damage.

4. The phase space based manifold learning technique shows a promising performance for structural damage detection based on long term SHM data. However, it can only alarm the presence of damage. It is beneficial for the decision maker to formulate more reasonable maintenance strategy if more detailed information can be provided. Therefore, future studies can be conducted to classify different types of damage by integrating the proposed methods with hierarchical clustering algorithms.

5. In Chapter 7 and Chapter 8, the finite linear representation of nonlinear structural dynamics using the coordinate system spanned by singular vectors of the phase space embedded Hankel matrix exhibits highly predictive performance and reliable nonlinear structural damage detection performance. However, a main limitation is that the introduced linearization framework is not applicable to nonlinear vibration responses without discrete frequency spectral peaks. As a result, the proposed method is not suitable for systems with a strong hysteresis effect without clean and discrete peaks in the frequency spectrum. This limitation may be addressed in future study by using the unsupervised deep learning network, such as auto-encoder to discover a low-dimensional coordinate system that is most representative of the vibration responses with hysteresis effect.

APPENDIX I

In this appendix, the derivation and implementation of obtaining the unbiased stochastic Koopman operator with the consideration of process noise and observation noise are detailed. The key objective is to isolate the finite-dimension unbiased stochastic Koopman operator \mathbf{A}_Ω with the process noise and observation noise term. The proof is based on the following assumptions:

Assumption 1: the process noise \mathbf{e}_t and observation noise \mathbf{w}_t considered in this study are independent and identically distributed in time, with zero mean, time-invariant finite variance and is temporally uncorrelated, namely, $E[\mathbf{e}_t] = 0$; $E[\mathbf{e}_t \mathbf{e}_t^*] = \mathbf{P}\sigma_{t,t}$; $E[\mathbf{w}_t] = 0$; $E[\mathbf{w}_t \mathbf{w}_t^*] = \mathbf{Q}\sigma_{t,t}$. For $\forall t$ and $t + \tau$, we have

$$E[\mathbf{e}_{t+\tau} \mathbf{e}_t^*] = E[\mathbf{e}_{t+\tau}]E[\mathbf{e}_t] + \text{Cov}(\mathbf{e}_{t+\tau}, \mathbf{e}_t) = \mathbf{0}_{n \times n}; \quad (\text{A.1})$$

$$E[\mathbf{w}_{t+\tau} \mathbf{w}_t^*] = E[\mathbf{w}_{t+\tau}]E[\mathbf{w}_t] + \text{Cov}(\mathbf{w}_{t+\tau}, \mathbf{w}_t) = \mathbf{0}_{n \times n}; \quad (\text{A.2})$$

$$E[\mathbf{e}_{t+\tau} \mathbf{w}_t^*] = \mathbf{R}\sigma_{t+\tau,t} \quad (\text{A.3})$$

with \mathbf{P} , \mathbf{Q} and $\mathbf{R} \in X^n$, $\tau > 0$.

Setting $\mathbf{G}_{t+\tau,t} = E_\Omega[g(\mathbf{x}_{t+\tau})g(\mathbf{x}_t)^*]$, from Eqs. (11) and (12), we have

$$\begin{aligned} \mathbf{G}_{t+\tau,t} &= E_\Omega[g(\mathbf{x}_{t+\tau})g(\mathbf{x}_t)^*] \\ &= E_\Omega[(g(\mathbf{x}_t))(A_\Omega^\tau g(\mathbf{x}_t)^* + \sum_{i=t}^{t+\tau-1} A_\Omega^{i-t} \mathbf{e}_i A_\Omega^{i-t} \mathbf{e}_i^*)] \\ &= E_\Omega[A_\Omega^\tau g(\mathbf{x}_t)g(\mathbf{x}_t)^*] + E_\Omega[g(\mathbf{x}_t) \sum_{i=t}^{t+\tau-1} A_\Omega^{i-t} \mathbf{e}_i^*] \\ &= E_\Omega[A_\Omega^\tau g(\mathbf{x}_t)g(\mathbf{x}_t)^*] = A_\Omega^\tau \mathbf{G}_{t,t} \end{aligned} \quad (\text{A.4})$$

where $\mathbf{G}_{t,t} = \mathbf{G}$ for simplification. The above derivation implies that the process noise can be eliminated by the inner product of $g(\mathbf{x}_t)$ and $g(\mathbf{x}_{t+\tau})$.

Similarly, defining the inner product of $h(\mathbf{x}_t)$ and $h(\mathbf{x}_{t+\tau})$ as follows

$$\begin{aligned} \mathbf{H}_{t+\tau,t} &= E_{\Omega,S}[h(\mathbf{x}_{t+\tau})h(\mathbf{x}_t)^*] = E_{\Omega,S}[(g(\mathbf{x}_{t+\tau}) + \mathbf{w}_{t+\tau})(g(\mathbf{x}_t) + \mathbf{w}_t)^*] \\ &= E_{\Omega,S}[g(\mathbf{x}_{t+\tau})g(\mathbf{x}_t)^* + g(\mathbf{x}_{t+\tau})\mathbf{w}_t^* + \mathbf{w}_{t+\tau}g(\mathbf{x}_t)^* + \mathbf{w}_{t+\tau}\mathbf{w}_t^*] \\ &= A_\Omega^\tau \mathbf{G}_{t,t} + \sum_{i=1}^{t+\tau} A_\Omega^{t-i} E_{\Omega,S}[\mathbf{e}_i \mathbf{w}_t^*] + \sum_{i=1}^t A_\Omega^{t-i} E_{\Omega,S}[\mathbf{w}_{t+\tau} \mathbf{e}_i^*] + E_{\Omega,S}[\mathbf{w}_{t+\tau} \mathbf{w}_t^*] \\ &= A_\Omega^\tau \mathbf{G}_{t,t} + A_\Omega^{\tau-1} \mathbf{R}\sigma_{t,t+\tau} \\ &= A_\Omega^{\tau-1} (A_\Omega \mathbf{G} + \mathbf{R}\sigma_{t,t+\tau}) \end{aligned} \quad (\text{A.5})$$

where $\tau > 0$. The expression of $\mathbf{H}_{t,t+\tau}$ for $\tau < 0$ is similar as that of $\tau > 0$, namely, $\mathbf{H}_{t+\tau,t} = \mathbf{H}_{t,t+\tau}^*$.

When $\tau = 0$, we have

$$\begin{aligned} \mathbf{H}_{t,t} &= E_{\Omega,S}[h(\mathbf{x}_t)h(\mathbf{x}_t)^*] \\ &= E_{\Omega,S}[(g(\mathbf{x}_t) + \mathbf{w}_t)(g(\mathbf{x}_t) + \mathbf{w}_t)^*] \\ &= E_{\Omega,S}[g(\mathbf{x}_t)g(\mathbf{x}_t)^* + g(\mathbf{x}_t)\mathbf{w}_t^* + \mathbf{w}_t g(\mathbf{x}_t)^* + \mathbf{w}_t \mathbf{w}_t^*] = \mathbf{G} + \mathbf{Q}\sigma_{t,t+\tau} \end{aligned} \quad (\text{A.6})$$

Overall, the expression of $\mathbf{H}_{t,t+\tau}$ is summarized as

$$\mathbf{H}_{t+\tau,t} = \begin{cases} \mathbf{A}_{\Omega}^{\tau-1}(\mathbf{A}_{\Omega}\mathbf{G} + \mathbf{R}\sigma_{t,t+\tau}), & \tau > 0 \\ \mathbf{G} + \mathbf{Q}\sigma_{t,t+\tau} & \tau = 0 \\ \mathbf{H}_{t,t+\tau}^* & \tau < 0 \end{cases} \quad (\text{A.7})$$

In this study, $\mathbf{H}_{t+\tau,t}$ can be explicitly expressed by substituting Eq. (8.14) into Eq. (A.5)

$$\mathbf{H}_{t+\tau,t} = E_{\Omega,S}[h(\mathbf{x}_{t+\tau})h(\mathbf{x}_t)^*] = \frac{1}{m} \mathbf{Y}_{t+\tau}^{t+\tau+m-1} \mathbf{Y}_t^{t+m-1} = \mathbf{H}_{\tau} \quad (\text{A.8})$$

The last equality holds because of the assumption of ergodicity [29, 41].

Finally, $\mathbf{O}^{aug} \in X^{2n \times r}$ predefined in Section 2.2 is expanded to

$$\begin{aligned} \mathbf{O}^{aug} &= \mathbf{Y}_f^{aug} (\mathbf{Y}_p^{aug})^* [\mathbf{Y}_p^{aug} (\mathbf{Y}_p^{aug})^*]^{-1} \mathbf{Y}_p^{aug} \\ &= [\mathbf{Y}_3^{m+2}; \mathbf{Y}_4^{m+3}] [\mathbf{Y}_1^m; \mathbf{Y}_2^{m+1}]^* [\mathbf{Y}_1^m; \mathbf{Y}_2^{m+1}] [\mathbf{Y}_1^m; \mathbf{Y}_2^{m+1}]^*]^{-1} \mathbf{Y}_p^{aug} \\ &= \begin{bmatrix} \mathbf{H}_{3,1} & \mathbf{H}_{3,2} \\ \mathbf{H}_{4,1} & \mathbf{H}_{4,2} \end{bmatrix} \begin{bmatrix} \mathbf{H}_{1,1} & \mathbf{H}_{1,2} \\ \mathbf{H}_{2,1} & \mathbf{H}_{2,2} \end{bmatrix}^{-1} \mathbf{Y}_p^{aug} = \begin{bmatrix} \mathbf{H}_2 & \mathbf{H}_1 \\ \mathbf{H}_3 & \mathbf{H}_2 \end{bmatrix} \begin{bmatrix} \mathbf{H}_0 & \mathbf{H}_1^* \\ \mathbf{H}_1 & \mathbf{H}_0 \end{bmatrix}^{-1} \mathbf{Y}_p^{aug} \\ &= \begin{bmatrix} \mathbf{I} \\ \mathbf{A}_{\Omega} \end{bmatrix} \begin{bmatrix} \mathbf{A}_{\Omega}^{\tau-1}(\mathbf{A}_{\Omega}\mathbf{G} + \mathbf{R}\sigma_{t,t+\tau}) \\ \mathbf{A}_{\Omega}\mathbf{G} + \mathbf{R}\sigma_{t,t+\tau} \end{bmatrix}^T \begin{bmatrix} \mathbf{G} + \mathbf{Q}\sigma_{t,t+\tau} & (\mathbf{A}_{\Omega}\mathbf{G} + \mathbf{R}\sigma_{t,t+\tau})^* \\ \mathbf{A}_{\Omega}\mathbf{G} + \mathbf{R}\sigma_{t,t+\tau} & \mathbf{G} + \mathbf{Q}\sigma_{t,t+\tau} \end{bmatrix}^{-1} \mathbf{Y}_p^{aug} \\ &= \mathbf{O}_1^{aug} \mathbf{O}_2^{aug} \end{aligned} \quad (\text{A.9})$$

in which, $\mathbf{O}_1^{aug} = \begin{bmatrix} \mathbf{I} \\ \mathbf{A}_{\Omega} \end{bmatrix}$;

$$\mathbf{O}_2^{aug} = \begin{bmatrix} \mathbf{A}_{\Omega}^{\tau-1}(\mathbf{A}_{\Omega}\mathbf{G} + \mathbf{R}\sigma_{t,t+\tau}) \\ \mathbf{A}_{\Omega}\mathbf{G} + \mathbf{R}\sigma_{t,t+\tau} \end{bmatrix}^T \begin{bmatrix} \mathbf{G} + \mathbf{Q}\sigma_{t,t+\tau} & (\mathbf{A}_{\Omega}\mathbf{G} + \mathbf{R}\sigma_{t,t+\tau})^* \\ \mathbf{A}_{\Omega}\mathbf{G} + \mathbf{R}\sigma_{t,t+\tau} & \mathbf{G} + \mathbf{Q}\sigma_{t,t+\tau} \end{bmatrix}^{-1} \mathbf{Y}_p^{aug}.$$

It should be noticed that the stochastic Koopman operator \mathbf{A}_{Ω} in \mathbf{O}_1^{aug} is separated with the process noise and observation noise terms included within \mathbf{O}_2^{aug} . Therefore, in theory, the change of process noise and observation noise amplitudes will only affect the specific values of \mathbf{P} , \mathbf{Q} and \mathbf{R} , while not affect the approximation of Koopman operator \mathbf{A}_{Ω} .

SVD is performed on the augmented matrix given by

$$\mathbf{O}^{aug} \stackrel{\text{def}}{=} [\mathbf{U}_{1:q1}; \mathbf{U}_{1:q2}] \mathbf{S}_{1:q} \mathbf{V}_{1:q}^* \quad (\text{A.10})$$

where $\mathbf{U}_{1:q1}$ and $\mathbf{U}_{1:q2}$ are associated with \mathbf{I} and \mathbf{A}_Ω of \mathbf{O}_1^{aug} .

The Koopman operator \mathbf{A}_Ω is estimated by

$$\mathbf{A}_\Omega \stackrel{\text{def}}{=} \tilde{\mathbf{U}}_{1:\tilde{r}}^* \mathbf{U}_{1:q2} \tilde{\mathbf{V}}_{1:\tilde{r}} \tilde{\mathbf{S}}_{1:\tilde{r}}^{-1} \quad (\text{A.11})$$

where $\tilde{\mathbf{U}}_{1:\tilde{r}} \in \mathbf{X}^{n \times \tilde{r}}$, $\tilde{\mathbf{S}}_{1:\tilde{r}} \in \mathbf{X}^{\tilde{r} \times \tilde{r}}$, $\tilde{\mathbf{V}}_{1:\tilde{r}} \in \mathbf{X}^{q \times \tilde{r}}$ are calculated by $[\tilde{\mathbf{U}}_{1:\tilde{r}}, \tilde{\mathbf{S}}_{1:\tilde{r}}, \tilde{\mathbf{V}}_{1:\tilde{r}}] \leftarrow \text{SVD}(\mathbf{U}_{1:q1}, \tilde{r})$, with $\tilde{r} = \text{rank}(\mathbf{U}_{1:q1})$.

APPENDIX II

ATTRIBUTION OF AUTHORSHIP

To whom it may concern,

I, Zhen Peng, conducted numerical, experimental investigations, data processing, analysis and wrote manuscripts of the papers titled as follows, which were revised and edited by the second and third co-authors. They also provided insights on experimental preparation, data processing and data analysis. The last author provided some help on the MATLAB program of the EWT-HT approach and simulation of a two-storey shear building under the 1940 El Centro ground motion.

High resolution time frequency representation for instantaneous frequency identification by adaptive duffing oscillator

(.....)

I, as a co-author, endorse that this level of contribution by the candidate indicated above is appropriate.

(Prof. Hong Hao)

(.....)

(Associate Prof. Jun Li)

(.....)

(Dr. Yu Xin)

(.....)

To whom it may concern,

I, Zhen Peng, conducted numerical, experimental investigations, data processing, analysis and wrote manuscripts of the papers titled as follows, which were revised and edited by the second and third co-authors. They also provided insights on experimental preparation, data processing and data analysis. The last co-author conducted the experimental test.

Nonlinear structural damage detection using output-only Volterra series model

(.....)

I, as a co-author, endorse that this level of contribution by the candidate indicated above is appropriate.

(Prof. Hong Hao)

(.....)

(Associate Prof. Jun Li)

(.....)

(Dr. Chao Li)

(.....)

To whom it may concern,

I, Zhen Peng, conducted numerical, experimental investigations, data processing, analysis and wrote manuscripts of the papers titled as follows, which were revised and edited by the second and third co-authors. The second, third and fourth co-authors provided insights on experimental preparation, data processing and data analysis.

Improving identifiability of structural damage using higher order responses and phase space technique

(.....)

I, as a co-author, endorse that this level of contribution by the candidate indicated above is appropriate.

(Prof. Hong Hao) (.....)

(Associate Prof. Jun Li) (.....)

(Prof. Zhenhua Nie) (.....)

To whom it may concern,

I, Zhen Peng, conducted numerical, experimental investigations, data processing, analysis and wrote manuscripts of the papers titled as follows, which were revised and edited by the second and third co-authors. The second and third co-authors provided insights on experimental preparation, data processing and data analysis.

1. Data driven structural damage assessment using phase space embedding and Koopman operator under stochastic excitations

2. Structural damage detection via phase space based manifold learning under changing environmental and operational conditions

3. Finite linear representation of nonlinear structural dynamics using phase space embedding coordinate

(.....)

I, as a co-author, endorse that this level of contribution by the candidate indicated above is appropriate.

(Prof. Hong Hao)

(.....)

(Associate Prof. Jun Li)

(.....)

To whom it may concern,

I, Zhen Peng, conducted numerical, experimental investigations, data processing, analysis and wrote manuscripts of the papers titled as follows, which were revised and edited by the second co-author. The second co-author provided insights on experimental preparation, data processing and data analysis.

Phase space reconstruction and Koopman operator based linearization of nonlinear model for damage detection of nonlinear structures

(.....)

I, as a co-author, endorse that this level of contribution by the candidate indicated above is appropriate.

(Associate Prof. Jun Li)

(.....)

APPENDIX III

COPYRIGHT CLEARANCE

The proof of the rights, granted by publishers for the publication that forms the chapters of this thesis, to reproduce the contribution in the thesis are attached below.

Peng, Z., Li, J., Hao, H., & Xin, Y. (2020). High-resolution time-frequency representation for instantaneous frequency identification by adaptive Duffing oscillator. *Structural Control and Health Monitoring*, 27(12), e2635. <https://doi.org/10.1002/stc.2635>.



Thank you for your order!

Dear Mr. Zhen Peng,

Thank you for placing your order through Copyright Clearance Center's RightsLink® service.

Order Summary

Licensee:	Mr. Zhen Peng
Order Date:	Feb 18, 2022
Order Number:	5252260105678
Publication:	Structural Control and Health Monitoring
Title:	High-resolution time-frequency representation for instantaneous frequency identification by adaptive Duffing oscillator
Type of Use:	Dissertation/Thesis
Order Total:	0.00 AUD

View or print complete [details](#) of your order and the publisher's terms and conditions.

Sincerely,

Copyright Clearance Center

Tel: +1-855-239-3415 / +1-978-646-2777
customercare@copyright.com
<https://myaccount.copyright.com>



RightsLink®

Peng, Z., Li, J., Hao, H., & Li, C. (2021). Nonlinear structural damage detection using output - only Volterra series model. *Structural Control and Health Monitoring*, e2802. <https://doi.org/10.1002/stc.2802>.



Thank you for your order!

Dear Mr. Zhen Peng,

Thank you for placing your order through Copyright Clearance Center's RightsLink® service.

Order Summary

Licensee:	Mr. Zhen Peng
Order Date:	Feb 18, 2022
Order Number:	5252251194600
Publication:	Structural Control and Health Monitoring
Title:	Nonlinear structural damage detection using output-only Volterra series model
Type of Use:	Dissertation/Thesis
Order Total:	0.00 AUD

View or print complete [details](#) of your order and the publisher's terms and conditions.

Sincerely,

Copyright Clearance Center

Tel: +1-855-239-3415 / +1-978-646-2777
customercare@copyright.com
<https://myaccount.copyright.com>



RightsLink®

Peng, Z., Li, J., Hao, H., & Nie, Z. (2021). Improving identifiability of structural damage using higher order responses and phase space technique. *Structural Control and Health Monitoring*, e2808. <https://doi.org/10.1002/stc.2808>.



Thank you for your order!

Dear Mr. Zhen Peng,

Thank you for placing your order through Copyright Clearance Center's RightsLink® service.

Order Summary

Licensee:	Mr. Zhen Peng
Order Date:	Feb 18, 2022
Order Number:	5252251485318
Publication:	Structural Control and Health Monitoring
Title:	Improving identifiability of structural damage using higher order responses and phase space technique
Type of Use:	Dissertation/Thesis
Order Total:	0.00 AUD

View or print complete [details](#) of your order and the publisher's terms and conditions.

Sincerely,


Copyright Clearance Center

Tel: +1-855-239-3415 / +1-978-646-2777.
customer@copyright.com
<https://myaccount.copyright.com>




RightsLink®

Peng, Z., Li, J., & Hao, H. (2022). Data driven structural damage assessment using phase space embedding and Koopman operator under stochastic excitations. *Engineering Structures*, 255, 113906. <https://doi.org/10.1016/j.engstruct.2022.113906>.

	<p>Data driven structural damage assessment using phase space embedding and Koopman operator under stochastic excitations</p> <p>Author: Zhen Peng, Jun Li, Hong Hao Publication: Engineering Structures Publisher: Elsevier Date: 15 March 2022</p> <p><small>© 2022 Elsevier Ltd. All rights reserved.</small></p>
<p>Journal Author Rights</p> <p>Please note that, as the author of this Elsevier article, you retain the right to include it in a thesis or dissertation, provided it is not published commercially. Permission is not required, but please ensure that you reference the journal as the original source. For more information on this and on your other retained rights, please visit: https://www.elsevier.com/about/our-business/policies/copyright#Author-rights</p> <p>BACK CLOSE WINDOW</p>	

Peng, Z., Li, J., & Hao, H. (2022). Structural damage detection via phase space based manifold learning under changing environmental and operational conditions. *Engineering Structures*, 263, 114420. <https://doi.org/10.1016/j.engstruct.2022.114420>.

	<p>Structural damage detection via phase space based manifold learning under changing environmental and operational conditions</p> <p>Author: Zhen Peng, Jun Li, Hong Hao Publication: Engineering Structures Publisher: Elsevier Date: 15 July 2022</p> <p><small>© 2022 Elsevier Ltd. All rights reserved.</small></p>
<p>Journal Author Rights</p> <p>Please note that, as the author of this Elsevier article, you retain the right to include it in a thesis or dissertation, provided it is not published commercially. Permission is not required, but please ensure that you reference the journal as the original source. For more information on this and on your other retained rights, please visit: https://www.elsevier.com/about/our-business/policies/copyright#Author-rights</p> <p>BACK CLOSE WINDOW</p>	

Peng, Z., & Li, J. (2022). Phase space reconstruction and Koopman operator based linearization of nonlinear model for damage detection of nonlinear structures. *Advances in Structural Engineering*, 25(7), 1652-1669. <https://doi.org/10.1177/13694332221082729>.



Phase space reconstruction and Koopman operator based linearization of nonlinear model for damage detection of nonlinear structures

Author: Zhen Peng, Jun Li
Publication: *Advances in Structural Engineering*
Publisher: SAGE Publications
Date: 04/01/2022

Copyright © 2022. © SAGE Publications

BIBLIOGRAPHY DISCLAIMER

Every reasonable effort has been made to acknowledge the owners of copyright material. I would be pleased to hear from any copyright owner who has been omitted or incorrectly acknowledged.